Nucleation, growth and behavior of dust particles in reactive low pressure radiofrequency plasmas: From nanocrystals to submicron polycrystalline grains.

Marjorie Cavarroc

UNIVERSITE D'ORLEANS

THESE PRESENTEE A L'UNIVERSITE D'ORLEANS

POUR OBTENIR LE GRADE DE

DOCTEUR DE L'UNIVERSITE D'ORLEANS

Discipline : Physique des plasmas

par

Marjorie CAVARROC

Nucléation, croissance et comportement de poussières dans les plasmas réactifs radiofréquence basse pression: Des nanocristaux aux grains submicroniques polycristallins

Soutenue le 22 octobre 2007

Membres du Jury :

- J.M. Pouvesle, Directeur de Recherche, GREMI, Orléans (F)	**Président du jury**
- J. Winter, Professeur, Institut für Experimentalphysik II, Bochum (D)	**Rapporteur**
- G.M.W. Kroesen, Professeur, CPPRT, Eindhoven (NL)	**Rapporteur**
- F. Arefi-Khonsari, Professeur, LGPPTS, Paris (F)	**Examinateur**
- G. Cernogora, Professeur, Service d'Aéronomie, Verrières le Buisson (F)	**Examinateur**
- P. Roca i Cabarrocas, Directeur de Recherche, LPICM, Palaiseau (F)	**Examinateur**
- H. Vach, Directeur de Recherche, LPICM, Palaiseau (F)	**Examinateur**
- L. Boufendi, Professeur, GREMI, Orléans (F)	**Directeur de thèse**

CENTRE NATIONAL DE LA RECHERCHE SCIENTIFIQUE

Région Centre

École polytechnique de l'université d'Orléans

Nucleation, growth and behavior of dust particles in reactive low pressure radio frequency plasmas: From nanocrystals to submicron polycristalline grains

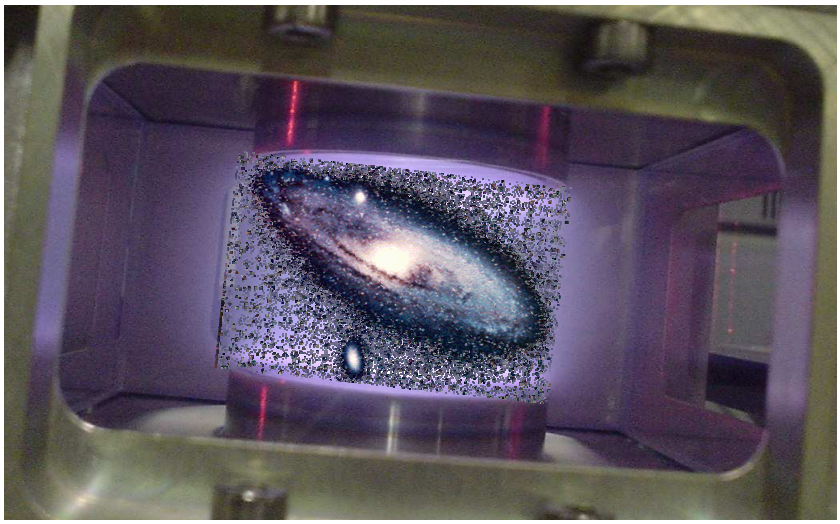

GREMI

With magic, you can turn a frog into a prince.
With science, you can turn a frog into a PhD,
and you still have the frog you started with.
Terry Pratchett

Acknowledgments

Le meilleur ami de "merci" est "beaucoup".
Michel Bouthot

Beaucoup de gens ont contribué à cette thèse, à différents niveaux. Eh oui, en thèse il n'y a pas que la Science qui compte...! Je voudrais les remercier tous ici, en espérant n'oublier personne.

Cette thèse a été réalisée principalement au GREMI où il fait bon travailler (et pas que travailler ;)). Un grand merci à TOUS.GREMI pour la bonne ambiance qui règne au labo. Et surtout merci à Jean-Michel POUVESLE, directeur du GREMI, pour m'avoir accueillie, mais aussi pour sa grande patience, son écoute attentive et ses immenses qualités humaines.

Merci à tout le staff administratif : Evelyne COUDERT, Sylvie JAUFFRION et Christophe DUBOIS. Sans vous je me serais perdue corps et biens dans les sables mouvants de l'administration. Merci d'avoir rempli tous les formulaires XX31262FW en 15 exemplaires à la plume d'oie sur papier bleu canari pour moi pendant ces 3 ans. Et surtout merci pour votre sourire quotidien, votre gentillesse et votre disponibilité.

Une spéciale dédicace aux membres passés et actuels de la Dusty Team :
Marie-Christine JOUANNY, Khalid RADOUANE, Aziz MEZEGHRANE, Lénaïc COUËDEL (courage, la fin est proche futur Dr!), Gaëtan WATTIEAUX.
Merci à Yves TESSIER pour sa gentillesse et son efficacité hors norme pour tout réparer ;)
Un immense merci à Maxime MIKIKIAN pour son encadrement "hyper haut de gamme", mais surtout pour sa patience, son écoute, sa gentillesse et son amitié sans faille. Sans toi cette thèse ne serait pas ce qu'elle est.

Merci à Philippe LEFAUCHEUX, Guy COUDRAT, Bernard DUMAX, Jacky MATHIAS et Sébastien DOZIAS pour m'avoir aidée à résoudre efficacement tout un tas de problèmes qui me passaient largement au-dessus de la tête.

Merci aussi à ma nouvelle équipe (au moins pour quelques temps...) : Pascal BRAULT, Anne-Lise THOMANN, Vincent DOLIQUE (excellent commercial surtout pour les meubles ;)) et Monsieur le nouvel Ingénieur de Recherche Hervé RABAT (j'ai rarement rencontré quelqu'un d'aussi sympa et qui mange autant de Kinder ;)).

Un grand merci à tous les thésards et ex-thésards (il paraît que dans ce cas-là on dit docteurs...) du GREMI et leur petite famille :

Steph' (Stéphanie GUILLOT), Vaness' et Yann (Vanessa VIAL et Yann WROTNY), Ouassi (Ouassima SARROUKH), Rati (Ratiba BENZERGA), Marie (Marie-Christine JOUANNY), Xav' et Fati (Xavier et Fatima MELLHAOUI), Mamaël (Amaël CAILLARD), Clément et Séverine et Chloé (Clément ZAEPPFEL et Séverine GOBET), Fakhri (Fakreddine OUNI), Edwardo (Edward ROMERO), Pascale et Thomas (Pascale PLANTIN et Thomas CAPELLE), Seb et Seb (Sébastien KOUASSI et POINT), Lénaïc (Lénaïc COUEDEL), Titi (Thierry DUFOUR), Alain (Alain LEUFROY), Binjie et Jinjia (Binjie et Jinjia DONG), Sylvain et Fanny (Sylvain TRICOT et Fanny NOURY)...

Tom (Thomas TILLOCHER) : merci pour tout (je suis sûre que tu comprendras ;))

Une spéciale dédicace au Girl Power du labo : Lisa (Dr Elise EL-AHMAR ;)), Coco (Corinne DULUARD) et Lolo (Laurianne PICHON), sans oublier Fafa (Bébé François, qui a eu le temps de rentrer en maternelle avant que je ne finisse cette thèse!)

Des encouragements pour ceux qui viennent de se lancer dans l'aventure : Gaëtan WATTIEAUX, Emmanuel LE BOULBAR, Eliane AMIN CHALHOUB, Hermane MBITSI, Ekaterina REZUGINA, Romain JOUSSOT... Vous verrez, la thèse c'est pas si mal ;)

Merci aussi à tous les "intermittents de la recherche" (on dit postdocs ?) du GREMI : Alexey LAZURENKO, Houcine OUBENSAID, Nadia SBAI, Frédéric GEGOT, Larbi BEDRA, Murielle MANIN, Elodie HENAFF (qui n'est pas vraiment postdoc, mais bon...), Karim KEDDADOUCHE (pas vraiment postdoc non plus...) et Jérôme PONS...

Et aux nombreux stagiaires avec qui j'ai eu l'occasion de travailler : Gaëlle PERRIER, Aurélie BRUN, Maxence MOUNIER, Enguerran DELAVAQUERIE, Sébastien LECOCQ, Julien PALISSON, Grégory BROUARD, Matthieu VOGT, Elodie BRUNEAU, Simon BULOU, Guillaume CLAIR...

Merci aussi à tous les permanents du GREMI qui assurent cette super ambiance : Olivier AUBRY, Jean-Marc BAUCHIRE, André BOUCHOULE (ok, ancien permanent ;)), Christophe CACHONCINLLE, Jean-Marie CORMIER, Rémi DUSSART, Tita GIBERT (et Ninon pour ses jolies cartes ;)), Dunpin HONG, Ahmed KHACEF, Chantal LEBORGNE, Erwan LE MENN, Eric MILLON, Pierre RANSON, Eric ROBERT, Nadjib SEMMAR, Raymond VILADROSA...

Et comme cette thèse ne s'est pas faite qu'au GREMI... je voudrais aussi remercier:

La Dusty Team du Service d'Aéronomie : Guy CERNOGORA (merci d'avoir pris part à mon jury), Cyril SZOPA et Grégoire ALCOUFFE.

La Dusty Team d'Experimental Physik II : Jörg WINTER (merci d'avoir été rapporteur de cette thèse, et de m'avoir accueillie à Bochum), Suk-Ho HONG, Christian SCHARWITZ, Janine SCHAUER, Jens RÄNSCH, Raphaela WEISS.

La Dusty Team du FEMAN : Enric BERTRAN, Sabine PORTAL.

La Dusty Team du LPICM : Pere ROCA i CABARROCAS (merci d'avoir pris part à mon jury).

La Dusty Team de l'EPG : Gerrit KROESEN (merci d'avoir été rapporteur de cette thèse), Loek BAEDE, Jérôme REMY et Misha SOROKIN.

Annie RICHARD du Centre de Microscopie Electronique pour ses super images MEB.

Marylène VAYER et Julien DUDOGNON du CRMD pour les images AFM.

Farzaneh AREFI-KHONSARI et Holger VACH pour avoir pris part à mon jury de thèse.

L'EDST et le service Recherche : Luc MORIN-ALLORY, Dominique BIZIERE et Sylvie BARGAIN.

Polytech'Orléans : Denis LEBRUN, Michel GRIFFAULT, Sophie RAGER, Marie-Hélène GOBBEY, Mahmoud IDIR, Pierre CHANSIGOT, Cécile PICHARD...

Les copains d'autres labos : Garrett CURLEY, Kathlin DE BLEECKER, Venardi SUENDO, Ivana RICHTEROVA, Gabriele THIEME, Jami HAFIZ...

Et comme il n'y a pas que le travail dans la vie...
Merci au trio infernal, j'ai nommé C2R2 (Maxime MIKIKIAN), Joe (Spider Pons, euh... Jérôme PONS), Super CD (Christophe DUTOUQUET)... et le célèbre blaireau fantôme, tous *Doctorum dermus balloe et balinus crinis* (j'assume l'entière responsabilité de ce titre ;)). C'est cool d'avoir des amis comme vous ;)
Et un immense merci à ma meilleure amie (Charlyne TACHE) : 24 ans d'amitié, ça se fête !!!

Pour finir, c'est bien connu, on garde toujours le meilleur pour la fin...
Merci à ma famille : aux Taties (Christine, Evelyne...), Tontons (Jean-Claude, Fabrice, Laurent...) et Cousins/Cousines (Audrey, Lulu et les autres...) et à Mamy Paulette.
Le plus grand des "MERCI" à Papa, Maman, Béreng' et Nat pour m'avoir toujours soutenue et donné l'envie (et les moyens) d'aller toujours plus loin.
Et une pensée pour Papy Génia, Mémé, Mamy Yvette et Tatie Evelyne qui n'étaient plus là pour me voir soutenir cette thèse. Mais je suis sûre que là où vous êtes, vous êtes fiers de moi...

Le 22 octobre 2007,
Marjo

Il n'existe que deux choses infinies,
l'univers et la bêtise humaine...
mais pour l'univers,
je n'ai pas de certitude absolue.

Albert Einstein

Contents

List of Figures

List of Tables

Introduction

Ce n'est qu'en essayant continuellement que l'on finit par réussir.
Autrement dit : plus ça rate, plus on a de chances que ça marche.
Les Shadoks

Les gaz ionisés contenant de fines particules solides (présentant des tailles allant du nanomètre au micromètre) sont communément appelés les plasmas poussiéreux, poudreux, voire plus récemment "complexes" (*dusty or complex plasmas*). On les rencontre aussi bien à l'état naturel que dans l'industrie, sur Terre ou dans l'Espace.

En astrophysique, les plasmas poussiéreux sont omniprésents : milieux interplanétaires, queues de comètes, nuages interstellaires, anneaux de planètes, atmosphères planétaires... Dans l'industrie, on les trouve principalement dans les procédés de microélectronique (dépôt, gravure par plasma) et de traitement de surface.

Dans l'industrie de la microélectronique, éviter l'apparition et surtout le dépôt des poussières lors des nombreuses étapes de procédé est un véritable défi technologique [1]. A l'opposé, la synthèse de ces mêmes poussières est un enjeu à la fois scientifique et technologique pour la production de poussières analogues à celles présentes en astrophysique [2], ou pour la production de cristaux de taille nanométrique [3]. C'est autour de ce second axe qu'ont été articulées les différentes études présentées dans cette thèse.

En effet, les plasmas poussiéreux sont de véritables sources de nanoparticules aux propriétés variées et novatrices. Ils constituent notamment des sources très attractives pour la production d'îlots quantiques (*quantum dots*) [4] présentant de nombreuses applications possibles en nanotechnologie. On peut par exemple citer le transistor à un électron [5] ou les mémoires silicium non-volatiles [6]. Les plasmas poussiéreux permettent aussi le dépôt de matériaux nanostructurés : des grains nanométriques sont inclus dans une matrice amorphe. Ces nouveaux matériaux présentent des propriétés mécaniques, optiques, électriques améliorées. Ainsi, le silicium polymorphe (*pm-Si*), constitué de nanocristaux de silicium inclus dans une matrice de silicium amorphe, permet de fabriquer des cellules photovoltaïques à rendement plus élevé et plus stable dans le temps que celles fabriquées en silicium amorphe [7, 8]. Les plasmas poussiéreux se sont aussi révélés plus récemment être de très bons outils

pour simuler la synthèse d'aérosols dans certaines atmosphères planétaires, notamment celle de Titan [2].

Cependant, afin d'exploiter efficacement la source de nanoparticules que représentent les plasmas poussiéreux, il est indispensable de développer les connaissances et les outils nécessaires au contrôle des propriétés de ces poussières.

Il existe en effet deux principaux moyens de synthétiser des poussières dans un plasma : soit par pulvérisation d'une cible ou d'un matériau déposé, soit en utilisant un gaz réactif tel que le silane, le méthane ou l'acétylène. Afin de pouvoir contrôler au mieux la décharge, et de ce fait la synthèse de poussières, un diagnostic électrique qui ne perturbe pas la décharge a été mis au point au laboratoire [9]. C'est d'ailleurs le principal diagnostic qui a été utilisé au cours de cette thèse.

L'objectif de cette thèse était de réussir à synthétiser des poussières de taille et/ou composition chimique maîtrisées en vue de différentes applications. Pour cela, nous nous sommes basé sur les quatre thèses réalisées précédemment au laboratoire et dédiées à ce type de plasmas. Les thèses de J.Ph. Blondeau [10] et L. Boufendi [11] ont servi de références sur les mécanismes de formation et de croissance des poussières. La thèse de S. Huet [12] a apporté les premiers élément concernant les effets notamment de la température de gaz sur les propriétés des nanocristaux de silicium (taille, structure), et la thèse de M.C. Jouanny [13] m'a servi de référence quant au diagnostic électrique développé et calibré pendant sa thèse.

Cette thèse a été réalisée dans le cadre d'une collaboration nationale et de séjours de recherche dans les laboratoires suivants :

- Le Service d'Aéronomie de Verrières le Buisson, en France, où nous avons partagé notre expertise en terme de diagnostics électriques dans une décharge en chimie méthane-azote.
- L'Institut für Experimentalphysik II de Bochum, en Allemagne, où j'ai acquis un certain nombre de connaissances sur l'ellipsométrie in-situ sur des poussières synthétisées en chimie acétylène-azote.
- Le groupe de Física i Enginyeria de Materials Amorfs i Nanoestructures (FEMAN) de Barcelone, en Espagne, où j'ai pu acquérir une vision plus globale des applications des nanocristaux de silicium tournées notamment vers les nanotechnologies.

Le travail présenté s'articule autour de trois principaux axes :

- La localisation et l'étude du démarrage de la phase d'agrégation des nanocristaux ont d'abord été réalisé au travers de l'étude paramétrique d'une instabilité. Ce travail a été suivi par une étude de la forme et du comportement du nuage de poudres au cours de la croissance de poussières dans deux décharges différentes. Ces études, présentées dans les chapitres III et IV de la thèse, ont été réalisées dans le but d'affiner notre compréhension des phénomènes de croissance de poussières et des perturbations

(spatiales, temporelles...) qu'ils induisent. Ces résultats nous ont notamment permis d'optimiser nos paramètres de dépôt pour la synthèse de nanoparticules de silicium monocristallines non-agglomérées.

- Une étude sur la synthèse de poussières en chimie à base d'hydrocarbures, dans le but de produire des poussières analogues aux tholins de Titan ou aux grains interstellaires, a été réalisée. Ce travail a été mené en collaboration avec Pr. Cernogora et Dr. Szopa au Service d'Aéronomie et, Pr. Winter and Dr. Hong à l'Institut für Experimentalphysik II. Ces études, présentées dans le chapitre V, m'ont permis d'appréhender la formation de poussières en chimie carbonée.
- Une étude visant à contrôler la taille des nanocristaux de silicium via une modification de la température de gaz dans la décharge est finalement présentée dans le chapitre VI.

Le synoptique ci-dessous présente la structure de cette thèse, organisée en six chapitres.

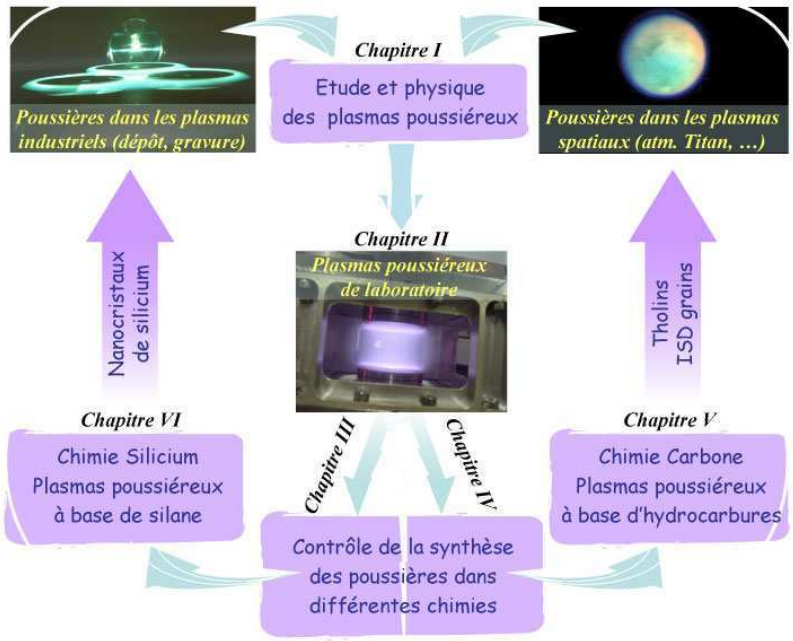

Cette thèse a été réalisée dans le cadre du label européen. Elle est donc rédigée en partie en anglais (tous les chapitres purement scientifiques), et en partie en français (introduction, conclusion et résumé de chaque chapitre scientifique).

This PhD thesis has been realized in the frame of the European label. It is therefore written part in English (all the scientific only chapters) and part in French (introduction, conclusion and summary of each scientific chapter).

Chapter I

Plasma Physics: Some notions

In physics and chemistry, a plasma is typically a partially or fully ionized gas. It is usually considered as the fourth state of matter after solid, liquid and gas (see figure I.1) and corresponds to the most disordered state of matter. A plasma is an electrically conductive collection of charged and neutral particles (electrons, ions, atoms, molecules, ...), that responds collectively to electromagnetic forces.

Plasma is the most common phase of matter. It is often said that 99% of the Universe consists of plasma. Even if it is quite impossible to verify or to disprove, we can be sure that the space between stars is filled with a plasma (a very sparse one). Our Solar system is also permeated with plasma such as the Sun, solar winds, planet atmospheres (Earth, Titan ...), Saturn's rings ... On Earth, some examples of natural plasmas are flashes and polar lights (see table I.1). Figure I.2 illustrates various kinds of plasmas.

Artificially produced plasmas are also easy to find. The most outstanding example is lighting (candle flame, fluorescent lamp, neon signs ...). They also occur in the array of industrial processes: thin film deposition, etching or sputtering ... Their range of applications is very wide: surface, gas and liquid treatments, solar cell or micro circuit fabrication are a few examples among lots of others. They are also found in fusion devices such as Tore Supra or the future reactor ITER. A simple discharge schematically consists of a voltage source that drives current through a low-pressure gas between two parallel conducting electrodes.

The plasma state is characterized by a charged particle density $n_e \approx n_i \approx n$ particles/m^3 (where e and i stand respectively for electrons and ions). A plasma is at thermodynamic equilibrium when temperature $T_e = T_i = T_g$ (this notion will be developed further in I.2). These two parameters are often used to make some plasma classifications (cold or hot plasmas, high or low density plasmas). Figure I.3 shows different kinds of plasmas on a log T_e versus log n diagram. There is a wide range of densities and temperatures for both laboratory and space plasmas.

I.1 A brief history of plasma physics

The first glow discharge vacuum tube was made by M. Faraday in 1838 using brass electrodes and a vacuum of approximatively 2 Torr. In 1857 the platinum-to-glass seal was invented allowing the production of sealed-off glow discharge tubes (Geissler tubes). In 1860, J.H. Hittorf noted that "cathode rays" projected "shadows" in a gas discharge tube. W. Crooke made some studies on these "cathode rays" in 1879. The nature of the Crooke tube "cathode rays" was identified by Sir J.J. Thompson in 1897. He identified them as negative particles that were the same as Stoney's "electrons". The Nobel prize-winning I. Langmuir was the first to use the term plasma to described an ionized gas in 1928 [14]. In Greek, plasma ($\pi\lambda\alpha\sigma\mu\alpha$) means "moldable substance" or "jelly". Several explanations for the choice of this term have been put forward. Maybe Langmuir was reminded of the way blood carries red and white corpuscles by the way electrified fluid carries electrons and ions. Or maybe the mercury arc plasma he worked with tended to diffuse throughout their glass vacuum chambers filling them like jelly in a mold. Who knows ...

After Langmuir, plasma research gradually spread in other directions. The development of radio broadcasting led to the discovery of the Earth's ionosphere leading E.V. Appleton and K.G. Budden to develop a theory of electromagnetic wave propagation through a non-uniform magnetized plasma. Astrophysicists quickly realized that most of the Universe consists of plasma, requiring a better understanding of plasma physics. H. Alfvén was a pioneer in this domain and developed the theory of magnetohydrodynamics around 1940. The creation of the hydrogen bomb in 1952 generated a great deal of interest in controlled thermonuclear fusion as a possible energy source. In the 1960's, the development of high powered lasers opened up the field of laser plasma physics. At the same period, the first "ion guns" were developed by the NASA for space propulsion. Presently, plasmas are used in numerous industrial processes. As an example, chemically reactive plasma discharges are widely used to modify the surface properties of materials for applications in the electronics, aerospace, automotive, steel, biomedical and environmental industries.

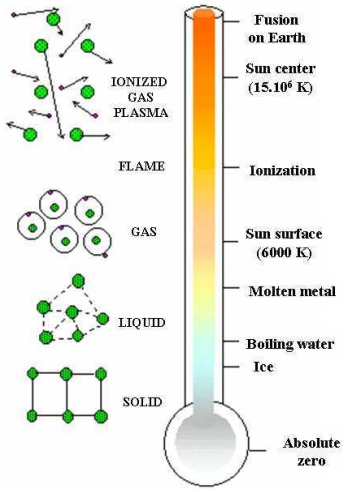

Figure I.1: The four states of matter (adapted from [15]).

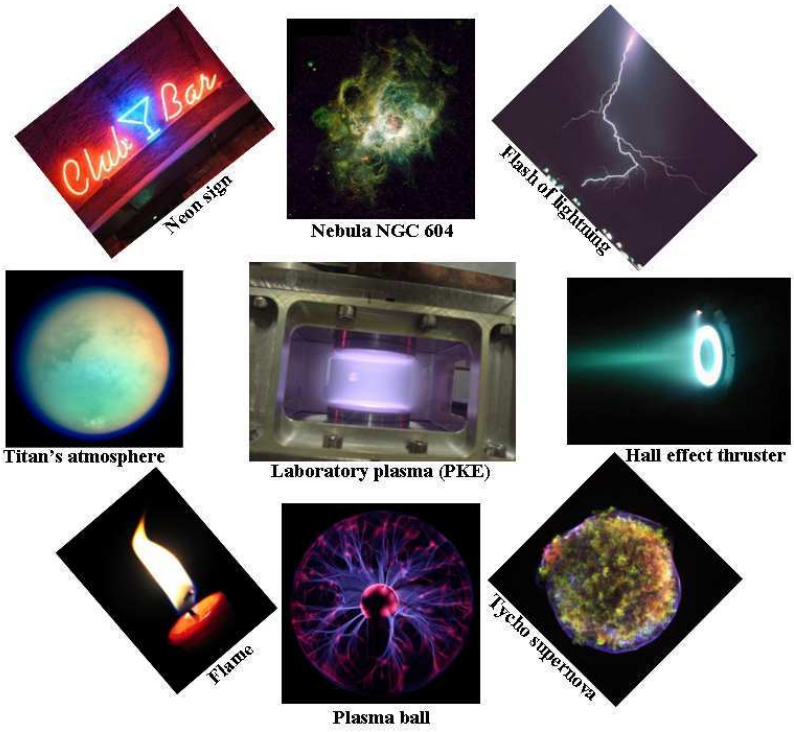

Figure I.2: Overview of various plasmas: laboratory plasma (GREMI's PKE), neon sign, nebula NGC 604 (Hubble Space Telescope photo PR96-27B), flash of lightning, plasma of a Hall effect thruster, Tycho supernova remnant (x-ray photo), plasma ball (Courtesy L. Viatour), candle flame, Titan's atmosphere (IR photo taken on January 14th 2006 by Cassini probe).

Space plasmas	Natural plasmas on Earth	Artificially produced plasmas
Sun and stars	Flashes	Candle flame
Solar wind	Polar lights	Fluorescent lamp
Nebulae	Aurora borealis	Neon signs
Interplanetary medium	Aurora australis	Plasma displays
Titan atmosphere	Ionosphere	Laboratory plasmas
Saturn's rings	St Elmo's fire	Hall effect thrusters
Io Jupiter flux tube	Sparks	Tokamak plasmas
...	...	...

Table I.1: Some examples of space plasmas, natural plasmas on Earth and artificially produced plasmas.

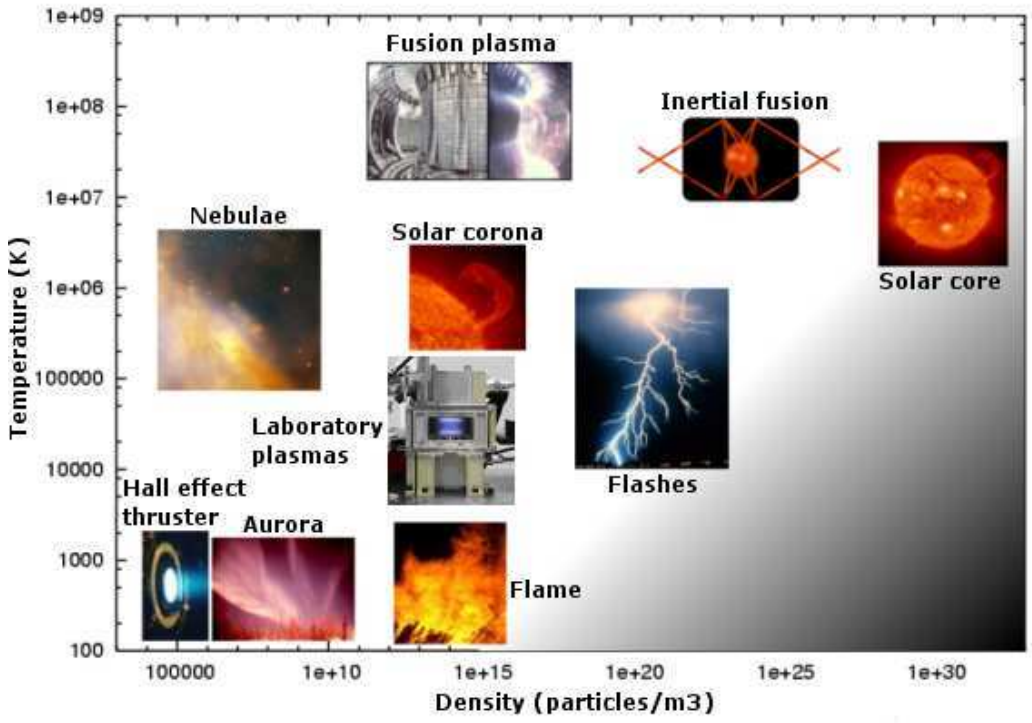

Figure I.3: Space and laboratory plasmas on a temperature versus density diagram.

I.2 Basic parameters

In this section, some fundamental parameters in plasma physics are introduced. More explanations and demonstrations can be found in books as well in English as in French (see for example [16, 17, 18, 19, 20, 21]).

I.2.a Densities and ionization degree

The plasma is composed of electrons, with a density n_e and a charge q_e, positive or negative ions, with a density n_i or n_- and a charge q_i or q_-, and neutral atoms or molecules with a density n_n.

The ionization degree is defined as follow:

$$\alpha_i = \frac{n_e}{n_e + n_n} \tag{I.1}$$

The collection of free charges is, on the average, electrically neutral thereby:

$$n_e q_e + n_i q_i + n_- q_- = 0 \tag{I.2}$$

The ionization degree permits to distinguish weakly ionized plasmas ($10^{-6} < \alpha_i < 0.1$) such as ionosphere, industrial or laboratory plasmas, and strongly ionized plasmas ($\alpha_i \approx 1$) such as stellar or thermonuclear plasmas.

I.2.b Thermodynamic state

The kinetic state of the various species is characterized by three temperatures T_e, T_i, T_n, respectively the electron, ion and neutral temperature, often given in eV ($1\ eV = 11605\ K$). Those temperatures have a rigorous signification only if the velocity distribution function $f_j(w_j)$ for the species j, defined as follow:

$$n_j = \iiint f_j(w_j) d^3 w_j \tag{I.3}$$

is maxwellian:

$$f_j = n_j \Big(\frac{m_j}{2\pi k_B T_j} \Big)^{3/2} e^{-\frac{m_j w_j^2}{2 k_B T_j}} \tag{I.4}$$

where n_j, m_j and T_j are respectively species j density, mass and temperature, and k_B the Boltzmann constant.

Thus, T_j is linked to the species j average kinetic energy by:

$$m_j \frac{< w_j^2 >}{2} = \frac{3}{2} k T_j. \tag{I.5}$$

The thermal velocity is defined as follow:

$$< w_j >= \sqrt{\frac{8 k_B T_j}{\pi m_j}}, \tag{I.6}$$

and can be written for the electrons as:

$$< w_e > (cm.s^{-1}) = 6.7.10^7 \sqrt{T_e(eV)}. \tag{I.7}$$

At complete thermodynamic equilibrium, all temperatures T_j are equal and constant in the medium. It is seldom the case in a discharge plasma. In accordance with the discrepancy to the equilibrium state, the plasma can be :

- at local thermodynamic equilibrium, such as temperatures from different species vary in space but are locally equal:

$$T_e(r) = T_i(r) = T_n(r) \tag{I.8}$$

- at partial thermodynamic equilibrium, for example with two temperatures:

$$T_e(r) > T_i(r) = T_n(r) \tag{I.9}$$

- out of equilibrium:

$$T_e(r) > T_i(r) > T_n(r) \tag{I.10}$$

I.2.c Debye length

Neutrality is only a macroscopic property of the plasma. In fact, a charged particle is surrounded by a number of other charged particles with an opposite sign. The particle charge is screened over a distance called Debye length. This is the distance on which the influence of a charged particle can be felt by other charged particles. λ_{De} and λ_{Di} are respectively electron and ion Debye length and are defined as follow:

$$\lambda_{De,i} = \left(\frac{\epsilon_0.k_B.T_{e,i}}{n_{e,i}.e^2}\right)^{1/2} \tag{I.11}$$

As the electron mobility is higher than the ion one, screening is mainly due to electrons. The Debye length λ_D gives the characteristic length scale of a plasma and can be written as:

$$\lambda_D \simeq \lambda_{De} = \left(\frac{\epsilon_0.k_B.T_e}{n_e.e^2}\right)^{1/2} \tag{I.12}$$

Practically, it can be given by:

$$\lambda_D(cm) \simeq \lambda_{De}(cm) = 6.9\sqrt{\frac{T_e(K)}{n_e(cm^{-3})}} = 743\sqrt{\frac{T_e(eV)}{n_e(cm^{-3})}} \tag{I.13}$$

In our typical experimental conditions where T_e = few eV and n_e = few 10^{15} m^{-3}, λ_D is of a few hundreds micrometers. The plasma can be considered as neutral on space scales larger than a Debye length.
In some particular cases, the linearized Debye length is used. It is defined as follows:

$$\lambda_{DL} = \frac{\lambda_{De}.\lambda_{Di}}{\sqrt{\lambda_{De}^2 + \lambda_{Di}^2}} \tag{I.14}$$

Further explanations will be given in section I.4.a.ii.

I.2.d Plasma frequency

When a plasma is instantaneously disturbed from its equilibrium, collective motions appear. They are characterized by an oscillation frequency called plasma frequency ω_p. This frequency is not the same for electrons and ions but depends on the mass, charge and density of the plasma particles. Particles (electrons and ions) oscillate around their equilibrium position with the plasma frequency:

$$\omega_p = \sqrt{\frac{q_p^2 n_p}{\epsilon_0 m_p}} \tag{I.15}$$

where q_p, n_p and m_p are respectively the particle mean charge, density and mass. The electron plasma frequency can also be written as:

$$f_{pe}(Hz) = \frac{\omega_{pe}}{2\pi} = 9000\sqrt{n_e(cm^{-3})} \tag{I.16}$$

and the ion plasma frequency, for ions carrying one charge, can be written as:

$$\omega_{pi} = \omega_{pe}\sqrt{\frac{m_e}{m_i}} \tag{I.17}$$

In our typical experimental conditions, f_{pe} is a few GHz while f_{pi} is a few MHz . As f_{pe} and f_{pi} give the order of magnitude of the particle response time to an electric field, one can conclude that in a 13.56 MHz excited rf discharge, electrons can oscillate in the rf field while ions can only see a time averaged field.

I.3 Introduction to radio frequency discharges

Radio frequency discharges are widely used in plasma processing technologies. Chemical reactive plasmas are often used to modify surface properties of material. Their range of applications is very wide: thin layer deposition, etching, surface functionalization... Typically, these discharges are performed at low pressure (a few μbar to a few mbar). They are characterized by a relatively low electron/ion density of approximatively 10^9 to 10^{10} cm^{-3}, an electron temperature comprised between 1 and 10 eV and an ion temperature equal to neutral temperature around 0.03 eV (room temperature). All the following information concerning rf discharges can be found in ref.[16].

I.3.a Rf diodes

Capacitively driven rf discharges are often called rf diodes. An idealized discharge in plane geometry consists in two planar electrodes, separated by a distance typically comprised between 2 and 10 cm, enclosed in a vacuum chamber and driven by a rf power source. The typical rf driving voltage is V_{rf} = 100-1000 V , and the most common used frequency is 13.56 MHz. The operation of capacitively driven discharges is reasonably well understood.

The mobile plasma electrons, responding to the rf field, oscillate back and forth within the positively charged cloud of ions. Oscillation of the electron cloud creates sheath regions near each electrode.

I.3.b Sheaths

Quasineutral plasmas are joined to wall surfaces across thin positively charged layers called sheaths. Sheath regions contain net positive charge when averaged over an oscillation period. In fact, as electrons have a higher thermal velocity (i.e. are faster) than ions, they are lost to the wall faster than the ions. The boundary potential is thus negative with respect to the plasma. The positive charge exceeds the negative one in the system (plasma bulk and sheaths), with the excess appearing within the sheaths. This excess produces a strong time-averaged electric field in each sheath directed from the plasma to the electrode. This field allows to keep the quasi-neutrality of plasma bulk by limiting electron losses to the wall. Typically, low voltage sheaths are a few Debye length wide.

According to the inhomogeneous model of a symmetric capacitive discharge developed by M.A. Lieberman and A.J. Lichtenberg in [16], the relationship between the rf voltage (V_{rf}) and rf current (I_{rf}), involving the total sheath capacitance (C_s), is non-linear:

$$I_{rf}(t) = C_s \frac{d}{dt} V_{rf}(t) \tag{I.18}$$

In a current-driven discharge, this leads to the appearance of harmonics in the rf voltage. By simulation, only odd harmonics are produced. No second harmonic is observed, and the third harmonic is estimated to be 4.2% of the fundamental.

I.3.c α and γ regimes of the discharge

Capacitively coupled rf discharges are known to exist in two different forms: α and γ regimes, corresponding to two different electron heating mechanisms. A visual difference in the glow emission distribution can be seen by naked eye. It is due to different processes at the electrodes.

The α regime is characterized by a diffuse glow, with dark sheaths and bright presheaths. The primary sustaining mechanism is the ionization due to the electrons in the plasma bulk, also called volume ionization. The ionized gas conductivity is weak. The low discharge current is mostly capacitively coupled, and is displacement current. This form is also characterized by the dominance of the surf effect for electron heating: electrons gain energy following the sheath wave movement (rf sheath expansion and contraction) [21].

When the voltage applied to an α discharge is increased, it suddenly transforms to the γ form, that is characterized by an intensive emission glow, nearly uniform. The sheath length decreases. The primary sustaining mechanism is then the secondary electron emission and the ionization due to the electron accelerated in the sheath. The ionized gas conductivity

is high, the discharge current is considerable and secondary emission takes place at the electrode (cathode mainly) [21].

A third form can be distinguished: the γ' form, characterized by a dominant ohmic heating of electrons, without any secondary emission. This form is observed in dusty plasmas, when dust particles are highly charged. In this case, the free electron density is drastically decreased. In order to maintain the discharge, the electron temperature increases, leading to this particular case of the γ mode.

The denotation α and γ has been adopted from the Townsend's first ionization coefficient (α) for the avalanche of charge carriers in the volume, and γ for the ion induced secondary emission [22].

I.3.d Self-bias voltage and area ratio law

A self-bias voltage is set at the driven electrode of a cc-rf discharge if both electrodes differ in size and when a coupling capacitor is inserted between the rf generator and the electrode (or when the electrode is non-conductive). In most cases, capacitive discharges are asymmetric, with more electrode surface grounded than driven. In the following, V_p is the plasma potential, V_{driven} is the average dc voltage drop between the plasma and the driven electrode and $V_{grounded}$ is the one between the plasma and the grounded electrode (see figure I.4). The self-bias voltage, set-up at the driven electrode, is defined as:

$$V_{dc} = -(V_{driven} - V_{grounded}) \tag{I.19}$$

and is negative in the usual case with $V_{grounded} < V_{driven}$.

Setting-up of the self-bias voltage

If one considers a given sinusoidal voltage, applied to the capacitor formed by the electrodes, first the voltage over the plasma is the same as the applied voltage. During the first half-period, when the voltage is positive, electrons are accelerated toward the driven electrode. The capacitor is charged up by the electron current, and the voltage over the plasma drops. On the second part of the cycle, the applied voltage changes polarity, hence the voltage over the plasma as well. The capacitor is now charged up by the ion current, and the voltage over the plasma drops as well. Nevertheless, this second drop is less pronounced due to the lower mobility of ions compared to electrons. At the next half-cycle, the applied voltage (and the voltage over the plasma) changes polarity once again. The charging process occurs until the capacitor is sufficiently negatively charged so that the electron and ion fluxes (integrated over a rf cycle) are equal. This process finally results in a time-averaged dc bias at the driven electrode. We can note that this process also occurs at the grounded electrode, but with a much lower effect [22].

Area ratio law

The self-bias voltage depends on the area ratio of the electrodes and can be deduced from the so-called area ratio law. The potential distribution in the inter-electrode space is shown in figure I.4 in the case of $A_{grounded} > A_{driven}$. A_{driven} and $A_{grounded}$ are the areas of respectively the driven and the grounded electrode.

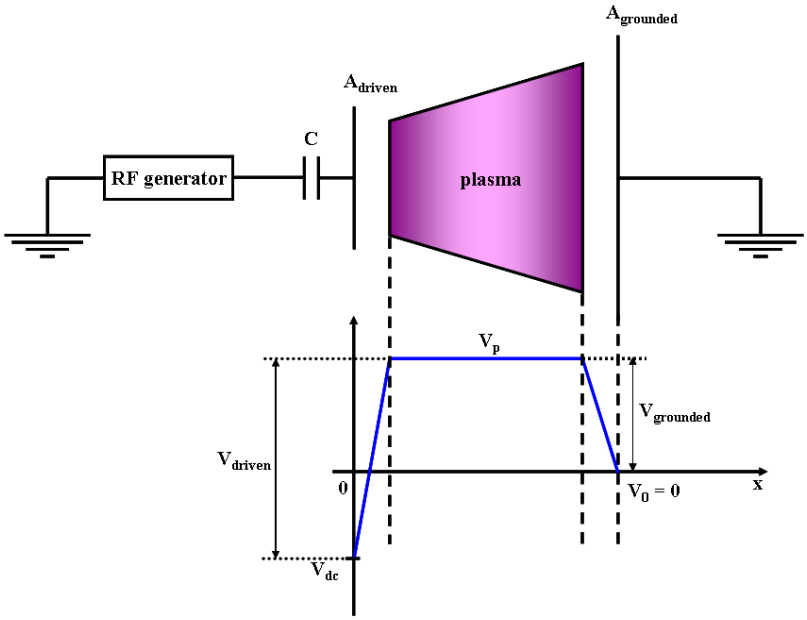

Figure I.4: Potential distribution in the electrode gap in the case of $A_{grounded} > A_{driven}$.

According to the capacitive sheath approximation, the average value of the plasma potential $\bar{V}_p$ depends on the rf voltage amplitude V_{rf} and the self-bias voltage V_{dc} as:

$$\bar{V}_p = \frac{1}{2}(V_{rf} + V_{dc}). \tag{I.20}$$

As V_{driven} and $V_{grounded}$ are respectively the average potential drops at the driven and at the grounded electrode, the area ratio law is given by

$$\frac{V_{driven}}{V_{grounded}} = \left(\frac{A_{grounded}}{A_{driven}}\right)^n \qquad 1 \leq n \leq 4 \tag{I.21}$$

The value of n depends both on the assumptions supporting a given model and on the considered plasma conditions. As $V_{driven} = \bar{V}_p - V_{dc}$ and $V_{grounded} = \bar{V}_p$, equation I.21 becomes

$$\left(\frac{1 - V_{dc}/V_{rf}}{1 + V_{dc}/V_{rf}}\right) = \left(\frac{A_{grounded}}{A_{driven}}\right)^n \tag{I.22}$$

In reference [23] M. Mohamed Salem and J.F. Loiseau give an overview of the exponent value obtained from four classical models (see table I.2).

Reference	Assumptions	Exponent value
Koenig and Maissel [24]	Current density of positive ions equal and uniform at both electrodes Collisionless and purely capacitive sheaths	$n = 4$
Maniv [25]	Ion currents equal and uniform at the electrodes Collisionless and purely capacitive sheaths	$n = 2$
Pointu [26]	"Frozen ions" model $\omega_{pi} \ll \omega \ll \omega_{pe}$	$n = 4$ collisionless sheaths $n = 3$ collisional sheaths, low field $n = 5/2$ collisional sheaths, high field
Turban [27]	Ion currents equal and uniform at the electrodes Purely capacitive sheaths	$n = 2$ collisionless sheaths $n = 3/2$ collisional sheaths, no ionization

Table I.2: Summary of four classical models on the area ratio law (adapted from [23]).

I.4 What about dusty plasmas?

A dusty plasma (also referred as "complex plasma" in the literature), is as its name indicates, a "classic plasma" that contains dust grains. This additional charged species makes the system even more complex than a plasma system. Dust grain size can range from nanometer to millimeter. They can be made of almost any sort of matter (silicon, carbon, ice, polymer, ...) and be of various shape (spherical, cauliflower, fractal structure...). The dust particle presence in the discharge implies new phenomena such as collective behavior of the dust cloud, inhomogeneities (void region), instabilities ...

There are different manners to get a dusty plasma in the laboratory. Calibrated dust particles can be introduced in the discharge (Melamine Formaldehyde (MF), silicates in the μm size range). Dust particles can be grown in the plasma by sputtering a target or a deposited layer (polymer, carbon, silicon ...), or using a reactive gas (silane, methane, acetylene, ...). The scope of this thesis is the study of dust particle formation and growth in silane/rare gas discharges, and more especially in silane/argon ones. First studies of dust particle formation in SiH_4 based discharges were performed in the 1980's using laser light scattering [28]. Since then, dust particle formation has been widely studied both in Europe and Japan. Lots of publications have been produced on this topic (see for example [29, 30, 31, 32, 33]) and some books are especially devoted to dusty plasma physics such as [34] or [18].

I.4.a Dusty plasma basic characteristics

The presence of dust particles in the plasma leads to the definition of some new parameters in order to describe phenomena linked to this additional charged species. Thus, macroscopic neutrality, Debye shielding and characteristic frequencies have to be re-examined in this particular case.

I.4.a.i Macroscopic neutrality

A dusty plasma, as a classic plasma, is macroscopically neutral. Due to their charge, dust particles have to be taken into account in the neutrality condition. Thus, in presence of charged dust particles, equation I.2 becomes:

$$n_e q_e + n_i q_i + n_- q_- + N_d Q_d = 0 \tag{I.23}$$

where N_d and Q_d are respectively dust particle density and charge. In most laboratory dusty plasmas, dust grain charging processes lead to a drastic depletion of free electrons in the plasma.

I.4.a.ii Linearized Debye length

The Debye length is a measure of the shielding distance or the thickness of the sheath. In a dusty plasma, the linearized Debye length defined by equation I.14 is often used. Indeed, dust particles can be considered as individually isolated particles only if the plasma physical dimensions are larger than the Debye length. In a dusty plasma with negatively charged dust grains, $\lambda_{DL} \simeq \lambda_{Di}$. The shielding distance (or the sheath length) is mainly determined by the ion temperature and density. In the case of positively charged dust particles (seldom), $\lambda_{DL} \simeq \lambda_{De}$ meaning that the shielding distance (or the sheath length) is mainly determined by the electron temperature and density.

I.4.a.iii Dust plasma frequency

In the same way as we defined an electron (ion) plasma frequency, a dust plasma frequency can be defined:

$$\omega_{pd} = \sqrt{\frac{Q_d^2 N_d}{\epsilon_0 m_d}} \tag{I.24}$$

Thus, when dust particles are displaced from their equilibrium position, they oscillate around this position with a frequency ω_{pd}. Depending on the dust particle size, charge and density, ω_{pd} can be comprised between a few hundred Hz and a few kHz.

I.4.b Dust formation in silane based plasmas

Presently dust particle formation is known to occur in various reactive gases such as silane or hydrocarbon, but the mechanisms leading to the formation are not totally elucidated yet. The behavior of "big" dust particles ($r_d \geq$ a few nm) is quite well understood, while the formation and the chemistry of the first proto-particles is still little-known.

It has been shown in previous works that dust formation in an Ar/SiH_4 rf discharge is a four step process [12, 11, 35]. It begins with the formation of proto-particles leading to the formation of the first primary clusters of atoms during a "*nucleation phase*" also called

"*polymerization phase*". Those clusters next accumulate up to a critical density during an "*accumulation phase*". Then the "*aggregation phase*", that consists in a fast agglomeration of these clusters, takes place leading to dust particles around 50 nm. Finally, those dust particles grow by accretion of plasma species during the "*surface deposition phase*".

In the following, the main characteristics of each step are summarized, and figure I.5 gives a synopsis of dust particle formation and growth in a typical Ar/SiH_4 rf discharge.

Nucleation and polymerization phase

At the ignition of the discharge silane molecules break into lower silicon hydrides due to collisions with electrons. Those hydrides can be neutrals, cations, or anions. In the presence of argon, the production of neutral radicals is enhanced due to high rate constant for dissociation of SiH_4 by collision with Ar^* or Ar^+. Hence, in Ar/SiH_4 discharges, the neutral radical density is much higher than cation and anion densities at the plasma ignition [36]. Neutral radicals, having one or more dangling silicon bonds, are highly reactive to polymerize into neutral clusters ($Si_nH_x, 0 \leq x \leq 2n+2$) with an average size of 0.5 nm ($n = 4$) [36]. Diffusion to the walls of these neutral clusters prevents them to grow into larger size. Direct formation of silicon hydride anions such as SiH_3^-, SiH_2^- and SiH^- can be caused by dissociative attachment of electrons with silane molecules:

$$e + SiH_4 \longrightarrow SiH_x^- + (4-x)H \tag{I.25}$$

Hollenstein et al. [37] demonstrated, thanks to mass spectroscopy measurements of neutral, positive and negative Si_nH_x, that the negative ion path is clearly involved in a discharge quite similar to the one we use. Thus, anions such as SiH_3^- or $Si_2H_5^-$ react with vibrationally excited SiH_4^* molecules in polymerization reactions:

$$\begin{array}{ccc} SiH_3^- + SiH_4^* & \longrightarrow & Si_2H_5^- + H_2 \\ Si_2H_5^- + SiH_4^* & \longrightarrow & Si_3H_7^- + H_2 \\ \vdots & \vdots & \vdots \\ Si_nH_{2n+1} + SiH_4^* & \longrightarrow & Si_{n+1}H_{2n+3}^- + H_2 \end{array} \tag{I.26}$$

leading to formation of bigger and bigger clusters [38]. Once the critical cluster size (around 2-3 nm in diameter at room temperature) is reached, polymerization reactions slow down and stop. In our experimental conditions, those 2-3 nm clusters have been shown to be single-crystal silicon nanoparticles in the fcc phase [39]. They will be referred as "nanocrystals" in the following. During this polymerization phase, the discharge is in the α regime exhibiting a capacitive behavior.

Accumulation phase

At the end of the polymerization phase, nanocrystals accumulate in the plasma until reaching a high density, evaluated around $10^{11} - 10^{12}$ cm^{-3} (by Laser Induced Particle Explosive Evaporation (LIPEE) measurements [35]) at room temperature. During this phase, the dust particle size remains constant and they are not able to attach and maintain one electron each. So their mean charge is relatively small (of the order of 0.03 electron). This value was deduced from the electron and ion densities, assuming that the plasma neutrality must be realized at any time [40]. The discharge is still in the α regime.

Aggregation phase

This fast agglomeration phase starts once the nanocrystal critical density is reached. Dust particle size increases by nanocrystal agglomeration while their density drastically decreases. Aggregation phase is a quite paradoxical phenomenon since dust particles are generally negatively charged, and thus have to overcome the Coulomb repulsion to coagulate. However, due to charge fluctuation of small clusters, two charged clusters (with radius smaller than a few nanometers) with different signs of electric charge, can attract each other and stick together by collision [41]. Agglomeration ends when dust particle charge becomes too important preventing them to stick together due to the Coulomb repulsion, that is to say once the dust particle sizes are around 40-50 nm in diameter. Once the coagulation started, already formed particles are very efficient traps for radicals, blocking the formation of new polymerization chains leading to nanocrystals. We assume that no more nanocrystals are formed in the discharge [40]. During this phase, dust particles collect more and more electrons on their surface (tens to hundreds electrons per dust particle), leading to an important decrease of free electron density. The ionization process needs to be increased to compensate electron losses. The $\alpha \rightarrow \gamma'$ transition takes place, the mean electron temperature increases from 2 to 8 eV [42]. The discharge behavior becomes resistive.

Surface deposition growth

This phase starts once the discharge is in the γ' regime. Dust particle growth is achieved through radical deposition on their surface, leading to an a-Si:H layer of growing thickness. The deposition rate is evaluated to 1.25 nm.s^{-1}. Dust particle density remains the same [40]. Ionization, dissociation and excitation rates increase a lot. When dust particles become too large (a few hundreds nm), they are expelled from the discharge.

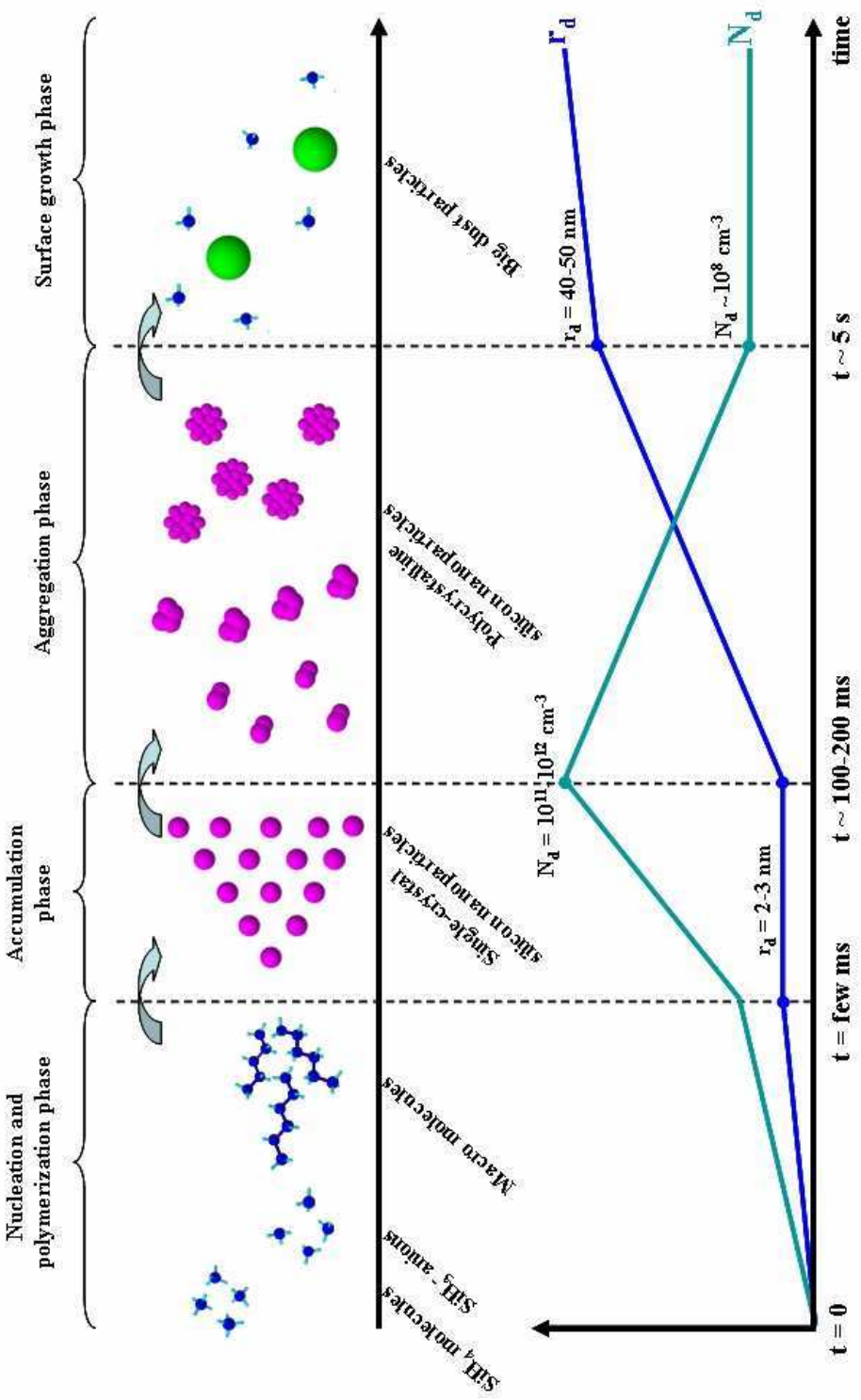

Figure I.5: Synopsis of the four step process of dust particle formation and growth in an Ar/SiH_4 plasma

I.4.c Isolated dust charge

In this section, we consider a spherical dust grain which is neither growing nor sputtered by the surrounding plasma. An isolated dust grain immersed in a plasma behaves like a small probe, collecting charges (i.e., electrons and ions) from the plasma. The dynamic charge Q_d of this grain is determined by:

$$\frac{dQ_d}{dt} = \Sigma I_k = 0 \tag{I.27}$$

where I_k are the different currents to the grain. The main species contributing to the net current are electrons and ions. Nevertheless, some other charging mechanisms can arise such as secondary emission at the grain's surface, photoelectric or thermoionic effect. In a low temperature laboratory plasma as the one we use, those three last effects can be neglected, and dust grain charge is assumed to be due to electrons and ions. As electrons are much more mobile than ions, an isolated dust grain immersed in a plasma will acquire a negative charge and thus exhibits a negative potential with respect to the plasma potential.

To be considered as isolated, a dust grain of radius r_d has to satisfy $r_d \ll \lambda_{DL} \ll d$, where d is the intergrain distance and λ_{DL} is the linearized Debye length. In this case, equation I.27 can be expressed as:

$$\frac{dQ_d}{dt} = I_e + I_i = 0 \tag{I.28}$$

where the electron (I_e) and ion (I_i) currents can be described by the orbital motion limited (OML) approach.

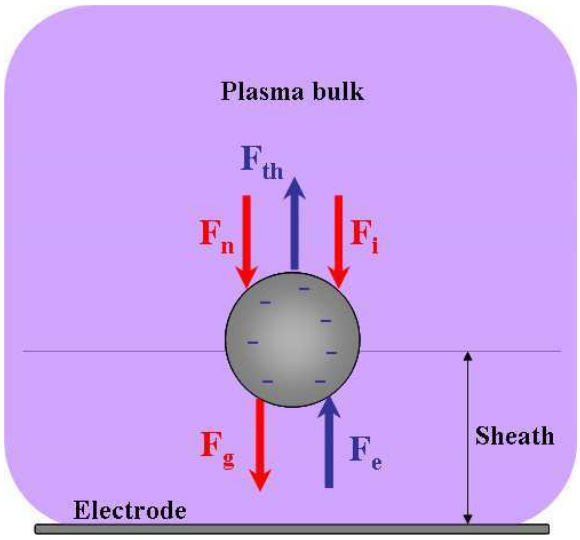

Figure I.6: Scheme of various forces experienced by an isolated charged dust particle immersed in a plasma.

The OML theory implies several hypothesis:

- electrons and ions move toward the dust grain from infinity on collisionless path
- electrons and ions are only subject to electronic interaction with the dust grain
- $r_d \ll l$: charge particle transport in the grain sheath is collisionless (l is the sheath thickness).

The OML charging current for ions is given by:

$$I_i = \pi r_d^2 e n_i \sqrt{\frac{8k_B T_i}{\pi m_i}} \Big(1 - \frac{eV_d}{k_B T_i}\Big) \tag{I.29}$$

and the OML charging current for electrons by:

$$I_e = -\pi r_d^2 e n_e \sqrt{\frac{8k_B T_e}{\pi m_e}} \quad e^{\Big(\frac{eV_d}{k_B T_e}\Big)} \tag{I.30}$$

where V_d is the potential difference between the dust grain surface and the plasma. Using those current expressions in equation I.28, we obtain:

$$e^{\Big(\frac{eV_d}{k_B T_e}\Big)} = \frac{n_i}{n_e} \Big(\frac{m_e T_i}{m_i T_e}\Big)^{\frac{1}{2}} \Big(1 - \frac{eV_d}{k_B T_i}\Big) \tag{I.31}$$

In a typical laboratory plasma (i.e. electropositive plasma), $n_i/n_e = 1$ and $T_e \gg T_i$, equation I.31 becomes:

$$V_d = \frac{k_B T_e}{2e}\, ln\Big(\frac{m_e T_e}{m_i T_i}\Big) \tag{I.32}$$

In an argon discharge, assuming $T_e \approx 100\, T_i$ [43]:

$$V_d \approx \frac{-2k_B T_e}{e} \tag{I.33}$$

Once the dust grain potential V_d is known, its charge can be deduced:

$$Q_d = 4\pi\epsilon_0 r_d V_d \tag{I.34}$$

This formula is for an isolated dust particle. However, the dust particle charge is not a static variable, but must be considered as a dynamical variable, especially when a whole cloud of charged particles is taken into account.

I.4.d Forces acting on an isolated dust particle

Dust particles immersed in a plasma experience various forces which confine them in the plasma or drag them outside (see figure I.6). In a capacitively coupled rf discharge, the electrostatic force tends to confine dust particles whereas other forces (gravity, ion and neutral drag) tend to eject them from the plasma [34]. Those different forces and their expression are given in the following sections, in the case of an isolated dust grain.

I.4.d.i Gravitation force

Earth's gravity force acting on a dust particle is proportional to the dust particle mass, or to its mass density and its volume:

$$\vec{F_g} = m_d\vec{g} = \frac{4}{3}\pi r_d^3 \rho \vec{g} \tag{I.35}$$

with $\vec{F_g}$ the gravitational force, $\vec{g}$ the gravitation field, m_d the dust particle mass, r_d its radius et ρ its mass density ($\rho = 2330$ kg.m^{-3} for silicon).

For submicron dust particles, this force is generally weak compared to the others. However, once the plasma is switched off, it can become the prevailing force.

I.4.d.ii Electrostatic force

This section gives a summary of the main results obtained by Daugherty, Porteous and Graves [44] and the ones obtained by Hamaguchi and Farouki [45].

Daugherty *et al* showed that the electrostatic force on a small dust particle (compared to the Debye length) due to an electric field in the plasma bulk can be approximated by the corresponding force on a charged sphere in vacuum $Q_d\vec{E_0}$. The main result to retain is that even if the sheath isolates the dust particle from the plasma, it does not screen the external applied field as well. Hamaguchi *et al* showed that the Debye sheath is not "attached" to the dust particle, but it behaves like a disruption of the surrounding plasma. Assuming that this sheath is not distorted by the external field, the resulting force is in the electric field direction $\vec{E_0}$ and is given by:

$$\vec{F_e} = Q_d\vec{E_0}\Big(1 + \frac{(r_d/\lambda_{DL})^2}{3(1 + r_d/\lambda_{DL})}\Big) \tag{I.36}$$

The first term of equation I.36 is the force which would be felt by the dust particle under the field $\vec{E_0}$ in vacuum. The second term corresponds to the dipolar force due to polarization of the surface charge. That means that the polarized surface charges induce an electric field which in turn exerts an electric force. Generally $r_d \ll \lambda_{DL}$ and the electrostatic force can be approximated by $Q_d\vec{E_0}$. Moreover, Hamaguchi *et al* pointed out that the field due to the polarization of charges on dust particles also exerts a force on the plasma, increasing the ion pressure on the dust grain. Assuming a Boltzmann ion density in the dust sheath, they showed that this ion pressure force exactly counterbalances the force due to surface charge polarization.

Hamaguchi *et al* also brought to the fore another contribution due to the Debye sheath distortion induced by the spatial dependence of the Debye length. Bouchoule showed that this additional force can be neglected in usual conditions ($r_d \ll \lambda_{DL}$) [34].

I.4.d.iii Thermophoretic force

When the gas temperature (and so the neutral temperature) is not uniform, a dust particle experiences a force induced by the thermal gradient. Considering molecules or atoms colliding with the dust grain, the warmest ones will transfer more momentum to the grain than the coldest ones. A force, called thermophoresis, results from this phenomenon, oriented in the heat flow direction (from warm to cold side).

Talbot *et al*, using the Chapman-Enskog method to solve the Boltzmann equation, gave the following expression of the thermophoretic force:

$$\vec{F_{th}} = -\frac{32}{15}\frac{r_d^2}{v_{th,n}}\Big(1+\frac{5\pi}{32}(1-\alpha_{th})\Big)\kappa_T \vec{grad}T_g \tag{I.37}$$

with $v_{th,n} = \sqrt{8k_BT_g/\pi m_n}$ the neutral thermal mean velocity, κ_T the gas thermal conductivity, T_g the gas temperature and α_{th} a corrective coefficient.

Talbot *et al* showed that for gas and dust grain temperatures lower than 500 K, α_{th} coefficient is approximatively 1 [46].

Rothermel *et al*, using elementary kinetics arguments, gave the following expression of the same force [47]:

$$\vec{F_{th}} = -\frac{8}{3}\frac{r_d^2}{v_{th,n}}\kappa_T \vec{grad}T_g \tag{I.38}$$

We can note that there is a gap of about 20% between these two formulae.

I.4.d.iv Neutral drag force

A dust grain immersed in a neutral gas is subject to a drag force due to the transfered momentum during collisions with atoms or molecules. Typically, in laboratory plasmas, the relative velocity between dust particles and molecules is smaller than the thermal velocity of gas molecules. In these conditions, the neutral drag force can be evaluated thanks to the Epstein relation [34]:

$$\vec{F_n} = -\frac{4}{3}\pi r_d^2 m_n n_n v_{th,n}(\vec{u_d} - \vec{u_n}) \tag{I.39}$$

with m_n the gas atom or molecule mass, n_n the gas density, $\vec{u_d}$ the dust particle velocity and $\vec{u_n}$ the gas atom or molecule velocity.

I.4.d.v Ion drag force

The ion drag force is due to momentum exchange between positive ions and the dust grain. This force may be important in regions where the ion flow is important. This force is made of two components: the collection force due to positive ion collection by the dust particle, and the Coulomb force due to electrostatic interactions between the dust particles and the ions.

The collection force can be expressed as follow:

$$F_{coll} = n_i \mu v_i^2 \sigma_{coll} = n_i \mu v_i^2 (\pi b_{coll}^2) \tag{I.40}$$

with n_i the ion density, v_i the ion velocity, $\mu = m_i m_d/(m_i + m_d)$ the reduced mass of the system, σ_{coll} the collection cross-section given by πb_{coll}^2 with b_{coll} the collection parameter.

The collection cross-section is given by:

$$\sigma_{coll} = \pi b_{coll}^2 = \pi r_d^2 \Big(1 - \frac{2eV_d}{m_i v_i^2}\Big) \tag{I.41}$$

As $m_d \gg m_i$, equation I.40 can be expressed as [48]:

$$F_{coll} = n_i \pi r_d^2 m_i v_i^2 \Big(1 - \frac{2eV_d}{m_i v_i^2}\Big) \tag{I.42}$$

The Coulomb force (also called orbit force) can be written as:

$$F_{coul} = n_i \mu v_i^2 \sigma_{coul} \tag{I.43}$$

with σ_{coul} the momentum cross-section. This parameter is obtained by calculating the following integral:

$$\sigma_{coul} = \int_{b_{coll}}^{\lambda_{DL}} 4\pi \frac{pdp}{1 + (p/b_{\pi/2})^2} \tag{I.44}$$

with p the impact parameter and $b_{\pi/2}$ is the parameter giving a $\pi/2$ deviation:

$$b_{\pi/2} = r_d \frac{-eV_d}{m_i v_i^2} \tag{I.45}$$

The integral I.44 is calculated between b_{coll}, in order to not take into account collected ions, and λ_{DL}, distance over which interactions become negligible.

Solving equation I.44 leads to the following expression for the momentum cross-section:

$$\sigma_{coul} = 2\pi b_{\pi/2}^2 ln\Big(\frac{\lambda_{DL}^2 + b_{\pi/2}^2}{b_{coll}^2 + b_{\pi/2}^2}\Big) \tag{I.46}$$

Finally the Coulomb force can be expressed as:

$$F_{coul} = n_i m_i v_i^2 2\pi b_{\pi/2}^2 ln\Big(\frac{\lambda_{DL}^2 + b_{\pi/2}^2}{b_{coll}^2 + b_{\pi/2}^2}\Big) \tag{I.47}$$

Another approach of the ion drag force can be found in [49].

I.4.d.vi Order of magnitude of the forces

In this section, the main forces acting on a dust particle are evaluated for different dust radii under typical conditions of a capacitively coupled (cc) rf Ar/SiH_4 discharge. In order to make the calculations, the following assumptions are made:

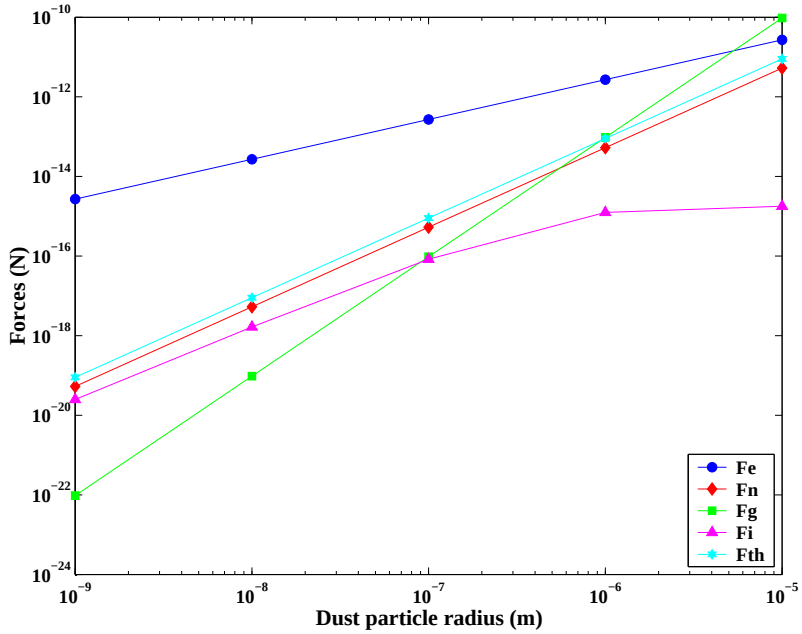

Figure I.7: Evolution of the main forces acting on a dust grain immersed in a plasma as a function of the grain radius.

- $E = 10^4\ V/m$ (in the sheath)
- $u_d - u_n = 0.1\ m.s^{-1}$ (assuming that the dust grain is immobile i.e. $u_d = 0$)
- $v_i = 400\ m.s^{-1}$
- $grad\, T_g = 10^3\ K.m^{-1}$ (10 K over 1 cm)

They permit to obtain the force expressions as a function of the dust particle radius:

- Electric force $F_e \approx 2.6.10^{-6}\ r_d$ (for $Q_d = 1e$)
- Gravity $F_g \approx 9.6.10^4\ r_d^3$
- Neutral drag force $F_n \approx 5.3.10^{-2}\ r_d^2$
- Ion drag force $F_i \approx 1.8.10^{-3}\ r_d^2\ ln\ (1 + 10^{-12}\ r_d^{-2})$
- Thermophoresis $F_{th} \approx 9.10^{-2}\ r_d^2$

Figure I.7 shows the evolution of the different force amplitudes for a dust particle radius from 1 nm to 10 μm. F_e is the dominant force in almost all cases (as far as $r_d \leq 5-6\mu m$) and confine dust particles in the plasma. It is important to note that $E = 10^4 V/m$ is the field value in the sheath. In the plasma bulk this value is much more lower, and in some cases F_i and F_{th} can overcome F_e. Dust particles are then expelled toward plasma boundaries where

the electric field is high enough to confine them back to the bulk. F_i and F_n are not able to counterbalance F_e but they are assumed to have an influence on dust particle transport in the discharge. F_g, which evolves as r_d^3, is negligible for nanoparticles but can become the dominant force for microparticles even overcoming F_e. In some cases, when $grad\, T_g$ is important enough and dust particles not too large, F_g can be counterbalanced by F_{th} allowing to trap microparticles in the discharge. Another way to investigate microparticles is the work under microgravity conditions during parabolic flights or during experiments on board the International Space Station (ISS) [50].

I.4.e Dust cloud shape and behavior

Depending on the dust particle size and the forces they experience, the dust cloud can exhibit various shapes. The most common shapes observed are: thin layers near the electrodes (figure I.8(a)), dome-like shape (figure I.8(b)) or dense cloud filling the whole interelectrode volume (figure I.8(c)). In some cases, crystalline regions (figure I.8(d)) and/or vortex (figure I.8(e)) can also be observed. The observed dust cloud structure is often very complex as can be seen in figure I.8(f).

When the dust particle density is sufficient, the appearance of a dust-free region inside the dust cloud can be observed (see figure I.9). These dust voids in complex plasmas have been observed for more than 10 years now. Their main distinctive feature is the sharp boundary between dust and dust-free regions. Dust voids are characterized by a higher ionization rate than the surrounding dust cloud. The theory of dust voids in complex plasmas is widely studied [51, 52, 53, 54]. Presently, the void is assumed to be maintained by a balance between an outward ion drag force (due to the high ionization rate) and an inward electrostatic force, both acting on dust particles.

The void region often exhibits an unstable behavior. This has been first brought to the fore by Praburam & Goree [55] and Samsonov & Goree [56] at the end of the 90's. They describe an instability having at least two distinct stages: the "filamentary mode" and the "great void mode" where they could observe void rotation. In 2004, Mikikian et al. reported on the so-called *heartbeat* instability consisting in successive contractions/expansions of the void region [57]. Moreover, the void region is often linked to dust particle growth, and especially to dust particle successive generations in complex plasmas. This will be developed further in chapter IV.

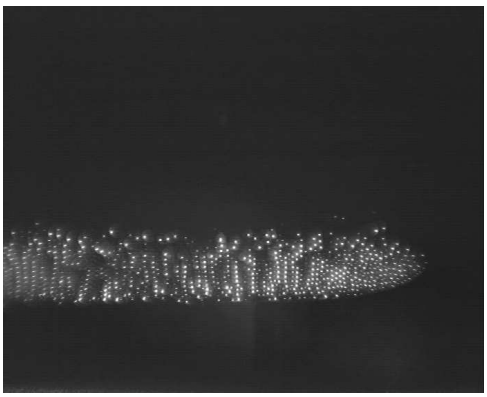

(a) Thin layers near the electrode.

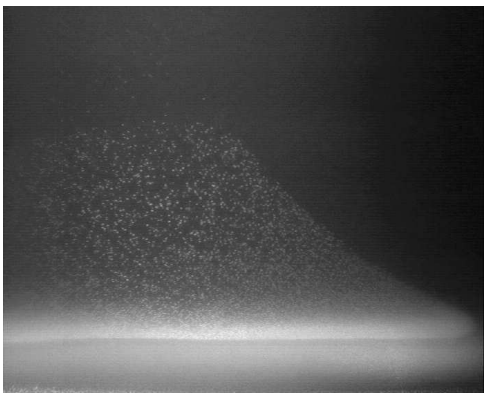

(b) Dome-like shape.

(c) Dense cloud.

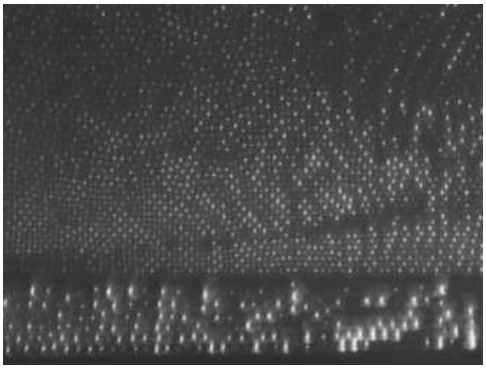

(d) Crystalline structure.

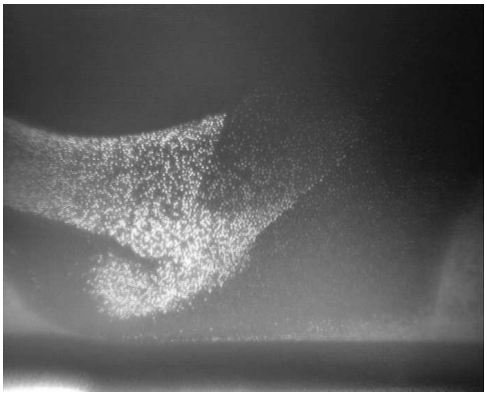

(e) Vortex.

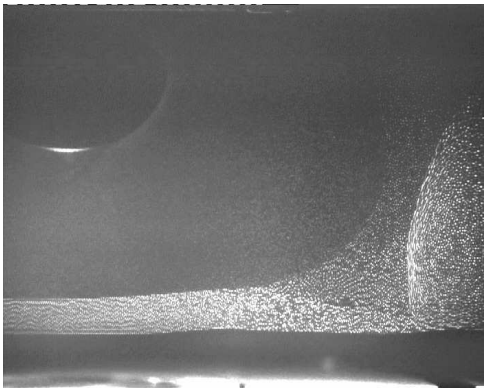

(f) Complex shape.

Figure I.8: Some examples of the various shapes of a dust cloud.

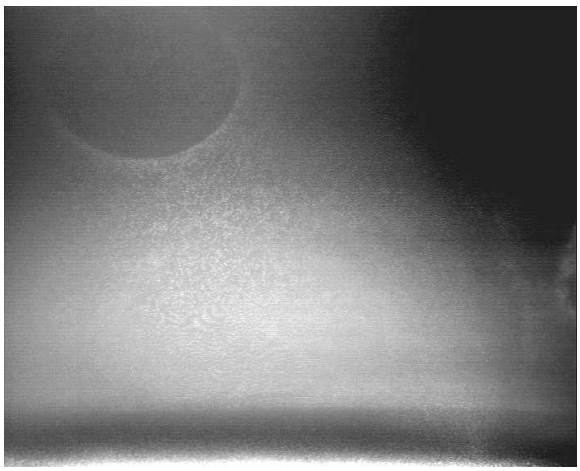

Figure I.9: Dust cloud exhibiting a void region.

I.5 French summary/Résumé en français

En physique/chimie, un plasma est typiquement un gaz partiellement voire totalement ionisé. On le considère habituellement comme le quatrième état de la matière après le solide, le liquide et le gaz comme le montre la figure I.1. C'est l'état le plus désordonné de la matière. Un plasma est un ensemble de particules chargées et neutres (électrons, ions, atomes, molécules, ...), qui répond collectivement aux forces électromagnétiques.

Le plasma est l'état de la matière le plus répandu. On dit souvent que l'Univers est constitué à 99% de plasma. Même si cette affirmation est impossible à vérifier ou à infirmer, nous pouvons être sûrs que l'espace entre les étoiles est un plasma (très peu dense). Notre système solaire est aussi grandement constitué de plasmas tels que le soleil, les vents solaires, certaines atmosphères de planètes (la Terre, Titan), les anneaux de Saturne, etc... Les éclairs et les aurores boréales sont des exemples de plasmas naturels sur Terre.

Il existe aussi de nombreux plasmas produits artificiellement. L'exemple le plus parlant est certainement l'éclairage (flamme d'une bougie, lampes fluorescentes, enseignes néon ...) On les trouve aussi beaucoup dans les procédés industriels tels que le dépôt de couches minces ou la gravure pour la microélectronique. Leur champ d'application est très étendu : le revêtement de surface, la fabrication de cellules solaires, la fabrication de micro-circuits sont quelques exemples parmi tant d'autres. Le tableau I.1 donne un aperçu des nombreux plasmas répertoriés. On les retrouve aussi dans les applications liées à la fusion telles que le réacteur Tore Supra ou le futur ITER. Typiquement, une décharge est constituée de deux électrodes parallèles entre lesquelles se trouve un gaz. Une source de tension permet de faire circuler un courant dans ce gaz, créant ainsi le plasma.

Physiquement parlant, l'état plasma est caractérisé par une densité de particules chargées $n_e \approx n_i \approx n$ particules/m^3 (où les notations e et i se rapportent respectivement aux élec-

trons et aux ions). Il est à l'équilibre thermodynamique lorsque $T_e = T_i = T$. Ces deux paramètres (température et densité) sont souvent utilisés pour classifier les plasmas (plasma chaud ou froid, plasma dense ou non). La figure I.3 donne un aperçu des différents types de plasmas sur un graphique $\log T_e/\log n$. On peut ainsi constater que les gammes de densités et de températures sont très vastes tant pour les plasmas spatiaux que pour les plasmas de laboratoire.

Petit historique de la physique des plasmas

Le premier tube à décharge a été réalisé par Faraday en 1838 à l'aide d'électrodes en laiton et d'un vide d'environ 2 Torr. En 1857, la soudure platine sur verre est mise au point, permettant la production de tubes à décharge scellés (les tubes de Geissler). En 1860, J.H. Hittorf remarque que des "rayons de cathode" projettent des "ombres" dans la décharge. W. Crooke mène une étude sur ces "rayons de cathode" en 1879. Leur nature est identifiée en 1897 par Sir J.J. Thompson. Il les identifie comme étant des particules négatives, les mêmes que les "électrons" de Stoney. Le lauréat du Prix Nobel, Irving Langmuir, est le premier à utiliser le terme plasma pour décrire un gaz ionisé en 1928 [14]. En grec, plasma ($\pi\lambda\alpha\sigma\mu\alpha$) signifie "substance modelable" ou "gelée". Différentes explications pour le choix de ce terme ont été avancées. Pour certains, la façon dont le plasma transporte les ions et les électrons lui aurait rappelé la façon dont le sang transporte les globules. Pour d'autres, le plasma d'arc de mercure sur lequel il travaillait aurait eu tendance à diffuser hors de la chambre, comme de la gelée remplissant un pot...

Après les recherches de Langmuir, la recherche dans le domaine des plasmas s'est développée dans d'autres directions. Le développement de la communication par ondes radio a permis la découverte de l'ionosphère terrestre, amenant E.V. Appleton et K.G. Budden à développer la théorie de la propagation des ondes électromagnétiques dans les plasmas magnétisés non-uniformes. Les astrophysiciens ont vite réalisé que la majorité de l'Univers était constituée de plasma, requérant de ce fait une meilleure compréhension de la physique des plasmas. H. Alfvén a été un pionnier dans ce domaine en développant la théorie de la magnétohydrodynamique dans les années 1940. La création de la bombe à hydrogène en 1952 a généré un grand intérêt pour la fusion thermonucléaire contrôlée comme possible source d'énergie. Dans les années 1960, le développement des lasers de puissance a permis l'essor de la physique des plasmas induits par laser. A la même période, les premiers "ion guns" ont été développés par la NASA pour la propulsion spatiale. A l'heure actuelle, les plasmas sont utilisés dans de nombreux procédés industriels. A titre d'exemple, les plasmas réactifs chimiquement sont utilisés pour modifier les propriétés de surface des matériaux pour des applications en électronique, dans l'aérospatiale, l'automobile, l'acier, le biomédical et l'industrie environnementale.

Les décharges radio-fréquence (rf) sont très largement utilisées dans le domaine des

procédés plasmas. On les utilise notamment en chimie réactive pour le traitement de surface (dépôt de couches minces, gravure, fonctionalisation de surface). En règle générale ces décharges se font à basse pression (quelques μbar à quelques mbar). Elles sont caractérisées par une densité électronique/ionique relativement faible aux alentours de 10^9 à 10^{10} cm^{-3}, une température électronique comprise entre 1 et 10 eV et une température ionique égale à la température des neutres autour de 0.03 eV (température ambiante) [16].

Les plasmas poussiéreux

Un plasma poussiéreux (aussi appelé "plasma complexe"), est, comme son nom l'indique, un plasma qui contient des grains de poussière. Cette espèce chargée supplémentaire rend le système encore plus compliqué qu'un plasma classique. La taille des grains peut aller du nanomètre au millimètre. Ils peuvent être constitués de divers matériaux (silicium, carbone, glace, polymère...) et être de formes variées (sphérique, chou-fleur, structure fractale ...). La présence des poussières dans la décharge implique de nouveaux phénomènes tels que le comportement collectif du nuage de poudres, des inhomogénéités ("void"), des instabilités...

Il y a différentes manières d'obtenir un plasma poussiéreux en laboratoire. Des grains de poussière calibrés peuvent être injectés dans la décharge (Mélamine Formaldéhyde ou silicate de taille micrométrique). Les poussières peuvent croître dans le plasma par pulvérisation d'une cible ou d'une couche de dépôt (carbone, polymère, silicium...) ou à partir d'un gaz réactif (silane, méthane, acétylène...). Dans le cadre de cette thèse, c'est la formation de poudres en chimie silane/gaz rare, et plus particulièrement silane/argon qui a été étudiée. Les premières études de formation de poudres en chimie silane ont été réalisées dans les années 1980 [28]. Depuis, ce sujet a été largement étudié notamment en Europe et au Japon. Ces études ont donné lieu à de nombreuses publications (voir par exemple [29, 30, 31, 32, 33]) et certains livres sont exclusivement dédiés à la physique des plasmas poussiéreux comme [34] et [18].

A l'heure actuelle, la formation de poudres est un phénomène avéré dans de nombreux gaz réactifs comme le silane ou les hydrocarbures, mais les mécanismes menant à cette formation ne sont pas encore totalement compris. Le comportement des "grosses poudres" (rayon supérieur à quelques nm) est relativement bien compris, tandis que la formation et la chimie des premières protoparticules sont toujours mal connues.

Schématiquement, la croissance de poudres dans un plasma de gaz réactif débute par la formation de protoparticules qui vont former les premiers clusters d'atomes pendant la "phase de nucléation" aussi appelée "phase de polymérisation". Ces clusters s'accumulent ensuite jusqu'à atteindre une concentration critique durant la "phase d'accumulation". Lorsque cette concentration est atteinte, la "phase d'agglomération" débute. Elle consiste en une agglomération ou coagulation rapide des clusters, menant à des poudres d'une cinquantaine de nm. Finalement ces poudres grossissent par accrétion en surface des rad-

icaux du plasma pendant la "phase de croissance par dépôt de surface". Ces différentes étapes de formation des poussières sont résumées sur le graphique I.5 dans le cas d'un plasma d'argon/silane.

Charge et forces sur les poussières

Lorsque qu'un grain de poussière est immergé dans le plasma, il se comporte comme une sonde de petite taille, collectant les espèces chargées (électrons et ions) du plasma. Le grain tend ainsi à se charger négativement. Ce même grain subit différentes forces qui tendent à le maintenir dans le plasma ou à l'en expulser. La force de gravité F_g est proportionelle à la masse du grain (ou à sa masse volumique et son rayon). Pour les grains submicroniques, elle est en général très faible comparée aux autres forces. Par contre, à l'extinction du plasma, elle devient la force prépondérante. La force électrostatique est due à la charge que porte le grain dans le champ électrique de la décharge. Elle s'exprime en général de la façon suivante: $\vec{F_e} = Q_d\vec{E_0}$ et c'est dans la majorité des cas la force la plus importante que subit le grain. Lorsque la température du gaz n'est pas uniforme, le grain est soumis à la force de thermophorèse F_{th} qui tend à le faire migrer vers les zones les plus froides. Le grain subit aussi une force de poussée F_n due aux atomes et aux molécules neutres du plasma, ainsi qu'une force F_i due aux échanges de quantité de mouvement avec les ions. Si l'on compare les ordres de grandeur de ces différentes forces pour différentes tailles de grains (voir figure I.7) on constate que F_e est prédominante dans la majorité des cas, et confine les poudres dans le plasma. F_i et F_n ne sont pas capables d'équilibrer F_e mais peuvent avoir une influence sur le transport des poudres dans le plasma. F_g est négligeable pour les nanoparticules mais peut devenir prédominante pour les microparticules. Dans certains cas, lorsque les particules ne sont pas trop grosses, F_{th} peut équilibrer F_g de façon à piéger les poudres dans la décharge. Il existe aussi deux autres moyens de s'affranchir de la force de gravité que subissent les grosses poudres : les expériences lors de vols paraboliques ou à bord de l'ISS (station spatiale internationale) [50].

L'équilibre entre les différentes forces agissant sur les poussières façonne le nuage de poudres, lui donnant des formes diverses et complexes. La figure I.8 donne un aperçu des formes les plus courantes : couches minces proches des électrodes, nuage en forme de dôme, nuage dense, structure cristalline du nuage... Des structures fluides telles que des vortex sont parfois observées. La figure I.8(f) donne un exemple de structure complexe du nuage de poudres. Lorsque la densité de poussières est suffisamment importante, on peut observer l'apparition d'une zone vide de poudres au sein du nuage, appelée le "void" (cf. figure I.9). Cette structure est largement étudiée à l'heure actuelle, tant sur le plan théorique [51, 52, 53, 54] que sur le plan expérimental. Il a notamment été montré que le "void" présentait souvent un caractère instable [55, 56, 57]. Cet aspect particulier du comportement du "void" sera développé plus amplement dans le chapitre IV de cette thèse.

Chapter II

Experimental setups and diagnostics

The main experimental setup described in this chapter (located in the GREMI laboratory) is the one I mainly used to perform the experiments presented in this thesis. Several other setups (located in partner laboratories for some of them) have also been used. We can especially cite the PAMPRE experiment (French acronym for Production d'Aérosols en Microgravité par Plasma REactif - Aerosol Production in Microgravity by REactive Plasma) and the PKE setup (Plasma Kristall Experiment). The PKE setup is briefly introduced in this chapter, while the PAMPRE setup will be introduced in chapter IV.
The GREMI setup has been widely described in several PhD thesis and publications [11, 12, 13, 30, 58]. However, several modifications have been performed in order to improve the setup. Thus all the setup vacuum components, rf equipment, optics installation and gas system are described in details in this chapter.

Standard experimental conditions are defined in terms of gas flow, total pressure, injected power, and gas temperature. They will be widely used in this thesis. The substrate preparation is detailed for various types of substrates (silicon wafer, stainless steel, Corning glass ...). The experimental protocol for depositions is explained both for substrates in the discharge box or in post discharge.

The main diagnostics we used are also introduced. *In-situ* diagnostics such as current and voltage measurements, V_{dc}/3H based diagnostics, Langmuir probes, microwave resonant cavity method, optical emission spectroscopy or laser light scattering are presented. The video imaging system is also shortly described. Several *ex-situ* diagnostics such as electron microscopy (scanning and transmission) or atomic force microscopy are also briefly explained.

II.1 Silane experiment

II.1.a Experimental setup

The whole experimental setup (figure II.1) has already been described in several papers and thesis [11, 12, 13, 30, 58]. As we realized some modifications, a detailed description is given in the following parts.

II.1.a.i Plasma chamber

The plasma chamber consists in a vacuum vessel with a cylindrical discharge box (135 mm in diameter and 37.5 mm in height) made of stainless steel enclosed, where the plasma is generated. This plasma box is grounded and behaves like the rf discharge anode (figure II.2). Its base is closed by a 20% transparency grid, allowing to get a laminary gas flow in our range of pressure (around 0.1 mbar). The rf electrode, also in stainless steel, closes the top of the plasma box. It is a shower-head type electrode (12.8 cm in diameter and 1 cm in height). Rf polarisation and gas flow are ensured by a stainless steel tube. A ceramic insulator is placed around the tube to electrically insulate the rf electrode from the ground. Inside the rf electrode, there are three parallel grids separated by 1 mm. They make a diffuser ensuring an uniform gas distribution in the plasma box. Rf and grounded electrodes are separated by 33 mm (figure II.3). The whole system (rf electrode and plasma box) can be vertically moved thanks to a stepper. Moreover, the lateral side of the plasma box is pierced by four vertical slits (2 mm by 4 cm), allowing optical access to the plasma in two perpendicular directions. In front of the slits, the vacuum vessel is equipped with three Suprasil III windows. Those windows are transparent for wavelengths comprised between 190 and 3500 nm (UV - near IR). The window sides are not parallel. One of them is tilted by 1^o, in order to avoid troubles linked to interferences (scattering and/or diffraction) when laser beams are used.

II.1.a.ii Gas and vacuum systems

Pumping is ensured by two vacuum systems (primary and secondary) having complementary purposes. The primary pump (chemical mechanical vacuum pump, Alcatel 2033 CP, 35 $m^3.h^{-1}$) is specially designed to pump reactive gases. It can reach a pressure around 10^{-3} mbar in the vacuum vessel. This pumping system has two purposes. First it is used to empty the vacuum vessel before using the secondary pump. Second, it pumps gases during the experiments and maintains the working pressure. This pump is separated from the reactor by an electropneumatic valve and a manual one.

When silane is added to the discharge, it is necessary to inject N_2 in a continuous flow in the primary pump (1.5 $l.min^{-1}$). This gas flow avoids silane accumulation in the pump and allows to dilute silane at less than 1%. It permits to avoid any risk of inflamation and/or

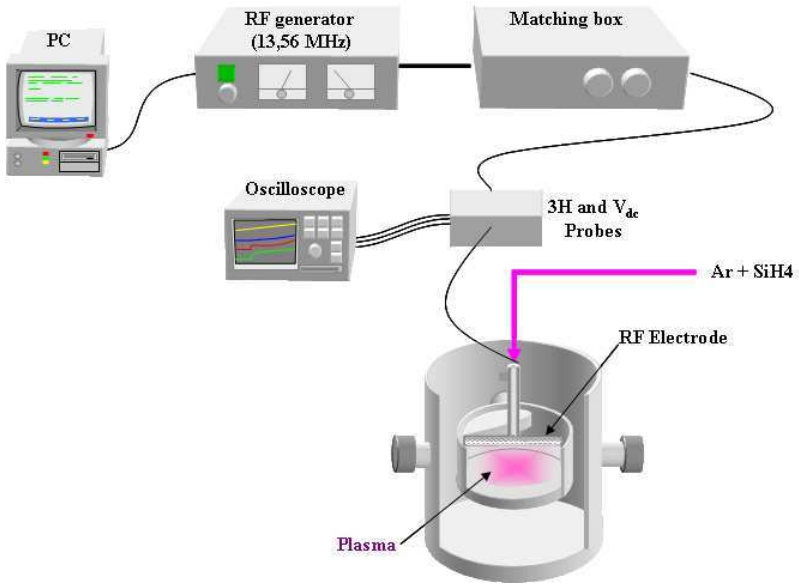

Figure II.1: General overview of the experimental setup in its most common configuration.

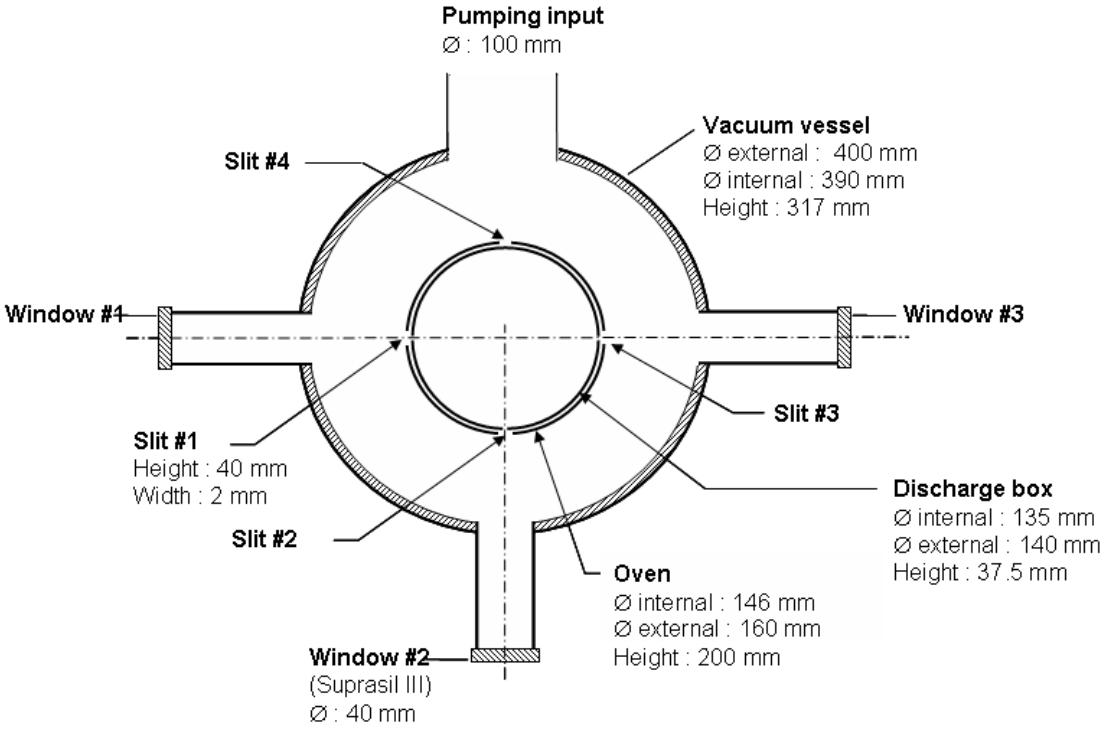

Figure II.2: Top-view of the whole reactor (including the oven).

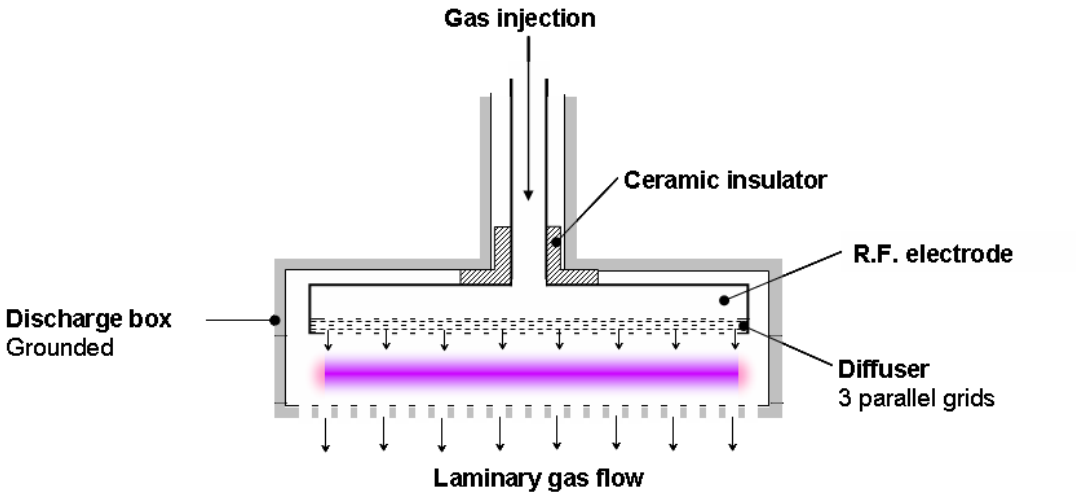

Figure II.3: Gas injection scheme in the plasma box.

explosion of this pyrophoric gas [59] (that can spontaneously inflame and burst in contact with air, $T_{inflamation}$ = 21°C).

The secondary vacuum system consists in a turbomolecular pump (Pfeiffer Vacuum TMH 260, 210 $l.s^{-1}$) and a rotary pump (Alcatel, 20 $m^3.h^{-1}$). This pumping system allows to reach the base pressure in the vessel, which is around a few 10^{-7} mbar. This system is separated from the reactor by two electropneumatic valves and a manual one.

Two gas lines, totally independent, ensure the gas supply of the plasma chamber: one is devoted to silane and the second is devoted to buffer gases (Ar, He, Ne, ...). Those lines are made of stainless steel tubes of 4 mm in diameter. The gas mixture is performed at the entrance of the plasma chamber. Two mass flowmeters equipped with controllers (one for silane, one for buffer gases) measure the gas flow rate in sccm (standard cubic centimeter per minute at 0°C and atmospheric pressure). The gas handling system scheme is given in figure II.4.

The reactor is equipped with two pressure gauges: a full-range one and a Baratron one. The capacitance Baratron gauge (MKS) is used to measure pressures comprised between 10^{-4} and 1 mbar. Capacitance gauges are made of a deformable membrane serving as a plane capacitance framework. The pressure variation induces a capacitance variation quite easy to measure. This gauge is located at the exit of the vacuum vessel and permits to follow the gas pressure during the experiments. Its membrane is very fragile, brutal pressure variations can damage it. The second gauge is a compact Fullrange gauge (Pfeiffer). It is designed for pressure measurement in the range of 5.10^{-9} to 1000 mbar. This gauge consists of two separate measurement systems (the Pirani and the cold cathode system according to the inverted magnetron principle). They are combined in such a way that for the user, they behave as one single measurement system. From 1000 mbar down to 10^{-2} mbar,

the pressure is measured by the Pirani circuit. For pressure lower than 10^{-2} mbar, the measurement is performed by the cold cathode circuit. This gauge has to be isolated from the plasma chamber when using silane in order to avoid contamination. Contamination of the gauge generally causes a deviation of the measured values.

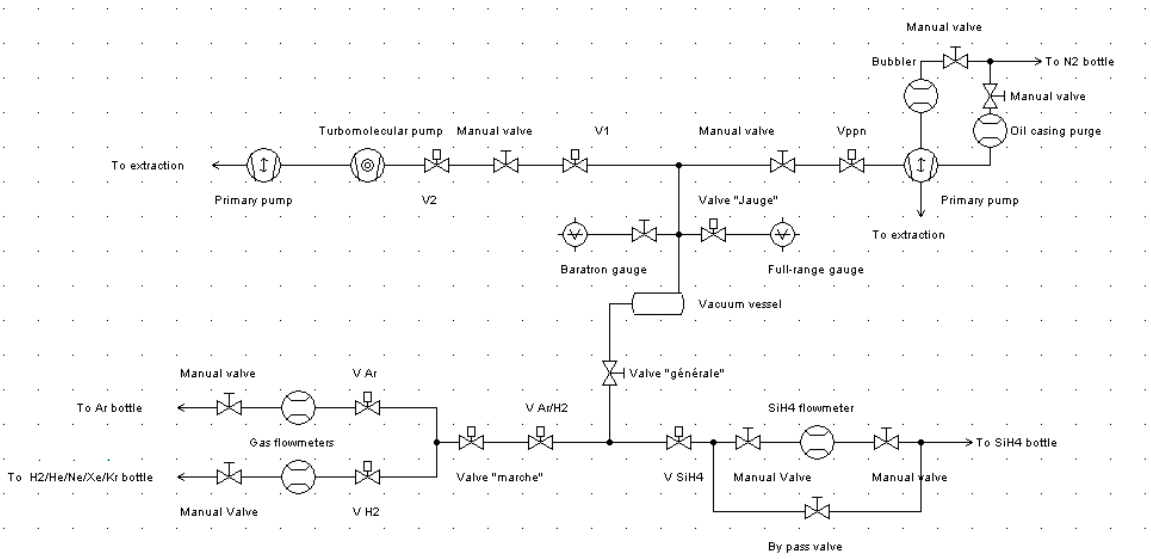

Figure II.4: Gas handling system scheme.

II.1.a.iii Radio frequency excitation

The discharge is excited thanks to a radio frequency wave at 13.56 MHz. The rf power is supplied by a GERAL ARF 101 generator that delivers 100 W at most, corresponding to 0.75 W.cm^{-2} in the plasma box. A computer, equipped with an acquisition board, allows to control the generator in pulsed way. The rf power coupling in the discharge is performed through a L-type matching network. The matching box permits to adapt the capacitive impedance of the discharge to the resistive impedance of the rf generator (50 Ω), in order to lower the reflected power. Thus, the coupled power is optimized and electronics is protected.

The matching box, shown in figure II.5, is composed of two capacitors in parallel C_C and C_F, a coil L and a capacitor C_B in series. C_F is a capacitor with a set capacitance of 500 pF. C_C is a off-setting varying capacitance (7 - 1000 pF), permitting to compensate for parasite capacitances in the circuit. L is an inductance of 3 μH. C_B is a cut-off varying capacitor (25 - 500 pF). This capacitor allows to get a high voltage to ensure the resonance condition in the circuit branch supplying the rf electrode. It also generates the self bias voltage on the rf electrode, due to the capacitive link it introduces in the circuit.

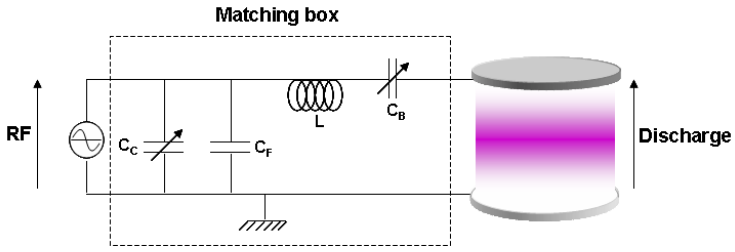

Figure II.5: Matching box scheme.

II.1.a.iv Gas temperature control

The gas temperature in the plasma chamber can be varied from -40°C to 200°C thanks to two independent systems. The first one, allowing to heat the gas, is an aluminum cylindrical oven in which a heating resistor ("Thermocoax") is located. This oven is placed inside the vacuum vessel, around the plasma box. It allows to increase the gas temperature from room temperature (RT) up to 200°C. The second system, allowing to cool down the gas, is a liquid nitrogen circulation all around the vacuum vessel. It is made of a copper tube winding (6 mm in diameter) in which liquid nitrogen (-196°C) is pushed by gaseous nitrogen. Gas temperature is measured using a type J thermocouple (iron/constantan) placed in the gas flow below the plasma box.

II.1.b General mode of operation

In this short part, some details are given concerning the experimental procedures. The most common experimental conditions (referred as standard conditions of experiment) we used are given. The sample preparation for deposition is explained for different types of experiments. And finally, we explain how to clean the plasma box.

II.1.b.i Standard conditions of experiment

Standard conditions of experiment are a tool of control and comparison in case of doubt concerning some results and/or experiments we performed. In those standard conditions, all parameters and common results are well-defined. Our standard conditions are defined as follow: argon flow rate of 20 sccm (corresponding to 120 μbar), silane flow rate of 1.2 sccm, giving a total pressure of 124 μbar. The injected rf power is of 10 W corresponding to a rf voltage of approximately 400 V peak-to-peak (depending on the matching conditions). The experiment is performed at RT (RT $\approx$ 25°C). Table II.1 summarizes all these data.

In those standard conditions, the characteristic duration of each dust formation step is well-known. The time evolution of the amplitude of the third harmonic of the discharge current and of the self-bias voltage is also well-defined. Most of the dust particle properties given in part I.4.b have also been evaluated in those conditions [42, 12, 13, 9].

Parameter	Symbol	Value
Ar flow rate	Q_{Ar}	20 sccm
SiH_4 flow rate	Q_{SiH_4}	1.2 sccm
Total pressure	P	124 μbar
Injected rf power	P_{rf}	10 W
rf voltage	V_{rf}	$\approx$ 400 V
Gas temperature	T_g	RT $\simeq$ 25°C

Table II.1: Summary of the different parameters of the experiment standard conditions.

II.1.b.ii Thin layer/dust particle deposition

Depositions can be performed in the plasma box (exposed to the plasma) or in post discharge (the substrate is not exposed to ion bombardment). In the first case, substrates are placed in the plasma box where they are fixed thanks to stainless steel fastener on the grounded electrode. Both thin films and dust particles can be deposited in such a way. In the second case, substrates are located downstream on a substrate holder. No plasma species can reach them and only dust particles can be deposited that way.

Several types of substrates have been used to perform depositions:

- monocrystalline silicon 100 covered with a thin layer of oxide SiO_2,
- polished stainless steel, which is a good conductor,
- polished aluminum, both conductor and amagnetic,
- Corning glass, having a very low roughness,
- copper grids covered with a thin layer of carbon (TEM grids).

Monocrystalline silicon and Corning glass have a very low roughness (0.5 and 0.2 nm respectively) that make them suitable for AFM studies. They yet have a significant drawback: they are not conductor and they disturb the discharge when they are placed in the plasma box (due to the fact that they are not grounded, they thus induce an added capacitance). They can be used without any troubles in post discharge (a few mm under the plasma box). Polished metallic substrates are conductor, they are suitable for deposition in the plasma box, and can be analyzed by SEM. They cannot be used for AFM analysis due to their high roughness (around 2-3 nm) compared to the dust particle size. Copper grids covered with a thin film of carbon ($\sim$ 50 nm) are used for TEM analysis. The carbon film is very thin and highly transparent to electrons. However, the deposition on these grids has to be performed in post discharge (in order to avoid sputtering of the carbon film by the plasma ions).

Generally, depositions are performed using a pulsed discharge. The time the discharge is on (T_{on}) is set functions of what we want to observe (from a few ms to one minute). Delay between plasmas (T_{off}) is of a few seconds. The number of plasmas can also be

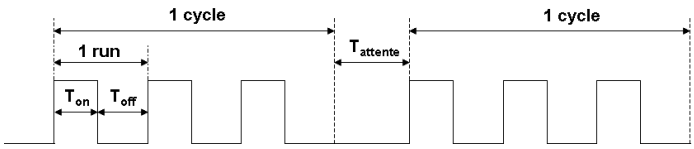

Figure II.6: Example of a cycle for a pulsed discharge used for deposition.

fixed. Once this cycle is defined, it can be reproduced identically several times with a delay $T_{attente}$ between each cycle (see figure II.6).

II.1.b.iii Plasma box cleaning

In order to eliminate silicon films in the plasma box, it has to be cleaned regularly. The cleaning is performed in five steps:

- the plasma box is immersed in a hot solution of diluted soda for one to two hours,
- it is rinsed out with water,
- it is rinsed out with ethanol,
- it is dried up with compressed air,
- it is placed in a drying oven at 100°C for one hour.

II.2 Plasma Kristall Experiment (PKE)

The PKE chamber has been described in details in several papers (see for example [50, 57]). Figure II.7 shows an overview of the PKE setup, and a brief description is given in the following.

II.2.a Context

One of the major constraint acting on dust particles in laboratory plasmas is the gravity. In order to study pure plasma effects and real interactions between dust particles, a way to suppress this force was needed. The best way to do it were microgravity experiments, considered since the early 1990's. First experiments were performed at the end of the 1990's, by the Max Planck Institute for Experimental Physics (MPE, Germany) using parabolic flights and sounding rockets [60], and by the Institute for High Energy Densities (IHED) of the Russian Academy of Sciences, on board the MIR station. Then, these two laboratories joined to work on the PKE-Nefedov program, on board the International Space Station (ISS). Experiments on clouds of injected dust particles started in 2001 on board the ISS. These experiments aimed to study 3D plasma crystals. The GREMI joined the MPE and the IHED in an extended program on dust particle growth. New series of experiments, prepared in the GREMI, were performed on board the ISS in October 2001 by the French-Russian crew of the ANDROMEDE mission [50].

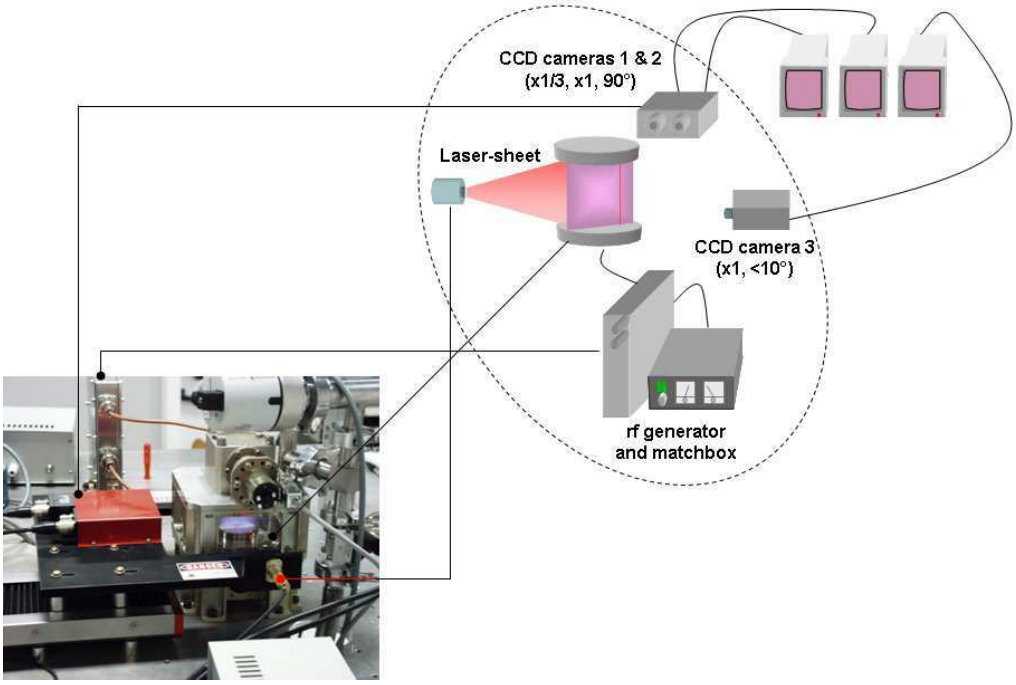

Figure II.7: Overview of the PKE setup.

II.2.b Experimental setup

The PKE chamber, shown in figure II.7 is a cube of approximatively 10 X 10 X 5 cm. The total volume is less than 1 l. Four sides of the chamber are made of glass, allowing a wide optical access to two perpendicular directions. The discharge is generated between two parallel circular electrodes of 4 cm in diameter, separated by a gap of 3 cm. They are power-supplied by a rf excitation (13.56 MHz) in a push-pull mode, through a matching box. The rf generator (MP1-SPACE type) can deliver a maximum power of 4 W. Two pumps ensure the pumping down of the chamber. The primary pump is a mechanical pump (Alcatel, 8 $m^3.h^{-1}$), while the secondary pump is a turbomolecular one (Pfeiffer Vacuum, 80 $L.s^{-1}$). This pumping system allows to reach a base pressure around 3.10^{-6} mbar, and is separated from the chamber by a manual valve. The gas supply consists in a small bottle of Ar (B1 type bottle) directly linked to the chamber by a manual valve. The reactor is equipped with two pressure gauges: a full range one and a Baratron one. In most cases, experiments on PKE are performed with no gas flow (static pressure).

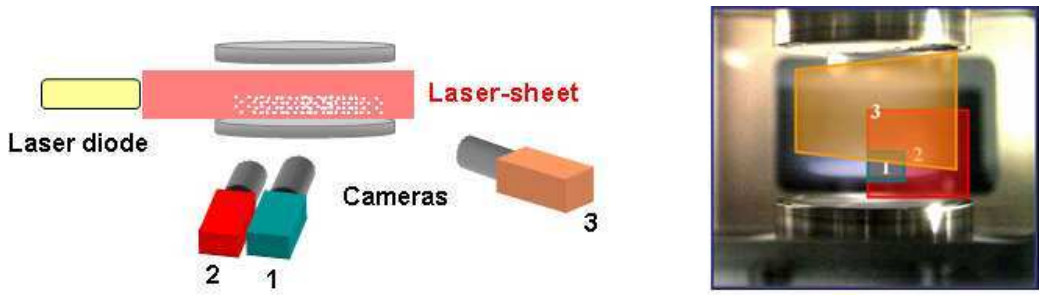

Figure II.8: Field of view of the cameras on the PKE setup.

II.2.c Video imaging

The PKE chamber is equipped with a laser-sheet (λ = 685 nm) and three standard CCD cameras (25 frames per second (fps)) as shown in figure II.8. The laser-sheet covers all the interelectrode gap and is 0.5 mm wide. Two cameras (1 and 2 in figure) watch perpendicularly to the laser-sheet. Camera 1 has a magnification of 1, allowing to observe details near the lower electrode, while camera 2 has a magnification of 1/3 allowing to observe the dust cloud on the right part of the interelectrode gap. Those two cameras and the laser-sheet are fixed on a traveling platform moved by a stepper. We can thus explore 3D dust structures in the discharge. The third camera forms a small angle relatively to the laser-sheet direction in order to observe small dust particles that don't diffuse at 90°. It allows to observe a large part of the interelectode gap. All cameras are equipped with interferential filters (λ = 685 nm, 10 nm wide).

II.3 *In situ* diagnostics

Multiple diagnostics are implemented on the Silane setup in order to monitor and characterize both the plasma and the dust particle formation *in situ* and in real-time as far as possible.

II.3.a Current and voltage measurements

The rf voltage is measured in real time using a high-frequency probe Lecroy PPE20KV.This probe allows to measure voltage up to 40 kV peak-to-peak, with an attenuation of 1000 in a 100 MHz bandwidth. It is made of a load resistance of 50 MΩ with a capacitance lower than 2 pF. Its response time is evaluated at 4 ns, which is much lower than a rf period (73.75 ns).

To measure the rf current, we use an EMCO 94430-1 probe with a load resistance of 50 Ω and a bandwidth from 10 to 250 MHz. Generally, current probes are transformers producing a voltage, in a load resistance, which is proportional to the current flowing

through the probe. The probe is located around the conductor in which the current has to be measured. The cable behaves like the primary of the transformer while the probe makes the secondary side. The current (I_p) flowing through the probe is determined by the output voltage (V_{out}) divided by the transfer impedance (Z_T):

$$I_p = \frac{V_{out}}{Z_T} \tag{II.1}$$

The value of Z_T is a function of the frequency of the measured signal. As an example, it is 6 Ω at 13.56 MHz and 6.9 Ω at 40.68 MHz.

II.3.b V_{dc} and 3H probes

A V_{dc}/3H based diagnostics has been built-up in the GREMI laboratory in order to monitor dust particle formation and growth in the discharge through the modifications they induce in the electric properties of the plasma. In a pure argon (or other rare gas) plasma, the V_{dc}/3H signal is stable, while it shows a time evolution linked to dust particle formation in silane-based plasmas [9]. This phenomenon is due at first to small dust particles interacting with electrons, and thus modifying their collision frequency, and in a second time to electron attachment on bigger dust particles modifying the plasma parameters.

V_{dc} probe

If one performs a precise analysis of the rf voltage, it can be shown that it is a pure sinusoidal 13.56 MHz signal, including a bias voltage (called self-bias voltage, V_{dc}), as can be seen in figure II.9 (yellow curve). This is due to the blocking capacitor and the counter-electrode capacitance, that together act as a filter suppressing the voltage harmonics and inducing a bias voltage. This self-bias voltage is closely linked to the reactor structure and to the particle kinetics in the discharge. As the reactor structure remains always the same, modifications in V_{dc} are only due to particle growth kinetics.

3H probe

In the same way, if we perform a precise analysis of the discharge current, we can notice two main points. First, the signal is not sinusoidal, but contains numerous harmonics (up to 20 in some cases). Second, the total discharge current is mainly composed of a capacitive current due to the counter-electrode, that tends to hide the real discharge current contribution. Low pressure rf discharges contain two or more different sheaths. Two cases can be distinguished : symmetrical and asymmetrical rf discharges. In the first case, the non linearity of the system is weakly pronounced. However, in the second case, the sheath at the smaller electrode has a great influence on the plasma characteristics. A time varying potential drop across the sheath causes a displacement current that makes the sheath

capacitive. The relation between the sheath voltage and the displacement current is non linear because of the electron and ion dynamics in the sheath. The generation of harmonics is due to this non linearity of the sheath on the rf electrode [61]. A precise analysis of these harmonics can lead to precious information about the electric field in the sheaths and also about the ion and electron energy distribution functions, and thus to a better control of particle formation in the discharge.

Our diagnostics has been based on the third harmonic because it is the dominant harmonic in the discharge (as a matter of course after the first one).

Setup

The V_{dc}/3H diagnostics is based on electronic filters. Concerning V_{dc}, it is based on a low pass filter to extract the direct current part of the signal. Concerning 3H, the probe is based on a frequency filter allowing to isolate the 40.68 MHz component of the signal. In both cases, the probes deliver the time evolution of the amplitude of the signals. The two probes are enclosed in the same box, which is located between the matching box and the rf electrode.

Advantages

The main advantage of this diagnostics is to be an industry compatible diagnostics. It doesn't need any optical access to the reactor. Its size is small-scale. It doesn't induce any contamination of the process. No special data processing is required, and meaningful results are obtained quite easily. Moreover, this diagnostics is both robust and stable. It can be used in various chemistries based on reactive gases. We have notably shown that it can be used in methane-based dust forming plasmas. This diagnostics has a high time resolution (mainly limited by the filter response time).

Drawbacks

The main drawback of this diagnostics is that it is very time-consuming to calibrate in terms of dust particle step of formation. The calibration involves the use of various other diagnostics such as laser light scattering or microscopy to determine dust particle size, density, cristallinity. This calibration is reliable only if the experiments are quite reproducible.

II.3.c Electrostatic (Langmuir) probe

An electrostatic probe is a small conductor immersed in the plasma, that can be polarized in order to collect a current. This current depends on the density and temperature of

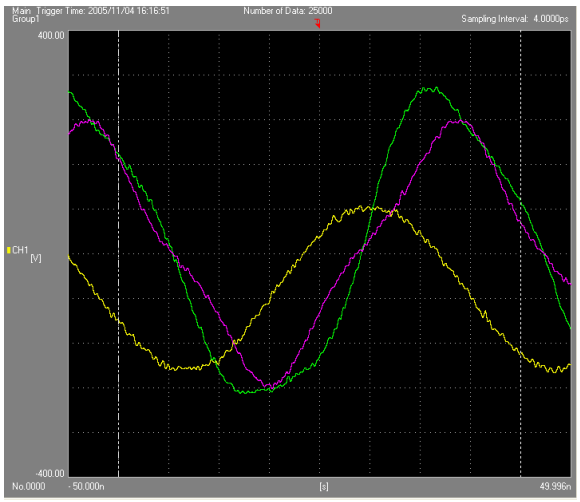

Figure II.9: Time evolution of the rf voltage (yellow), the total discharge current (green) and the capacitive current (purple).

charged species. This dependence takes into account the species dynamics in the electric field induced by the probe. This electric field is located in the probe sheath which is a few Debye lengths wide. Most commonly used probes are made of metal (W, Ta, Mo, stainless steel, Pt, ...) chosen for its high-resistance to sputtering, chemical attacks and heat. It must also have a high work function in order to avoid secondary emission [20].

Electrical probe measurements allow to determine different plasma parameters: electron density and temperature, distribution function, ion density, plasma potential and floating potential. The main advantage of the probe method is its simplicity in terms of equipment and experiment. Its main drawback is due to the complexity of the theory used to extract the plasma characteristics from the probe measurements. In fact, there are few experimental conditions under which the theory gives quite simple relations. This method is finally reliable principally in rarefied gases where the mean free path is greater than the size of the probe and the sheath length.

In this work, we used the Langmuir probe only to determine the ion density. Indeed, the determination of the electron density using a Langmuir probe in a rf discharge is quite complicated and needs a compensation circuit (not available on our probe). For this purpose, we used the microwave resonant cavity method as explained in section II.3.d. Moreover, using a Langmuir probe in a silane-based discharge has several drawbacks : due to negative ions, the determination of the free electron density is difficult to achieve and the modified Böhm criterion has to be used. The pollution of the probe by the deposition has also to be taken into account: the probe has to be cleaned after a few experiments.

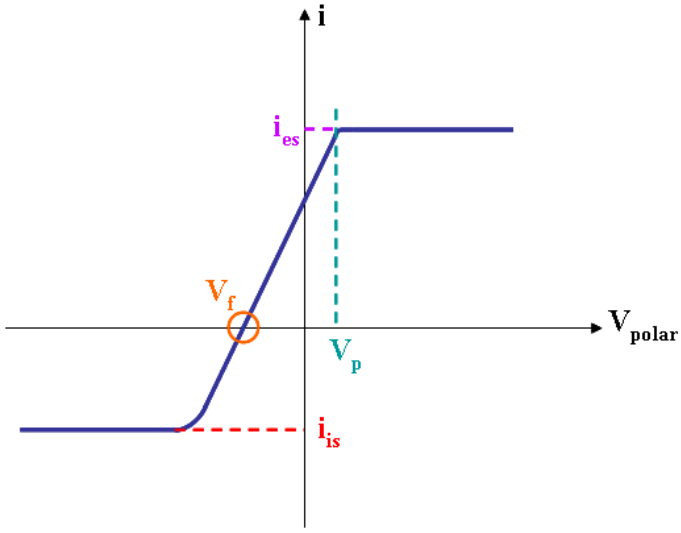

Figure II.10: Idealized current-voltage characteristic of a single probe.

Current - voltage characteristic of a single probe

Figure II.10 shows an idealized probe characteristic: the value of the current collected by the probe (i) is plotted as a function of the applied potential (V_{polar}). The probe only collects charged species from the plasma, it does not emit any. The current sign is defined using the following convention: $i = i_e - i_+$. As electrons move faster than ions, in the absence of potential difference between the probe and the surrounding plasma ($V_{polar} = V_p$) the current collected by the probe is practically equal to the electron current ($i \approx i_e$). When the probe potential is positive with respect to the plasma potential, ions are repelled and electrons are attracted. The electron flux is weakly dependent on the probe potential. The probe current coincides with the saturation electron current (which is more or less constant). This corresponds to the plateau I on figure II.10. When the probe potential is negative with respect to the plasma potential, the decrease of V_{polar} causes a drastic decrease in i. The electron temperature can be deduced from the slope of this part of the curve. For a certain potential $V_{polar} = V_f$, called floating potential, $i = 0$. The electron flux is exactly compensated by the ion flux. This potential V_f is the potential experienced by an isolated surface immersed in the plasma. For even more negative potentials, the probe repels electrons and collects ions. The probe is surrounded by an ionic sheath and the collected current is purely ionic. This ion flux is nearly independent of the probe potential, and induces the ionic saturation current.

Determination of the ion density

Assuming an electropositive plasma with two maxwellian populations, when the probe potential is highly negative, the collected current (ion saturation current) can be expressed by:

$$i_{is} = 0.61\, n_i\, q_i\, v_i\, S \tag{II.2}$$

with n_i the ion density, q_i the ion charge, v_i its velocity and S the probe surface. The ion velocity is given by the Bohm criteria:

$$v_i = \sqrt{\frac{k_B\, T_e}{m_i}} \tag{II.3}$$

with k_B the Boltzmann's constant, T_e the electron temperature and m_i the ion mass.

II.3.d Microwave resonant cavity method

Electron density measurement by the microwave resonant cavity method is based on the variation of the dielectric constant value of the medium in the plasma box. When there is no plasma in the plasma box, the dielectric constant is ϵ_0 (dielectric constant for vacuum), associated to a resonance frequency f_0. Once the plasma is switched on, the dielectric constant is modified and becomes $\epsilon_0\, \epsilon_r$. The associated resonance frequency shifts towards a higher value f_r. The modification of the dielectric constant of the medium is due to its free electron density. Thus, the frequency deviation $\Delta f = f_r - f_0$ is directly linked to the free electron density in the plasma. The main advantages of this method is that it is non-intrusive, quite easy to implement and it has a high time resolution. The main drawback is the lack of spatial resolution: we can only access to mean value of the electron density averaged over all the plasma volume.

Theory

The electromagnetic field associated to a standing wave inside a cavity can be described as a linear combination of various resonant modes of the cavity, exhibiting each its own characteristic frequency. The wavelength of the different modes depends on the cavity dimensions [62, 63, 64, 65].

In a cylindrical cavity, any mode can be expressed as:

$$\vec{E}(\vec{x},t) \;=\; \vec{E}_0(\vec{x},t)\, e^{(\pm ikz\, -\, i\Omega t)} \tag{II.4}$$

where k and $E_0(\vec{x},t)$ are respectively the field wave vector and amplitude, determined by the cavity geometry. Ω is the complex pulsation. Generally the term $i\Omega t$ is complex and expresses the oscillations (imaginary parts) and the damping of the oscillations (real part).

Its dispersion relation is given by:

$$\Omega^2 \;=\; k^2\,\frac{c^2}{n^2} \;=\; k^2\,\frac{c^2}{\mu_r\,\epsilon_r} \tag{II.5}$$

with n the refraction index of the medium, μ_r its dielectric permeability (taken equal to 1) and c the light velocity. The relative dielectric constant of the cavity containing the plasma depends on the frequency ω of the exciting wave:

$$\epsilon_r \;=\; 1 \;+\; i\,\frac{1}{Q_0} \;+\; i\,\frac{\omega_{pe}^2}{\omega\,(\nu_e \;-\; i\omega)} \tag{II.6}$$

where ω_{pe} is the electron plasma frequency, ν_e is the electron collision frequency and Q_0 the empty cavity quality factor. The term $\frac{1}{Q_0}$ accounts for perturbations due to the non-ideality of the cavity. The dissipation in the plasma is due to electron collisions with a frequency ν_e. The relevance of the cavity method becomes obvious once we note that ω_{pe} is directly linked to the electron density n_e:

$$\omega_{pe} \;=\; \sqrt{\frac{n_e\,e^2}{m_e\,\epsilon_0}} \tag{II.7}$$

Assuming that the deviation of ϵ_r from the ideal case (ϵ_0) is small, the dispersion relation can be linearized:

$$\Omega \;=\; \omega_0 \;+\; \Delta\omega \;-\; i\,\frac{\omega_0}{2\,Q} \tag{II.8}$$

where ω_0 is the oscillation frequency of the resonant mode in the cavity without plasma, and Q is the quality factor of the cavity when the plasma is ignited. The frequency shift due to the plasma is given by:

$$\Delta\omega \;=\; \frac{1}{2}\,\omega_0\,\frac{\omega_p^2}{\omega^2 \;+\; \nu_e^2} \tag{II.9}$$

and the electron density can be deduced as:

$$n_e \;=\; 2\,\omega^2\,\frac{\Delta\omega}{\omega_0}\,\frac{m_e\,\epsilon_0}{e^2} \;=\; 8\,\pi^2\,f_r^2\,\frac{\Delta f}{f_0}\,\frac{m_e\,\epsilon_0}{e^2} \tag{II.10}$$

Corrective factor A

However, this calculation does not take into account the spatial repartition of the electron density in the cavity. It is thus necessary to add a corrective factor A accounting for the spatial repartition of the microwave field. The electron density becomes:

$$n_e \;=\; A\,8\,\pi^2\,f_r^2\,\frac{\Delta f}{f_0}\,\frac{m_e\,\epsilon_0}{e^2} \tag{II.11}$$

If we assume that the electron density profile has a cylindrical symmetry and that the r and z dependences can be separated, n_e can be written as:

$$n_e = n_{e0}\, f(r)\, g(z) \tag{II.12}$$

where r and z are the radial and axial coordinates and n_{e0} the electron density in the center of the discharge ($r = 0$ and $z = 0$). In this case, $f(0) = g(0) = 1$. The factor A can be written as:

$$A = \left[\frac{\iiint_{rz\phi} E^2\,(r,z,\phi)\, f(r)\, g(r)\, 2\,\pi\, r\, dr\, d\phi\, dz}{\iiint_{rz\phi} E^2\,(r,z,\phi)\, 2\,\pi\, r\, dr\, d\phi\, dz} \right]^{-1} \tag{II.13}$$

Generally several modes can be evidenced in the cavity. In order to perform our measurements, we used the TM110 mode. Its spatial distribution is given by:

$$\vec{E} = \begin{cases} E_x = E_y = 0 \\ E_z = J_1\left(\frac{3.83}{r_c}\, r\right) cos\phi\, E_0 \end{cases} \tag{II.14}$$

with J_1 the first-order Bessel function and r_c the cavity radius. For this mode, the corrective factor becomes:

$$A = \left[\frac{\iiint_{rz\phi} E_z^2\,(r,\phi)\, f(r)\, g(r)\, 2\,\pi\, r\, dr\, d\phi\, dz}{\iiint_{rz\phi} E_z^2\,(r,\phi)\, 2\,\pi\, r\, dr\, d\phi\, dz} \right]^{-1} \tag{II.15}$$

Thanks to spectroscopic measurements, Haverlag *et al* showed that the electron density can be considered as quasi-constant in the whole plasma volume in various plasmas [65]. They evaluate the value of A between 1 and 1.8 with a strong dependence on pressure.

In dusty plasmas, the spatial repartition of the electron density evolves as a function of time, the value of A cannot be fixed. For the sake of simplicity, we took $A = 1$ in all the calculations.

Experimental setup

The plasma box serves as resonant cavity. We thus use a cylindrical cavity of 135 mm in diameter and 33 mm height. Two antennas (10 mm in diameter) are inserted in the cavity with a distance of 60 mm in between. The microwave signal is generated thanks to a Rhode & Schwarz signal generator with a 100 kHz - 4320 MHz bandwidth. Its spectral resolution is 1 kHz and the delivered signal is 5 dBm (corresponding to 3 mW). A negative detector (Schottky diode, Agilent Technologies) is used to convert the output signal into a voltage measured with an oscilloscope. An overview of this setup is presented in figure II.11.

According to the calculations [62], in the frequency range from 0 to 4.3 GHz, only three resonant modes are present: TM010 (1732 Mhz), TM110 (2723 MHz), TM210 (3811 MHz).

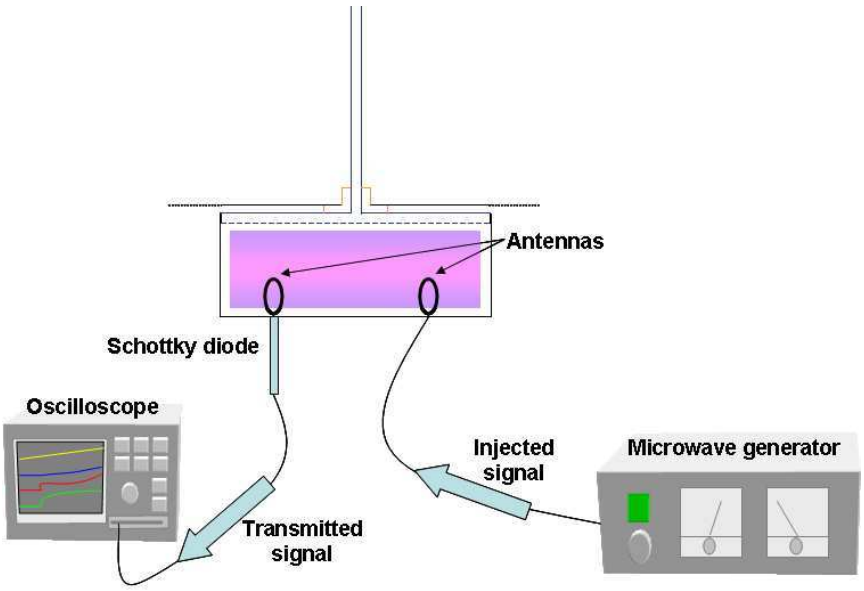

Figure II.11: Overview of the microwave resonant cavity setup.

Due to the non-ideal form of the cavity (slits and antennas) and to the signal reflection in the cables, one can observe more than 3 peaks in the cavity spectrum (see figure II.12). Some of them never change in frequency, whatever the experimental conditions.

II.3.e Optical emission spectroscopy

Optical emission spectroscopy (OES) is the study of the interaction (emission, absorption) between light and matter. OES is often used to identify the different elements present in the plasma. OES examines discrete photon emissions as a spectrum radiated by a given element. This element first absorbs energy, that elevates its electrons to higher energy levels, and then radiates this energy as a photon (emission light) with a characteristic energy (wavelength), linked to the decrease in electron energy as it drops in orbitals. For an electron dropping from an excited level (of energy E") to a lower level (of energy E'), we have:

$$E'' - E' = h\nu \tag{II.16}$$

with h the Planck's constant and ν the emitted photon frequency ($h\nu$ corresponding to the energy of the emitted photon). An emission spectrum is typically a collection of lines with wavelengths from the ultraviolet to the mid-infrared.

The excitation energy can be due to various phenomena such as collisions, chemical reactions, photon absorption, etc... Lots of plasma parameters can be investigated by means of OES: gas temperature, electron temperature, electron distribution function, rotational and/or vibrational temperature, species densities, emission rate coefficient, excitation coefficient, etc... In this work, the use of OES is restricted to the tracking of some plasma

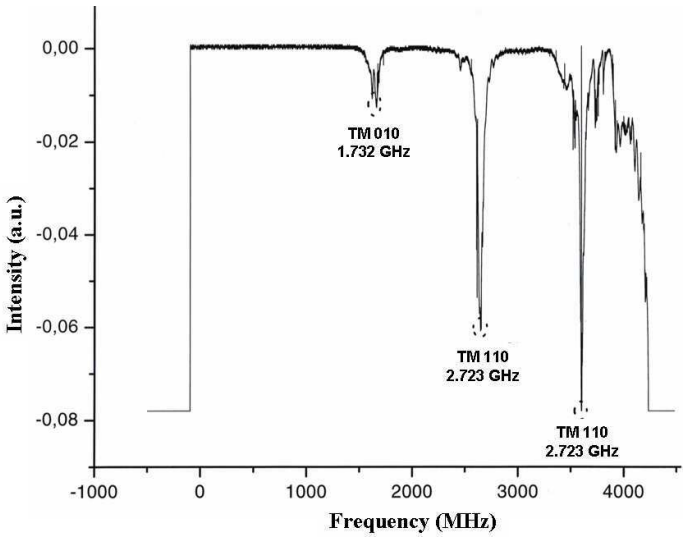

Figure II.12: Cavity spectrum.

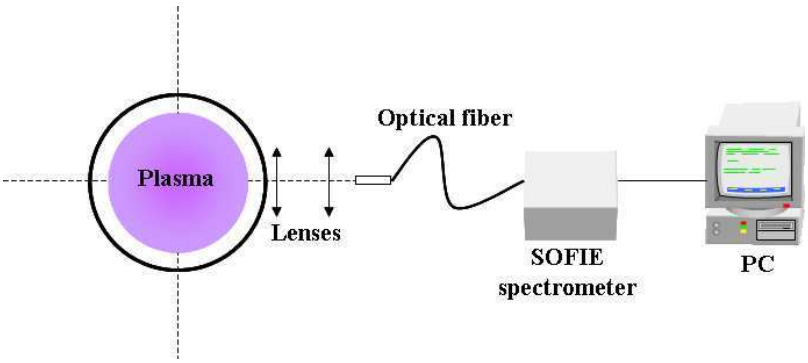

Figure II.13: Overview of the optical emission spectroscopy setup.

species during dust particle formation. We will use it to get an idea of the plasma composition and/or to follow the time evolution of some specific lines of known wavelength (such as the Ar* line at 750.38 nm).

OES experimental setup

OES measurements are performed thanks to a SOFIE spectrometer. This spectrometer is made of two monochromators: one dedicated to the UV range (200 - 600 nm) and a second one for the visible range (500 - 900 nm). The detector consists in a photomultiplier tube. Its standard focal length is 20 cm, and its resolution is quite low ($\leq$ 1 nm). The global plasma emission is collected on an optical fiber using two 100 mm lenses. An overview of the setup is given in figure II.13.

II.3.f Laser light scattering

First experiments on light scattering were performed at the end of the 19$^{\text{th}}$ century, quasi-simultaneously by Tyndall (1869, light scattering by aerosols) and Rayleigh (1871, molecular scattering). The theory of scattering by arbitrary sized spheres has been developed later by Mie (1908) and Debye (1909). This theory is known as Mie scattering theory or Mie-Lorentz scattering theory.

Theory

Figure II.14 gives an overview of the scattering conditions we consider in the theory. The scattering plane is defined by the incident wave direction $\vec{e_y}$ and the scattered wave direction $\vec{e_r}$. We assume that the material of the dust particle has a linear and isotropic behavior. We also assume that all the polarization state of the monochromatic field can be described as a superposition of two linearly polarized waves. Two orthogonal directions are used to describe the incident electromagnetic field: $\vec{E}_{i\perp}$ is the component perpendicular to the scattering plane and $\vec{E}_{i//}$ is the parallel component. In the same way, the scattered field is described using $\vec{E}_{s\perp}$ and $\vec{E}_{s//}$.

If we consider an incident wave of wavelength λ and a sphere of radius r_d, the scattered

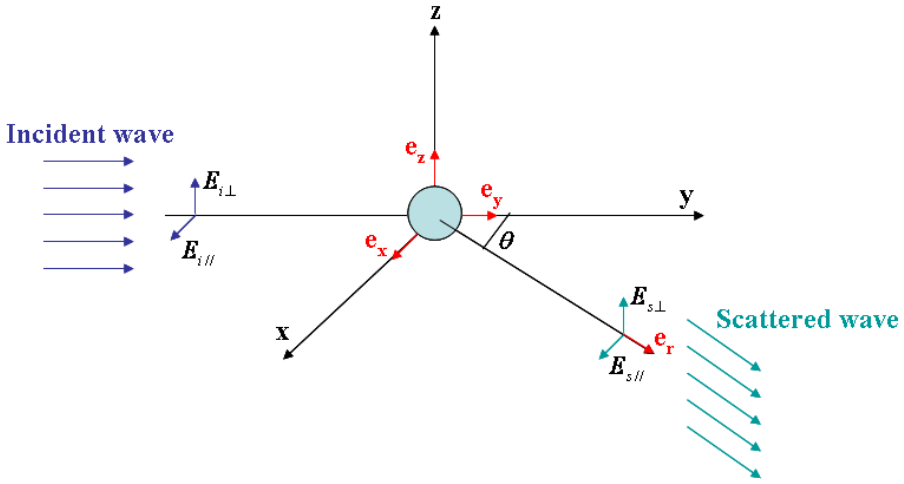

Figure II.14: Laser light scattering by a sphere.

field can be written as [34]:

$$\begin{pmatrix} E_{s//} \\ E_{s\perp} \end{pmatrix} = \frac{e^{-j\vec{k}_s\vec{r}}}{j\vec{k}_s\vec{r}} \begin{pmatrix} S_2 & S_3 \\ S_4 & S_1 \end{pmatrix} \begin{pmatrix} E_{i//} \\ E_{i\perp} \end{pmatrix} \tag{II.17}$$

where $\vec{r}$ is the distance to the particle ($r \gg r_d$, λ), $\vec{k}_s$ is the wave vector of the scattered field and S is the Stockes' matrix.

In the particular case of spherical particles, the S_3 and S_4 terms of the Stockes' matrix vanish. The two terms of the scattered field are thus defined by the terms S_1 and S_2, which depend on the scattering angle θ, the particle radius r_d and its optical index m.

In fact, the parameters $x = 2\pi r_p/\lambda$ and $y = m * 2\pi r_p/\lambda$ would be used for the equation resolution.

S_1 and S_2 are deduced from the Maxwell's equations. Thus, the scattered field, far away from a particle of radius r_d, lighted by a plane wave propagating on $\vec{e}_y$ and polarized in the $\vec{e}_z$ direction can be expressed thanks to the two following amplitude functions [34, 66]:

$$S_1 = \sum_{n=1}^{\infty} \frac{2n+1}{n(n+1)} \Big(\frac{P_n^1(\cos\theta)}{\sin\theta} a_n + \frac{\partial}{\partial\theta} P_n^1(\cos\theta) b_n \Big) \tag{II.18}$$

$$S_2 = \sum_{n=1}^{\infty} \frac{2n+1}{n(n+1)} \Big(\frac{P_n^1(\cos\theta)}{\sin\theta} b_n + \frac{\partial}{\partial\theta} P_n^1(\cos\theta) a_n \Big) \tag{II.19}$$

where P_n^1 is the n$^{\text{th}}$ Legendre's polynome. The Mie scattering coefficients a_n and b_n are defined by [34, 66]:

$$a_n = \frac{m\psi_n'(x)\psi_n(y) - \psi_n'(y)\psi_n(x)}{mT_n'(x)\psi_n(y) - \psi_n'(y)T_n(x)} \tag{II.20}$$

$$b_n = \frac{\psi_n'(x)\psi_n(y) - m\psi_n'(y)\psi_n(x)}{T_n'(x)\psi_n(y) - m\psi_n'(y)T_n(x)} \tag{II.21}$$

where the notation "'" indicates the derivative function. Moreover:

$$\psi_n(x) = \sqrt{\frac{\pi x}{2}} J_{n+1/2}(x) \tag{II.22}$$

$$T_n(x) = \psi_n(x) + j\sqrt{\frac{\pi x}{2}} Y_{n+1/2}(x) \tag{II.23}$$

where $J(x)$ and $Y(x)$ are the Bessel's functions of 1^{st} and 2^{nd} order.
In the case $n = 1$ and for small arguments ($x \ll 1$), the functions ψ and T can be approximated by [66]:

$$\psi_1(x) = \frac{\sin(x)}{x} - \cos(x) \tag{II.24}$$

$$T_1(x) = e^{ix}(-ix^{-1} - 1) \tag{II.25}$$

Thus, for small values of x, scattering coefficients are approximatively given by [66] :

$$a_1 \sim \frac{\cos(mx)\Big(x(\frac{1+2m^2}{3m}) - x^3(\frac{1+4m^2}{30m})\Big) + \sin(mx)\Big(- (\frac{1+2m^2}{3m^2}) + x^2(\frac{1+14m^2}{30m^2})\Big)}{\cos(mx)\big(x^{-2}(\frac{-i+imp^2}{m} - \frac{i+im^2}{2m})\big) + \sin(mx)\Big(x^{-3}(\frac{i-im^2}{m}) + x^{-1}(\frac{i-im^2}{2m^2})\Big)} \tag{II.26}$$

$$b_1 \sim \frac{\cos(mx)(x - x^3/6) + \sin(mx)\Big(-1/m + x^2(\frac{1+2m^2}{6m})\Big)}{\cos(mx)(-i + x) + \sin(mx)\Big(x^{-1}(\frac{i-im^2}{m}) - 1/m - x(\frac{i+im^2}{2m})\Big)} \tag{II.27}$$

In the case of small spheres, $\mid m \mid x \ll 1$, the scattering coefficients are [66]:

$$a_1 \sim -\frac{2ix^3}{3}\frac{m^2-1}{m^2+2} \tag{II.28}$$

$$b_1 \sim 0 \tag{II.29}$$

$$a_n \sim b_n \sim 0 \qquad \forall n > 1 \tag{II.30}$$

It is thus possible to determine (from II.17) the intensity scattered by a spherical particle in the direction making an angle θ with the incident one, at a distance r [67]:

$$I_d(r, \theta, m) = I_0 \frac{\lambda^2}{8\pi^2 r^2}(\mid S_1 \mid^2 + \mid S_2 \mid^2) \tag{II.31}$$

with I_0 the incident wave intensity. From equations II.18, II.19, II.28, II.29, and II.30, it gives in our case:

$$I_d(r, \theta, m) = I_0 \frac{8\pi^4}{\lambda^4}\frac{N r_p^6}{r^2}\left|\frac{m^2-1}{m^2+2}\right|^2(1 + \cos^2\theta) \tag{II.32}$$

where N is the number of diffusing dust particles.

LLS experimental setup

Figure II.15 gives an overview of the experimental setup used for LLS experiments. The laser we used is an Ar* laser (λ = 488 nm) Spectra-Physics that can deliver 2 W in continuous wave. The focusing system is composed of two convergent lenses with a focal distance of 75 and 50 mm, two mirrors (only one shown in the sketch) and a cone-shaped diaphragm (in order to limit diffraction phenomena). The laser beam crosses the plasma box: it enters by the first window, goes through the first slit, crosses the plasma, goes through the second slit, get out through the second window, and finally meets the light trap (to avoid reflexion). The scattered light is collected 90° apart from the laser beam direction. A 100 mm lens allows to collect the light and an interferential filter (λ = 488 nm, $\Delta\lambda$ = 10 nm) limits the observed range of wavelengths. A photomultiplier (Hamamatsu C659-72, water-cooled) coupled to a photon counter (Hamamatsu C5410) collects the output data.

In order to isolate the scattered signal, three measurements have to be performed. First, the global emission of the plasma is recorded to suppress the contribution of the plasma Ar* line from the signal. Second, the background light (scattering on the walls) due to the laser is measured without plasma. Finally, a measurement is performed during dust particle formation. The scattered signal can be extracted from this measurement by subtracting the two signals first measured.

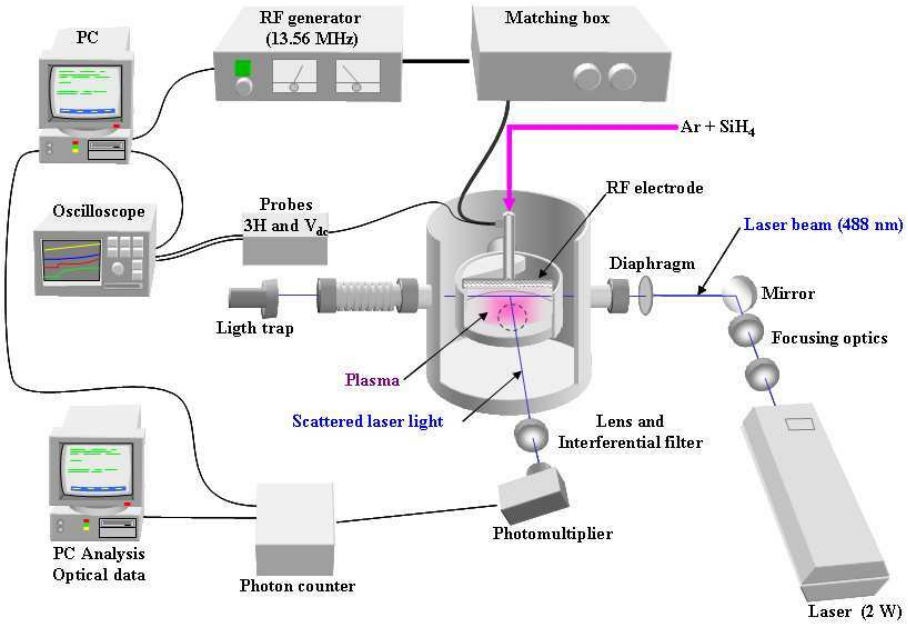

Figure II.15: General overview of the LLS experimental setup.

II.4 *Ex-situ* diagnostics

In order to characterize dust particles synthesized in the discharge, we used several *ex situ* diagnostics. They are all based on microscopy techniques, and gave us information concerning the dust particle size, density, structure and shape. We principally used electron microscopy and atomic force microscopy.

Electron microscopes are used to magnify small details (up to 2.10^6 times) using a beam of highly energetic electrons. Ruska and Knoll built the first electron microscope in the 1930's, and Ruska received the Nobel Prize for this invention in 1986. The principle is quite simple: the sample is scanned by a thin beam of accelerated electrons (see figure II.16). This examination can bring various information concerning the sample topography, morphology, composition and/or crystallographic state.

II.4.a Scanning Electron Microscopy (SEM)

The Scanning Electron Microscope (SEM) is a type of electron microscope that can produce high resolution images of a sample. SEM images have a 3D aspect and can be used to evaluate the surface structure of the sample. Typically, electrons are thermoionically emitted from a cathode and accelerated toward an anode. The produced electron beam has an energy ranging from a few tens of eV to a few tens of keV. This beam is focused by several condenser lenses into a beam with a fine focal spot of a few nm. A pair of scanning coils in the objective lens allows to deflect the beam. As primary electrons strike the sam-

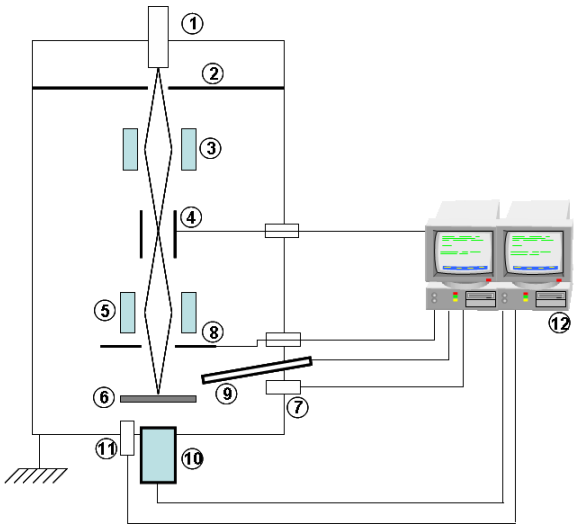

Figure II.16: Scheme of a typical Electron Microscope: (1) Electron beam (2) Anode (3) Condenser (4) Deflection-scanning system (5) Objective (6) Sample (7) Electron detector (8) Backscattered electron detector (9) x-ray spectrometer (10) Transmitted electron detector (11) Absorbed current measurement (12) Electronics and visualization.

ple surface, various signals are emitted (secondary electrons, backscattered electrons, Auger electrons, photons, x-rays ...) [68, 69].

In this study, we specially paid attention to secondary electrons emitted by the sample surface. Those low energy electrons (50 - 200 eV) are the result of inelastic collisions of the incident electrons with the surface. The detection of secondary electrons is the most common imaging mode of SEM. Due to their low energy, those electrons have a small mean free path in the matter and only electrons emitted close to the surface will be detected. Using this technique, it is possible to get resolutions around 1 nm. Figure II.17 shows a typical image obtained thanks to a SEM.

II.4.b Transmission Electron Microscopy (TEM)

An electron source at the top of the microscope emits the electrons that travel through vacuum in the column. Electromagnetic lenses focus electrons into a very thin beam. The electron beam then travels through the sample we want to study. Depending on the density of the material, some of the electrons are scattered and disappear from the beam. At the bottom of the microscope the unscattered electrons hit a fluorescent screen, which gives rise to a "shadow image" of the specimen with its different parts displayed in varied darkness according to their density. The TEM technique allows the direct observation of crystal structure. A crystalline material interacts with the electron beam mostly by

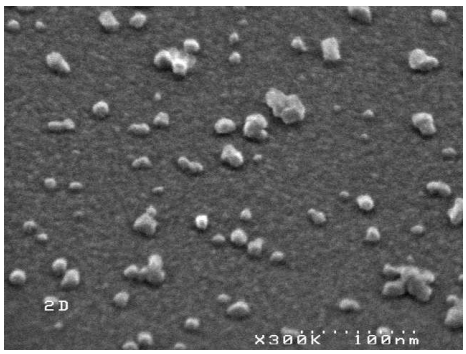

Figure II.17: SEM image of dust particles deposited on a silicon substrate.

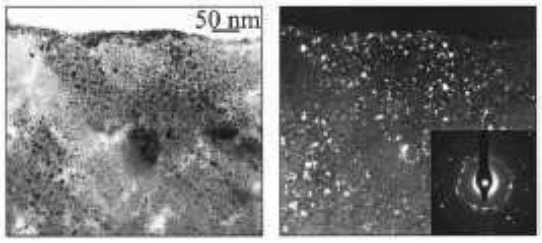

Figure II.18: TEM image of dust particles deposited on a silicon substrate (left: bright field, right: dark field) [39].

diffraction. The diffraction intensity depends on the orientation of the atom planes relative to the electron beam: at certain angles the beam is strongly diffracted, while at others it is mostly transmitted. Two techniques of imaging are thus available. The *Bright Field* technique consists in the detection of only transmitted (unscattered) electrons, and provides information on the crystal structure. The *Dark Field* method produces an image from electrons deflected by a particular crystal plane. Figure II.18 gives an example of images obtained by TEM. The TEM technique exhibits a number of drawbacks. Sample preparation is a limiting factor: they have to be thin enough to be electron transparent. The field of view is relatively small and the sample may be damaged by the electron beam.

II.4.c Atomic Force Microscopy (AFM)

The Atomic Force Microscopy (AFM) is a technique of scanning probe microscopy. It allows to image a surface in the real direct space, with a spatial resolution around 1 nm. The principle, brought to the fore by G. Binnig and H. Rohrer (Nobel Prize in 1986), is quite simple: a small probe (a few nanometers) is approached to the surface and interaction forces between the tip atoms and the surface atoms are measured. By scanning the probe, a 3D image of the surface can be obtained.

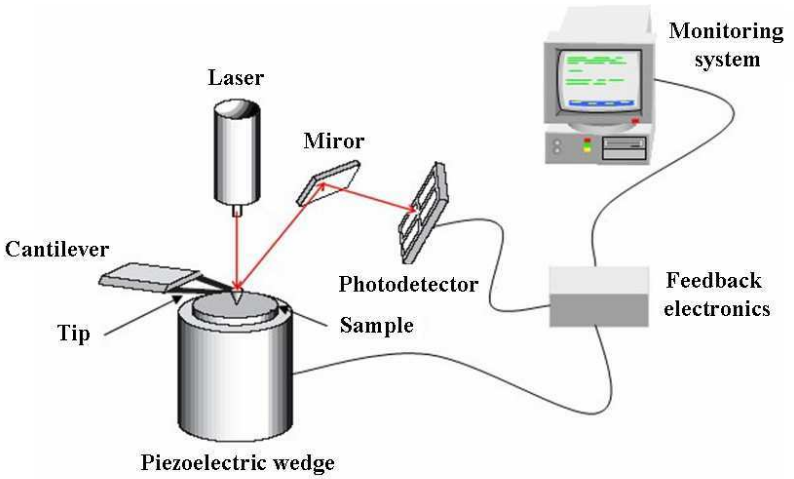

Figure II.19: Scheme of a typical Atomic Force Microscope.

Figure II.19 illustrates how an AFM works. The probe is made of a tip connected to an elastic cantilever. The cantilever deformation is proportional to the force experienced by the tip. This deflection is measured thanks to reflection of a laser beam on the tip, directed towards a photodetector (2 or 4 photodiodes). Generally, the sample, located on the piezoelectric wedge, is moving in the three space directions close to the probe.

The tip is not scanned at constant height to avoid the tip to collide with the surface, causing damage to both. In most cases, the tip-to-sample distance is adjusted by a feedback mechanism in order to keep a constant force between the tip and the sample (around 10^{-8} N). The sample is scanned in the x and y directions, and the resulting map represents the sample topography (see figure II.20). In this case, the forces measured are due to electronic repulsion (Lennard-Jones potential). Nevertheless, frictions induced by the scan can damage the sample.

Another mode can be used to scan the sample: the intermittent contact or tapping mode. A high frequency oscillation (around 300 kHz) is forced on the cantilever. In this mode, changes in the oscillation amplitude yield topographic information about the sample [70, 71].

The AFM has several advantages over electron microscopes. AFM provides a true 3D surface profile while electron microscope provides a 2D projection. Moreover, AFM can be operated at atmospheric pressure while electron microscopes need a vacuum environment. The main drawback, compared to electron microscope, is the image size. The maximum area shown by the AFM is around 150 by 150 μm. Moreover, it can take several minutes for a region to be scanned with the AFM while SEM is able to scan faster.

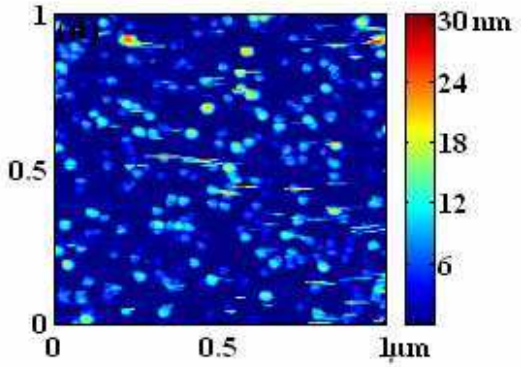

Figure II.20: AFM image of dust particles deposited on a silicon substrate (contact mode), white lines are artefacts due to damages on the sample.

II.5 French summary/Résumé en français

Le principal dispositif expérimental (situé au GREMI) décrit dans ce chapitre, est celui sur lequel la majorité des expériences de cette thèse a été réalisée. Plusieurs autres dispositifs ont cependant été utilisés, dont certains se trouvent dans des laboratoires avec lesquels nous collaborons. On peut notamment citer le dispositif PAMPRE (Production d'Aérosols en Microgravité par Plasma REactif) ou le dispositif PKE (Plasma Kristall Experiment). Ce dernier dispositif sera présenté brièvement dans ce chapitre, tandis que le dispositif PAMPRE sera introduit dans le chapitre V.

Le dispositif utilisé au GREMI a été décrit dans plusieurs thèses et publications [11, 12, 13, 30, 58]. Cependant, certaines modifications ont été apportées afin d'améliorer le dispositif. C'est pourquoi une description complète, comprenant les systèmes de pompage, l'alimentation électrique, la gestion des gaz et les dispositifs optiques, est reprise dans ce chapitre.

Afin de faciliter la lecture du manuscrit, des conditions standards d'expérience seront définies en termes de flux de gaz, pression, puissance injectée et température de gaz. Elles seront par la suite utilisées largement dans cette thèse. La préparation des substrats pour les dépôts sera détaillée pour différents types de substrats (silicium, acier inoxydable, verre...). Le protocole expérimental pour réaliser les dépôts aussi bien dans la décharge qu'en post-décharge sera détaillé.

Les principaux diagnostics utilisés sont aussi introduits dans ce chapitre. Des diagnostics *in-situ* tels que les mesures de courant et de tension, le diagnostic V_{dc}/3H, la sonde de Langmuir, la cavité résonante micro-onde, la spectroscopie optique d'émission ou la diffusion de la lumière laser sont présentés. Le système d'imagerie vidéo est aussi brièvement

décrit. De plus, quelques diagnostics *ex-situ* comme la microscopie électronique (à balayage et en transmission) et la microscopie à force atomique sont aussi expliqués.

Le dispositif expérimental "Silane"

Le réacteur est constitué d'une chambre cylindrique, dans laquelle est insérée la boîte à décharge en acier inoxydable (d = 135 mm et h = 37.5 mm) où est généré le plasma. La boîte à décharge est fermée à la base par une grille à 20% de transparence. Elle est de plus reliée à la masse et se comporte comme l'anode de la décharge. L'électrode rf, en forme de "pomme de douche", ferme le haut de la boîte. Cette électrode sert à la fois à la polarisation rf et à l'introduction de gaz dans le réacteur. Le flux de gaz introduit est laminaire grâce aux trois grilles insérées dans l'électrode rf. Les accès optiques se limitent à quatre fentes verticales (2 mm par 4 cm) placées perdendiculairement les unes aux autres, en regard des hublots en Suprasil III. Les figures II.1 et II.2 donnent un aperçu du dispositif "Silane".

Le pompage de l'enceinte est assuré par deux groupes distincts. La pompe primaire (pompe chimique Alcatel 2033 CP, 35 $m^3.h^{-1}$) est spécialement adaptée aux gaz réactifs. Elle sert à la fois au prévidage de l'enceinte et au maintien de la pression de travail lors des expériences. Le groupe de pompage secondaire est constitué d'une pompe turbomoléculaire (Pfeiffer Vacuum TMH 260, 210 $L.S^{-1}$) et d'une pompe primaire (Alcatel, 20 $m^3.h^{-1}$). Il permet d'atteindre un vide limite dans l'enceinte de l'ordre de quelques 10^{-7} mbar. L'alimentation en gaz est assurée par deux lignes de gaz totalement indépendantes : une dédiée au silane (gaz pyrophorique) et l'autre aux gaz de dilution. Le contrôle de la pression s'effectue grâce à une jauge de type "full-range" et une jauge Baratron pour les pression de travail.

L'excitation rf est assurée par un générateur de type GERAL ARF 101 permettant de délivrer au maximum 100 W. Ce générateur peut être contrôlé via un ordinateur afin de pulser la puissance injectée. Une boîte d'accord de type L est utilisée afin de d'adapter l'impédance entre le circuit et la décharge de façon à optimiser le couplage de l'énergie et à protéger l'électronique de commande.

La température de gaz dans l'enceinte peut être variée de -40°C à 200°C grâce à deux dispositifs distincts : un four et une circulation d'azote liquide. La température est contrôlée grâce à un thermocouple de type J (fer/constantan).

Les conditions standards d'expérience définies ici sont un outil de contrôle et de comparaison en cas de doute sur les résultats obtenus. Dans ces conditions standards, tous les paramètres et les résultats habituels sont bien définis. Ces conditions sont données dans le tableau II.1. L'évolution de la troisième harmonique ainsi que celle de la tension d'autopolarisation sont bien connues dans ce cas particulier, de même que la durée approximative des phases de croissance des poudres. Les principales caractéristiques des poussières données dans la section I.4.a ont été déterminées dans ces conditions.

Afin de réaliser des dépôts, différents types de substrats ont été utilisés : du silicium monocristallin 100 recouvert d'une couche de SiO_2 et de l'acier inoxydable ou de l'aluminium poli pour réaliser les analyses au MEB, du verre Corning pour réaliser les analyses AFM et des grilles de cuivre recouvertes d'une couche de carbone pour les analyses MET. Généralement, les dépôts sont réalisés en décharge pulsée de façon à pouvoir accumuler les dépôts à un temps donné. La durée d'exposition au plasma (T_{on}) peut varier de quelques ms à quelques secondes, tandis que la durée entre deux dépôts est de l'ordre de quelques secondes en général.

La boîte à décharge nécessite des nettoyages très fréquents pour éliminer le dépôt de silicium. Le nettoyage se fait en cinq étapes : bain de soude concentrée, rinçage à l'eau, rinçage à l'éthanol, séchage à l'air comprimé et séchage à l'étuve.

Le dispositif expérimental PKE

Le dispositif PKE (figure II.7) a été décrit en détails dans plusieurs publications (voir par exemple [50, 57]). Le réacteur PKE a été spécialement conçu afin de réaliser des expériences en microgravité à bord de la station spatiale internationale (ISS). Ces expériences sont le fruit d'une collaboration entre le MPE (en Allemagne) et l'IHED (en Russie) au sein du programme PKE-Nefedov. Les expériences ont débuté en 2001 à bord de l'ISS, afin d'étudier la formation de structures cristallines 3D. Le GREMI a rejoint le MPE et l'IHED pour une extension du programme à la formation de poussières. De nouvelles expériences, préparées au GREMI, ont été menées sur l'ISS en octobre 2001 par l'équipe franco-russe de la mission ANDROMEDE [50].

Le réacteur PKE consiste en une chambre cubique en verre d'environ 10 x 10 x 5 cm, d'un volume total inférieur à 1 l. La décharge est produite entre deux électrodes circulaires de 4 cm de diamètre, séparées de 3 cm. Elles sont alimentées par une excitation rf en mode "push-pull", au travers d'une boîte d'accord. Le pompage est assuré par une pompe primaire et une pompe turbomoléculaire permettant d'atteindre un vide limite de l'ordre de 3.10^{-6} mbar. Le réacteur est alimenté en Argon par une bouteille B1 directement reliée au dispositif. La pression est contrôlée par deux jauges : une "full range" et une Baratron. En règle générale, les expériences sont réalisées sans flux de gaz (pression statique).

Le réacteur PKE est équipé d'une nappe laser et d'un système de trois caméras standards (25 images par seconde). Deux caméras filment perpendiculairement à la nappe laser avec des grandissements de 1 et 1/3. La troisième caméra filme selon un plan formant un angle faible avec la nappe laser de façon à observer les petites poussières qui diffusent peu de lumière à 90°. Toutes les caméras sont équipées d'un filtre interférentiel centré sur la longueur d'onde de la diode laser (λ = 685 nm).

Diagnostics *in-situ*

De nombreux diagnostics sont installés sur les réacteurs afin de pouvoir suivre et contrôler à la fois les caractéristiques du plasma, et la formation de poudres, *in-situ* et autant que possible en temps réel. Nous disposons notamment d'une mesure de la tension rf d'excitation (sonde Lecroy PPE20KV) et d'une mesure de courant induit (sonde EMCO 94430-1). Le principal diagnostic utilisé dans cette thèse est le couple de sondes V_{dc}/3H développé au GREMI. Lorsque l'on analyse précisément la tension rf, on montre que c'est une tension purement sinusoïdale incluant une composante continue (appelée tension d'autopolarisation, notée V_{dc}). Cette dernière est due à la présence d'un condensateur de blocage dans le boîte d'accord. V_{dc} est liée à la fois à la structure du réacteur et à la cinétique de croissance des poussières dans la décharge. Comme la géométrie du réacteur est invariante, les évolutions de V_{dc} sont donc principalement liées à la présence des poussières dans le plasma. De la même façon, lorsque l'on analyse le courant de décharge, on obtient deux résultats marquants. Le premier est que le signal n'est pas sinusoïdal, mais contient de nombreuses harmoniques (jusqu'à une vingtaine dans certains cas). Ensuite, ce courant de décharge est principalement composé d'une composante capacitive, due à la contre-électrode du réacteur, qui tend à masquer la contribution du "vrai" courant de décharge. Ainsi, une analyse précise des harmoniques peut mener à de précieuses informations sur le champ électrique dans les gaines et les fonctions de distribution des électrons et des ions, permettant ainsi de mieux contrôler la décharge. Notre diagnostic est basé sur la troisième harmonique car elle s'avère être l'une des plus prononcées dans les différents gaz rares.

Les densités électronique ioniques étant deux facteurs-clés dans une décharge, deux diagnostics sont mis en oeuvre pour les évaluer. La densité ionique est évaluée grâce à des mesures de sonde de Langmuir dans le régime de saturation ionique, tandis qu'une cavité résonante micro-onde est utilisée pour l'évaluation de la densité électronique.

Par ailleurs, la spectroscopie optique d'émission a aussi été utilisée, principalement dans le but de suivre l'évolution temporelle de certaines raies de l'argon pendant la formation des poudres dans le plasma. Un diagnostic de diffusion de la lumière laser a de même été mis en oeuvre pour suivre la formation et la croissance des poussières dans la décharge.

Diagnostics *ex-situ*

Dans le but de caractériser les poussières formées, plusieurs diagnostics *ex-situ* ont été utilisés. Ce sont principalement des diagnostics basés sur la microscopie, permettant d'obtenir des informations sur la taille, la densité, la structure et la forme des poudres. Nous pouvons notamment citer la microscopie électronique à balayage (MEB) qui nous a fourni des images d'apparence 3D nous permettant d'apprécier la surface des échantillons.

En utilisant le mode de détection des électrons secondaires, il est ainsi possible d'obtenir des images ayant une résolution de l'ordre du nanomètre, ce qui permet d'identifier les nanoparticules sur les échantillons. La microscopie électronique en transmission (MET) donne des informations sur la cristallinité des échantillons, mais présente l'inconvénient majeur d'une préparation relativement contraignante. La microscopie à force atomique (AFM), bien qu'elle endommage dans certains cas les échantillons, permet d'obtenir des relevés topographiques très précis de la surface des échantillons et d'accéder à certaines mesures de taille de poussières inaccessibles par microscopie électronique.

Chapter III

Aggregation instability in a silane-based plasma

Some instabilities induced by the presence of dust particles in plasmas have been reported for more than ten years now [55, 56, 57, 72]. All these instabilities have been observed in dusty plasmas obtained by sputtering. The instability reported in this chapter is observed in a silane based dust forming plasma, during the earlier phase of dust formation. However, this instability seems to be comparable to those already reported.

A detailed study of this self-excited instability occurring during dust nanoparticle formation is presented in this chapter. The formation and growth of nanoparticles is followed thanks to the analysis of the time evolution of two signal amplitudes: the third harmonic (3H, 40.68 MHz) of the discharge current and the self bias voltage (V_{dc}). In most cases, at the end of the nanocrystal accumulation phase an instability occurs. It seems to be an attachment induced-ionization instability as observed in electronegative plasmas [73, 74]. A detailed study of the influence of different operating conditions (injected power, gas temperature, silane flow rate) on this instability behavior and frequency is presented. Some experiments have been performed to determine the exact localization of the instability with respect to dust particle formation steps. A very particular case of instability is also examined. The main appearance areas of the instability with respect to the experimental conditions are also determined.

We show in this chapter that the instability can be used as a mark of the end of the nanocrystal accumulation phase. This last point is of special interest for applications in nanotechnologies such as single-electron device [5] or solar cell [8] fabrication.

The content of this chapter has been published in two papers :

- M. Cavarroc, M.C. Jouanny, K. Radouane, M. Mikikian, L. Boufendi
  J. Appl. Phys. **99**, 064301 (2006) [75]

- M. Cavarroc, M. Mikikian, G. Perrier, L. Boufendi
  Appl. Phys. Letter **89**, 013107 (2006) [76]

III.1 Description of the aggregation instability

The main dust formation steps (accumulation phase, aggregation and growth by surface deposition) can be clearly identify thanks to the V_{dc}/3H electrical diagnostics (fig.III.1). Even though, some uncertainties are remaining concerning the exact transition from one step to another. As can be seen in figure III.1 insert, a self-excited instability occurs in between accumulation and aggregation phase. Due to this instability, until now it was still quite difficult to exactly define when the aggregation starts.

The typical behavior of the self bias voltage and the third harmonic of the discharge current during the instability is shown in figure III.2(a) (Q_{Ar} = 20 sccm, Q_{SiH_4} = 0.8 sccm, p = 124 μbar, P_{rf} = 6W, T = RT). This instability appears as oscillations on the signals. It is self-excited: it does not need any external excitation to appear. The typical appearance time is between 100 and 200 ms after plasma ignition. The typical duration is of a few to a few tens of ms. The frequency of this signal, given by a Fast Fourier Transform (FFT) analysis, is shown in figure III.2(b) and evolves during the instability. The typical frequencies are comprised between 1 and 3 kHz.

It is interesting to note that the instability appears as oscillations on all the diagnostics used. It can be observed on electrical potentials: radiofrequency voltage (V_{rf}), self-bias voltage (V_{dc}), floating potential (V_f), but also on discharge current fundamental and third harmonic (1H and 3H), or on the ion flux measurement (V_i). As an example, figures III.3(a) and III.3(b) show the time evolution of the fundamental harmonic of the discharge current (1H) and its frequency spectrum during the instability (Q_{Ar} = 20 sccm, Q_{SiH_4} = 1.2 sccm, p = 124 μbar, P_{rf} = 10 W, T = RT). The shape of the signal and its frequency spectrum are very similar to the ones observed on 3H and/or V_{dc} signals. The different diagnostics affected by this instability show that many physical properties of the plasma are concerned by the oscillations observed on the electrical diagnostics.

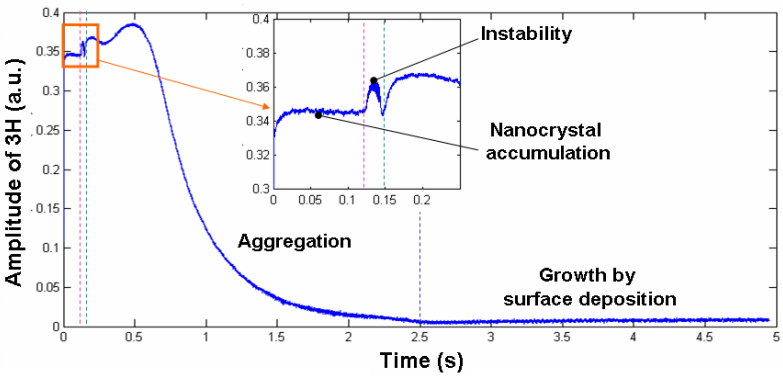

Figure III.1: Time-evolution of the third harmonic of the discharge current in an argon-silane plasma under standard conditions.

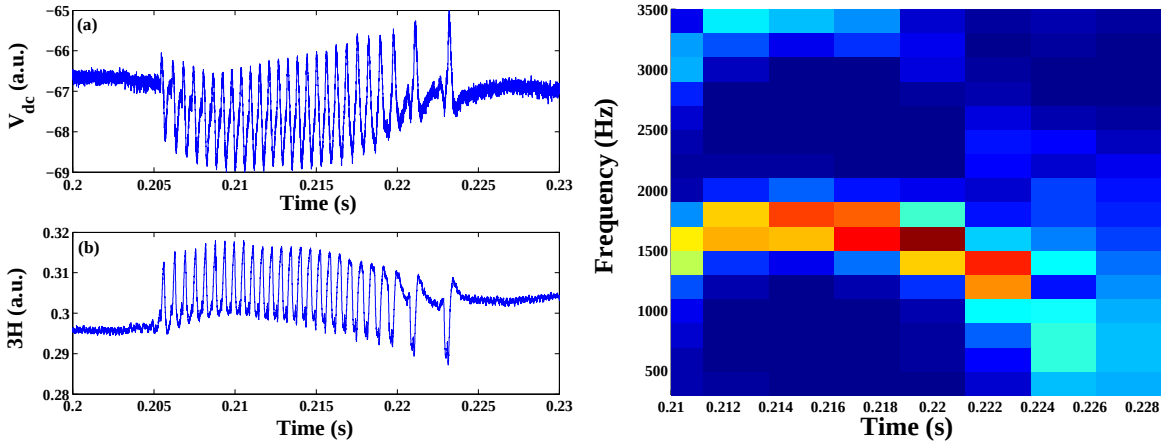

(a) Instability (a) on V_{dc} (b) on $3H$.

(b) Instability frequency (FFT from the 3H signal).

Figure III.2: Time-evolution of the aggregation instability on V_{dc} and 3H.

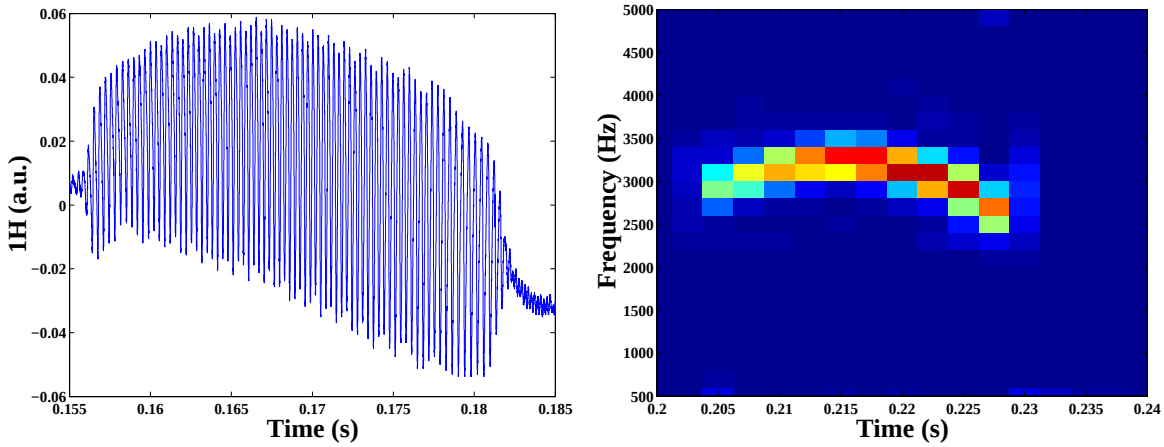

(a) Instability on $1H$.

(b) Instability frequency (FFT from the 1H signal).

Figure III.3: Time-evolution of the aggregation instability on the current fundamental harmonic.

III.2 Localization of the instability

In order to exactly determine the instability localization with respect to the dust formation steps, we realized different depositions at different instants during the dust formation [76]. Structural morphology of the deposited dust particles is qualitatively analyzed from topographical observations of the samples by means of atomic force microscopy (AFM) operating in the tapping mode and scanning electron microscopy (SEM).

III.2.a Depositions

Three different types of depositions have been performed in order to locate the instability: a first one just before (sample a), a second one during (samples b and c), and a last one after the instability (sample d). The substrates we used are made of Si covered by a thin film of SiO_2. This type of substrate can be used as well for SEM analysis (not too many charge effects) as for AFM analysis (the roughness of the sample is around 0.5 nm). However, those SiO_2/Si substrates have a significant drawback: they are not conductor. Thus each new sample modifies the impedance and thus the energy deposition in the discharge box. Figure III.4 gives an overview of the different instants of deposition. All depositions were performed in the standard conditions (Q_{Ar} = 20 sccm, Q_{SiH_4} = 1.2 sccm, p = 124 μbar, P_{rf} = 10 W, T = RT), with 32 runs (successive depositions on the same sample). The deposition instant is adjusted for each sample thanks to the electrical diagnostics in order to locate the deposition instant with respect to the instability.

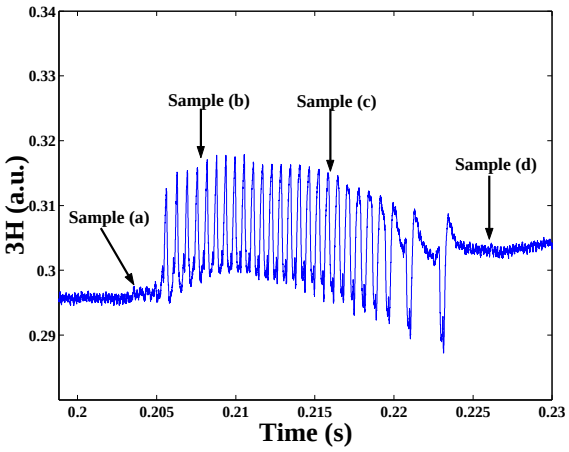

Figure III.4: Deposition instant of the samples a, b, c and d with respect to the instability

III.2.b SEM analysis

The SEM images obtained from the samples are shown in figure III.5. Just before the instability (figure III.5(a)), there are only single nanocrystals (around 2-3 nm) on the substrate. At the beginning and in the middle of the instability (figure III.5(b) and (c)), two populations can be distinguished: there are both nanocrystals and small polycrystalline aggregates. At the end of the instability (figure III.5 (d)) deposited dust particles are mainly small polycrystalline aggregates. These results seem to place the beginning of the aggregation phase at the beginning of the instability.

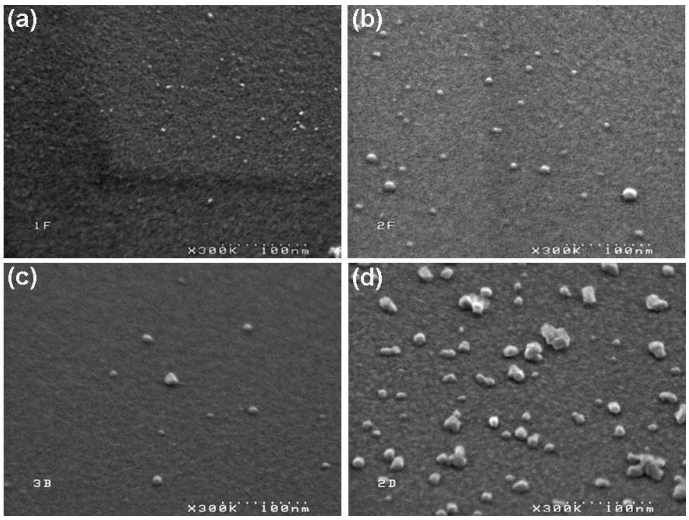

Figure III.5: SEM images of the samples deposited (a) just before (b) at the beginning of (c) during (d) after the instability.

III.2.c AFM analysis

The AFM images obtained from the same samples are shown in figure III.6. They are all normalized to the same height size scale in order to make the comparison easier. In the nanocrystal case, the AFM tip size is of the same order as the nanocrystal size. We are confronted to convolution troubles in the x and y directions. The only dimension we can use is the height because this dimension is less concerned by convolution troubles. To estimate the net dust particle size, the image baseline has to be subtracted to the measured size. The results are quite similar to the ones obtained by SEM. Before the instability (figure III.6(a)), there are only small nanocrystals around 2-3 nm in height. At the beginning and in the middle of the instability (figure III.6(b) and (c)), two populations of dust particles are present, one around 2-3 nm and another one around 4-5 nm. After the instability (figure III.6(d)), a single population is visible, around 10 nm. Those results confirm the ones obtained by SEM.

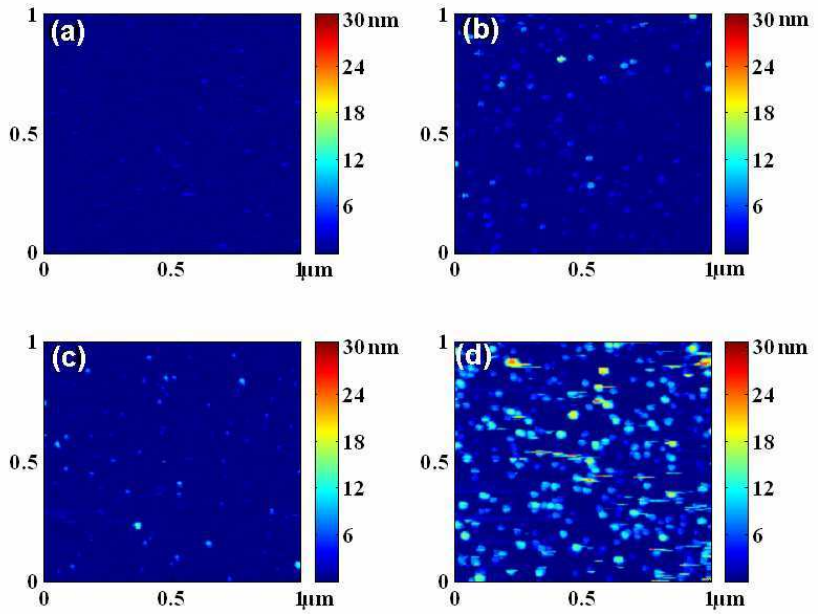

Figure III.6: AFM images of the samples deposited (a) just before (b) at the beginning of (c) during (d) after the instability.

III.2.d Radius distribution

The study of the radius distribution has been performed from AFM analyses of the samples. For each sample, 8 to 10 images have been realized. This statistic allows us to get significant distributions: the average number of dust particles taken into account for each sample is of a few thousands. The radius distribution of dust particles corresponding to the first sample (figure III.7(a)) shows a single peak centered at $r_d = 1.5$ nm (corresponding to 3 nm in height). The same analysis performed on a sample deposited during the instability (figure III.7(b)) shows two peaks located at different heights. The higher peak around $r_d = 1.5$ nm corresponds to the nanocrystals and the smaller one around $r_d = 4$ nm corresponds to the first coalesced polycrystalline nanoparticles. On the last sample (figure III.7(c)), a single peak appears around $r_d = 5$ nm, corresponding to bigger aggregated polycrystalline nanoparticles. Those dust particle radius distributions confirm our qualitative topographical observation.

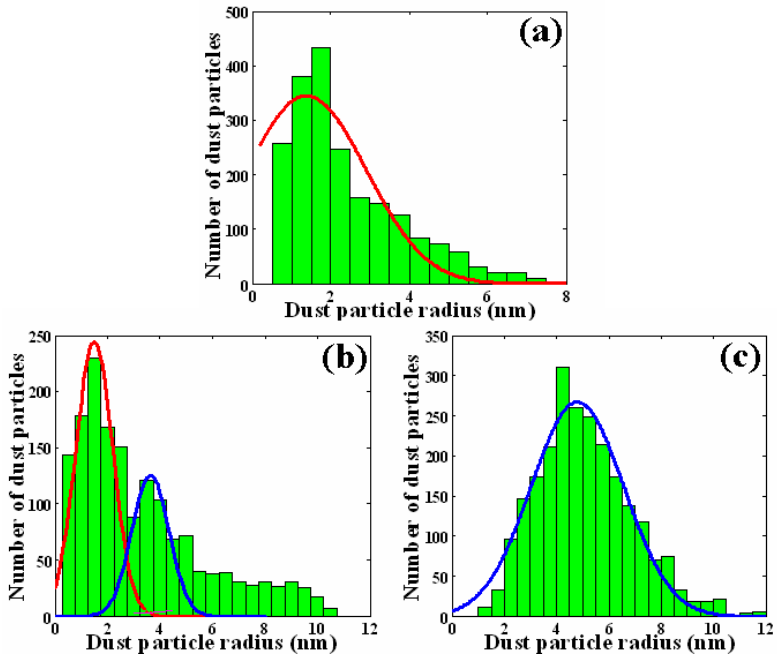

Figure III.7: Radius distribution diagrams corresponding to a sample deposited (a)before (b) during (c) after the instability.

III.2.e Conclusion concerning the instability location

Presently, we can conclude that before the instability, dust particles are single-crystal silicon nanoparticles of 2-3 nm in diameter in the face centered cubic (fcc) phase [39]. Their shape appears to be spherical and their density increases during the accumulation phase until reaching the critical value estimated to 10^{11} to 10^{12} cm^{-3} at room temperature [9]. Thereby, just before the instability the single-crystal silicon nanoparticle density in the plasma is the highest that can be reached. During the instability, nanocrystals agglomerate together to form the first polycrystalline dust nanoparticles of 4-5 nm. All the nanocrystals begin to agglomerate at least two by two. This is the early beginning of the aggregation phase and two populations can be distinguished. The first one corresponds to nanocrystals while the second one corresponds to first aggregated polycrystalline particles. At the end of the instability, no more single nanocrystals remain in the gas phase. Thus, the onset of the instability exactly corresponds to the beginning of the aggregation phase.

III.3 Instability frequency

As can be seen in figure III.2(b), the instability frequency evolves as a function of time. We can first observe an increase of the frequency that could correspond to the instability setting-up. Once the instability is established, the frequency decreases until the end of

the phase where it becomes difficult to define the frequency. During the instability, there is an increase in the mean mass of dust particles due to the beginning of the aggregation phase. This increase of the particle mean mass could explain the decrease of the instability frequency. Thus, if we calculate the dust plasma frequency from equation I.4.a.iii, assuming N_d to be the critical particle density ($10^{12} cm^{-3}$) [9], $Q_d \approx 10^{-3} e$ and 1 nm $\leq r_d \leq$ 2 nm for silicon particles [42], we get 1 kHz$\leq f_{pd} \leq$ 3 kHz (assuming $f_{pd} = \omega_{pd}/2\pi$). These frequencies correspond to the ones we observed for the instability in different conditions.

In the following, we will present some parameter effects on instability characteristics. It is important to note that the frequency at the beginning and at the end of the instability are not measured in the same way. As the frequency at the beginning is well defined its given value is the average value of the frequency taken on the six first periods. As the frequency at the end is much more difficult to define, its value is given by the last value of the FFT, with an uncertainty range due to the software and the method used to compute the data (Matlab code).

III.4 Parameter effect

As the different phases of particle formation and growth, the region of the instability is affected by different discharge parameters such as injected power, silane flow rate, gas temperature or pressure. In the following sections, the effects of injected power, silane flow rate and gas temperature on the instability are studied [75]. The instability is very sensitive to changes in pressure. An increase of a few tens of microbars (10 or 20) leads to the instability disappearance. That is why in the following the pressure effect won't be studied. At the end of this section, a very particular case of instability is reported. This phenomenon is very sensitive to the operating conditions and only appears in two very tight sets of parameters.

III.4.a Injected power effect

The effect of injected power has been studied for different gas mixture rates of Ar/SiH_4 with silane flow rate varying from 0.4 sccm up to 1.6 sccm. In all cases the following parameters were kept constant: Q_{Ar} = 20 sccm, p $\simeq$ 120 μbar, T = RT. The following observations correspond to a synthesis of all the results obtained. Figure III.8 shows the time evolution of the self bias voltage for different injected powers. In this particular case, the amount of silane in the gas mixture was relatively small (Q_{SiH_4} = 0.8 sccm), as when the silane flow rate is too high, the instability rapidly disappears when injected power is increased, and no pertinent study can be done. In this case, the instability appears only for low powers between 6 W and 14 W. For higher silane flow rate, the instability tends to disappear around 10 W.

When the power is increased in the discharge, all the phases of particle formation and growth become shorter and so does the instability (see fig.III.9(a)). This is due to the fact that increasing the injected power increases the ionization process, thus increasing the electron density. As the electron density is increased, dissociative attachment process is accelerated. Consequently particle formation becomes faster. This acceleration of the kinetics is also traduced by the instability starting earlier for high injected power as shown in figure III.9(a). The amplitude of the instability also decreases when power increases. For high injected power the kinetics is very fast leading to the disappearance of the instability.

The frequency of the instability has been shown to evolve in time, decreasing between

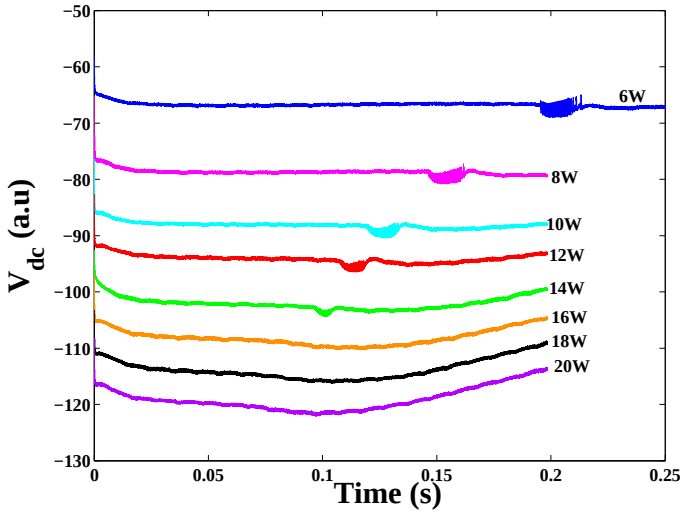

Figure III.8: Time-evolution of the self-bias voltage versus the injected power for Q_{SiH_4} = 0.8 sccm.

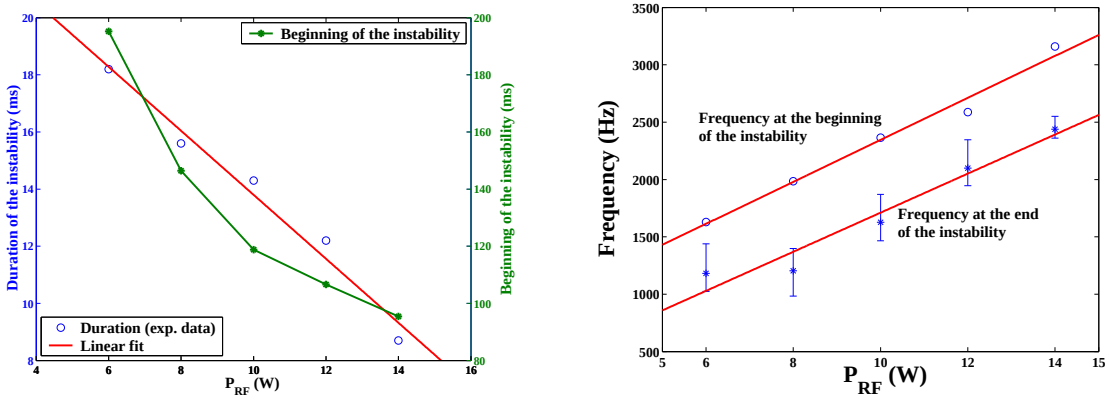

(a) Beginning and duration of the instability as a function of the injected power.

(b) Frequency at the beginning and at the end of the instability as a function of the injected power.

Figure III.9: Effect of the injected power on the instability characteristics.

the beginning and the end of the phase. In addition, the frequency at the beginning and at the end seem to depend linearly on the injected power (see fig.III.9(b)). Indeed, assuming that at the end of the accumulation phase r_d and N_d are constant whatever the injected power, then ω_{pd} is proportional to the particle charge Q_d. When injected power is increased, electron density is also increased. Nevertheless, between 6 W and 20 W, electron temperature remains constant (around 2 eV before $\alpha - \gamma$' transition). That means that newly created electrons are attached by dust particles. Hence when the injected power is increased, the particle mean charge also increases.

III.4.b Silane flow rate effect

The effects of the silane flow rate have been studied in an Ar/SiH_4 plasma with an injected power of 10 W. The amount of silane in the discharge was varied from 0.4 sccm up to 1.6 sccm, keeping all the other parameters constant (Q_{Ar} = 20 sccm, P_{rf} = 10 W, T = RT). The induced pressure variation is negligible ($\sim$ 3-4 μbar) with respect to the total pressure (p $\approx$ 120 μbar). Figure III.10 shows the time evolution of the self-bias voltage as a function of the silane flow rate in the discharge. The curves are shifted in the self-bias voltage axis in order to give a better overview. In the case we present here, the injected power is low, since, as it has been shown before, when the injected power is too high, no instability can be observed. For 10 W injected power, the instability appears even for very small flow rates and tends to disappear for silane flow rates higher than 1.5 sccm. The instability

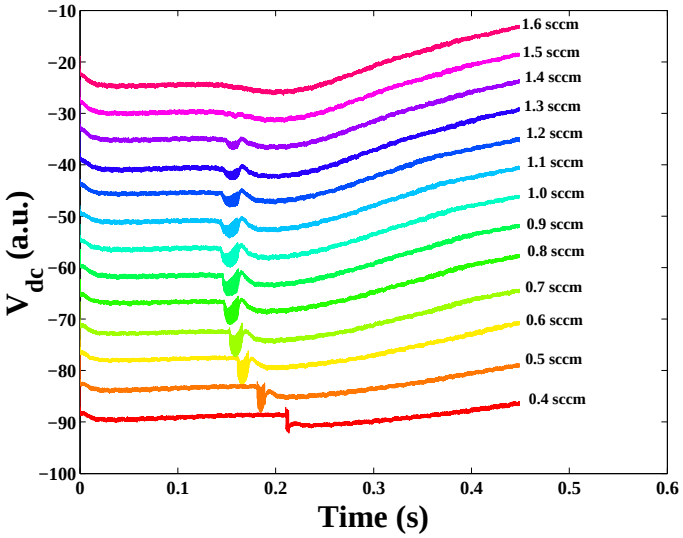

Figure III.10: Time-evolution of the self-bias voltage versus the silane flow rate. The curves are shifted on the self-bias voltage axis in order to have a better overview.

duration is maximum for 1 sccm silane flow rate as shown in figure III.11(a). From 0.4 sccm to 1 sccm the duration of the instability increases when silane flow rate is increased. For

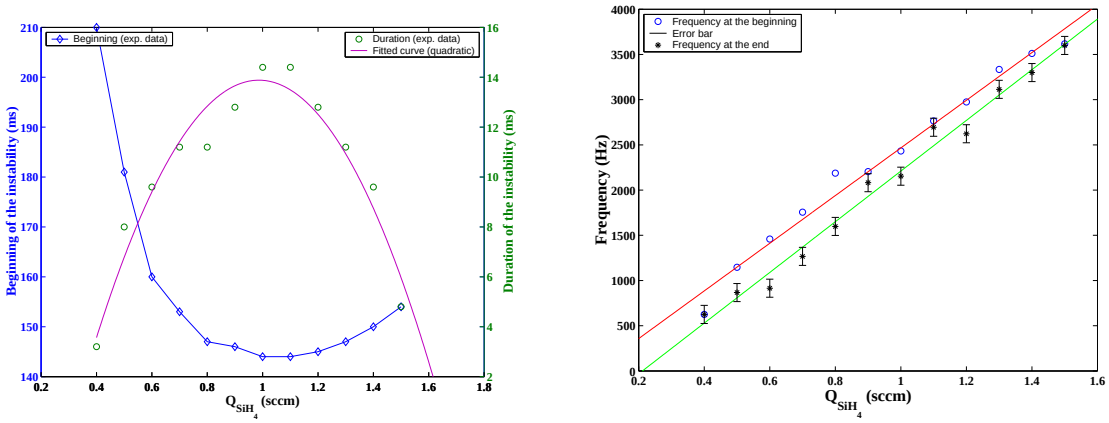

(a) Beginning and duration of the instability as a function of the silane flow rate.

(b) Frequency at the beginning and at the end of the instability as a function of the silane flow rate.

Figure III.11: Effect of the silane flow rate on the instability characteristics.

silane flow rate higher than 1 sccm, the instability is increasingly short until it disappears. However, overall the amplitude of the instability seems to decrease when increasing silane flow rate, until it becomes undetectable on the curves. For silane flow rates comprised between 0.4 sccm and 1 sccm, the instability was observed to begin earlier when increasing the flow rate. From 1 sccm, this value seems to increase slightly until the disappearance of the phenomenon (see fig.III.11(a)). However it seems that above a given limit (around 1 sccm in our case) an equilibrium is reached, and the reactions are no longer sped up. When the quantity of silane in the discharge is increased, the amount of precursors is increased. Indeed, the dissociation degree of silane is constant and independent of the silane flow rate [77]. The initial, accumulation and aggregation, phases are therefore quicker. It is interesting to note that in the particular case of silane flow rate variation, the instability does not behave like the other formation steps. When all phases are quicker, the instability lasts longer, certainly due to the fact that the silane flow rate acts on chemical reactions in the discharge. The frequency of the instability has been shown to have a time evolution. Figure III.11(b) shows the evolution of the frequency at the beginning and at the end of the instability as a function of the silane flow rate. These two frequencies seem to depend linearly on the amount of silane in the discharge.

III.4.c Gas temperature effect

The influence of the gas temperature on particle formation and growth was the subject of many papers [38, 35, 78, 79, 80]. When the gas temperature is increased, particle formation is delayed. In this work, the influence of the gas temperature has been studied from room temperature (RT) up to 120°C (measured in the gas flow with a thermocouple just below the plasma box) in a first part, and from 16°C down to -24°C (measured in the gas flow with

a thermocouple near the plasma box). All the experiments were performed at constant gas number density. We observed that the instability region is also affected by the temperature.

From RT to 120°C

Figure III.12 shows the time evolution of the self-bias voltage versus high gas temperature from RT to 120°C. The curves are shifted in the self-bias voltage axis in order to have a better overview. When the gas temperature is increased, the appearance of the instability is delayed (see fig III.13(a)). The duration of the instability is also affected by the gas temperature: the higher the temperature, the longer the instability (fig.III.13(a)). The instability behaves like the different phases of particle formation and growth: it is delayed and it lasts longer when the gas temperature is increased. Figure III.13(b) shows instability frequencies as a function of high gas temperature. The frequency at the beginning decreases linearly as the gas temperature increases, while the frequency at the end remains the same at around 0.6 kHz (except on the curve taken at 30°C).

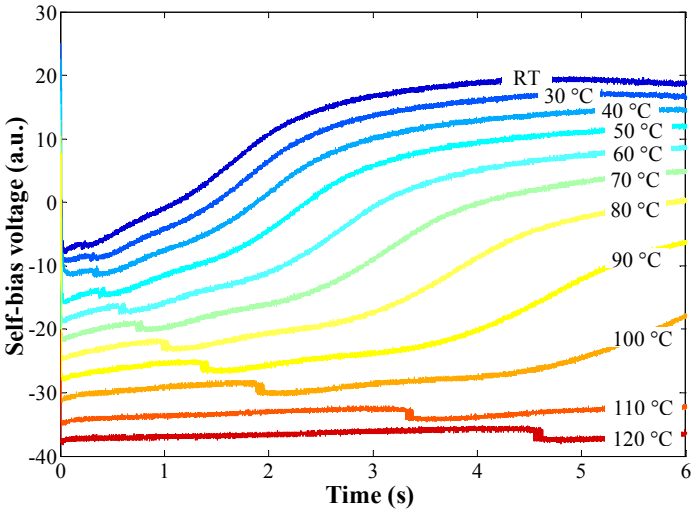

Figure III.12: Time-evolution of the self-bias voltage versus high gas temperature. The curves are shifted on the self-bias voltage axis in order to have a better overview.

From 16°C to -24°C

Figure III.14 shows the time evolution of the current third harmonic amplitude for different low gas temperatures ranging from 16°C to -24°C. The curves are shifted in the 3H axis in order to have a better overview. When the gas temperature is decreased, the appearance of the instability is brought forward as can be seen in figure III.15(a). The duration

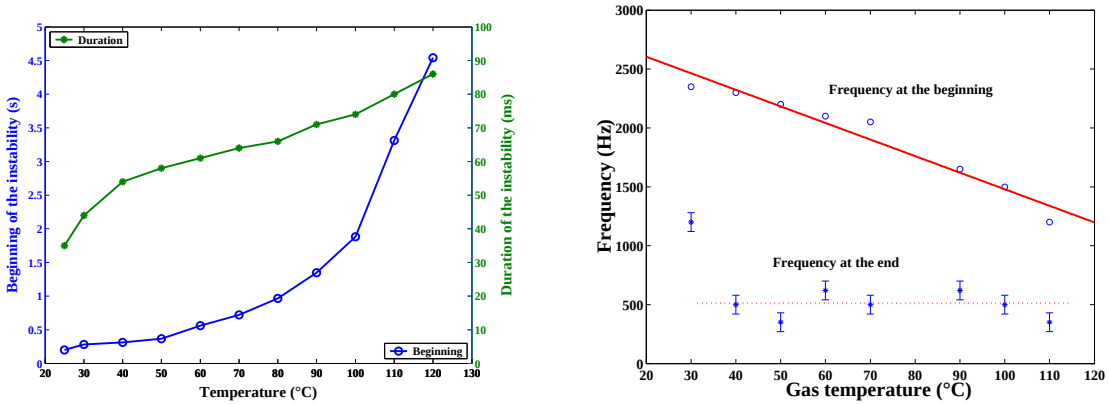

(a) Beginning and duration of the instability as a function of high gas temperature.

(b) Frequency at the beginning and at the end of the instability as a function of high gas temperature.

Figure III.13: Effect of high gas temperature on the instability characteristics.

of the instability is also affected by low gas temperature: the lower the temperature, the shorter the instability (fig.III.15(a)). The instability behaves like the different phases of particle formation and growth: it is accelerated and it is shorter when the gas temperature is decreased. Figure III.15(b) shows the evolution of the mean frequency of the instability as a function of low gas temperatures. Actually, for low gas temperature, the instability frequency does not evolve much in time. Nevertheless, we can point out that for very low gas temperature (under 0°C) the frequency at the end of the instability tends to be a little bit higher than the one at the beginning.

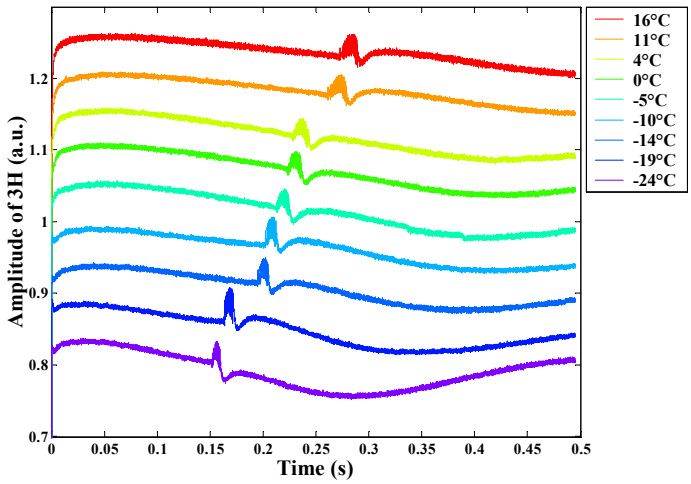

Figure III.14: Time-evolution of the current third harmonic versus low gas temperature. The curves are shifted on the 3H axis in order to have a better overview.

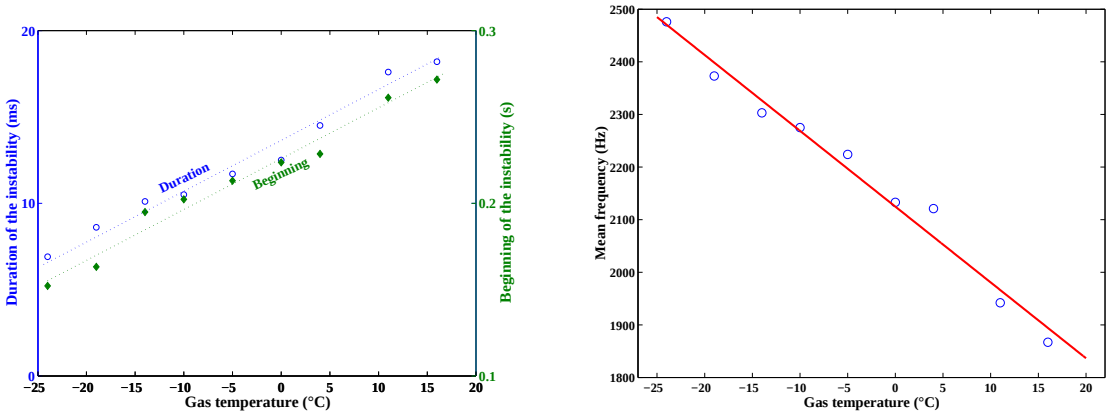

(a) Beginning and duration of the instability as a function of low gas temperature

(b) Mean frequency as a function of low gas temperature

Figure III.15: Effect of low gas temperatures on the instability characteristics

III.4.d Particular case

In some very specific conditions a particular case of the instability was observed. The figure III.16(a) shows the shape of the instability in this case. In a first part, it behaves in the same way as the "common" instability, then it finishes before briefly restarting. This has been confirmed by a frequency analysis (FFT analysis) (see fig.III.16(b)). We can observe a time evolution of the frequency and a range of frequencies similar to those previously observed (between 2 kHz and 3 kHz). The second part seems to be a sort of replica of the end of the first part, with exactly the same frequencies. This phenomenon is highly sensitive to the operating conditions, appearing only for very low injected power (around 6 W) and in a very tight range of silane flow rates (several appearances between 2 and 3 sccm). Moreover, a temperature variation of only a few degrees leads to the disappearance of the phenomenon. This particular case of the instability seems to correspond to dust critical formation conditions, as the slightest modification of one of the parameters leads to the disappearance of the phenomenon. However, we observed this particular instability in at least six different sets of parameters. This observation leads us to surmise that a special pair particle density/particle radius could favor a special behavior of the dense particle cloud trapped in the discharge.

III.4.e Instability appearance conditions

As we saw in previous sections, the instability develops under specific conditions. In the whole temperature range we investigated, the instability systematically appears (excepted the particular case of instability appearing only at RT). A pressure threshold (around 150 μbar) was observed for its disappearance. However, the instability needs very specific conditions of injected power and silane flow rate to take place. Figure III.17 represents

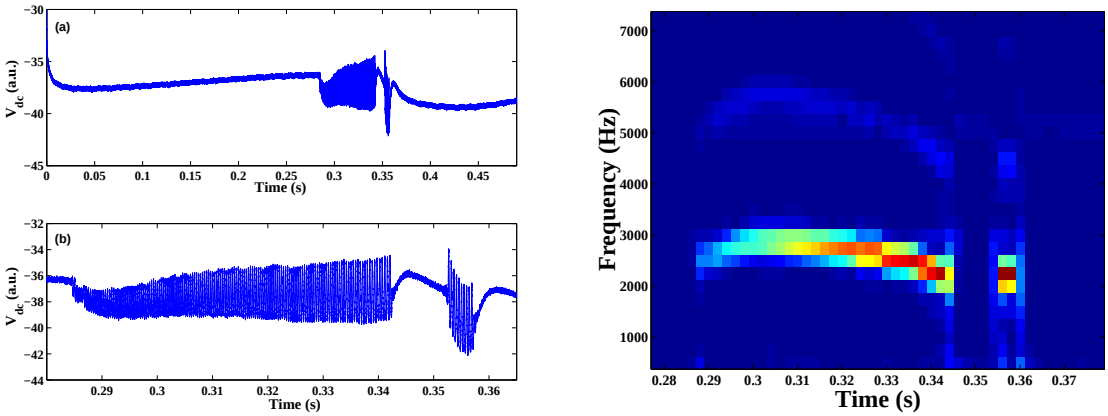

(a) Particular case of the instability on the self-bias voltage (a) on the plasma duration (b) zoom

(b) Time-evolution of the frequency of the aggregation instability in the particular case

Figure III.16: Particular case of the aggregation instability

the instability appearance areas in a P_{rf}/Q_{SiH_4} plane. Areas where the instability appears are represented with circles, the ones where the instability does not appear are represented with crosses. Diamonds represent the particular case of instability. The line delimiting the different areas corresponds to a $P_{rf} \propto Q_{SiH_4}^{-3/4}$ curve. Instabilities are best observed for low P_{rf} and low Q_{SiH_4}. When increasing one of these parameters, the instability tends to disappear: for a determined value of P_{rf} (respectively Q_{SiH_4}), an increase of Q_{SiH_4} (respectively P_{rf}) leads to the disappearance of the instability. Moreover, we can note that the particular case of instability appears for special P_{rf}/Q_{SiH_4} pairs, very close from the limit, underlining the threshold effect linked to the instability.

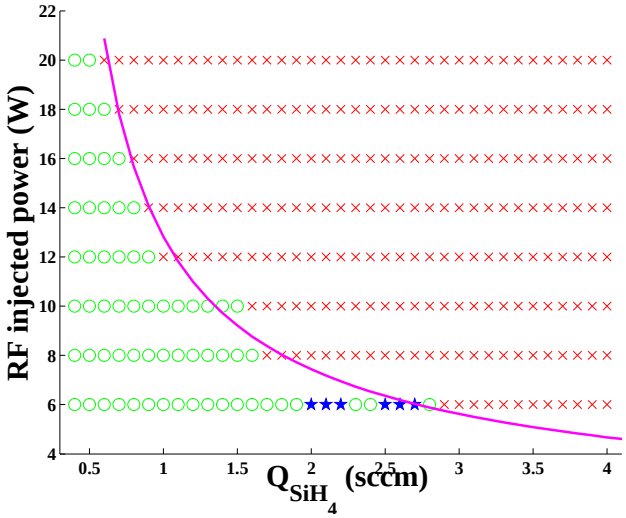

Figure III.17: Aggregation instability appearance areas in a P_{rf}/Q_{SiH_4} plane. Instability: ○, no instability: ×, particular case: ⋆

III.5 Comparison with attachment induced-ionization instabilities observed in electronegative gases

A wide range of instabilities is observed in dusty and non-dusty plasmas. In their work, Descoeudres *et al* describe some oscillations in the kHz range appearing on all their diagnostics in electronegative gases [74]. These oscillations seem to be quite similar to the ones we described in this chapter. A possible explanation for this phenomenon is the attachment induced-ionization instabilities observed in low pressure rf discharges in electronegative gases [73]. The main parameters responsible for these instabilities are the electron temperature T_e and density n_e. Nighan and Wiegand [73] gave a criterion for the appearance of the instability. The physical basis of this criterion are the conservation equations of electronic and ionic densities. The plasma can be unstable if

$$\frac{\partial k_a/\partial T_e}{\partial k_i/\partial T_e} > 1, \tag{III.1}$$

where k_a and k_i are respectively the attachment and ionization coefficients [73]. In practice, the criterion III.1 is fulfilled if the attachment rate coefficient increases with electron temperature faster than the ionization rate. Nighan and Wiegand also deduce that the electron and negative ion densities must be of the same order of magnitude, otherwise the perturbation is stabilized.

As dust particles are charged, they behave like large negative ions. The instabilities we observed may therefore be related to attachment-induced ionization instabilities. During the accumulation phase, the nanocrystals have been shown to grow and accumulate in the gas phase [35]. Their concentration increases until it reaches a critical value from which the aggregation phase starts. This critical value has been measured to be around 10^{11} to 10^{12} cm^{-3} [9]. However less than 0.1% of the dust particles are charged by electron attachment. The concentration of negatively charged nanocrystals is therefore of the same order of magnitude as the electron density, just before the instability. Furthermore the electron temperature has been shown to be constant and equal to 2 eV during the accumulation phase [38]. Figure III.18 shows the time evolution of the electron density n_e measured by the microwave resonant cavity method for different gas temperatures. The first very narrow peak (shown in the insert) corresponds to the SiH_3^- ion formation. Those ions are the first nuclei involved in the particle formation. Then, the electron density remains almost constant during the accumulation phase. Just at the onset of the aggregation, a slight decrease of the electron density can be observed while the ion mean density, measured by Langmuir probe [13], remains constant. That means that at the beginning of the instability k_a increases while k_i remains constant ($\partial k_i/\partial T_e \longrightarrow 0$). And so the ratio becomes larger than one.

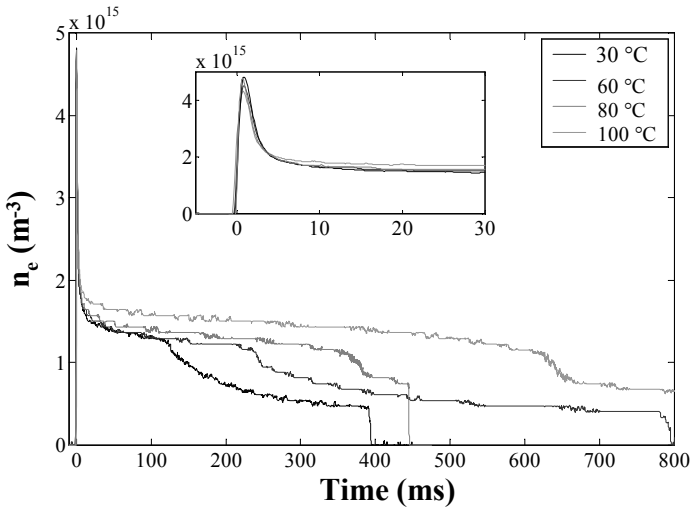

Figure III.18: Time-evolution of the electron density for different gas temperatures. The insert is a zoom of the early beginning of the curve.

III.6 Conclusion

In this chapter we present a wide study of a self-excited instability occurring in the earlier phases of dust particle synthesis. This instability appears as oscillations on all the diagnostics used: potential measurements (V_{rf}, V_{dc}, V_f), current harmonic measurements (1H, 3H) and ion flux measurement (V_i). It affects many properties of the dusty plasma.

Typical characteristics of the instability have been determined: frequency in the kHz range, duration of a few to a few tens of ms and appearance time between 100 and 200 ms after the plasma ignition. Some depositions have been performed at different instants during dust formation process in order to locate the instability in terms of dust formation step. The samples have been analyzed by SEM and AFM and show that the onset of the instability exactly corresponds to the beginning of the aggregation phase (or the end of the nanocrystal accumulation). The instability frequency has been shown to evolve in time thanks to a FFT analysis. This evolution can be explained by the increase of the particle mean mass during the instability, leading to modifications of the plasma-dust frequency.

The effects of operating conditions on the instability have also been investigated. A pressure threshold of disappearance around 150 μbar has been evidenced. The rf injected power and the silane flow rate have been shown to have a significant effect on the instability characteristics (appearance, duration, frequencies...). The gas temperature, investigated from -24℃ to 120℃ has also a significant effect on the instability, but does not seem to affect the appearance of the phenomenon. Finally, a very particular case of instability, showing a short replica of its end, has been evidenced in six very tight sets of parameters. An experimental criterion for the instability appearance in the most common cases has been

determined.

Thanks to a comparison with the work of Descoeudres *et al* [74], a possible explanation of the instability is given. It seems to be an attachment induced-ionization instability as observed in electronegative gases [73, 74]. Nighan and Wiegand gave a criterion for the appearance of the instability. We showed that in our conditions the criterion is met. The instability we observe can thus be linked to the attachment induced-ionization instability.

The exact location of the instability at the end of nanocrystal accumulation phase makes it a very good mark for single-crystal silicon nanoparticle deposition. The V_{dc}/3H based diagnostics does not need any optical access to the plasma. Once it is calibrated, this diagnostics can provide precise information concerning the dust particle nature in the discharge. We performed the calibration for the first phases of formation (formation and accumulation of nanocrystals and beginning of the aggregation) in a typical dust forming Ar/SiH_4 plasma generated in a rf discharge. Presently, we can conclude that before the instability, the dust particles are single-crystal silicon nanoparticles of 2-3 nm in diameter in the FCC phase [39] at room temperature. Their shape appears to be spherical and their density increases during the accumulation phase until reaching the critical value estimated to 10^{11} to 10^{12} cm^{-3} [9]. Thereby, just before the instability the single-crystal silicon nanoparticle density in the plasma is the highest that can be reached. The single-crystal nanoparticles obtained by this way can be incorporated in thin film layers in order to improve their mechanical and/or optoelectronical properties [8], or used for single electron device fabrication [5].

During the instability, nanocrystals agglomerate together to form the first polycrystalline dust nanoparticles of 4-5 nm. All the nanocrystals begin to agglomerate at least two by two. This is the early beginning of the aggregation phase and two populations can be distinguished. The first one corresponds to nanocrystals while the second one corresponds to first coalesced polycrystalline particles. At the end of the instability, no more single nanocrystals remain in the gas phase. Thus, the onset of the instability exactly corresponds to the beginning of the aggregation phase. After the instability the dust nanoparticles are made of agglomerated nanocrystals. Their size increases from 5 nm at the beginning of the aggregation to about 45 nm at the end of the phase [81]. The dust particles are now polycrystalline with a cauliflower form and exhibit a high specific surface (up to 115 $m^2.g^{-1}$ [82]) that can be of interest for applications in catalysis.

III.7 French summary / Résumé en français

Différents types d'instabilités induites par la présence de poudres dans un plasma ont été rapportés depuis plus de dix ans maintenant [55, 56, 57, 72]. Toutes ces instabilités ont été observées dans des plasmas poussiéreux obtenus par pulvérisation. L'instabilité décrite dans ce chapitre est observée dans un plasma poussiéreux à base de silane, pendant les premières étapes de formation des poudres. Elle semble tout de même comparable aux instabilités décrites précédemment.

Une étude complète de cette instabilité auto-excitée, apparaissant pendant la formation des nanopoudres, est présentée dans ce chapitre. La formation et la croissance des poussières sont suivies grâce à l'analyse de l'évolution temporelle de l'amplitude de deux signaux électriques : la troisième harmonique du courant de décharge (3H, 40.68 MHz) et la tension d'autopolarisation (V_{dc}) (figure III.1). Dans la plupart des cas, à la fin de l'accumulation des nanocristaux, une instabilité apparaît. Cette instabilité se présente sous forme d'oscillations sur les signaux (figure III.2(a)), et n'est pas due à une excitation extérieure. Elle apparaît typiquement 100 à 200 ms après l'allumage du plasma. Sa durée est de l'ordre de quelques ms à quelques dizaines de ms. Sa fréquence, comprise entre 1 et 3 kHz, évolue dans le temps comme le montre la figure III.2(b). Il est par ailleurs intéressant de noter que l'instabilité apparaît sur tous les signaux mesurés : V_{rf}, V_{dc}, V_f, 1H, 3H, V_i. Les figures III.3(a) et III.3(b) montrent un exemple d'instabilité sur 1H. La variété des diagnostics affectés par l'instabilité montre que de nombreuses propriétés physiques du plasma sont concernées.

Afin de situer exactement l'instabilité par rapport aux étapes de formation des poudres, des dépôts ont été réalisés à différents instants (avant, pendant et après l'instabilité, cf. figure III.4). La morphologie des poudres déposées a été étudiée grâce à la microscopie électronique à balayage (*SEM*/MEB) et à la microscopie à force atomique (*AFM*) en mode contact intermittent (*tapping mode*). L'étude des images obtenues (figures III.5 et III.6) et de la fonction de distribution des rayons (figure III.7) permet de localiser l'instabilité. L'échantillon déposé avant l'instabilité présente une seule population, centrée autour de r_d = 1.5 nm. Pendant l'instabilité, on observe deux populations : une autour de r_d = 1.5 nm (nanocristaux) et la seconde autour de r_d = 4 nm (agrégats). A la fin de l'instabilité une seule population apparaît autour de r_d = 5 nm, ce qui correspond à des nanocristaux agglomérés. Le début de l'instabilité correspond donc au début de la phase d'agrégation.

Nous avons observé que la fréquence de l'instabilité évolue dans le temps (figure III.2(b)). L'augmentation de fréquence semble correspondre à l'établissement de l'instabilité. La décroissance observée par la suite peut être expliquée par l'augmentation de la masse moyenne des poudres pendant l'agrégation. Une étude détaillée de l'influence des conditions opératoires (puissance injectée, température de gaz, débit de silane et pression) sur le comportement et les fréquences de l'instabilité est présentée ici. L'instabilité est très sensible aux changements de pression. Une augmentation de quelques dizaines de μbar

conduit à la disparition du phénomène. Le seuil de disparition a été mis en évidence autour de p = 150 μbar. L'augmentation de la puissance injectée (P_{rf}) a un effet sensible sur l'instabilité (figure III.8). Lorsque P_{rf} est augmentée, l'instabilité démarre plus tôt et dure moins longtemps (figure III.9(a)), comme toutes les phases de formation de poudres. Les fréquences de début et de fin augmentent linéairement avec P_{rf} (figure III.9(b)), ce qui peut s'expliquer par l'augmentation de la charge moyenne des poudres lorsque la puissance injectée augmente. Dans le cadre de l'étude en fonction du débit de silane (figure III.10), la variation de pression induite (3 - 4 μbar) est considérée comme négligeable par rapport à la pression totale (p = 124 μbar). Le démarrage et la durée de l'instabilité présentent une évolution en forme de "cloche" lorsque le débit de silane est augmenté (figure III.11(a)), avec un extremum pour Q_{SiH_4} = 1 sccm. Paradoxalement, les fréquences de début et de fin d'instabilité augmentent linéairement avec la quantité de silane dans la décharge (figure III.11(b)). Les effets de l'élévation de la température de gaz sur la formation des poudres ont été largement étudiés [38, 35, 78, 79, 80]. Dans le cadre de notre étude, nous avons étudié deux gammes de température : de RT à 120°C et de RT à -24°C (cf. figures III.12 et III.14). Globalement, le démarrage et la durée de l'instabilité sont proportionnels à la température de gaz : plus cette dernière est élevée plus l'instabilité démarre tard et dure longtemps (voir figures III.13(a) et III.15(a)). L'effet de la température sur les fréquences semble être différent selon la gamme considérée. A basse température, les fréquences diminuent linéairement quand la température est augmentée (figure III.13(b)). A plus haute température, la fréquence de début diminue linéairement quand la température augmente, tandis que la fréquence de fin reste quasiment stable (figure III.15(b)). Il est intéressant de noter qu'à aucun moment les conditions de température ne mènent à la disparition de l'instabilité. Dans quelques conditions expérimentales spécifiques, on peut observer un cas particulier de l'instabilité. Cette dernière apparaît en deux parties, la deuxième semblant être une réplique de la fin de la première (cf. figures III.16(a) et III.16(b)). Cette instabilité apparaît et est reproductible dans six jeux de paramètres différents, ce qui laisse penser que certains couples taille/densité de poudres pourraient favoriser son apparition. Finalement, au terme de cette étude, des zones de présence de l'instabilité peuvent être définies en fonction des paramètres. Les principaux paramètres entrant en jeu sont la puissance injectée et le débit de silane (figure III.17). La limite entre les différentes zones peut être décrite par une courbe du type $P_{rf} \propto Q_{SiH_4}^{-3/4}$.

Dans la référence [74], Descoeudres *et al* décrivent des instabilités semblables aux nôtres, apparaissant sur tous leurs diagnostics en gaz électronégatifs. Une explication possible du phénomène que nous observons pourrait être les instabilités dues à l'attachement dissociatif [73]. Nighan et Wiegand donnent un critère (voir équation III.1) pour l'apparition de l'instabilité. Ils y ajoutent aussi une condition nécessaire pour que celle-ci se maintienne : il faut que la densité d'ions négatifs et d'électrons soient du même ordre de grandeur [73]. En considérant que les poudres chargées négativement se comportent comme de gros

ions négatifs, on peut montrer, grâce à des études réalisées précédemment dans l'équipe [35, 9, 38], que les conditions sont remplies pour que l'instabilité apparaisse dans notre cas.

Le diagnostic électrique basé sur V_{dc} et 3H ne nécessite aucun accès optique au plasma. Une fois calibré, ce diagnostic peut fournir des informations précises sur la nature des poudres dans la décharge. Nous avons réalisé la calibration du système pour les premières phases de formation des poudres dans un plasma Ar/SiH_4. Ainsi l'instabilité étudiée dans ce chapitre peut être utilisée comme un repère de la fin de l'accumulation des nanocristaux dans le plasma. A l'heure actuelle nous savons qu'avant l'instabilité, les poudres sont monocristallines (cubique face centrée) de 2-3 nm de diamètre à température ambiante [39]. Leur forme semble sphérique et leur densité augmente pendant la phase d'accumulation jusqu'à atteindre la valeur critique ($10^{11} - 10^{12}$ cm^{-3}) permettant le début de l'agrégation [9]. Ainsi, juste avant l'instabilité, la densité de nanopoudres monocristallines est la plus haute qui puisse être atteinte dans la décharge. Ce dernier point s'avère particulièrement intéressant pour les applications dans le domaine des nanotechnologies telles que la fabrication de dispositifs à un électron [5] ou de cellules solaires [8]. Après l'instabilité, il ne reste plus de monocristaux dans le plasma. Les poudres sont constituées de monocristaux agglomérés. Leur taille augmente de 5 nm au début de l'agrégation jusqu'à environ 45 nm à la fin de cette phase [81]. Les poudres sont alors polycristallines, en forme de chou-fleur et présentent une grande surface spécifique (jusqu'à 115 $m^2.g^{-1}$ [82]) particulièrement intéressante pour les applications en catalyse.

Le contenu de ce chapitre a fait l'objet de deux publications référencées [75] et [76] dans la bibliographie de cette thèse.

Chapter IV

Other self-excited instabilities in complex plasmas

The void region and various instabilities linked to this dust-free region in dusty plasmas are now well-attested, especially in sputtering discharges as the PKE experiment [57]. In most cases, these instabilities are due to dust particle growth and/or presence in the plasma.

In this chapter, the behavior of the dust cloud during the growth of dust successive generations has been explored. A void region has been evidenced and a strong inhomogeneity of the depositions has been brought to the fore. Moreover, an overview of three different instabilities linked to dust particle formation and/or void region is presented. Those experiments have been performed both on the Silane experiment and the PKE one. All of them are self-excited instabilities. The first one, observed on the Silane experiment, occurs during dust particle successive generations. It is closely linked to the growth/expelling cycle of dust particles from the center of the discharge. Finally, the Successive Generation Instability (SGI) seems to be a void instability due to new dust generations formed in this region. In a second part, we focused on the so-called *heartbeat* instability in the PKE experiment. A new diagnostic, spatially resolved optical emission spectroscopy, has been implemented on the setup. It allows to get an insight in local behaviors of both the plasma and the void region. Moreover, the threshold behavior of the heartbeat is underlined by bringing to light its damping and shutdown period. To finish, the complex scheme of Dust Particle Growth Instabilities (DPGI) in the PKE experiment is presented. This instability is due to the growth of the first dust particle generation in a sputtering discharge. A seven-step development of the DPGI has been evidenced, and the three first steps are detailed here.

The content of this chapter has been published in three papers:

- M. Mikikian, M. Cavarroc, L. Couëdel, L. Boufendi
  Phys. Plasmas **13**, 092103 (2006) [83]

- M. Mikikian, L. Couëdel, M. Cavarroc, Y. Tessier, L. Boufendi
  New J. Phys. **9**, 268 (2007) [84]

- M. Cavarroc, M. Mikikian, Y. Tessier, L. Boufendi
  Phys. Rev. Lett. *submitted* (2007) [85]

IV.1 Successive generations in Ar/SiH$_4$ plasmas

Dust particle formation in an Ar/SiH$_4$ plasma is a continuous phenomenon. As long as Silane precursors are provided , new generations of dust particles are formed in the discharge [86]. The phenomenon we study in this section is located around one hundred seconds after plasma ignition. From figure IV.1 we can distinguish: ① (insert) nanocrystal formation and accumulation, aggregation instability (see section III.1), nanocrystal aggregation and growth by surface deposition, ② second and third dust particle generations.

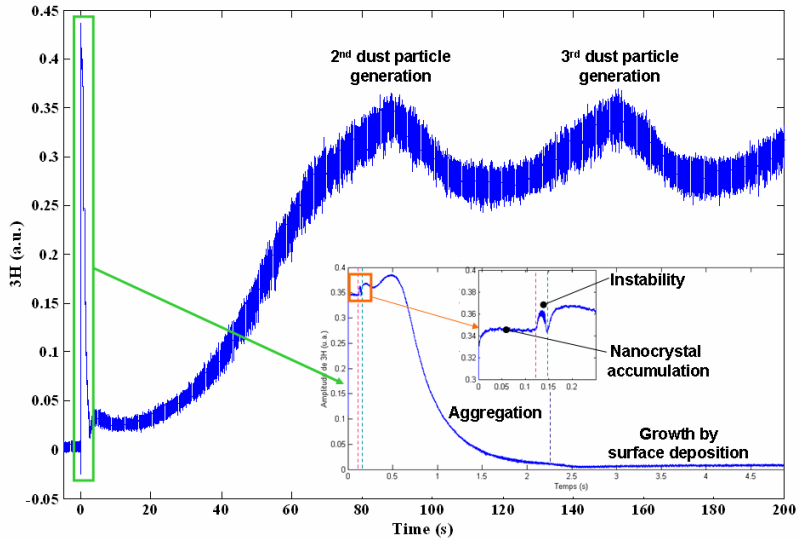

Figure IV.1: Time-evolution of the third harmonic of the discharge current amplitude during dust particle successive generations in an argon-silane plasma for different time-scales. The insert corresponds to figure III.1.

IV.1.a Experimental evidence of dust particle successive generations

Successive generations of dust particles can be monitored thanks to the V_{dc}/3H diagnostic. They appear as quasi-sinusoidal low-frequency oscillations of the signal, with a period of the order of typically one minute as can be seen in figure IV.1. The decrease of 3H corresponds to a decrease of the electron density: this can be explained both by the presence of big dust particles attaching lots of electrons, or by numerous little dust particles that could produce the same effect. The increase of 3H corresponds to an increase of the electron density, meaning that less electrons are attached by dust particles: big dust particles could be expelled from the plasma, or the density of smaller dust particles is small. All classical parameters affecting dust particle formation have an influence on the time-period of these oscillations. As an example, when gas temperature is increased, dust particle formation is delayed and the time-period of these oscillations can rise above several minutes.

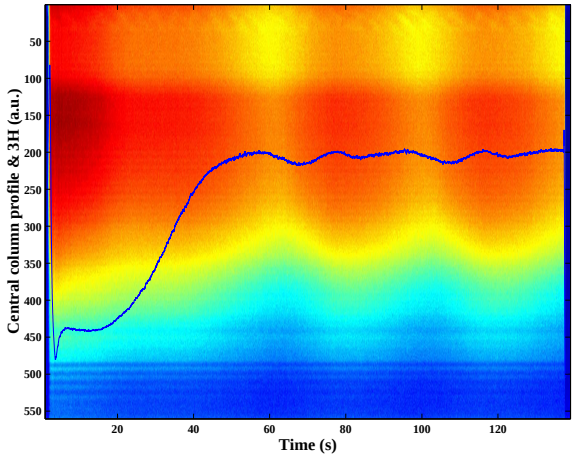

Figure IV.2: Superimposition of 3H signal on the central column profile from standard video during dust successive generations.

Dust particle successive generations can also be monitored using optical diagnostics. As an example, we used a standard camera (25 fps) to record the plasma glow emission during dust particle growth. If one correlates the central column profile and the 3H signal (see figure IV.2), an obvious correlation can be observed. On the left hand side of the figure, the plasma ignition is clearly identified, while on the right hand side, nearly three new dust particle generations are evidenced.

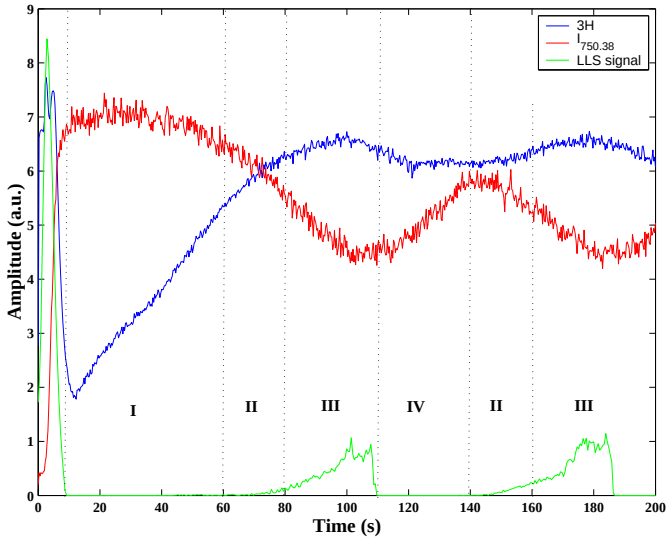

Figure IV.3: Time-evolution of 3H, I_{Ar^*} and LLS during dust particle successive generations in an Argon-Silane plasma.

Thanks to correlations with Laser Light Scattering (LLS) signal and the time evolution of the Argon line at 750.38 nm, we can refine our hypothesis concerning the behavior of 3H (see figure IV.3). For this purpose, we need to assume the presence of a void region in the dust cloud as in [13]. We will see further (in the next section) that this assumption has been validated by several experimental evidence.

For the sake of clarity, figure IV.3 has been divided in several parts numbered from I to IV. The early stages of dust particle formation (between 0 and 10 s on the figure) have already been discussed previously (see chapter III). So the analysis starts around 10 s after plasma ignition:

- Part I (from 10 to 60 s): in this first part, 3H increases while $I_{750.38}$ first increases before reaching a maximum value and then decreases, and there is no detectable LLS signal. The increase in $I_{750.38}$ corresponds to the opening of a void region, where the ionization rate is enhanced. The enhancement of the ionization rate favors the growth of a new dust particle generation in the void region. Once this new generation started to grow, $I_{750.38}$ starts to decrease. In this part, new dust particles are neither big enough nor numerous enough to be detected by LLS, so the LLS is zero. However, new synthesized dust particles push away bigger ones from the discharge center. The expelling of bigger dust particles, which had attached numerous free electrons, causes an increase of the free electron density in the plasma. Newly created small dust particles attach far less electrons than the expelled bigger ones. There is thus a net increase of the free electron density in the discharge, leading to 3H increase. This confirms the hypothesis of a void opening when 3H starts to increase [13].

- Part II (from 60 to 80 s): 3H exhibits a slope modification and keeps on increasing but more smoothly. $I_{750.38}$ is still decreasing as in part I and a small increase in the LLS signal is detected. Newly created dust particles grow in the void region and become detectable by LLS. They also start to attach more and more free electrons due to their increasing size. They keep on pushing bigger dust particles away, and tend to fill the whole void region, leading to the decrease of $I_{750.38}$. As new dust particles become bigger, and so more charged, the balance between free electrons lost by attachment and free electrons recovered due to dust expelling is modified. There is still an increasing amount of free electrons in the plasma, but the net increase is lower than in part I, and thus explain the slope modification in 3H.

- Part III (from 80 to 110 s): 3H increases to its maximum value before starting to decrease. $I_{750.38}$ decreases to its minimum value, and the LLS signal increases until reaching a plateau. The new generation of dust particles is growing in the void region and is now clearly detected thanks to LLS. This new generation now almost fill the whole void region, leading to the decrease of $I_{750.38}$ that reaches its minimum value. The net increase in the free electron density is less and less important due to the

strong attachment on the growing particles, leading 3H to reach a maximum value. Then, a plateau appears on the LLS signal and $I_{750.38}$: the void region is now totally filled by the new generation of dust particles. As these grains are still growing, they keep on attaching more and more electrons, leading to the beginning of 3H decrease.

- Part IV (from 110 to 140 s): The LLS signal suddenly falls to zero, while $I_{750.38}$ starts to increase. A new void is opening in the discharge center. 3H decreases until reaching a plateau: an equilibrium is reached between free electrons recovered from dust appellation and free electrons lost by attachment. $I_{750.38}$ keeps on increasing until a new dust particle generation starts to grow in the void region. The phenomenon is then cyclic and the following part is a new part II, followed by a part III and so on, as long as Silane is provided in the discharge.

IV.1.b Evidence of a void region

Dust voids are experimentally observed in various dusty plasmas. They have been observed in sputtering discharges [55, 56, 50, 57] or with calibrated injected dust particles, both under microgravity conditions or in the laboratory [50]. They also occur in reactive plasmas using Silane [87] or Acetylene [88] produced in typical GEC cell (i.e. without plasma box). Moreover, some cases of dust particle successive generations growing inside a void region have already been reported both in sputtering plasmas [50] and in reactive gas plasmas [88]. In this case, a void region appears in the dust cloud and the new generation starts to grow inside this void region as can be seen in figure IV.4.

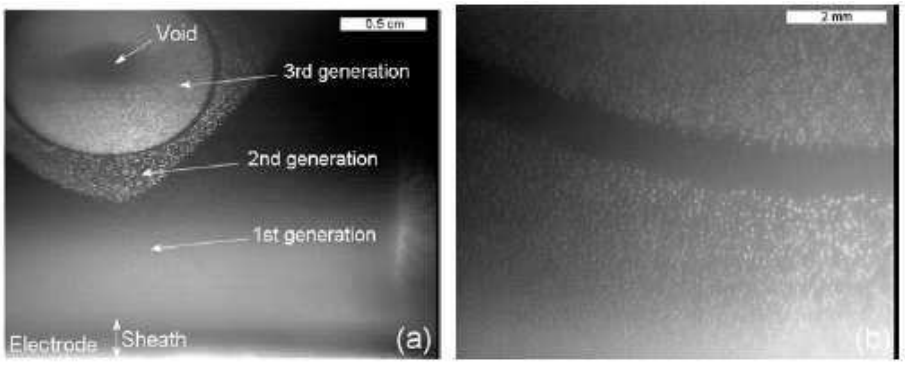

Figure IV.4: (a) Successive generations of grown dust particles on the PKE experiment (b) high-resolution camera showing the separation between a previously grown cloud (bottom) and a new growing one (top) in the void region [50].

A first correlation between 3H, LLS signal and the intensity of the Ar*(750.38 nm) line, presented in figure IV.3 lets think that a void region could appear in the dust cloud. Indeed, as can be seen in figure IV.3 (part IV for example), when no dust particles are detected in the plasma center (no LLS signal), an increase of the ionization rate (i.e. in $I_{750.38}$) is observed, just before the beginning of a new generation growth on 3H. This increase of the ionization is typical of a void region in dusty plasmas [57].

In order to determine the validity of this assumption, we performed several observations of the plasma during the instability using a standard and a high speed camera. These experiments were very fussy to perform due to the lack of optical accesses on our reactor. In order to get a larger optical access to the plasma, we used a discharge box pierced by a hole of 12 mm in diameter. Figure IV.5 shows a typical frame extracted from a movie: the center of the circle hardly corresponds to the center of the discharge, while the dark blue part corresponds to the plasma box. Thus, as can be seen in figure IV.5, a central area of higher glow emission (in red), meaning that the ionization is higher as well, is evidenced in the movies. This result confirms the one previously obtained by optical spectroscopy, and tends to validate the void region hypothesis.

If we refer to figure IV.5, the assumed void region is off-center (the center of the circle

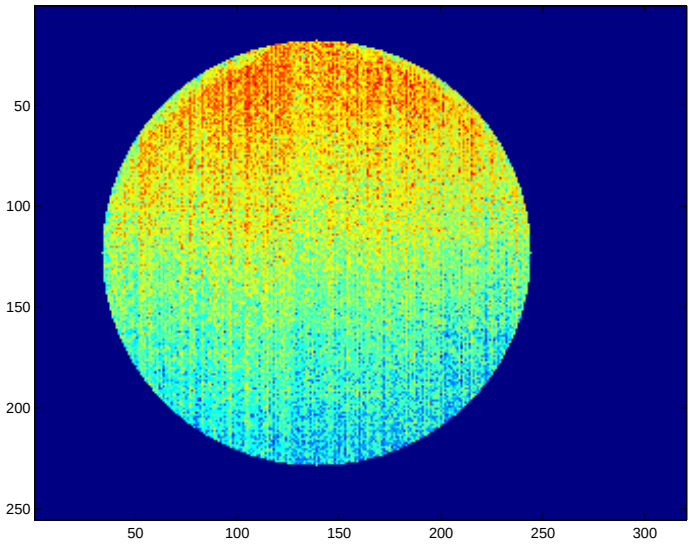

Figure IV.5: Typical frame extracted from a high-speed movie.

corresponds approximatively to the center of the discharge). The "red region" is obviously in the upper part of the dust cloud. This effect can be explained by the thermophoretic force on dust particles: the upper (powered) electrode is assumed to be 60°C while the lower one (grounded) is at RT. The dust cloud is consequently attracted toward the lower electrode, thus exhibiting a void region off-center toward the upper electrode.

To get evidence of the void region, spatially resolved depositions were performed during dust particle successive generations. Five samples were located on the grounded (lower) electrode in the discharge box. The first one was in the center, and the others were evenly dissevered on the electrode radius. They were placed at r = 0, 17, 32, 47, 62 mm respectively. These samples have then been observed thanks to SEM using different magnifications. Finally, the two most representative scales for this study were 5 or 10 μm and 200 nm. On the images with a scale of 5 μm (see figures IV.7 (a) to (e)), very few big dust particles are detected in the discharge center, while more and more are present when the radius is scanned. On the other hand, the images with a scale of 200 nm (see figures IV.8) indicate that lots of small nanoparticles (around 10 nm in diameter) are deposited in the discharge center, while the deposition becomes less and less dense when we look toward the edge of the plasma, with nanoparticles bigger and less numerous. Finally, the constitution of the deposited layer is very dependent on its location in the discharge. In the discharge center, the layer is made of very numerous nanoparticles around 10 nm (giving a dense sublayer) and fewer bigger particles (between few tens of nm to 1 μm). The more we go away of the center, the less the sublayer is dense and its smaller constituents tend to increase in size (up to around 20 nm). Moreover, more and more bigger dust particles are detected on the sample near the plasma edge. These results are totally consistent with a void region, where new dust particle generations would grow.

Figure IV.6 gives a rough sketch of the proposed void region in the Ar/SiH_4 discharge. As proposed in our model, several dust particle generations coexist in the plasma (five in this example). Each new generation grown in the void pushes away the previous one, leading to a concentric structure with the newest dust particles (i.e. smallest ones) in the discharge center, and "shells" made each ones of "older" (i.e. bigger) dust particles. In fact, each ellipse stands for a dust particle generation, with the smallest (newest) in the discharge center and the biggest (oldest) at the edge. The five colored blocks stand for the volume of deposition on each sample.

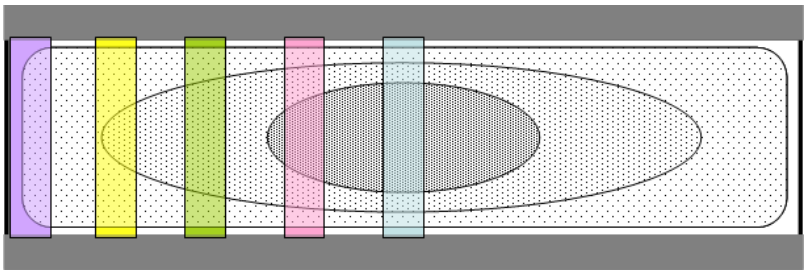

Figure IV.6: Model of the void region in the Ar/SiH_4 discharge.

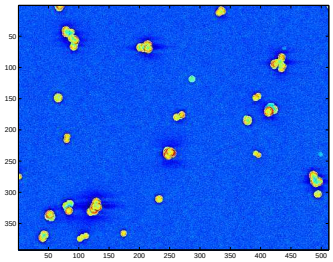

(a) r = 0 (discharge center)

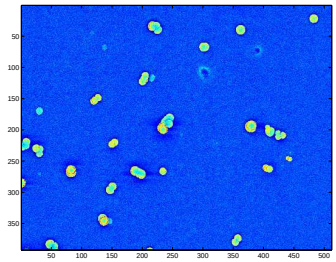

(b) r = 17 mm

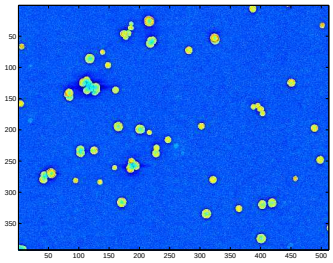

(c) r = 32 mm

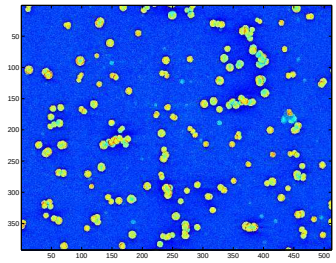

(d) r = 47 mm

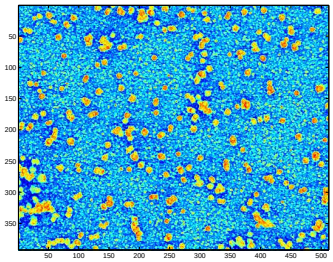

(e) r = 62 mm (discharge edge)

Figure IV.7: SEM images of the spatially resolved depositions (scale = 5μm).

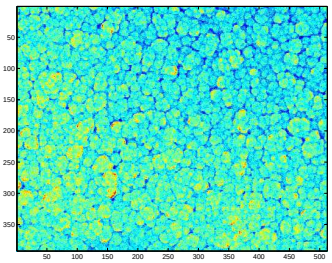

(a) r = 0 (discharge center)

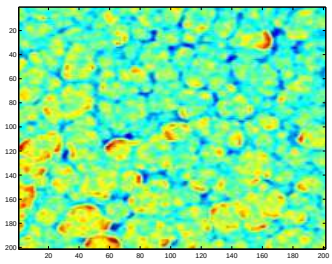

(b) r = 0 mm, zoom of (a)

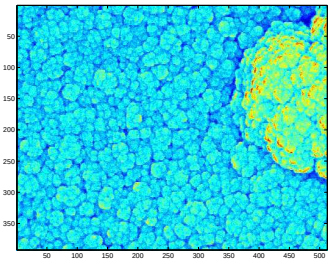

(c) r = 17 mm

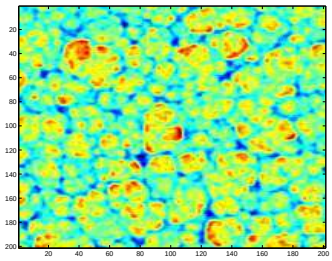

(d) r = 17 mm, zoom of (c)

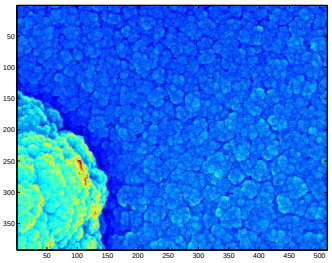

(e) r = 32 mm

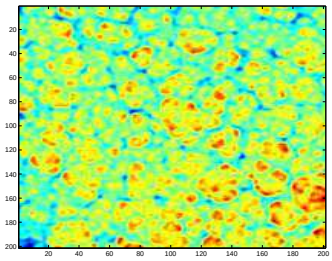

(f) r = 32 mm, zoom of (e)

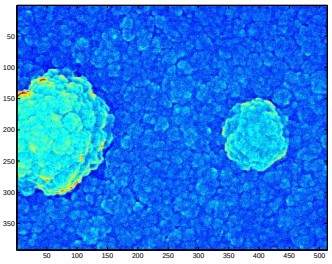

(g) r = 47 mm

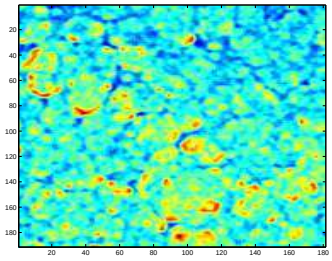

(h) r = 47 mm, zoom of (g)

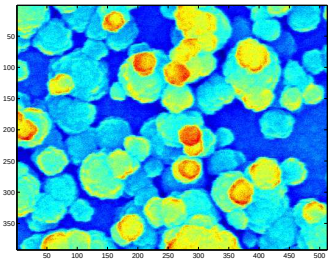

(i) r = 62 mm (discharge edge)

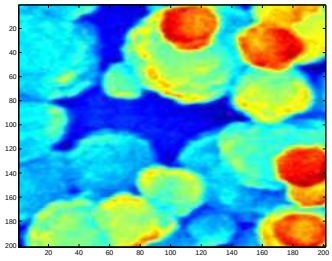

(j) r = 62 mm, zoom of (i)

Figure IV.8: SEM images of the spatially resolved depositions (scale = 200 nm).

IV.2 Successive generation instability

If we have a look to the inner structure of the 3H signal during the oscillation due to dust particle growth, we can bring to the light the unstable behavior of the signal (see figure IV.9(a)). It is important to note that this successive generation instability (SGI) is self-excited (no external excitation) and lasts as long as the plasma is on. A global FFT of the signal exhibits a broadband spectrum typically comprised between 30 and 90 Hz. As an example, figure IV.9(b) shows a spectrum ranging from 55 to 85 Hz. The electrical characterization of the SGI is corroborated by an optical one. In order to get an insight in the instability behavior, several movies were recorded during the instability, using a high speed camera (1789 fps). The global emission (glow) of the plasma was recorded over 4000 frames corresponding to 2.25 s approximately.

By looking at the integrated glow over each frame as a function of time (figure IV.9(c)), we get signals very similar to the ones obtained thanks to the electrical measurements. Moreover, the FFT spectrum of the optical signals is comparable to the one of electrical signals. It generally exhibits a broadband spectrum comprised between 30 and 90 Hz. As an example, figure IV.9(d) shows a spectrum extracted from one of the movies, with typical frequencies comprised between 50 and 90 Hz. Due to experimental constraints, synchronization between the 3H signal and the recorded movies has not been possible. As the SGI is a very reproducible phenomenon, we compared data that do not proceed from the same experiment. This can explain the small discrepancies observed in figures IV.9(b) and IV.9(d). Moreover a direct comparison between the FFT of the 3H signal and the one of the $I_{750.38}$ line of ArI (see figure IV.10) recorded simultaneously during dust successive generations, shows that these two spectra are very similar. This first result allows to conclude that the SGI is not an artefact due to the power coupling system for example. Thus, a more detailed study has been performed in order to better understand this instability.

IV.2.a Beginning of the SGI

The beginning of the instability occurs generally a few seconds after the plasma ignition. The setting-up of this instability appears as an increase in the oscillation amplitude at the beginning of the phenomenon (see figure IV.11). The start of the instability exhibits a very complex scheme with several frequency-branches in the spectrogram as can be seen in figure IV.12. At the beginning of the instability, five branches can be evidenced. The two lowest tend to meet in one branch around between 50 and 60 s. This new branch disappears quickly (between 70 and 80 s). The three highest branches tend to meet in a unique branch, which persists as long as the plasma is on. This complex scheme does not depend on experimental parameters. It is the same whatever the conditions and is very reproducible. It can bring to mind some other complex schemes of instabilities observed in the PKE experiment [57, 83].

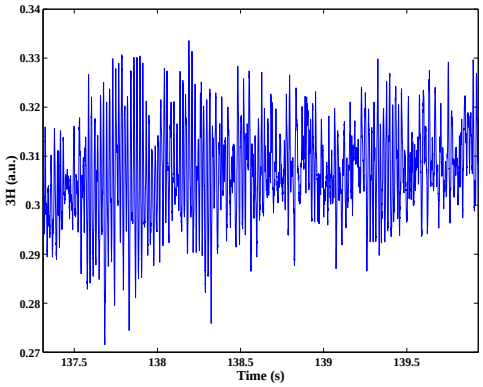

(a) Inner structure of 3H during the SGI.

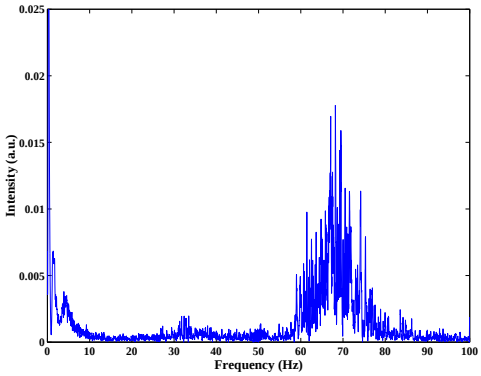

(b) Global FFT of 3H during the SGI.

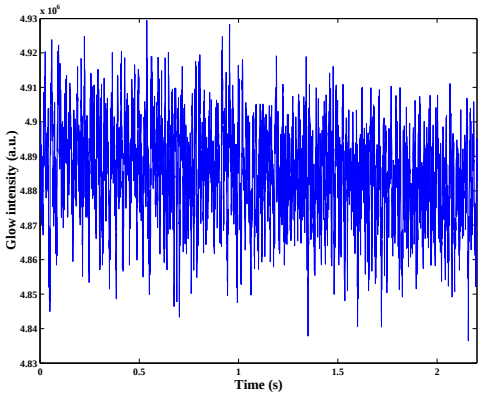

(c) Inner structure of plasma glow during the SGI.

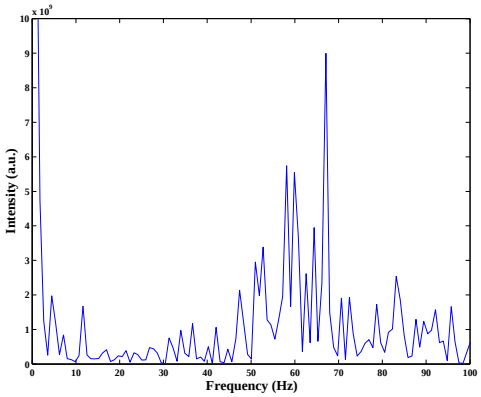

(d) Global FFT of the glow signal during the SGI.

Figure IV.9: Time-evolution of 3H and plasma glow with their corresponding FFT during the SGI.

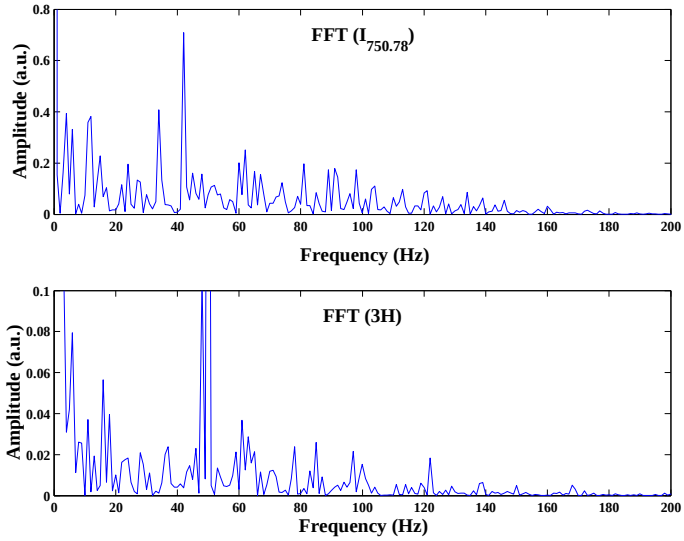

Figure IV.10: FFT spectra of 3H and Ar line (at 750.38 nm).

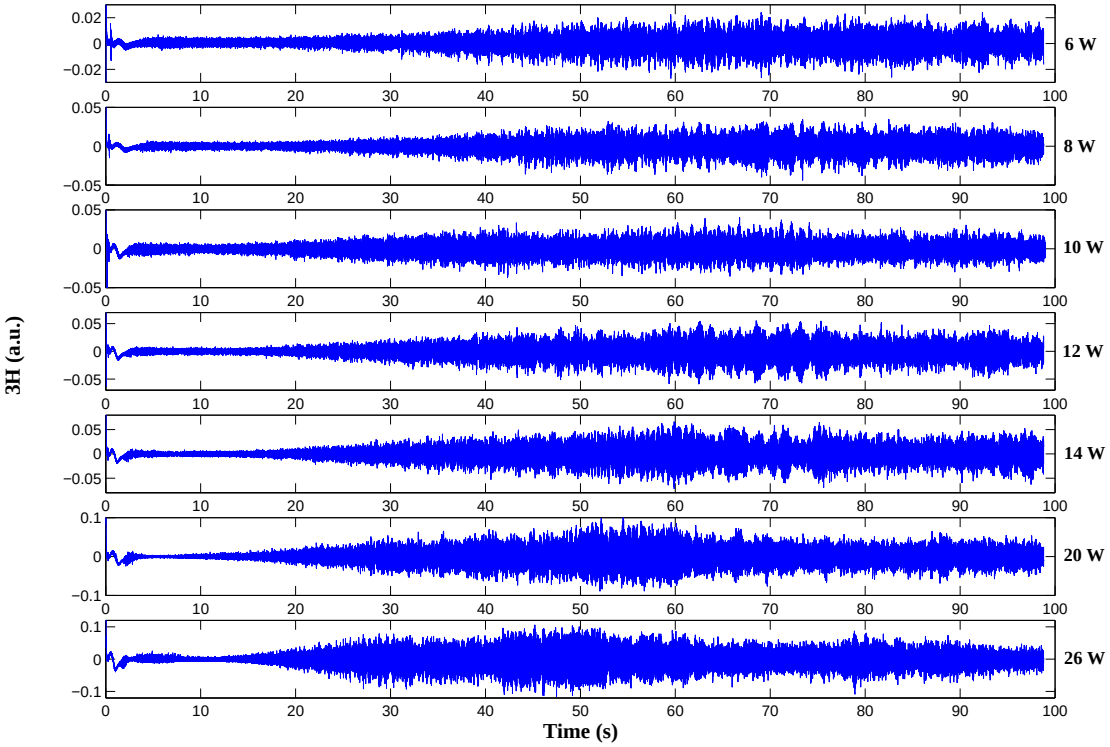

Figure IV.11: Time evolution of 3H (alternative component) for different injected powers at SGI beginning.

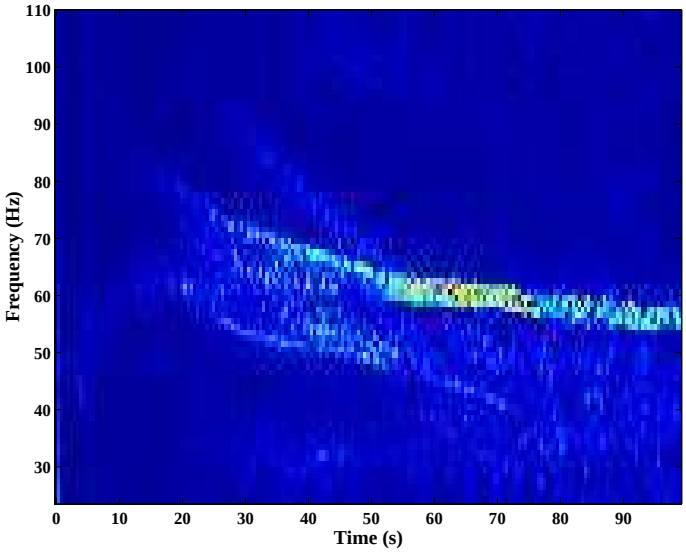

Figure IV.12: Spectrogram of the SGI beginning.

IV.2.b Behavior of the SGI

When performing a time-resolved FFT of the 3H signal, we obtain a spectrogram as the one in figure IV.13. This spectrogram shows an alternation of very ordered phases with low frequencies (between 40 and 60 Hz) and less ordered phases with higher frequencies. The ordered phases seem to correspond to dust particle formation for each new generation. During theses phases, the instability frequency linearly decreases on an interval of about 10 Hz. The less ordered phases seem to correspond to dust expelling from the plasma. During these phases, the frequency is not well-defined, but is globally higher than the one of the ordered phases. However, this frequency still remains under 100 Hz. Figure IV.14 shows a transition from a less-ordered phase to a highly-ordered one in the 3H signal. In this figure, it clearly appears that the oscillations are not well-defined in the left-hand part and that they have a small amplitude, while they are quasi-sinusoidal on the right-hand part with a greater amplitude. An estimation of the oscillation frequency on the two parts of this signal gives a frequency around 61 Hz for the less-ordered part compared to a frequency around 56 Hz for the highly-ordered part.

Using a high-speed video camera to record the plasma glow, we found quite similar results in the optical measurements. Figure IV.5 shows a typical frame extracted from the movie. The dark blue part corresponds to the discharge box, while the part inside the circle (in false colors) corresponds to the plasma glow emission. In this figure, we can clearly identify an area in red corresponding to a high ionization rate. Figure IV.15(a) and IV.15(b) give the time evolution of the central column profile and the line 75 profile. The line 75 profile is much more representative than the central one due to the off-centered void (the void boundary crosses the line 75 while it seldom crosses the central one). In order to get a better understanding, the time evolution of the integrated value of the column (line) is superimposed on the matrix. These two profiles bring to the fore an intensity oscillation of the area of maximum ionization in the plasma. The obtained signals are very close to the ones obtained thanks to the electrical diagnostics. The main frequencies are the same. By exploring the column and line profiles over several movies, we can find back the succession of highly-ordered and less-ordered phases. Some strong intensity decreases (over one or two frames) of the central region can even been evidenced.

IV.2.c Sensitivity to parameters

Compared to the aggregation instability, the successive generation instability is globally not very sensitive to experimental parameters. As a matter of fact, no case of disappearance of the instability has been observed by modifying the experimental conditions. As soon as a second dust particle generation starts to grow in the plasma, the instability arises. It seems to be an intrinsic characteristic of dust successive generations in Ar/SiH_4 low-pressure plasmas. Nevertheless, some slight modifications in the instability frequencies have been

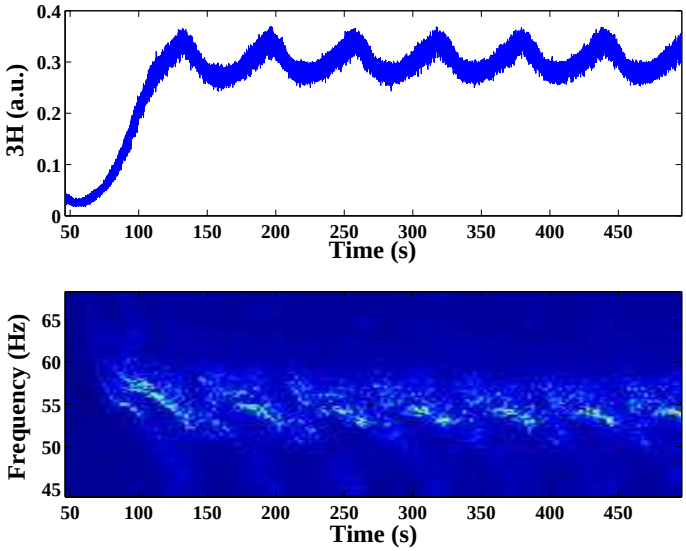

Figure IV.13: (a)Time-evolution of the third harmonic of the discharge current during dust particle successive generations in an argon-silane plasma (b) Spectrogram of 3H during the successive generation instability.

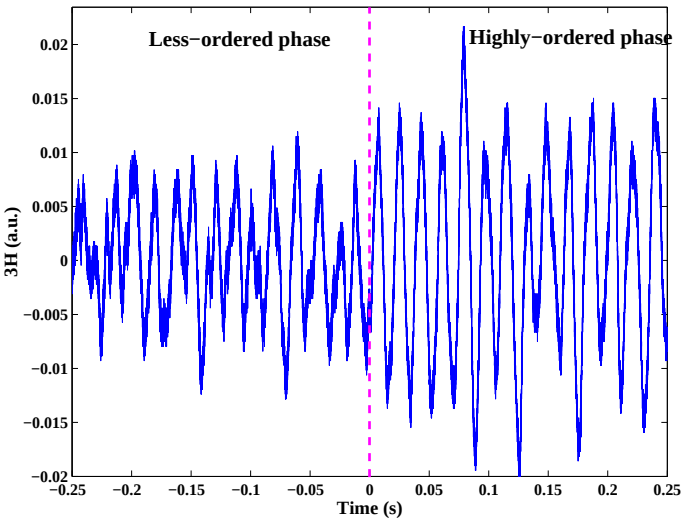

Figure IV.14: Transition from a less-ordered phase to a highly-ordered phase on 3H during the SGI.

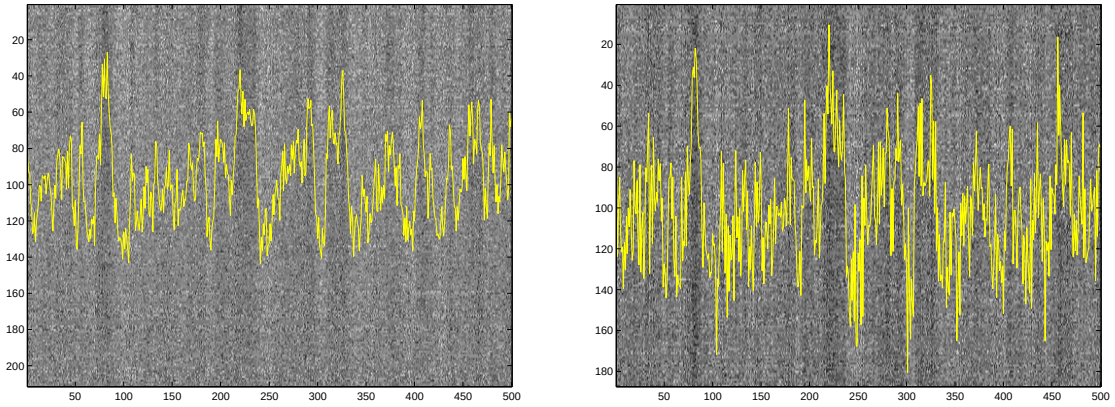

(a) Central column profile.

(b) Line 75 profile.

Figure IV.15: Column and line profiles of the plasma glow during the SGI, the superimposed yellow curve is the time evolution of the integrated value of the column (line).

observed, depending on the experimental conditions. The frequency of the instability is quite difficult to determine. Actually, by looking at figure IV.12, we can determine that the instability is mainly characterized by two very close frequencies (around 62 and 68 Hz for t = 40 s for example), that become closer and closer. From t = 50 s it is hard to discern the highest frequency and the lowest one. These two close frequencies could explain the noticeable modulation of the electrical signal that can be observed on figure IV.16 for different injected powers. When the injected rf power is increased, the frequencies of the instability tend to increase as can be seen in figure IV.17(a). We can also notice that the instability begins earlier for higher injected powers (see figure IV.11) as expected from our experience. On the contrary, these same frequencies tend to decrease when the silane flow rate in the discharge is increased (see figure IV.17(b)). The gas temperature effects are even more difficult to border. It seems to have no effect on the frequency of the highly-ordered phases while it seems that the frequency of the less-ordered phases increases when decreasing gas temperature. Furthermore, pressure does not seem to have any outstanding effect on the instability behavior.

IV.2.d Possible causes of the instability

As we showed in the description of the SGI, this instability is closely linked to dust particle successive generations. The highly-ordered phases correspond to new dust formation, while less-ordered ones correspond to the expulsion of bigger dust particles toward the plasma edge. In the previous section, we evidenced the presence of a void region in the dust cloud, where new dust generations grow, pushing previously formed and bigger dust particles toward the plasma edge.

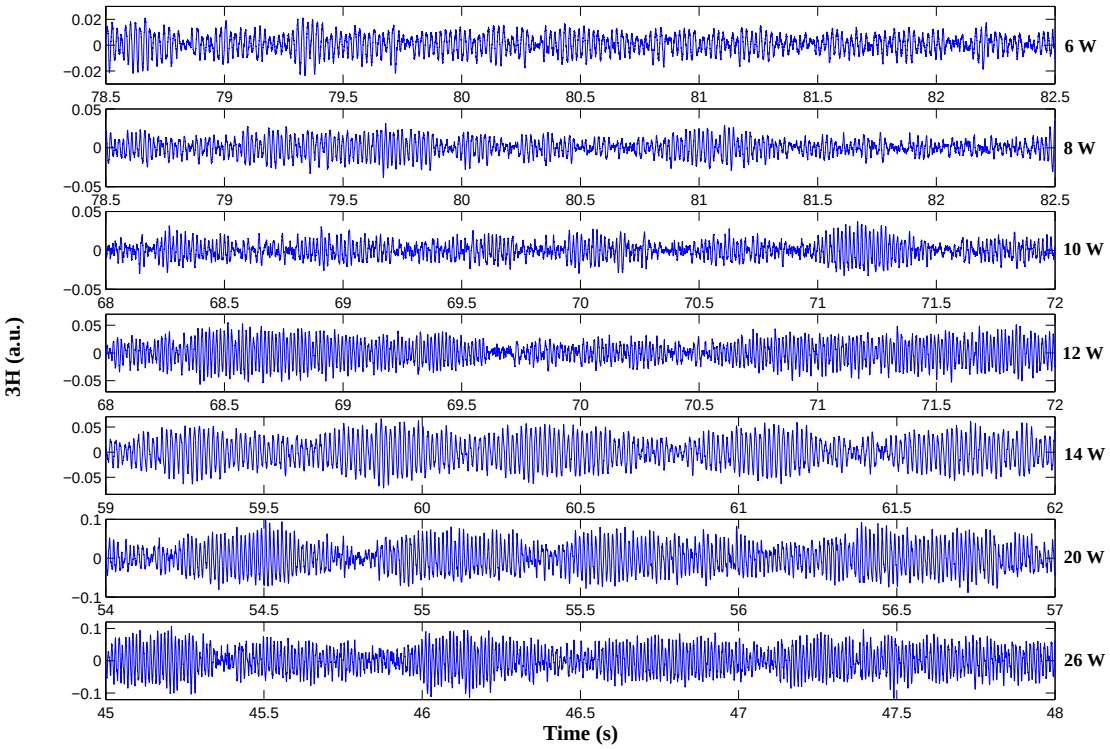

Figure IV.16: Time evolution of 3H during the SGI for different injected powers.

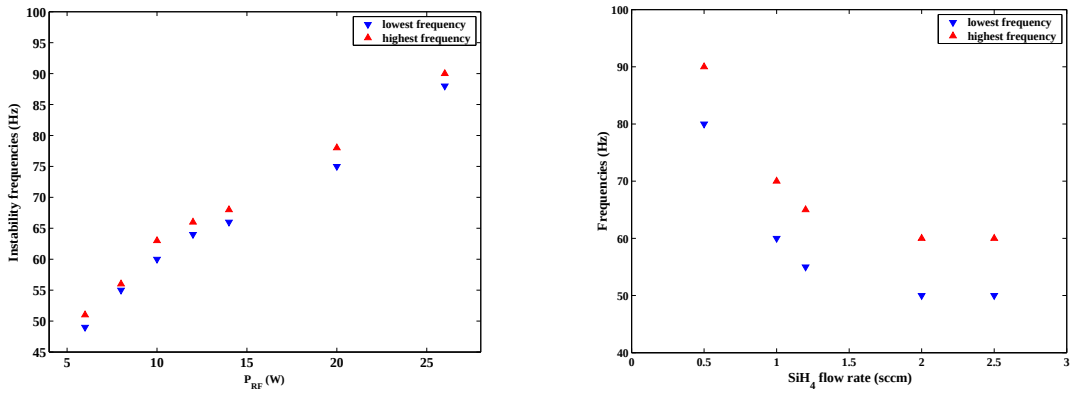

(a) Evolution of the SGI frequencies for different injected powers.

(b) Evolution of the SGI frequencies for different silane flow rates.

Figure IV.17: Evolution of the SGI frequencies for different injected powers and silane flow rates.

The formation of a new dust generation highly modifies the ionization rate, and thus the ion drag force, in the void region. The equilibrium between the ion drag and the electric force becomes then unbalanced, leading to an oscillation of the void region. A very similar phenomenon has also been observed in the PKE experiment, where the void region tends to be instable when new dust generations grow inside.

In the following, two instabilities linked to dust formation and/or void region have been investigated using the PKE setup.

IV.3 *Heartbeat* instability

Experiments concerning the *heartbeat* instability are performed in the PKE-Nefedov chamber. A 3D dust cloud is grown in an Ar plasma by sputtering carbon-based layers deposited on the electrodes. This cloud tends to fill the whole plasma volume, excepted a void region in the plasma center. In some specific conditions, the void region can exhibit an unstable behavior, corresponding to a self-excited oscillation, named. This instability consists in successive contractions and expansions of the void size. It has been first observed during microgravity experiments (with injected dust particles around 3-7 μm) [89] and then in laboratory experiments (with grown dust particles around a few hundreds of nm) [57]. Figure IV.18 shows several frames (separated by 2 ms) during a typical *heartbeat* instability. The void expansion, and then its contraction, can be clearly distinguished. The dark central part of the void region is never filled by dust particles, even during contraction, as can be seen in figure IV.18.

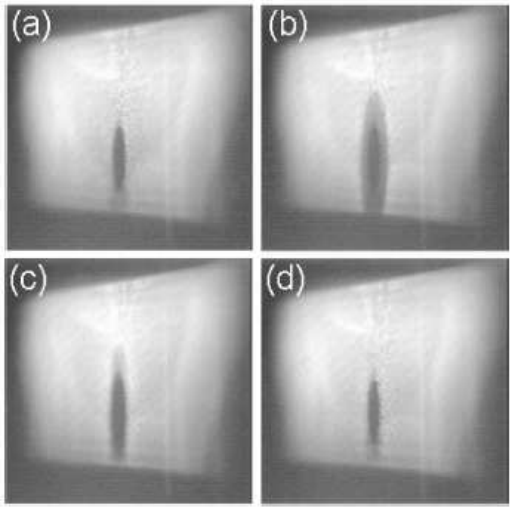

Figure IV.18: Consecutive frames taken at 20° – 30° with respect to the laser direction during the *heartbeat* instability. The black region at the top is the upper sheath. The black region at the bottom marks the laser sheet limit.

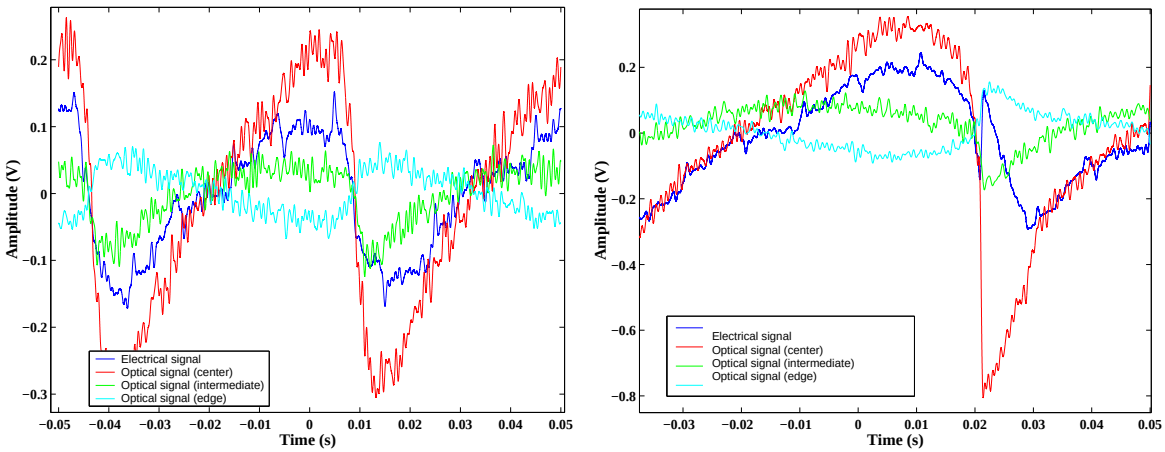

(a) Two successive contractions/expansions.

(b) Zoom on an inner motif.

Figure IV.19: Time-evolution of 1H and SR-OER signals during the *heartbeat* instability.

IV.3.a Electrical and optical characterization of the *heartbeat*

The analysis of the *heartbeat* instability is performed thanks to electrical measurements (time evolution of the amplitude of the current fundamental harmonic, 1H), spatially resolved optical emission recording (SR-OER) and video imaging.

Figure IV.19 shows the typical evolution of the 1H and SR-OER signals during the *heartbeat* instability. The general shape of these signals (see fig. IV.19(a)) underlines the complex plasma changes leading to these contractions and expansions of the void size. From experience, it seems that the fast signal decrease occurs during the void contraction.

Generally, the *heartbeat* signature is quite easy to recognize on both 1H and SR-OER signals. On 1H, we first observe a small increase in the current, looking like a shoulder. Then a sharp increase followed by a drastic decrease. In most cases, a small peak can be identified during this last decrease. This peak is not always visible. It appears always on the right-hand side of the main motif and its correlation with a specific event during the contraction/expansion sequence is not easy to perform only from 1H signal [57]. Moreover, we have to keep in mind two important points: first, the current is an integrated signal while the void motion is local in the discharge, second, the dust cloud cannot respond to a fast change in the current. That's why the void motion cannot be precisely correlated to 1H signal, and why a spatially-resolved diagnostic is needed. SR-OER allows us to follow simultaneously the integrated emission of the plasma light in three different points of the discharge. The first one is in the center of the discharge, corresponding to the void center, the second one corresponds to the edge of the plasma and the third one is an intermediate point between the two previous ones that could correspond more or less to the void edge.

First observation we can make is that the optical signal in the void region is globally in phase with the electrical signal, as can be seen in figure IV.19(a). However, the minimum

of the optical signal exactly corresponds to the sharp peak in the 1H decrease (see fig. IV.19(b)). The optical signal on the edge of the plasma is globally in phase opposition with the electrical signal (fig. IV.19(a)). But once more, this observation is contradicted in the sharp peak region where the two signals are maximum (fig. IV.19(b)). The intermediate optical signal is fussy to interpret. It quite looks like the opposite of the edge signal with its minimum in the sharp peak region (fig. IV.19(b)): it globally appears more like the signal in the plasma center. The optical results raise an important point concerning the electrical sharp peak. First, this peak is not an artefact, second it seems to be related to a local phenomenon in the discharge. Unfortunately this last point is not totally elucidated yet. Some high-speed camera measurements recently analyzed tend to confirm a reversal of the plasma glow emission (from bright center/dark edge to dark center/bright edge). Moreover, SR-OER allows us to formulate some assumptions concerning the void motion. The fact that the emission inside the void and at the plasma edge are in phase opposition lets think about an ionization wave propagation in the plasma. We still have to determine whether it comes from the void region or from the plasma edge, and in which direction it spreads over the plasma and the dust cloud.

IV.3.b Evolution of the *heartbeat* instability as a function of experimental conditions

The effect of rf power and pressure on the *heartbeat* instability was investigated. First, the rf power was varied at constant pressure (see figure IV.20), and then the pressure was varied keeping the rf power constant (see figure IV.21). The evolution of the instability can be quantified on three different points: the shape of the signal, its amplitude and its frequency.

The *heartbeat* instability is very sensitive to the injected power [57]. Its frequency increases slowly when decreasing the rf power. Between 2.2 and 3.8 W this evolution is linear. For rf power lower than 2.2 W, this linear evolution is not well-attested due to the fact that we are near the instability threshold. The range of frequencies observed is not very wide: from 5 to 20 Hz at p=1.6 mbar, and from 15 to 35 Hz at p=0.6 mbar. When the power is decreased, the instability shape is more and more distorted. For power lower than 2.05 W, the signal looks like successive Dirac functions and the instability occurs in an erratic way, with sometimes a single contraction/expansion sequence in a stable void sequence. Concerning the amplitude of the oscillation, we observed that when the power is decreased, the amplitude of the signal also tends to decrease. An interesting point is that the most affected part of the oscillation is the variation below the continuous part of the signal (corresponding to the open stable void). For high power (3.3 W for example), the variations below and above the continuous part are of the same order of magnitude while for low power (2.05 W for example), the variation below the continuous part becomes negligible compared to the variation above. This last observation underlines the complex phenomena driving the *heartbeat* instability.

Pressure variations also have a strong effect on the *heartbeat* frequency [57]. From 1.6 mbar to 1 mbar, the frequency decreases in a very tight range: 21 to 15 Hz at 3.3 W. Then, when the pressure is lowered from 1 mbar to 0.3 mbar, the *heartbeat* frequency increases faster and faster until reaching more than 100 Hz at 0.3 mbar. This frequency increase can be related to the lower friction with gas. Concerning the shape of the instability, it is not well-defined for high pressure (1.6 and 1.4 mbar). An outstanding point concerning this pressure range is that the amplitude variation below the continuous part of the signal is more important than the variation above the continuous part. From 1 mbar to lower pressures, this tendency reverses and the signal looks like the one described before, with a "below part" being less and less important when the pressure is decreased.

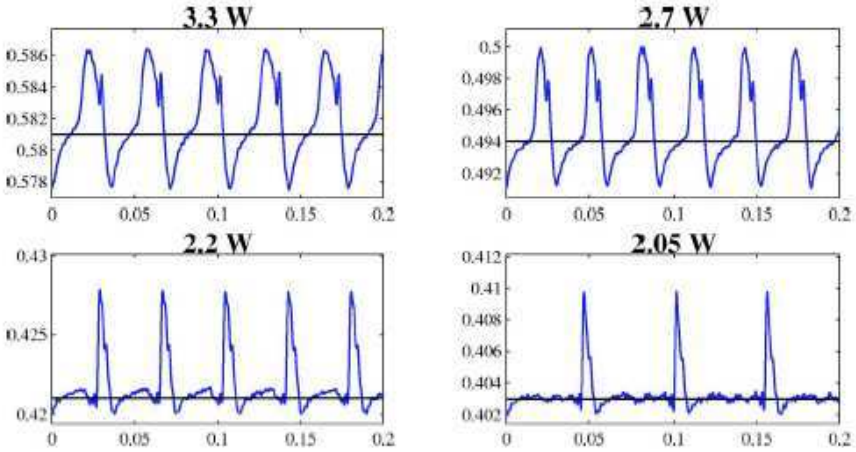

Figure IV.20: Power dependence of the electrode current during the *heartbeat* instability. The x axis is time in seconds and the y axis is the current amplitude in arbitrary units.(from [57])

IV.3.c Damping and shutdown period of the *heartbeat* instability

By decreasing the rf power to a sufficiently low value, the *heartbeat* instability can be stopped. Electrical and optical signals reveal that the end of the instability is foregone by a shutdown period corresponding to a damping of the instability through more and more failed peaks appearing in both signals. Figure IV.22 shows an example of two failed peaks before the peak of instability. These failed peaks can be clearly identified on the electrical signal, and on the optical signals from the void and the plasma edge regions. But they are almost impossible to detect on the intermediate optical signal, maybe due to the low signal-to-noise ratio of this signal.

The transition from n to $(n+1)$ failed peaks occurs without any forerunner. Figure IV.23(a) shows a transition from 1 to 2 failed peaks in the optical signal (horizontal arrow).

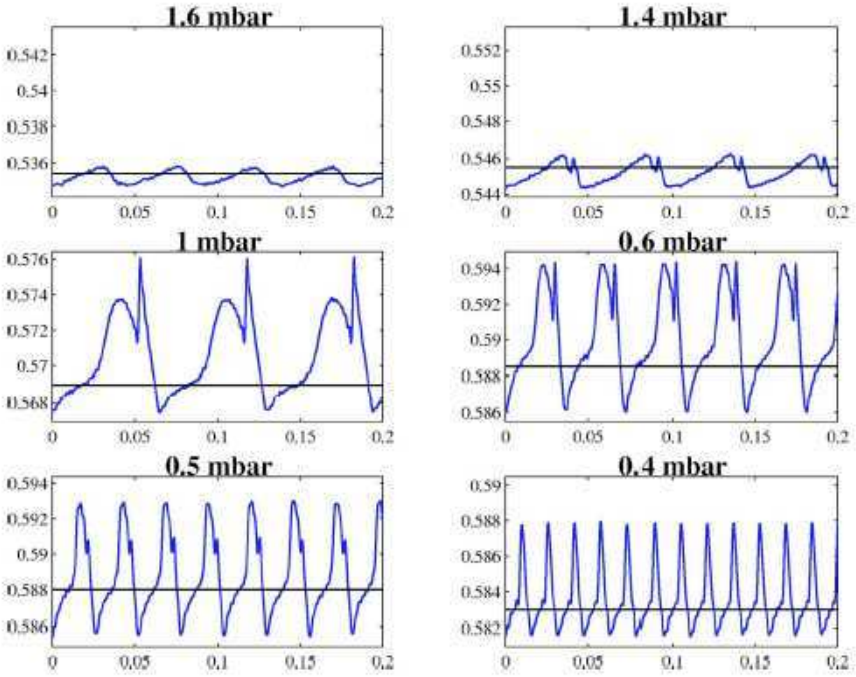

Figure IV.21: Pressure dependence of the electrode current during the *heartbeat* instability. The x axis is time in seconds and the y axis is the current amplitude in arbitrary units. (from [57])

The vertical arrow indicates the expected position of a high peak. This one is delayed and only a failed peak occurs. The number of observed failed peaks during this shutdown period can rise over more than 10 failed peaks as can be seen in figure IV.23(b) to (d). Every failed peak corresponds to a failed closure of the void region, leading to a damping of the *heartbeat* instability. The instability loses energy step by step until it stops. As the void is assumed to be maintained by an equilibrium between an outward ion drag force and an inward electrostatic force, this shutdown period could confirm the assumption of an oscillation of the ionization rate in the discharge [51]. Thus a failed peak could correspond to ionization conditions giving advantage to the outward force maintaining an open void [72, 90].

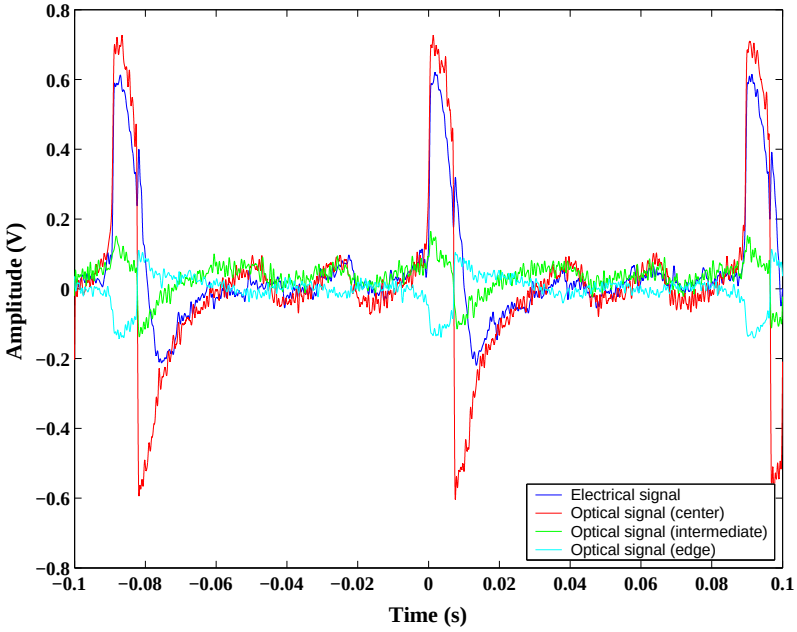

Figure IV.22: Example of the time-evolution of 1H and SR-OER during the shutdown period of the *heartbeat* instability.

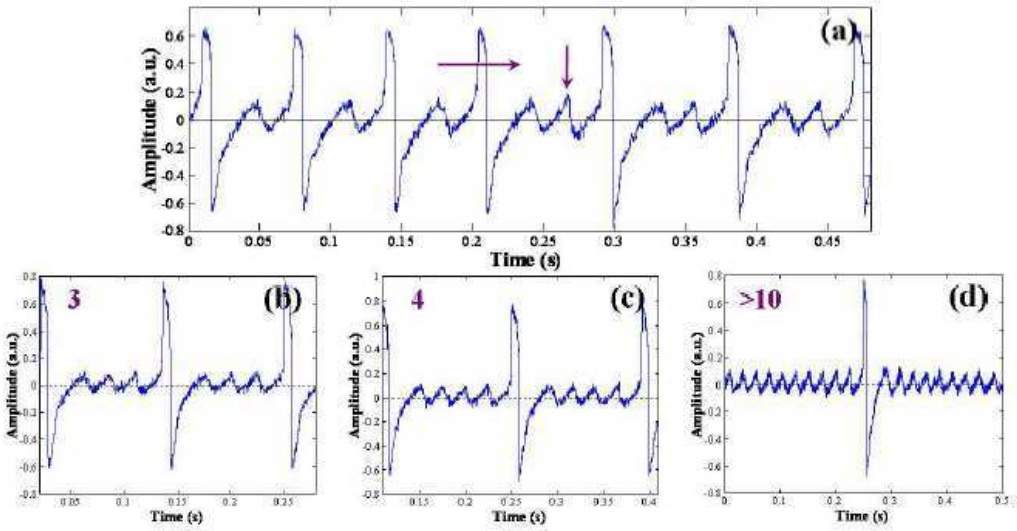

Figure IV.23: Last beats of the *heartbeat* instability. More and more failed peaks appear before the complete stop (a) transition from 1 to 2 failed peaks, (b) 3 failed peaks, (c) 4, (d) more than 10.

IV.4 Dust particle growth instabilities

Dust particle growth instabilities (DPGI) are observed on the PKE experiment, when a huge density of dust particles is obtained. They typically appear a few tens of seconds after plasma ignition. They can be observed both on electrical and optical signals [72, 90]. Due to their low frequency and strong amplitude, the beginning of DPGI can also be well-detected by the naked eye. DPGI clearly appear on the electrical signal, as an increase of the fluctuation amplitude becoming a real oscillation. The duration of these instabilities can reach several minutes (more than 12 in figure IV.24) and different phases are evidenced.

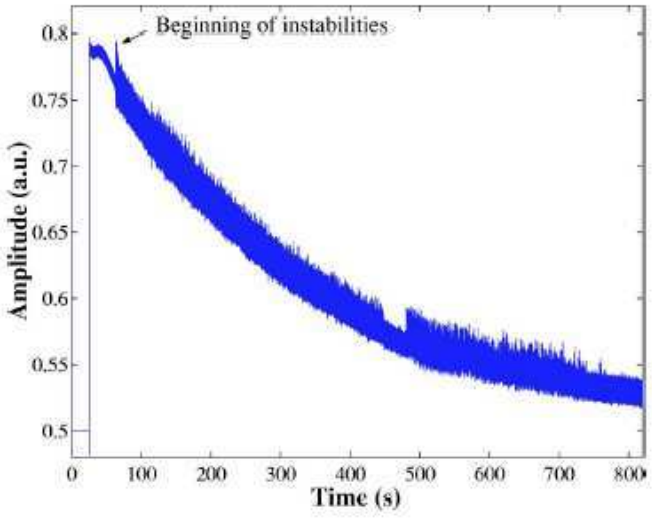

Figure IV.24: Time evolution of the amplitude of the discharge current fundamental harmonic during dust particle growth.

In spite of a lack of reproducibility of the experiments, statistics performed on several experiments allow to determine some general behaviors.

IV.4.a Phase identification on the electrical and optical measurements

As can be seen in figure IV.24, DPGI are characterized by different regimes. These different phases are evidenced by performing the same measurement in the ac mode in order to improve the vertical resolution of the oscilloscope. This measurement is shown in figure IV.25(a). The beginning of DPGI is detected around 40 s and seven clear phases are observed. These phases are even better evidenced by performing a Fourier analysis of the signal, as can be seen in figure IV.25(b). The same Fourier analysis performed on the optical signals gives roughly the same spectrogram.

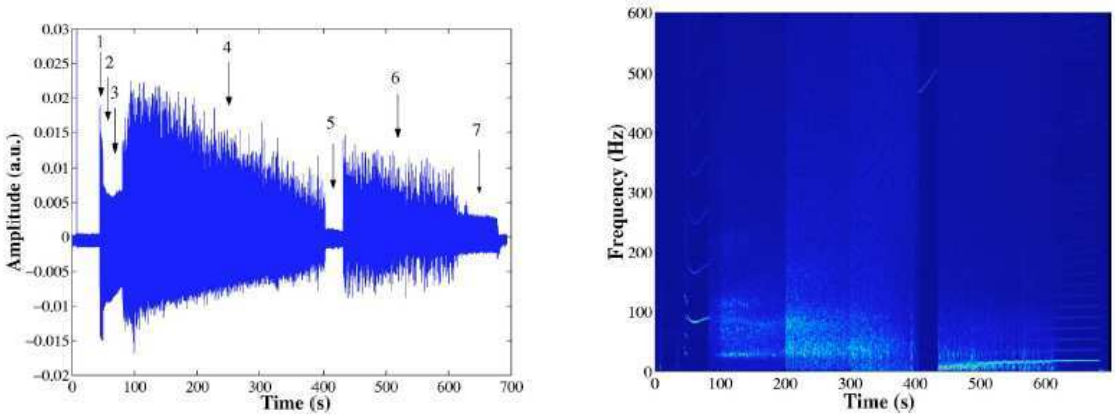

(a) Time evolution of the amplitude of the discharge current fundamental harmonic during dust particle growth (ac component). Instabilities appear around 40 s after plasma ignition. Successive phases are numbered from 1 to 7.

(b) Spectrogram of electrical measurements corresponding to (a) and describing the frequency evolution of DPGI as a function of time.

Figure IV.25: Time-evolution of 1H and its frequency during the DPGI

From figure IV.25 we can evidence seven different phases:

- Three ordered phases P1, P2 and P3, from $\simeq$ 40 s to $\simeq$ 80 s.
- A chaotic phase P4, from $\simeq$ 80 s to $\simeq$ 405 s.
- A high frequency phase P5, from $\simeq$ 405 s to $\simeq$ 435 s.
- A second chaotic phase (becoming more and more regular) P6, from $\simeq$ 435 s to $\simeq$ 600 s.
- A regular oscillation phase P7, from $\simeq$ 600 s to $\simeq$ 680 s.

All theses phases are observed both on electrical and optical measurements. They are thus obviously linked to an unstable state of the system plasma + dust particles. In the following, only the first three ordered phases are described. The study of the four other phases is reported in a publication [83] and in Lénaïc Couëdel's PhD thesis (to be defended in 2008).

IV.4.b First three ordered phases

DPGI begin with three successive ordered phases (P1, P2 and P3), separated by clear transitions as can be seen in figure IV.26.

The two early phases P1 and P2 are short (a few seconds typically) and are not detected in all experiments, while the P3 phase is regularly observed and lasts longer (a few tens of seconds typically). These three phases are clearly separated and their frequency evolves as a function of time (both on electrical and optical measurements).

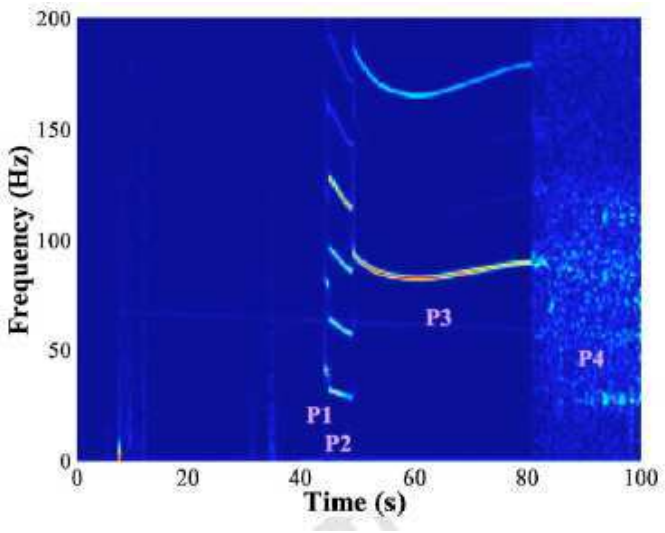

Figure IV.26: First three ordered phases of DPGI and transition to a chaotic regime.

IV.4.b.i Electrical measurements

Figure IV.27(a) represents an electrical measurement of P1, P2 and P3 phases. On this particular measurement, the P2 phase is very short, allowing to display the three phases and the transition from one to the following on the same figure. The first phase (P1) is characterized by wide separated peaks with a mean frequency around 40 Hz. The transition between P1 and P2 appears as the growth of two small peaks between these high amplitude patterns. On the Fourier analysis, this transition appears as a frequency decrease from around 40 Hz to around 30 Hz. This result can be explained by the fact that the two new peaks have a weak amplitude and don't appear on the spectrum at first. During the P2 phase, the two small peaks are still growing while the higher one decreases. Finally, the P3 phase is reached, characterized by three peaks of the same amplitude. The P3 phase frequency is thus roughly three time the P2 phase frequency, around 94 Hz. The P3 phase is the most robust of the first three ordered phases, and is observed in almost all of our experiments. It lasts a sufficiently long time to show a time evolution linked to dust particle growth (see fig. IV.26). The frequency time evolution of P3 is always the same: first decreasing, reaching a minimum value, and then slightly increasing until DPGI enter the chaotic phase P4. Furthermore, the frequency range of P3 seems to be linearly dependent on the phase duration: the higher the frequency, the shorter the time duration. The frequency time evolution of P1, P2 and P3 is better observed on the frequency harmonics (figure IV.26) due to the quite sawtooth shape of the electrical signal (see figure IV.27(a)).

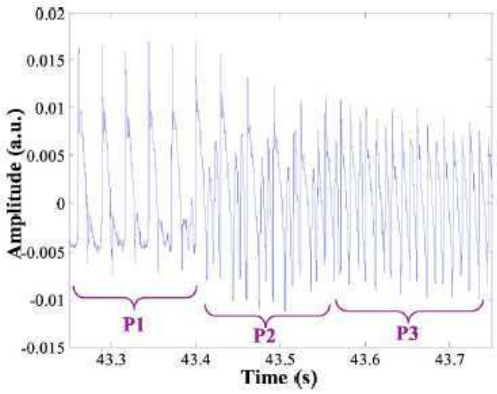

(a) Observation on electrical measurements.

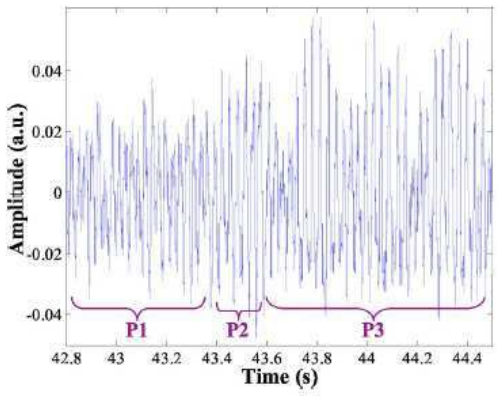

(b) Observation on optical measurements (near the plasma edge).

Figure IV.27: Transition between the first three ordered phases of DPGI.

IV.4.b.ii Optical measurements

Optical measurements, recording the plasma light integrated over all the wavelengths and at different positions, also show three ordered phases at the beginning of DPGI, as can be seen in figure IV.27(b). However, P1, P2 and P3 phases don't exhibit the same behavior as in optical signals. In particular, the transition between P1 and P2 is not as clear as in the electrical signal. It is here revealed by an increase in the oscillation amplitude (see fig. IV.27(b)). The P3 phase is here characterized by a clear amplitude modulation, better evidenced near the plasma edge than in the center. Concerning the oscillation frequency, some discrepancies with the electrical signal are also observed, especially in the P3 phase (see figs. IV.26 and IV.28). Indeed, phases P1 and P2 frequencies are quite similar on both measurements while P3 phase frequency exhibits a different behavior: on optical measurement, the frequency remains almost the same as P2 phase one, while it is tripled on electrical measurements. Furthermore, the behavior of the P3 phase is not exactly the same depending on the observed plasma region. As can be seen in figure IV.28, the signal recorded in the plasma center (a and c) is slightly different from the one recorded near the plasma edge (b and d). In the plasma center, two frequencies are evidenced: the main one around 26 Hz and a weaker one around 31 Hz. Near the plasma edge, these two frequencies are evidenced and a third one, around 3 Hz, also appears. This last frequency corresponds to the strong modulation observed in figure IV.27(b). These observations underline that some spatial considerations have to be taken into account to interpret the P3 phase.

First, the frequency is three times lower on optical signals compared to electrical signals. This point could be explained by a phenomenon oscillating around 94 Hz in the plasma, affecting the electrical measurements, but detected only one time out of three by the optical fibers. A plasma modification appearing successively in different places or moving in the plasma could explain this observation. Indeed, in both cases, the optical fiber could see

this phenomenon only when it is located in front of it, while the electrical measurement traduces an integrated behavior. Presently, a modification appearing in different points of the plasma seems to be more probable and investigations using a high-speed camera are underway in order to confirm (or undermine) this hypothesis.

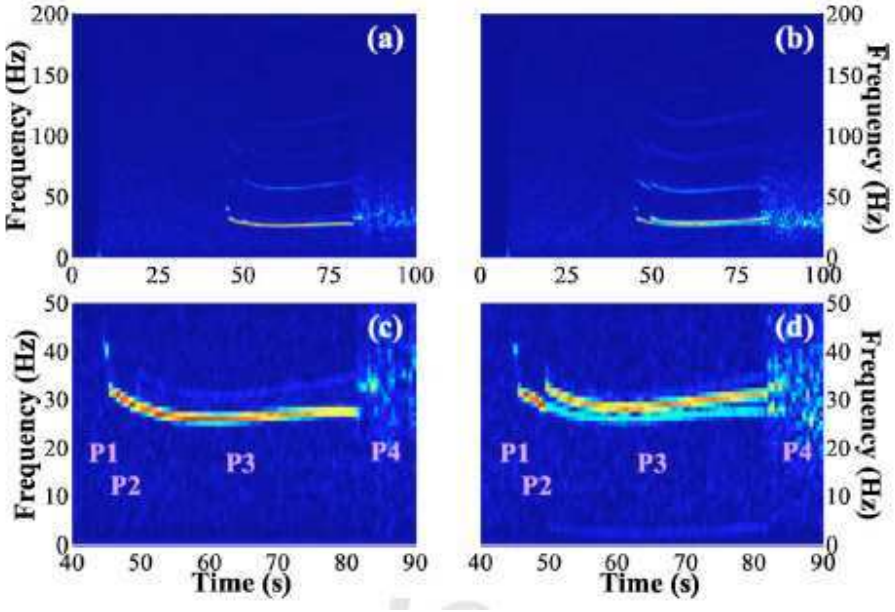

Figure IV.28: Spectrogram of optical measurements recorded (a) in the plasma center, (b) near the plasma edge, (c) zoom of (a), (d) zoom of (b).

IV.5 Conclusion

In this chapter, we presented studies concerning three self-excited instabilities in different dusty plasmas. In each case, instabilities are closely linked to dust particle growth and/or the presence of a void region in the dust cloud.

The first study, performed in a silane-based plasma, brought to the fore the presence of a void region using LLS, OES measurements, video imaging and depositions. This result is of major interest: the void region was known to occur and was observed in non-confined discharges, both in sputtering plasmas [50, 55, 56, 57] or using reactive gases [87, 88] or injecting calibrated dust particles [60, 50]. Nevertheless, even if a void is assumed in confined discharges (produced in a discharge box) [13], it had never been experimentally attested until now. This first result tends to prove that void regions are a general and intrinsic feature of dense dust cloud in plasmas. Indeed, they are observed in a wide range of dusty plasmas aside of the chemistry, the dust particle origin, the geometry of the discharge, the gas flux, the rf excitation and the gravity conditions. Moreover, it appears that it is finally quite

difficult to avoid the appearance of this dust free region in a dense cloud of dust particles.

The Successive Generation Instability (SGI), observed in a silane-based plasma, has been shown to be closely linked to dust particle formation in the void region, and especially to the cycle growth/expelling from the center of the discharge. The SGI exhibits a very complex scheme at its setting-up, which is not fully understood. This instability is very few sensitive to experimental conditions and no cases of disappearance have been observed in the explored parameter range. This self-excited instability lasts as long as dust particles are formed in the discharge and can be observed in different silane-based plasmas using various buffer gases (Ar, Ne, He). This instability seems to be quite similar to another one, observed in the PKE experiment, occurring during dust particle growth in the void region. Their similarities are currently investigated.

A new diagnostic, consisting in Spatially Resolved Optical Emission Recording (SROER), implemented on the PKE setup, allowed us to improve our observations of the *heartbeat* instability. Some local behaviors have been underlined, showing that the glow emission has a different response in the plasma center and at the plasma edge. Some high speed camera measurements are currently analyzed in order to better understand the correlation between electrical and optical signals. A special attention will be devoted to the understanding of the sharp peak appearing in electrical measurements. Thanks to this study, a very interesting point has been brought to the fore concerning the threshold behavior of the *heartbeat* instability. A damping and a shutdown period have been evidenced. They are characterized by failed peaks in both electrical and optical signals, showing that the instability loses energy step by step before finally ceasing.

A complete study of the setting-up of the Dust Particle Growth Instabilities (DPGI) in the PKE experiment has been realized. A seven-step process has been evidenced thanks to electrical and optical measurements. The different behaviors of the electrical and optical signals during the three first ordered phases (especially the factor 3 in frequencies in the P3 phase) is explained by a local phenomenon "moving" in the plasma. High speed video measurements have been performed to validate this hypothesis. Their analysis is underway. However, this instability, closely linked to the dust particle first generation in a sputtering discharge, reminds in some ways the aggregation instability (see chapter III) also linked to the first generation of dust particles growing in a silane-based plasma.

Finally, instabilities linked to dust particles are found to occur in a wide variety of dusty plasmas. In this study, we thus evidenced that both void region and instabilities are observed in various types of dusty plasmas as summarized in table IV.5.

By crossing all these data, instabilities, and the void region, appear to be intrinsic phenomena in dusty plasmas. This study would need to be extended to other types of discharges (such as dc discharges) in order to get more data concerning the influence of the excitation on these features.

		Void	Instabilities
Chemistry	Silicon-based	[87] and **this work**	[75, 76]and **this work**
	Carbon-based	[50, 88, 91] and **this work**	[55, 56, 50, 83, 91] and **this work**
Dust origin	Injected	[60, 50]	[50]
	Sputtering	[50, 55, 56, 57] and **this work**	[50, 55, 56, 57, 83] and **this work**
	Reactive gas	[87, 88, 91] and **this work**	[75, 76, 91] and **this work**
Geometry	Confined	**this work**	[75, 76] and **this work**
	Non-confined	[50, 55, 56, 57, 87, 88, 91] and **this work**	[50, 55, 56, 57, 83, 91] and **this work**
Gas flux	With	[55, 56, 87, 88, 91] and **this work**	[55, 56, 75, 76, 91] and **this work**
	Without	[50, 57] and **this work**	[50, 57, 83] and **this work**
rf excitation	Classic	[55, 56, 87, 88, 91] and **this work**	[55, 56, 75, 76, 91] and **this work**
	Push-pull	[50, 57] and **this work**	[50, 57, 83] and **this work**
Gravity	Laboratory	[55, 56, 87, 88, 50, 57, 91] and **this work**	[55, 56, 75, 76, 50, 57, 91, 83] and **this work**
	Microgravity	[60, 50]	[50]

Table IV.1: Overview of the different dusty plasmas exhibiting a void region and/or instabilities

IV.6 French summary / Résumé en français

La région de *void*, ainsi que différentes instabilités liées à cette région vide de poudres, sont à l'heure actuelle bien connues, en particulier dans les décharges de pulvérisation comme l'expérience PKE [57]. Dans la plupart des cas, ces instabilités sont dues à la présence et/ou à la croissance de poussières dans le plasma.

Dans ce chapitre, nous avons étudié le comportement du nuage de poussières lors de la croissance de générations successives de poussières dans un plasma d'argon-silane confiné. Une région de *void* a été mise en évidence, ainsi qu'une forte inhomogénéité des dépôts due à ce *void*. De plus, nous présentons l'étude de trois instabilités auto-excitées liées à la formation des poussières et/ou à la région de *void*. Ces expériences ont été réalisées sur les expérience Silane et PKE. La première instabilité rapportée est observée sur l'expérience Silane, pendant la croissance de générations successives de poudres (SGI). Elle est étroitement liée au cycle croissance/expulsion des poudres du centre du plasma. Cette instabilité semble finalement être une instabilité du void, due à la formation des nouvelles générations de poudres dans cette zone du plasma. Par la suite, nous abordons l'instabilité *heartbeat* sur l'expérience PKE. Un nouveau diagnostic (la spectroscopie optique d'émission résolue spatialement) a été mis en oeuvre sur ce dispositif. Il permet d'avoir une idée des comportements locaux du plasma et de la région de *void*. De plus, le comportement à seuil du *heartbeat* est souligné par son amortissement et sa période d'extinction. Enfin, nous présentons le schéma complexe de l'instabilité liée à la croissance des poussières (DPGI) dans l'expérience PKE. Cette instabilité est provoquée par la croissance de la première génération de poudres dans une décharge de pulvérisation. Un schéma de développement

en sept étapes a été mis en évidence, et les trois premières étapes sont développées dans ce manuscrit.

Générations successives en plasmas Ar/SiH_4

La formation de poussières en plasmas Ar/SiH_4 est un phénomène continu. Tant que l'on fournit du silane dans la décharge, de nouvelles générations de poussières se forment [86]. Le phénomène que nous étudions ici a lieu quelques centaines de secondes après l'allumage du plasma. Ainsi, sur la figure IV.1, on peut distinguer : ① (insert) l'accumulation des nanocristaux, l'instabilité due à leur agrégation (voir chapitre III) puis l'agrégation et la croissance par dépôt de surface, ② la deuxième et la troisième générations de poussières. La croissance de générations successives de poussières apparaît clairement sur les caractéristiques électriques (V_{dc}/3H) sous la forme d'oscillations des signaux, avec une période de l'ordre de la minute. Tous les paramètres qui affectent classiquement la formation des poussières ont une influence sur cette période. A titre d'exemple, une augmentation de la température de gaz peut allonger cette période à plusieurs minutes.

Les générations successives de poudres sont aussi mises en évidence par les diagnostics optiques. Nous avons notamment utilisé une caméra standard (25 images par seconde) pour enregistrer l'émission lumineuse du plasma pendant la formation des poussières. La figure IV.2 présente le profil temporel de la colonne centrale des images de la vidéo ainsi que l'évolution de 3H associée. Une nette corrélation est observée, avec à gauche l'allumage du plasma clairement identifiable, et sur la droite, presque trois générations de poudres visibles.

Grâce à la corrélation entre 3H, le signal de diffusion de la lumière laser et l'évolution de l'intensité de la raie d'argon à 750.38 nm (figure IV.3), nous pouvons avancer une explication quant aux cycles de formation des poussières. Pour cela, nous ferons l'hypothèse de la présence d'un void dans la décharge. Nous verrons par la suite que cette hypothèse a été validée. Pour plus de clarté, la figure IV.3 est divisée en plusieurs parties numérotées de I à IV. La partie associée à la formation de la première génération de poudres (entre 0 et 10 s ici) a déjà été discutée précédemment. L'analyse commence donc environ 10 s après l'allumage du plasma :

- Partie I (de 10 à 60 s) : 3H augmente pendant que $I_{750.38}$ d'abord augmente puis atteint un maximum avant de commencer à diminuer, et il n'y a aucun signal de diffusion détectable. L'augmentation de $I_{750.38}$ correspond à l'ouverture du void, dans lequel le taux d'ionisation est plus élevé. L'augmentation du taux d'ionisation favorise la croissance d'une nouvelle génération de poussières dans le void. Une fois que cette nouvelle génération commence à croître, $I_{750.38}$ commence à diminuer. Les poussières ne sont ni suffisamment nombreuses ni suffisamment grosses pour diffuser la lumière, le signal de diffusion est donc nul. Cependant, les poussières nouvellement créées

poussent les précédentes loin du centre de la décharge. L'expulsion de ces poudres plus grosses, qui avaient attaché beaucoup d'électrons, provoque une augmentation de la densité d'électrons libres dans le plasma, qui n'est pas compensée par l'attachement sur les nouvelles poussières, trop petites. Il y a de fait une augmentation nette de la densité électronique, qui provoque une augmentation de 3H.

- Partie II (de 60 à 80 s) : 3H change de pente et continue à augmenter plus doucement. $I_{750.38}$ continue à diminuer comme dans la partie I, et une légère augmentation du signal de diffusion est détectée. Les poussières nouvellement formées grossissent dans le void, et deviennent détectables par diffusion de la lumière. Elles attachent aussi de plus en plus d'électrons libres du fait de leur taille plus importante. Elles continuent à pousser les poudres plus grosses sur les bords de la décharge, et commencent à remplir toute la région de void, menant à la décroissance de $I_{750.38}$. Comme les nouvelles poussières grossissent et attachent plus d'électrons, l'équilibre entre le gain et la perte d'électrons libres par le plasma est modifié. La quantité totale d'électrons libres persiste à augmenter mais de façon moins prononcée, ce qui explique le changement de pente de 3H.
- Partie III (de 80 à 110 s) : 3H augmente jusqu'à sa valeur maximale avant de commencer à décroître. $I_{750.38}$ atteint sa valeur minimale, et le signal de diffusion augmente jusqu'à atteindre un plateau. La nouvelle génération de poudres qui grossit dans le void est maintenant clairement détectée par diffusion de la lumière. Elle remplit maintenant quasiment toute la région de void, provoquant la chute de $I_{750.38}$ jusqu'à sa valeur minimum atteinte lorsque le void est empli de poudres. Le gain d'électrons libres est de moins en moins important du fait du fort attachement électronique sur la nouvelle génération de poudres : 3H atteint sa valeur maximum. Le plateau apparaissant sur le signal de diffusion indique que les poussières emplissent entièrement le void. Comme elles continuent à grossir, elles attachent de plus en plus d'électrons, provoquant la décroissance de 3H.
- Partie IV (de 110 à 140 s) : Le signal de diffusion chute subitement à zéro, tandis que $I_{750.38}$ commence à augmenter. Un nouveau void est en train de s'ouvrir au centre de la décharge. 3H décroît avant d'atteindre un plateau : un nouvel équilibre est atteint entre le gain et la perte d'électrons libres par le plasma. $I_{750.38}$ continue à augmenter jusqu'à ce qu'une nouvelle génération de poussières se forme dans le void. Le phénomène est alors cyclique et peut être décrit par l'enchaînement de la partie II puis III etc... tant que l'on fournit du silane dans la décharge.

Présence d'un *void*

Afin de valider l'hypothèse d'une région de *void* dans le nuage de poudres de notre décharge, différentes observations ont été réalisées à l'aide d'une caméra standard et d'une caméra rapide. Ces expériences sont très difficiles à réaliser du fait du peu d'accès optiques disponibles sur le réacteur. Cependant, grâce à l'imagerie vidéo (figure IV.5), une zone centrale de plus forte émission (en rouge), où le taux d'ionisation est donc plus élevé, a été mise en évidence. Cette observation tend à confirmer l'hypothèse d'une zone de *void* dans le nuage. Cette zone apparaît clairement décentrée vers le haut de la boîte à décharge. Cela pourrait être expliqué par la force de thermophorèse, due au gradient de température entre l'électrode rf (60°C) et l'électrode à la masse (RT), qui attire les poudres vers le bas de la décharge et décentre donc le void vers le haut.

Par la suite, des dépôts spatialement résolus ont été faits pendant les générations successives de poudres. Cinq échantillons ont été placés le long du rayon de la boîte à décharge également espacés les uns des autres. Les dépôts ainsi obtenus ont ensuite été observés au MEB. Les images à l'échelle 5 μm (figure IV.7) montrent que plus on s'éloigne du centre de la décharge, plus les poudres de taille importante sont nombreuses sur les dépôts. A l'échelle 200 nm (figure IV.8), on observe que plus on s'éloigne du centre de la décharge, moins la sous-couche du dépôt, composée de nanoparticules, est dense. Finalement, la structure des couches déposées s'avère extrêmement dépendante de la situation du substrat dans la décharge. Ces résultats sont parfaitement cohérents avec l'hypothèse d'un *void* dans le nuage de poudres, où les nouvelles générations de poudres se formeraient. La figure IV.6 propose un modèle schématique du *void* en Ar/SiH_4. Dans cet exemple, cinq générations coexistent (de la plus récente au centre à la plus ancienne au bord). Les blocs colorés représentent le volume de dépôt associé à chaque substrat.

Instabilités liées aux générations successives (SGI)

Si l'on regarde de plus près la structure interne de 3H lors des générations successives de poudres, on observe que le signal est très instable (figure IV.9(a)). Les SGI sont des instabilités auto-excitées qui durent tant que le plasma est allumé. La FFT globale du signal donne un spectre large bande typiquement compris entre 30 et 90 Hz (figure IV.9(b)). Cette caractérisation électrique est corroborée par la caractérisation optique. Ainsi, grâce à l'enregistrement de l'émission globale du plasma à l'aide d'une caméra rapide (1789 images par seconde), nous obtenons des signaux similaires aux signaux électriques, tant au niveau de l'allure générale que de la FFT. De plus la comparaison de la FFT de 3H et de celle de $I_{750.38}$ montre que les deux spectres sont tout à fait comparables. Ces premiers résultats nous permettent de conclure que les SGI ne sont pas un artefact mais bien une instabilité liée au plasma et/ou au nuage de poudres.

Le démarrage des SGI a généralement lieu quelques minutes après l'allumage du plasma et se traduit par une augmentation progressive de l'amplitude d'oscillation du signal. Ce démarrage affiche un schéma très complexe avec notamment un spectre présentant plusieurs branches de fréquences (figure IV.12) qui tendent à fusionner par la suite. Ce schéma s'avère très robuste et peu sensible aux conditions expérimentales.

Lorsque l'on réalise une FFT en fonction du temps de 3H, on obtient une alternance de phases très ordonnées à basse fréquence (40-60 Hz) et de phases moins ordonnées à plus haute fréquence. Les phases très ordonnées semblent correspondre à la formation d'une nouvelle génération de poussières, tandis que les phases moins ordonnées semblent correspondre à l'expulsion massive des plus grosses poussières. L'observation de l'émission du plasma grâce à une caméra rapide donne des résultats très similaires. De plus, de très fortes baisses d'intensité de l'émission apparaissent parfois.

Les SGI sont très peu sensibles aux conditions expérimentales. A titre d'exemple, aucun cas de disparition du phénomène n'a été observé dans la gamme de paramètres explorés. Ces instabilités semblent intrinsèquement liées aux générations successives en plasmas Ar/SiH_4. Cependant, quelques légères modifications dans les fréquences peuvent être observées en fonction des paramètres expérimentaux. Une fois les SGI établies, elles sont principalement caractérisées par deux fréquences qui deviennent de plus en plus proches, au point qu'il devient difficile de les distinguer. Ces deux fréquences proches expliquent l'importante modulation des signaux électriques observée (figure IV.16). Lorsque la puissance injectée est augmentée, ces fréquences augmentent légèrement tandis que les SGI démarrent plus tôt. A l'opposé, ces mêmes fréquences diminuent lorsque l'on augmente la quantité de silane dans la décharge. L'effet de la température de gaz est très difficile à cerner : ce paramètre ne semble affecter que la fréquence des phases peu ordonnées et être sans effet sur les phases ordonnées. Aucun effet lié à la pression n'a été mis en évidence.

Le comportement des SGI, intimement lié à la formation de nouvelles générations de poussières dans le void, laisse penser que ces instabilités pourraient être des instabilités du *void*. Un cas très similaire est observé sur le dispositif PKE, et est actuellement étudié.

Heartbeat

Le *heartbeat* est une instabilité observée sur le dispositif PKE, consistant en une série de contractions et d'expansions du *void* (figure IV.18). La figure IV.19, qui donne l'évolution du signal électrique et de l'émission du plasma en trois points de la décharge, souligne le comportement complexe du plasma pendant cette instabilité. D'expérience, nous pensons que la brusque chute du signal électrique a lieu durant à la contraction du void. On notera par ailleurs la présence d'un pic dans cette chute qui apparaît dans la plupart des cas. Cependant, les mouvements du *void* sont difficiles à corréler avec le signal électrique qui n'est pas résolu spatialement. L'utilisation de la spectroscopie d'émission optique résolue

spatialement (SR-OER) permet de résoudre en partie ce problème. Il apparaît ainsi que le signal SR-OER au centre de la décharge est en phase avec le signal électrique, tandis que ces deux signaux sont en opposition de phase si l'on considère le bord du plasma. De plus, le pic mis en évidence dans le signal électrique correspond bien à une variation du signal optique, et n'est donc pas un artefact. Il semble par ailleurs lié à un phénomène local dans le plasma. Une étude par caméra rapide à été réalisée pour élucider ce phénomène et les données sont actuellement en cours de traitement. Les résultats de SR-OER nous permettent par contre de formuler une hypothèse quant aux mouvements du *void* : ils semblent être dus à la propagation d'une onde d'ionisation au sein du plasma et du nuage. Des expériences complémentaires sont nécessaires pour confirmer cette hypothèse.

Lorsque l'on diminue suffisamment la puissance injectée, il est possible de stopper le *heartbeat*. Les signaux électrique et optiques révèlent que l'arrêt de l'instabilité est précédé par une période d'amortissement, qui consiste en l'apparition de pics avortés de plus en plus nombreux dans le signal (figure IV.23). Les transitions de n à (n+1) pics avortés se font sans signe précurseur. Le nombre de pics avortés observés peut dépasser la dizaine, et chacun de ces pics correspond à une contraction avortée du *void*. L'instabilité semble perdre de l'énergie pas à pas avant de cesser.

Instabilité liée à la croissance de poussières dans PKE (DPGI)

Les DPGI sont caractérisées par la succession de sept phases différentes dans les signaux électrique (figure IV.25) et optiques. Ces phases apparaissent très clairement lorsque que l'on réalise la FFT des signaux [83]. On peut ainsi mettre en évidence trois phases ordonnées (P1, P2 et P3), une phase chaotique (P4), une phase à haute fréquence (P5), une seconde phase chaotique (P6) et finalement une phase d'oscillations régulières (P7). Seules les trois premières phases ont été étudiées ici.

La phase P1 se présente sous forme de pics bien séparés sur le signal électrique et sous forme d'oscillations sur le signal optique, avec une fréquence typique autour de 40 Hz. La transition vers la phase P2 est caractérisée par l'apparition de deux petits pics entre les pics principaux sur le signal électrique et par une augmentation de l'amplitude d'oscillation sur les signaux optiques. La fréquence est légèrement inférieure à celle de la phase P1. Dans la phase P3, on observe un triplement de la fréquence des signaux électriques, tandis que le signal optique est modulé. De plus, on assiste à une évolution temporelle de la fréquence au cours de chaque phase. Les différences de comportement entre les signaux électrique et optiques sont certainement dues à un phénomène local dans le plasma qui se répercute différemment selon que le diagnostic est ou non résolu spatialement. Afin de valider cette hypothèse, une étude par caméra rapide a été réalisée et les données sont actuellement analysées.

Conclusion

Dans ce chapitre, nous avons démontré la présence d'une région de void au sein du nuage de poudres dans un plasma d'argon/silane confiné. Ce résultat est particulièrement intéressant car, jusqu'à présent, le void était bien connu dans les décharges non-confinées tant en pulvérisation qu'en gaz réactifs ou en injectant des poudres calibrées [50, 55, 56, 57, 60, 87, 88]. Cependant, sa présence, bien que supposée [13], n'avait jamais était démontrée dans un plasma généré dans une boîte à décharge. Ce résultat tend à prouver que le void est un phénomène intrinsèque aux plasmas poussiéreux.

Les trois instabilités présentées exhibent des schémas de développement complexes liés à la fois à la formation des poussières, au comportement du nuage et/ou à la région de void. Une étude bibliographique complète, présentée dans le tableau IV.5, montre que les phénomènes d'instabilités et de void se retrouvent dans de très nombreux plasmas poussiéreux, quels que soient la chimie, la géométrie, l'origine des poussières, le flux de gaz, l'excitation rf et les conditions de gravité. La comparaison de toutes ces données met en lumière le caractère intrinsèque des instabilités aux plasmas poussiéreux. Cependant, cette étude nécessiterait d'être étendue à d'autres types de décharges afin de vérifier l'influence du type d'excitation sur ces phénomènes.

Chapter V

Hydrocarbon-based dusty plasmas

Dust particles play an important role both in the interstellar medium or in planets' atmospheres such as Titan. As an example, interstellar dust (ISD) grains are known to influence the spectra of galaxies [92], while Titan's atmosphere is known to contain a large amount of aerosols [2]. Very few data from direct observations are available concerning those dust grains (radius, composition, optical properties...). Thus the composition of Titan's tholins or of ISD grains is still not precisely determined. That's why different laboratory experiments have been developed in order to produce analogues to Titan's tholins and/or ISD grains.

The experimental results presented in this chapter have been obtained on two of these laboratory experiments. First, experiments concerning Titan's tholins have been performed on the PAMPRE set-up, in the "Service d'Aéronomie" in France, thanks to a collaboration with Pr Cernogora and Dr Szopa. The results presented in the second part, concerning ISD grains, have been obtained on an experiment at the "Institut für Experimentalphysik II" in Germany during a scientific visit, thanks to the help of Pr Winter and Dr Hong.

V.1 Titan's tholins production: Plasma characterization on the PAMPRE experiment

First documents citing Saturn are attributed to Assyrian around 700 BC. They described the planet as a twinkling in the sky, and called it "Ninib star". In 1610, Galileo observed a strange phenomenon in his refracting telescope: the planet seems to stretch on its sides. The Dutchman Christian Huygens elucidated this enigma in 1659: it has to do with rings gravitating around the planet. He also discovered the presence of a natural satellite Titan. A few years later, Jean-Dominique Cassini observed four more moons smaller than Titan: Japet, Rhéa, Téthys and Dioné.

Titan is the largest moon of Saturn, with a radius of 2575 km (compared to 6400 km for Earth) and a mass of 1.34 10^{23} kg (corresponding to 2.2% of the Earth's mass). Its surface temperature is estimated to be 93.65 $\pm$ 0.25 K and its surface pressure to be 1.467 $\pm$ 1 hPa [93]. It is located 1.4 billion kilometers away from the Sun, and it collects a solar flux corresponding to 1.1% of the Earth's one.

Why such an interest for Titan? In fact, the actual composition of Titan's atmosphere seems to be quite similar to the one of the primitive Earth, that's to say the Earth's atmosphere before the first living beings start to produce oxygen. The presence of complex organic molecules, identical to those that could be the source of life on Earth, makes of Titan an interesting case of study for exobiologists. Presently Titan is the only known planetary body that has characteristics similar to the Earth's ones in terms of dense atmosphere, solid surface with liquid areas...

Launched on October 15$^{\text{th}}$ 1997, Cassini-Huygens is the first space mission devoted to Saturn exploration. It is conducted by the NASA, which realized the orbital module Cassini, and the European Space Agency (ESA) which provided the probe Huygens. The space craft and its passenger inserted in Saturn's orbit on July 1$^{\text{st}}$ 2004 after a seven-year and 3.5 billion-kilometer trip. Cassini will collect essential data on the structure and the environment of Saturn and its satellites during 4 years. The Huygens probe was released on December 25$^{\text{th}}$ 2004 and it reached Titan on January 14$^{\text{th}}$ 2005 after a descent of more than 2 hours in its atmosphere [94]. Figure V.1 gives the synopsis of the Cassini-Huygens mission.

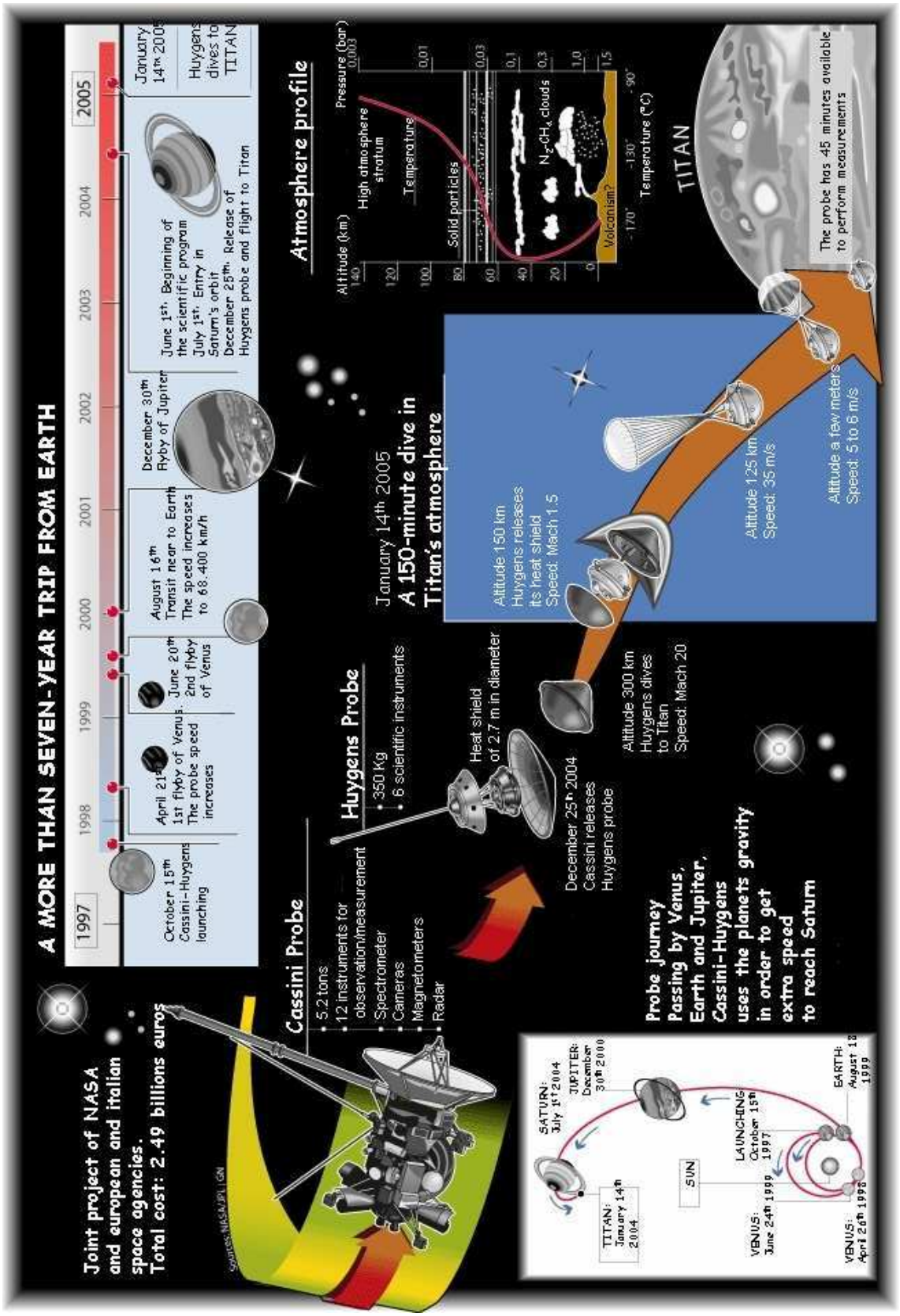

Figure V.1: Synopsis of the Cassini-Huygens mission.

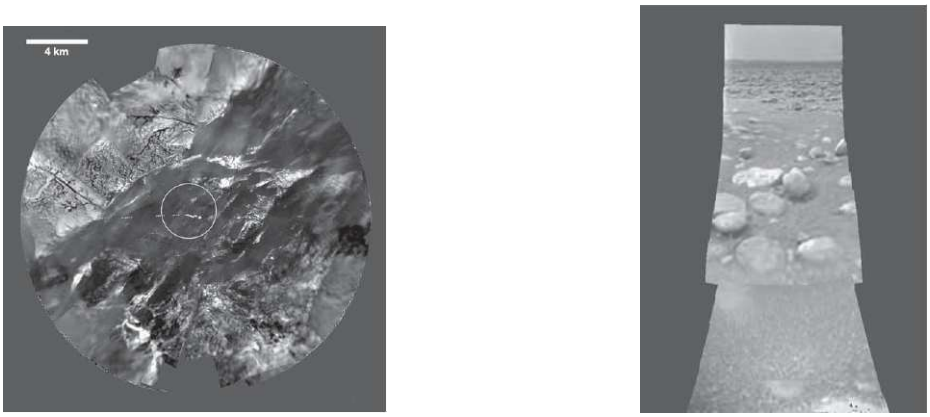

(a) View of Titan from 8 km.

(b) View from Titan's surface after the Huygens probe landing.

Figure V.2: Views from Titan [96].

The analysis of Titan's atmosphere from the Gas Chromatograph Mass Spectrometer (GCMS) revealed the presence of nitrogen (N_2) at 98% and methane (CH_4) at 1.8%. The only noble gas detected was argon (Ar). Some hydrogen (H_2) and hydrocarbon have also been detected. The GCMS did not detected any vaporized H_2O or O_2 [95].

When we observe Titan, the planet seems to be orange-brown, and the soil is not visible. This is due to the presence of aerosols in its atmosphere. Those aerosols are produced by the conversion of methane into higher hydrocarbons in Titan's stratosphere, and fall slowly on its surface. Images recorded during the Huygens probe descent revealed the moon geology as can be seen in figure V.2(a). The view of Titan's surface after the landing of the probe shows a sort of "sand" and some "stones" of 10-15 cm in size (fig. V.2(b)).

Organic aerosols play an important role in Titan's atmosphere properties and evolution. Presently, their formation and properties are little-known due to the fact that the only data are obtained by space probes or observation of Titan from Earth. That's why laboratory experiments are needed to simulate the chemistry of Titan's atmosphere, in order to improve our understanding concerning these aerosols [2].

V.1.a Why using a cc-rf low-pressure discharge to simulate Titan's atmosphere?

Titan's aerosols are produced by an organic chemistry due to solar UV irradiation and energetic particle bombardment of the atmosphere main compounds N_2 and CH_4. As photons are thought to be the main energy source in Titan's atmosphere [97], several laboratory experiments based on light sources have been developed. The main drawback of these experiments is that short UV photons (energy > 6.2 eV for wavelengths < 200 nm) are not transmitted through the silicate windows of the source, thus eliminating the energetic

photons responsible for N_2 photodissociation ($E_{dissociation} = 9.76\,eV$). Moreover, tholins production by this method is very time-consuming [2].

Different types of electrical discharges have also been used to simulate Titan's atmosphere. We can cite, for instance, spark discharges, rf inductively coupled plasma (rf-icp) discharges, direct current (dc) discharges or corona discharges. Some experiments based on laser or γ-ray irradiations have also been used. In all these experiments, aerosols are deposited as thin films on the reactor walls or on substrates while they are produced in the gas phase in Titan's atmosphere [2].

Cc-rf discharges are widely used in industries to grow silicon thin films. In silane-based plasmas, dust particles are known to grow from the dissociation of silane (cf chapter II) and to be trapped in the plasma. Those phenomena are widely studied for more than a decade now and start to be better understood. In particular, it has been shown that dust particle size ranges from a few nanometers to a few micrometers. This last point is of special interest: dust particles have globally the same size as Titan's aerosols. Thus using a cc-rf discharge allows to study dust particle formation and behavior in the gas phase. Nevertheless, it is important to note that the electrical charge on dust particles in the plasma must be much higher than the one of Titan's aerosols [98], possibly introducing biases in the mechanisms.

In weakly ionized plasmas, chemistry is induced by electron inelastic collisions with neutral gas. Thus, molecular dissociation of N_2 and CH_4 is due to electron impact. In their paper, Szopa *et al* [2] show that in some cases the electron energy distribution function of a plasma can be quite similar to the photon energy distribution function of a measured solar spectrum. Thus even if electron chemistry and photochemistry are different, some similarities can be brought to light in terms of energy range.

V.1.b The PAMPRE experiment

The PAMPRE experiment (French acronym for *Production d'Aérosols en Microgravité par Plasma REactif* - Aerosol Production by REactive Plasma under Microgravity) is devoted to the study of tholins produced in a N_2/CH_4 mixture. The experimental setup (see fig. V.3) is based on a cc-rf discharge, originally used for microelectronics processes (deposition). The reaction chamber is a stainless-steel cylinder of 30 cm diameter and 40 cm height. The powered electrode is of 10 cm diameter and the plasma is confined by a grounded metallic grid cage of the same diameter [2]. It is a parallel plate discharge quite similar to the one described in Chapter II.

V.1.c V_{dc} measurements

In order to monitor dust particle formation and growth in N_2-CH_4 plasmas, V_{dc} measurements have been performed on two different time scales. The shorter one aimed to observe the early stage of dust formation, while the longer one aimed to determine whether or not

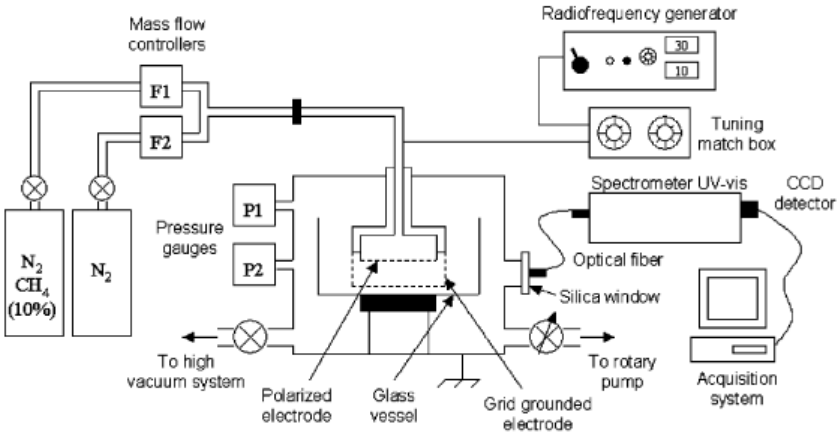

Figure V.3: PAMPRE experimental setup [2].

there were dust particle successive generations and/or a stationary state of the discharge.

A first series of measurements has been performed in typical dust forming conditions (Q_{N_2} = 44 sccm, Q_{N_2/CH_4} = 11 sccm, p = 0.86 mbar) for different injected powers. Figure V.4 shows the V_{dc} signal over 1000 s for 30 W and 21 W of injected power. In this figure, some damped oscillations are evidenced, with a period around 150 s. These oscillations are quite similar to the ones observed in silane-based plasmas during dust particle successive generations (see chapter IV). Nevertheless, no damping is observed in Ar/SiH_4 plasmas. Dust growth is much more difficult to initiate in methane-based plasmas as demonstrated by Hong and Winter [99]. The appearance of dust successive generations seems to be very dependent on the surface state and/or the cleanness of the chamber. Dust growth in carbon-based chemistries is known to need C_2H_2 radicals to be initiated. When previous depositions have been performed, those radicals can be produced by sputtering the deposited layer, hence helping to initiate dust particle formation and successive generations. The sputtering of this layer would also explain why successive generations are more easily observed in methane-based plasmas when Ar is used as a buffer gas instead of N_2. Indeed Ar^+ ions are more efficient to sputter than N_2^+ ions [100].

These measurements also evidenced a stationary regime of the discharge (at least on the electrical signal point of view) arising typically a few hundreds seconds after the plasma ignition. In the following, the evaluation of electron and ion densities have been performed during this stationary state of the discharge.

V.1.d Correlation between spectroscopy and V_{dc} measurements

Simultaneous measurements of V_{dc} and the emission of the nitrogen line at 337.1 nm have been performed at the ignition of the discharge over a few hundreds seconds (around 250 s).

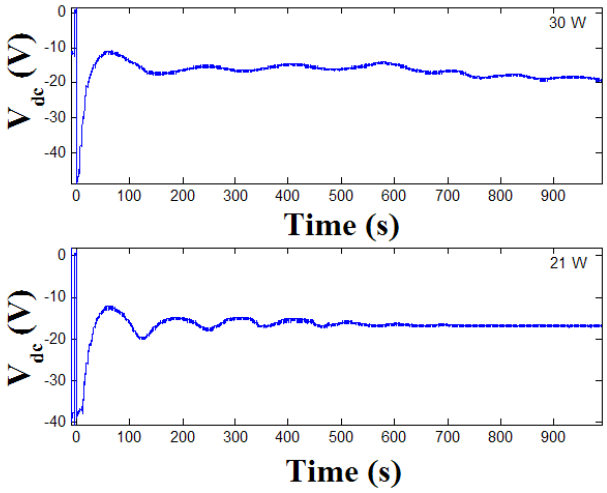

Figure V.4: Time evolution of V_{dc} on long time scales.

The nitrogen line at 337.1 nm is associated to the second positive system of N_2, depending on both the electron density and temperature. This time scale of 250 s typically corresponds to the formation of the first dust particle generation in our typical experimental conditions. As can be seen in figure V.5 both V_{dc} and I_{3371} respond to the dust particle formation in the plasma. V_{dc} exhibits a well-defined time evolution, revealing dust particle formation in the

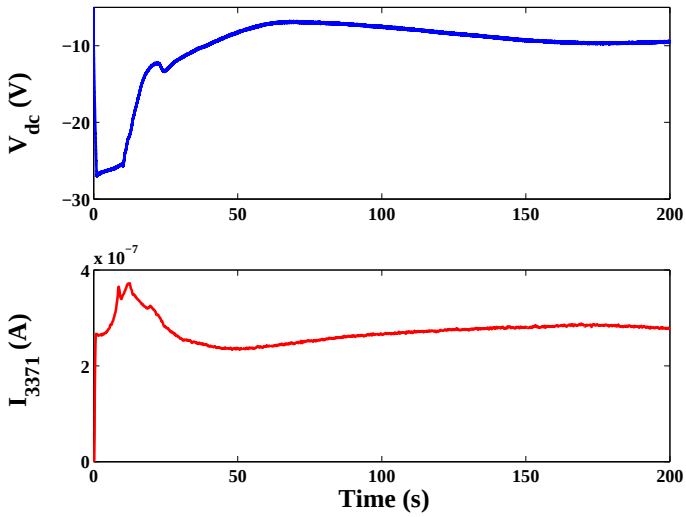

Figure V.5: Time evolution of V_{dc} and I_{3371} at the plasma ignition.

plasma. On the first part of the curve, we can identify a slightly decreasing part (between 0 and 10 s). It can be explained by the formation and accumulation of very small dust

particles (around 1-3 nanometers in diameter) that are not big enough to attach electrons, but modify the electron collision frequency. In a second part, a drastic decrease in the amplitude of V_{dc} indicates that dust particles become big enough (around 5-10 nanometers in diameter, from our experience in silane-based plasmas) to attach electrons and thus modify the value of the self-bias voltage. This fast decrease can be compared to the aggregation phenomenon, well-known in silane-based plasmas (see chapter III). Moreover, after around 100 s, V_{dc} tends to a stable value. After a transient regime corresponding to very first particle formation, in this case, the discharge tends to a stationary regime.

By looking at the time evolution of I_{3371}, we can notice that both V_{dc} and I_{3371} respond to the plasma modifications, but not in the same way. At the plasma ignition, V_{dc} increases while I_{3371} increases too. This behavior is due to the large amount of free electrons in the plasma. In a second time, V_{dc} exhibits a slightly decreasing plateau while I_{3371} reaches a maximum and then begins to decrease. Then V_{dc} decreases faster than I_{3371} for a while. After this, the line evolution seems to anticipate the behavior of V_{dc}. The differences we observe between these two diagnostics can be explained by two phenomena. First, V_{dc} reflects the evolution of both the electron density and temperature in the whole plasma volume, while I_{3371} is a spatially resolved diagnostics looking at the center of the plasma. Moreover, the different response times associated to these diagnostics are not the same : V_{dc} is associated to electrons while I_{3371} is associated to both N_2 molecules and electrons.

V.1.e Parametric study of the dust production in N_2-CH_4 plasmas

A parametric study of the evolution of V_{dc} has been performed. It has been studied for different dilutions of CH_4 in N_2 (0, 2, 6, 10%), different pressures (from 0.5 to 1.7 mbar), and different injected powers. As an example, figure V.6 shows the time evolution of V_{dc} for P_{rf} = 30 W and p = 1 mbar for several dilutions. Two main features can be identified. First, the more amount of methane in the discharge, the slower the dust particle formation. Indeed, a 2% dilution appears to be the best choice to form dust particles. The presence of an optimal dilution was expected. Indeed, in Ar/SiH_4 plasmas an optimal dilution has also been evidenced (see chapter III). For a 10% dilution, the curve is quite similar to the one of the 0% dilution (pure nitrogen), where no dust particles are formed. For the 10% case, it doesn't mean that no dust particles are formed, and indeed experiments showed that some are formed. We can only conclude that dust particles are neither big enough nor numerous enough to affect sufficiently the discharge and thus modify V_{dc}.

Figure V.7 shows the time evolution of V_{dc} for a dilution of 2% and P_{rf} = 30 W. The curves are shifted in the vertical axis in order to get a better overview of their evolution. The uppest curve corresponds to p = 1.70 mbar, and the lowest one to p = 0.52 mbar. As the pressure increases, we observe that the formation kinetics becomes faster. However, the most drastic decrease of V_{dc} are observed for p = 0.75 mbar and p = 0.86 mbar.

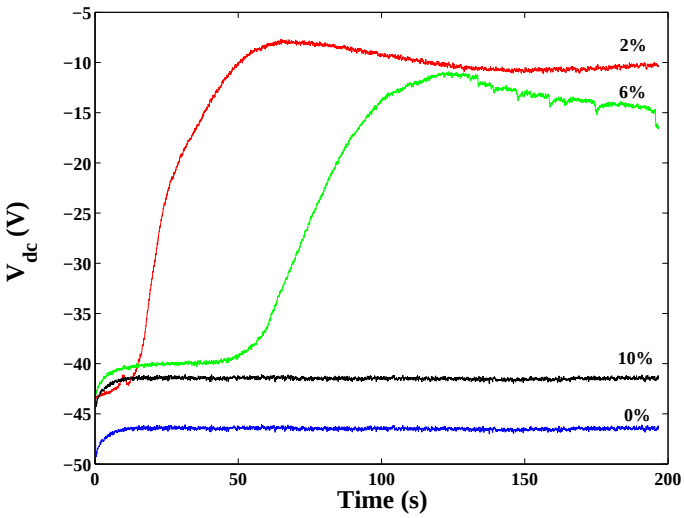

Figure V.6: Time evolution of V_{dc} for different dilutions.

These decreases are due to electron attachment on dust particles, and thus indicate that the amount of synthesized particles is more important in these cases than for the other explored pressures. This pressure range seems to favor dust particle synthesis in terms of amount of formed dust particles. This result has been confirmed by collecting the produced dust particles. Concerning the injected power, figure V.8 presents the time evolution of V_{dc} for a dilution of 2% and p = 0.86 mbar. When the injected power is increased, V_{dc} increases too: the uppest curve corresponds to P_{rf} = 13 W and the lowest one to P_{rf} = 32 W. This figure evidences an optimum in kinetics around 28 W (next to the last curve). For this injected power, we obtained the fastest kinetics of dust particle formation.

This parametric study allowed us to evidence which experimental conditions are favorable to dust particle production in our setup. The 2% dilution seems to be the most favorable to dust particle formation both in terms of kinetics and amount of synthesized particles. In the same way (by varying pressure and rf power), we showed that dust particles are better formed (in terms of quantity) for pressures around 1 mbar. These results are quite interesting because it shows that the conditions in Titan's atmosphere are really favorable to obtain tholins. Moreover, an injected power around 30 W leads to an optimal fast kinetics allowing to produce huge quantities of particles.

V.1.f Electron and ion density measurements

Some electron and ion density measurements have been performed in the PAMPRE experiment. The microwave resonant cavity method is used to determine n_e from the shift of the

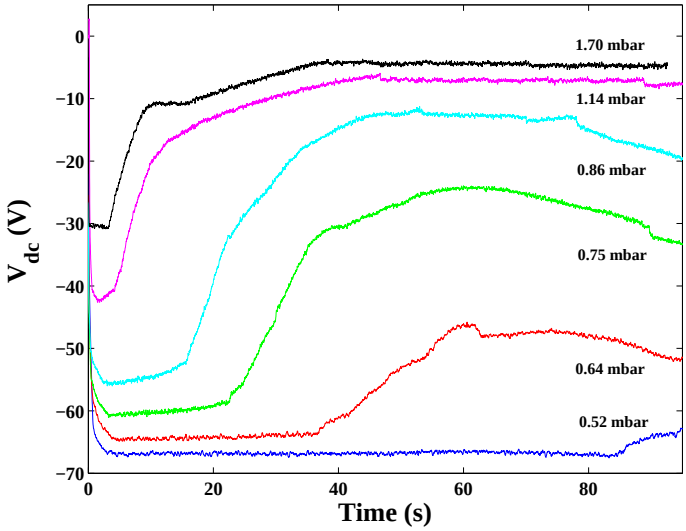

Figure V.7: Time evolution of V_{dc} for different pressures. The curves are shifted on the self-bias axis in order to have a better overview.

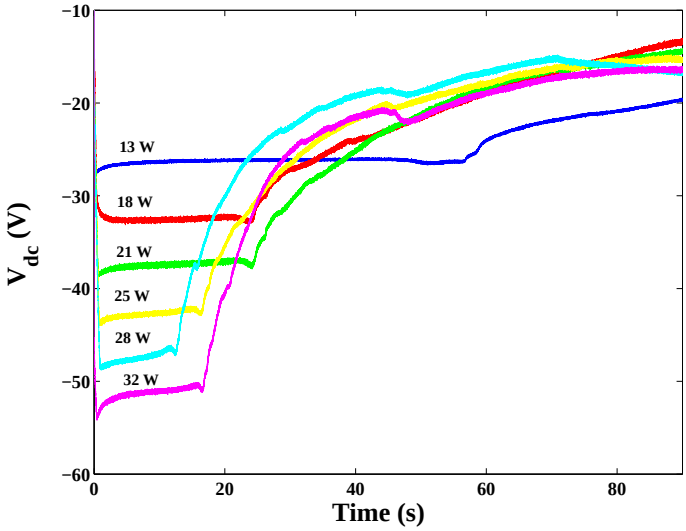

Figure V.8: Time evolution of V_{dc} for different rf powers.

resonance frequency. The plasma box is used as a resonant cavity and the TM 210 mode is used (because it is the strongest in our case). A plane Langmuir probe, located a few mm above the grounded electrode (just above its sheath), and in the ionic saturation regime, is used to evaluate the ion density (see equations II.2 and II.3). In order to perform those measurements, several assumptions are made. First, electron and positive ion densities are assumed to be equal. Second, we assume that the electron temperature is 2 eV (typical

value in a nitrogen plasma under our experimental conditions). This value needs to be validated by numerical plasma modeling in the case of a dust forming plasma. Moreover, all the results presented in the following part concern the stationary state of the discharge. Figure V.9 presents an overview of the obtained results. Empty symbols stand for cavity measurements, while full ones stand for probe measurements.

First measurements have been performed in pure nitrogen plasmas in order to validate

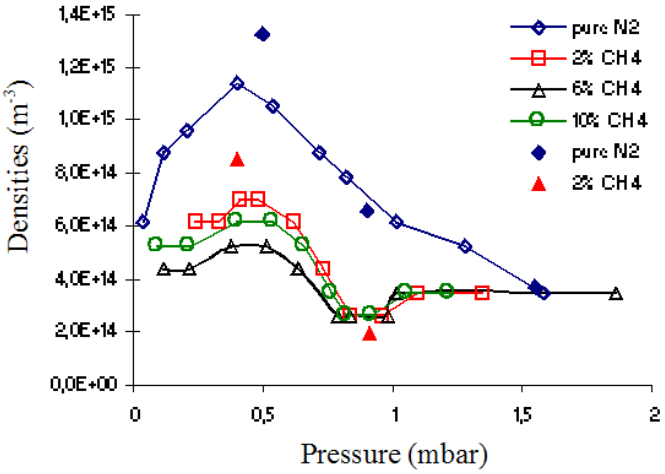

Figure V.9: Evolution the electron (empty symbols, microwave resonant cavity measurements) and ion (full symbols, Langmuir probe) densities as a function of pressure both in N_2 and N_2/CH_4 plasmas.

the method. The electron density, blue curve with empty diamonds in figure V.9, increases for pressures comprised between 0.1 and 0.4 mbar. A maximum is reached for this last value (0.4 mbar), then the electron density decreases as pressure increases. The second part of the curve, corresponding to the decay of the electron density, is confirmed by Langmuir probe measurements (blue full diamonds), assuming that electron and positive ion densities are equal. The discrepancies between the measured values can be explained by the uncertainty remaining on the electron temperature used to deduced the ion density (taken constant and equal to 2 eV). The part of the curve concerning pressures lower than 0.4 mbar, obtained using Langmuir probe, is not displayed here due to many uncertainties leading to unexploitable results. These uncertainties are principally about the electron temperature, the thickness of the electrode sheath and the accuracy of very low current measurements.

Then, measurements have been performed the same way for three different methane amounts in the discharge. Figure V.9 presents the results for 2% (red empty squares), 6% (black empty triangles) and 10% (green empty circles). The variation of the electron density as a function of the pressure is quite similar to the one observed in pure nitrogen. However,

the addition of methane in the plasma considerably lower the electron density (by about a factor 2). For all the dilutions, a maximum is observed around 0.4 mbar (as in pure nitrogen plasma) and a minimum is observed around 0.8 mbar (not observed in pure nitrogen). This minimum is not well-understood yet, but it corresponds to a peak of efficiency in tholins production. Nevertheless, it is important to note that the electron density measured here corresponds to the lower density that can be measured by the microwave resonant cavity method. Thus, the values given in the graph are only indicative values in the particular case of the minimum. Ion density measurements using a Langmuir probe are very fussy to perform in N_2/CH_4 plasmas due to the oganic material that deposits on the probe collecting surface. This deposition tends to make the probe insulating, leading to large measurement errors. Globally, in N_2/CH_4 plasmas, the probe remains conductive only for a few seconds before being covered by the organic deposition. Thus, very few measurements are available in mixtures: only two pressures have been investigated for a 2% mixture (red full triangles in figure V.9). These results are consistent with the ones obtained for the electron density. For these two points, no real difference can be found between the electron and ion densities. Electron attachment on tholins cannot be accurately measured using this method.

V.2 Rayleigh-Mie scattering ellipsometry in N_2/C_2H_2 plasmas

Hydrocarbon-based plasmas can be used to synthesize analogs of ISD grains. In this context, one of the most important point is the optical index of the dust grains.

V.2.a Ellipsometry

Ellipsometry is an optical characterization technique having applications in various fields (semi-conductors, thin layers...). This non-destructive method is very sensitive to the interface between two media with which the optical characteristics of a thin film can be measured.

Ellipsometry is based on the measurement of the polarization state of a light ray, which polarization has been modified by a reflection on a sample surface. The change of polarization between the incident wave and the reflected one allows to deduce information concerning the physical nature of the sample: thin film thickness and optical index. Data obtained from the measurement are expressed by two ellipsometric angles Ψ and Δ.

Figure V.10 gives an overview of the geometry of an ellipsometric measurement. The measured quantity is light intensity which gives the ratio of the parallel reflection coefficient (R_p) to the perpendicular reflection coefficient (R_s). The fundamental equation of ellipsometry is then given by:

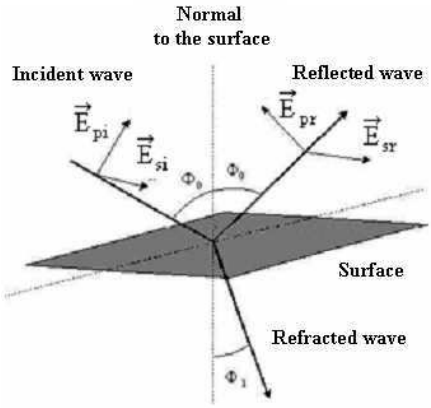

Figure V.10: Typical geometry of an ellipsometric measurement. The p-direction is parallel to the plane of incidence and the s-direction (from *Senkrecht* in German) is perpendicular to the p-direction.

$$\frac{R_p}{R_s} = tan\Psi e^{i\Delta} \tag{V.1}$$

TanΨ corresponds to the amplitude variation after the reflection on the sample under study, while Δ is the phase difference between p-polarized and s-polarized components.

Typically, an ellipsometer consists of a light source, a detector and a variety of optical components in between. The type of ellipsometer is determined by the arrangement of these optical components. Usually ellipsometers use at least two polarizers: the first one between the light source and the sample (called the polarizer) and the last one between the sample and the detector (called the analyzer). In some cases a retarder (called the compensator) is inserted between the sample and the analyzer.

V.2.a.i Rotating element ellipsometer

The rotating element method is based on the measurement of the reflected light intensity as a function of angle of the rotating element. The rotating element can be either the polarizer, the analyzer or the compensator. The most commonly used setup is the one with a rotating analyzer as presented in figure V.11. This type of ellipsometer is relatively easy to implement. Moreover, polarizers are achromatic in a wide spectral range and can have a nearly ideal behavior. Nevertheless, the alignment of the optical components and the light source is critical to get a sufficiently high precision during the measurements. Furthermore uncertainty increases as the Δ angle approaches to 0° and 180° due to the fact that the measured light at the detector is almost linearly polarized for those angles. Moreover, as the angle Δ is mapped between 0° and 180°, it is impossible to determine handedness of the light, i.e., if the light is right-handed or left-handed polarized. That is the reason why a

rotating compensator setup is used instead of a rotating analyzer setup. The angular speed of the rotating element is typically comprised between 10 and 60 Hz, which can significantly affect the time resolution of data acquisition.

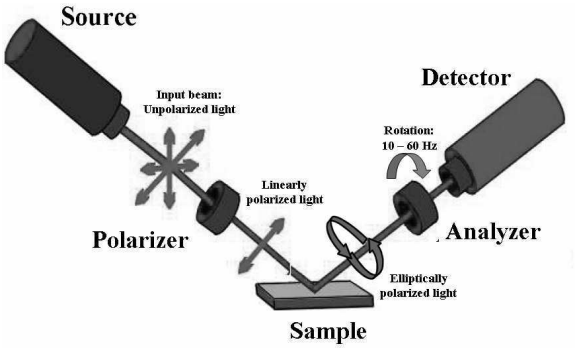

Figure V.11: Typical geometry of a rotating analyzer ellipsometer.

In the following, an analytical overview of a rotating element ellipsometer is given. For the sake of simplicity, we consider a rotating analyzer ellipsometer (RAE), with which the physical pictures and meanings can be easily understood. RAE is made of a light source, a polarizer, a rotating analyzer and a detector (photo-multiplier). The input beam is linearly polarized by the polarizer before reaching the sample. After the reflection, the reflected beam becomes elliptically polarized and reaches the detector through the rotating analyzer. The resulting signal is a linear combination of dc and sinusoidal signals, that can be written as:

$$V(t) = dc + a\,cos(2\omega t) + b\,sin(2\omega t) \tag{V.2}$$

In equation V.2, a and b are related to the normalized Fourier coefficients (α and β) of the signal measured by the detector:

$$\alpha = \frac{a}{dc} = \frac{tan^2\Psi\ -\ tan^2 P_e}{tan^2\Psi\ +\ tan^2 P_e} \tag{V.3}$$

$$\beta = \frac{b}{dc} = \frac{2tan\Psi\ cos\Delta\ tanP_e}{tan^2\Psi\ +\ tan^2 P_e} \tag{V.4}$$

with P_e the input polarizer azimuth with respect to the incidence plane ($P_e = 0$). The ellipsometric angles Ψ and Δ can be obtained by the inversion of equations V.3 and V.4:

$$tan\Psi = \sqrt{\frac{1+\alpha}{1-\alpha}}\ |\ tanP_e\ | \tag{V.5}$$

$$cos\Delta = \frac{\beta}{\sqrt{1-\alpha^2}}\frac{tanP_e}{|\ tanP_e\ |} \tag{V.6}$$

V.2.a.ii Jones matrix analysis of the RAE

The light intensity of the reflected beam, measured by the detector is proportional to the square of the electric field. In order to describe the polarization state of the beam along the entire path, the Jones matrix analysis is used to describe each optical component. In the case of the RAE, the electric field at the detector is represented as:

$$E_{detector} = (Analyzer)(Sample)(Polarizer)E_{incident} \tag{V.7}$$

Considering a p-polarized input light, the beam reaching the sample can be written as:

$$Beam\,on\,the\,sample = (Polarizer)E_{incident} = \begin{pmatrix} cosP_e & -sinP_e \\ sinP_e & cosP_e \end{pmatrix} \begin{pmatrix} 1 \\ 0 \end{pmatrix} \tag{V.8}$$

Assuming that the sample is homogeneous, isotropic and not too rough, its matrix is described as:

$$Sample = \begin{pmatrix} R_p & 0 \\ 0 & R_s \end{pmatrix} \tag{V.9}$$

The Jones matrix of the analyzer is written as:

$$Analyzer = \begin{pmatrix} 1 & 0 \\ 0 & 0 \end{pmatrix} \begin{pmatrix} cosA_e & sinA_e \\ -sinA_e & cosA_e \end{pmatrix} \tag{V.10}$$

with A_e the angle between the analyzer azimuth and the plane of incidence. Finally, the electric field at the detector is:

$$\begin{aligned} E_{detector} &= \begin{pmatrix} 1 & 0 \\ 0 & 0 \end{pmatrix} \begin{pmatrix} cosA_e & sinA_e \\ -sinA_e & cosA_e \end{pmatrix} \begin{pmatrix} R_p & 0 \\ 0 & R_s \end{pmatrix} \begin{pmatrix} cosP_e & -sinP_e \\ sinP_e & cosP_e \end{pmatrix} \begin{pmatrix} 1 \\ 0 \end{pmatrix} \\ &= \begin{pmatrix} R_p\, cosP_e\, cosA_e + R_s\, sinP_e\, sinA_e \\ 0 \end{pmatrix} \end{aligned} \tag{V.11}$$

The light intensity is

$$\begin{aligned} I_{detector} \propto\ & E_{detector}E^*_{detector} = \mid E_{detector} \mid^2 \\ =\ & \mid R_p \mid^2 cos^2P_e + \mid R_s \mid^2 sin^2P_e + \big(\mid R_p \mid^2 cos^2P_e - \mid R_s \mid^2 sin^2P_e \big) cos(2A_e) \\ & + 2Re(R_p.R^*_s) sinP_e cosP_e sin(2A_e) \end{aligned} \tag{V.12}$$

To compare the theoretical value from equation V.12 and the value measured by the detector (V.2), equation V.12 has to be normalized:

$$I_{detector} \propto 1 + \frac{|\frac{R_p}{R_s}|^2 - tan^2 P_e}{|\frac{R_p}{R_s}|^2 + tan^2 P_e} cos(2A_e) + \frac{2Re(\frac{R_p}{R_s}) tan P_e}{|\frac{R_p}{R_s}|^2 + tan^2 P_e} sin(2A_e) \quad \text{(V.13)}$$

Then, using equation V.1, V.3 and V.4, we obtain:

$$\begin{aligned} I_{detector} &\propto 1 + \frac{tan^2\Psi - tan^2 P_e}{tan^2\Psi + tan^2 P_e} cos(2A_e) + \frac{2 tan\Psi cos\Delta tan P_e}{tan^2\Psi + tan^2 P_e} sin(2A_e) \\ &\propto 1 + \alpha cos(2A_e) + \beta sin(2A_e) \end{aligned} \quad \text{(V.14)}$$

Finally, using equations V.5 and V.6, Ψ and Δ can be calculated from the voltage measured by the detector, and the sample properties can be deduced.

V.2.a.iii Rayleigh-Mie ellipsometry

Ellipsometry can be performed on levitating dust particles instead of a thin film on a sample. In such a case, a linearly polarized light is scattered by dust particles and the polarization state of the scattered light is measured. The Mie theory for light scattering by dust particles has been reviewed in section II. As in the previous section concerning a thin film on a sample, the polarization state of the light scattered by dust particles can also be described by the two ellipsometric angles Ψ and Δ.

In order to perform Rayleigh-Mie-ellipsometric measurements, a rotating compensator ellipsometer (RCE) was used. The RCE has one more retarder (the compensator), inserted between the sample and the analyzer. In the case of the RCE, the analyzer is fixed, and the rotating element is the compensator. Using the Müller matrix analysis for the RCE, the normalized light intensity at the detector is:

$$I_{detector} = A_0 + A_2 cos2C_e + B_2 sin2C_e + A_4 cos4C_e + B_4 sin4C_e \quad \text{(V.15)}$$

where C_e is the angle between the compensator azimuth and the plane of incidence.
The Fourier coefficients A_0, A_2, B_2, A_4 and B_4 (with fixed azimuth angles of polarizer (45°) and analyzer (0°)) are given by [101, 102, 103]:

$$A_0 = 1 - \frac{1}{2}(1 + y_c) cos2\Psi \quad \text{(V.16)}$$

$$A_2 = x_c(1 - cos2\Psi) \quad \text{(V.17)}$$

$$B_2 = x_c sin2\Psi cos\Delta + z_c sin2\Psi sin\Delta \quad \text{(V.18)}$$

$$A_4 = -\frac{1}{2}(1 - y_c) cos2\Psi \quad \text{(V.19)}$$

$$B_4 = \frac{1}{2}(1 - y_c) sin2\Psi cos\Delta \quad \text{(V.20)}$$

The non-ideal optical behavior of the rotating compensator is represented by the terms x_c, y_c and z_c:

$$\begin{cases} x_c \approx 0 \\ y_c \approx 0 \\ z_c \approx 1 \end{cases} \quad \text{(V.21)}$$

Using the terms of V.21, we obtain $A_2 \approx 0$. Moreover, the use of A_0 has to be avoided because it contains the dc component of the intensity including external light sources. Finally, the last Fourier coefficients can be written as:

$$\frac{B_2}{A_4} = -\frac{2x_c}{1-y_c} tan2\Psi cos\Delta - \frac{2z_c}{1-y_c} tan2\Psi sin\Delta \quad \text{(V.22)}$$

$$\frac{B_4}{A_4} = -tan2\psi cos\Delta \quad \text{(V.23)}$$

The ellipsometric angles are:

$$tan2\Psi sin\Delta = \frac{x_c}{z_c}\frac{B_4}{A_4} - \frac{1-y_c}{2z_c}\frac{B_2}{A_4} \equiv X_1 \quad \text{(V.24)}$$

$$tan2\Psi cos\Delta = -\frac{B_4}{A_4} \equiv X_2 \quad \text{(V.25)}$$

and can be written:

$$tan2\Psi = \sqrt{X_1^2 + X_2^2} \quad \text{(V.26)}$$

$$tan\Delta = \frac{X_1}{X_2} \quad \text{(V.27)}$$

In the case of Rayleigh-Mie-ellipsometry, the sample matrix (V.9) has to be replaced with a matrix that is a function of the Mie-scattering formulas. The Müller matrix for a single, spherical, homogeneous particle is:

$$\frac{1}{2k^2r^2}\begin{pmatrix} |S_1|^2 + |S_2|^2 & |S_2|^2 - |S_1|^2 & 0 & 0 \\ |S_2|^2 - |S_1|^2 & |S_1|^2 + |S_2|^2 & 0 & 0 \\ 0 & 0 & 2Re(S_1S_2^*) & -2Im(S_1S_2^*) \\ 0 & 0 & 2Im(S_1S_2^*) & 2Re(S_1S_2^*) \end{pmatrix} \quad \text{(V.28)}$$

V.2.a.iv Data fitting

The fitting method used in this thesis is based on the method suggested by Hong et al [104]. In order to find out the optical characteristics of the dust particles, the measured Ψ and Δ are compared with Ψ and Δ calculated by Mie-theory. Furthermore, the particle properties at small radii could be properly described by using the small particle approximation [105]. Nevertheless, a strategy for the fitting has been used since three parameters: complex refractive index $m = n - ik$ and radius, have to be determined from two angles. In order to determine n and k for nanoparticles uniquely, it is necessary to employ a time-dependent radius profile in order to reduce the ambiguity in radii [104].
This radius profile is based on the idea that the growth of the particles measured by SEM ex-situ shows a strong nonlinear behavior during the nucleation and coagulation phases, and that the growth becomes quasi-linear as a function of time for later phases [34, 106, 103].

Hong et al [104] have constructed a time dependent radius profile as a combination of a power function and linear functions as follows:

$$r(t) = \left[\frac{(R_1 - R_2)}{1 + (t/t_0)^p} + R_2\right] + \sum_i^N (F_{1,i} + F_{2,i} \cdot t) \tag{V.29}$$

where R_1 and R_2 are the lower and the upper limit (both in nm) of the nonlinear growth, t_0 is the time (in seconds) when the radius reaches the half of the sum of R_1 and R_2, i.e. $r(t_0) = (R_1 + R_2)/2$, p is a power factor, $F_{1,i}$ and $F_{2,i}$ are prefactors for linear functions with the block index i.

V.2.b Experimental setup

The chamber used for these experiments is a standard Gaseous Electronic Conference (GEC) cell. The electrodes are two parallel plates of 10.2 cm in diameter, separated by a gap of 3.1 cm. A 13.56 MHz rf generator is capacitively coupled, through a matching network, to one electrode. The other one is grounded. A more precise description can be found in [41, 106, 99] for example.

For dust particle formation, N_2-C_2H_2 gases are used with two different mixture ratios: 8:1 and 8:2 sccm, resulting in a pressure around 10^{-1} mbar. The injected power is varied from 10 W up to 60 W.

The following detailed experimental setup for Rayleigh-Mie ellipsometry measurements is given by Hong and Winter in [41]. An Ar ion laser at 488 nm is placed at a view port. A $\lambda/2$ plate right after the laser maximizes the polarized laser intensity passing through the entrance polarizer. The laser beam scattered by particles is measured under a well-defined angle, in our case under 90° relatively to the primary laser beam. The polarization state of the scattered light is defined by its modulation. The modulation of the signal is carried out via rotation of a $\lambda/4$ plate (rotating compensator). The signal is then passed through the analyzer and recorded by a photomultiplier (Hamamatsu R5929). Using the Fourier analysis, the polarization state of the scattered light is determined from the modulated light intensity. The angle of the rotating compensator and the light intensity at the photomultiplier are acquired by a personal computer. The accuracy of the polarization angle measurement (Ψ and Δ) was determined in a previous publication ($\pm 0.5°$) [107]. A simple sketch of the setup is given in figure V.12.

V.2.c Experimental results

In the following, preliminary experimental results of Mie-Rayleigh ellipsometric measurements in N_2/C_2H_2 plasmas are presented.

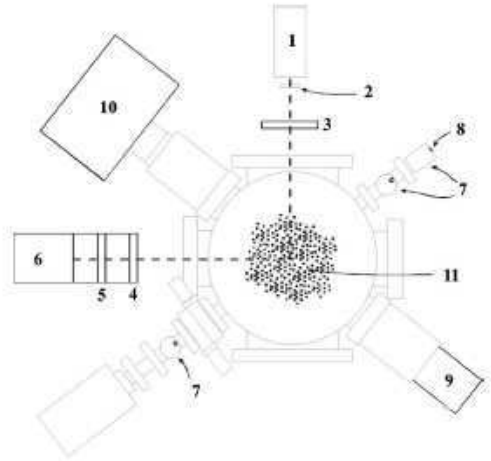

Figure V.12: A simple sketch of the experimental setup (top view). (1) Ar ion laser (488 nm), (2) $\lambda/2$ plate, (3) Rayleigh-Mie ellipsometry polarizer, (4) rotating compensator ($\lambda/4$ plate), (5) Rayleigh-Mie ellipsometry analyzer, (6) photomultiplier, (7) pressure gauge, (8) gas inlet, (9), (10) not concerned in this experiment, and (11) nanoparticles. [41]

V.2.c.i Typical spectrum of Rayleigh-Mie ellipsometry in N_2/C_2H_2 mixtures

Figure V.13 gives an example of a typical data acquisition (time evolution of Δ and Ψ) during a Rayleigh-Mie ellipsometric measurement. The time evolution of Δ and Ψ shows typical trends indicating the growth of nanoparticles. In this figure, dust particle formation and growth in N_2/C_2H_2 plasmas clearly appears as a periodic phenomenon. Three cycles of growth can be evidenced in figure V.13 both on Δ and Ψ evolution, with a typical period comprised between 3 and 4 minutes. This first result is in good agreement with the observation of successive dust generations that we performed in Ar/SiH_4 plasmas (see chapter IV) and the ones performed by Hong and Winter in [41].

At the early beginning of the data acquisition (encircled in figure V.13), the signal to noise ratio is very low and no conclusion can be given from these data. In fact, the results from simulation show that when there are no nanoparticles in the plasma, Ψ is around 45° and Δ varies from 0 to 360° as in figure V.13. If there is a small absorption (i.e. in the usual non-ideal case), results from simulation show that Ψ and Δ are also scattered around respectively 45° and 0 to 360°. So, in such a case, we can not distinguish signal from noise in the measurement, and interpretation is hazardous.

When the particles are detectable, and scatter the laser light, Ψ decreases spontaneously to a value close to zero (1-3° in our case), and delta becomes close to 360° (330-360° in our case). This is the point that we can consider as the starting point for particle growth. This point is located at around 100 s in figure V.13.

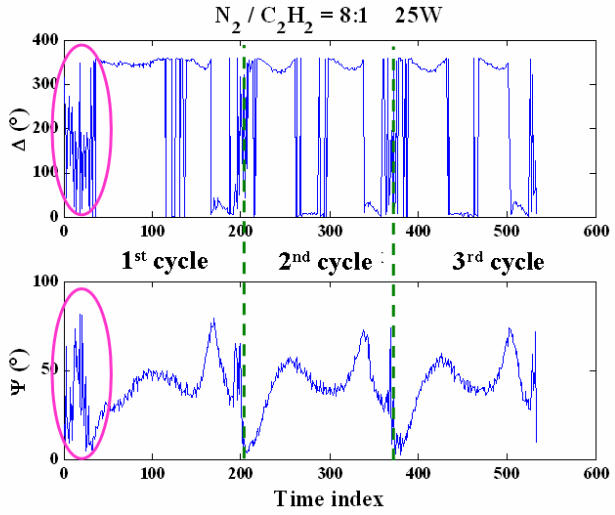

Figure V.13: Typical ellipsometric spectra: time evolution of Δ and Ψ.

Moreover, the time evolution of Δ and Ψ over one cycle exhibits several features (increases and decreases in the signal). By correlating the ellipsometric angle time evolution and the radius profile defined previously, we can get "real time" information concerning the dust particles. Thus, the optical index as a function of the radius can be extracted. The internal structure of dust particles can thereby be deduced from the fit of Δ and Ψ. Figure V.14 represents a diagram of the deduction process. The produced nanoparticles are expected to have a radius dependent onion-like structure (core + shell(s)), as it has been previously observed in Ar/C_2H_2 plasmas in [108, 41].

V.2.c.ii Study as a function of injected power and dilution

The measurements of the time evolution of the ellipsometric angles Ψ and Δ have been performed for two different mixture rates: N_2:C_2H_2 = 8:1 and N_2:C_2H_2 = 8:2. For both dilutions, the injected power was varied from 10 W up to 60 W. Figure V.15 gives an overview of the obtained data in both dilutions for a low injected power (10W) and a higher one (60W). In this figure, each spectrum exhibits 3 growth cycles. From these spectra we can see that the growth during first cycle is always different from the following ones. This result is consistent with the ones we obtained in Ar/SiH_4 plasmas.

As can be seen in figure V.15, the behavior of Δ and Ψ is quite different in the N_2/C_2H_2 = 8:1 mixture and in the N_2/C_2H_2 = 8:2 one. At low injected power (figures V.15(a)), in a 8:1 sccm mixture, Δ and Ψ exhibit several discrete transitions by growth cycle. This typical trend means that the growth of dust particles (plasma chemistry and thus kinetics) is modified during the cycle, i.e. not homogeneous. For a 8:2 mixture (figure V.15(c)), Δ

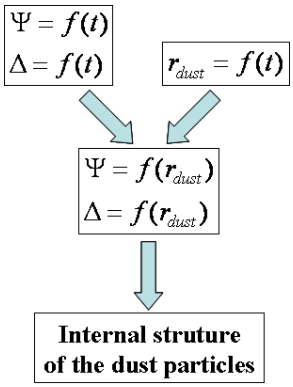

Figure V.14: Synthesis of the deductive reasoning allowing to deduce the internal structure of dust particles from their radius profile and the measurement of Δ and Ψ.

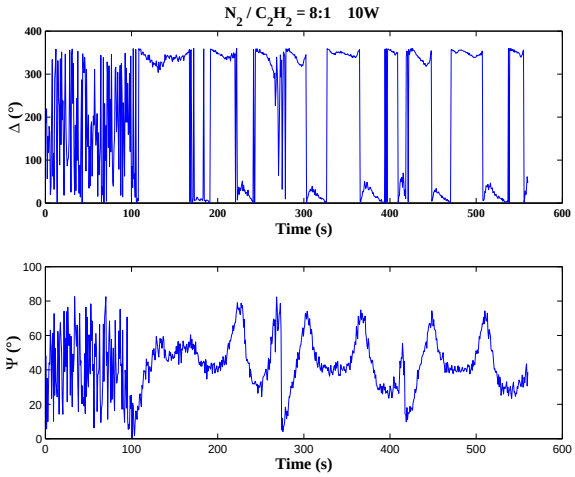

(a) N_2/C_2H_2 = 8:1 P_{rf} = 10 W

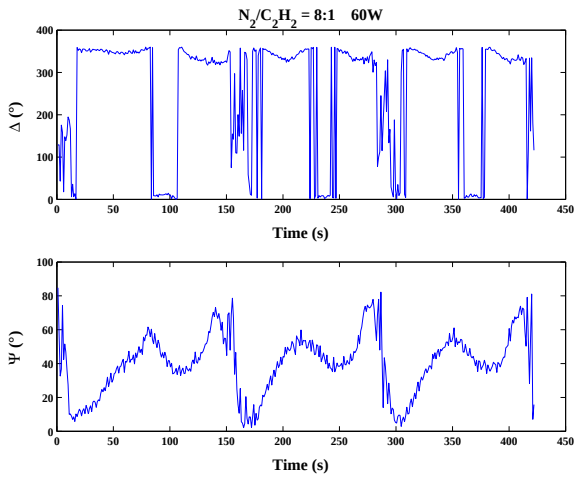

(b) N_2/C_2H_2 = 8:1 P_{rf} = 60 W

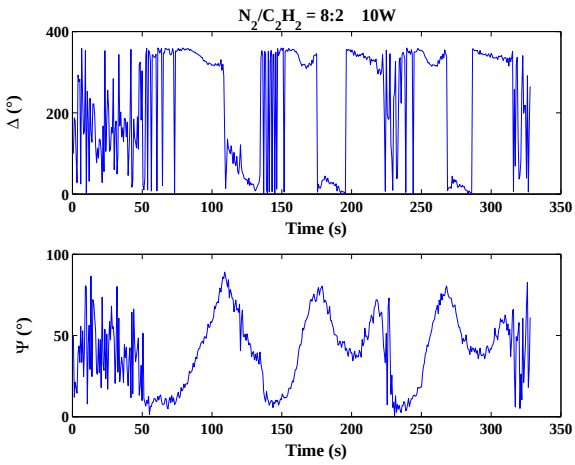

(c) N_2/C_2H_2 = 8:2 P_{rf} = 10 W

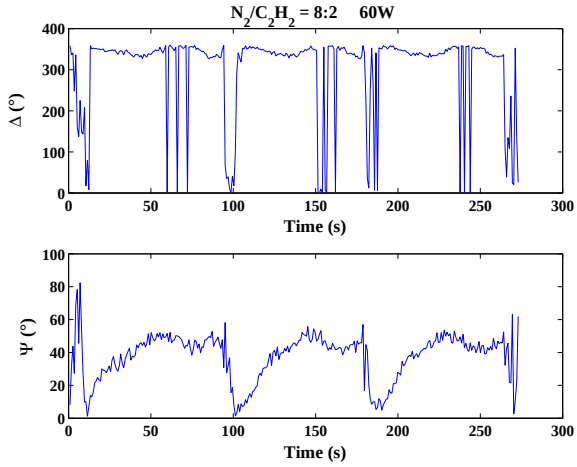

(d) N_2/C_2H_2 = 8:2 P_{rf} = 60 W

Figure V.15: Time evolution of Δ and Ψ for different parameters.

and Ψ exhibit less discrete transitions during the growth cycle. Thus, the particle growth appears to be more homogeneous for a higher amount of acetylene in the discharge.

By comparing in the same way figures V.15(b) and V.15(d), for higher injected powers, we can evidence that in a 8:1 mixture, Δ and Ψ exhibit more discrete transitions by growth cycle than in a 8:2 mixture. In this last case (figure V.15(d)), the particle growth appears to be a "relatively" homogeneous process.

The amount of C_2H_2 in the discharge seems to play an important role on the dust particle inner structure. When more acetylene is added, dust particle structure becomes more homogeneous, and the growth is more isotropic. Furthermore, for a given injected power, the growth kinetics is accelerated when the acetylene amount is increased. This result is relatively intuitive if we consider that in first approximation, the precursor number is proportional to the amount of acetylene in the discharge.

It is interesting to note that the effects of increasing the injected power for a given dilution are really similar to the effects of increasing the acetylene amount for a given injected power. Thus, in a 8:1 mixture (figures V.15(a) and V.15(b)), increasing the injected power from 10 W to 60 W tends to make the growth more homogeneous. The same observation can be made by comparing figures V.15(c) and V.15(d). Moreover, for low dilution rate (8:1), increasing the injected power increases the kinetics. Indeed, increasing the coupled energy leads to a larger quantity of precursors in the plasma. However, this observation is no more valid for a higher amount of acetylene in the discharge (8:2). In this particular case, increasing the injected power doesn't accelerate the kinetics anymore. This phenomenon could be linked to a kind of saturation in terms of precursor amount in the discharge.

V.2.d A fitting example

Figure V.16 (kindly made available by S.H. Hong) shows an example of fit. As explained in section V.2.a.iv, from the time evolution of Ψ and Δ, and a time dependent radius profile, it is possible to obtain the evolution of the two ellipsometric angles Ψ and Δ as a function of the dust particle radius. Then by fitting these data, the evolution of the optical index as a function of the radius can be deduced.
This figure evidences that the first growth cycle (green diamonds) differs from the following ones (blue squares and red dots) which are quite similar. The first growth cycle is well-fitted by the red curve, corresponding to an optical index m = 1.95 - 0.2i, while two different optical indexes (m = 1.95 - 0.2i in red, m = 1.87 - 0.12i in black) are needed to fit the following growth cycles. It is important to note that the fits of the data are fussy to perform due to the fact that Ψ and Δ must be fitted simultaneously. The retained optical index is the one that fits best both Ψ and Δ.

The fits of several data series have been performed in Bochum University in Germany. The first conclusions that can be drawn from those fits are that the smaller the particles, the higher the optical constants n and k. The dust particles exhibit a hard core (r $<$ 50

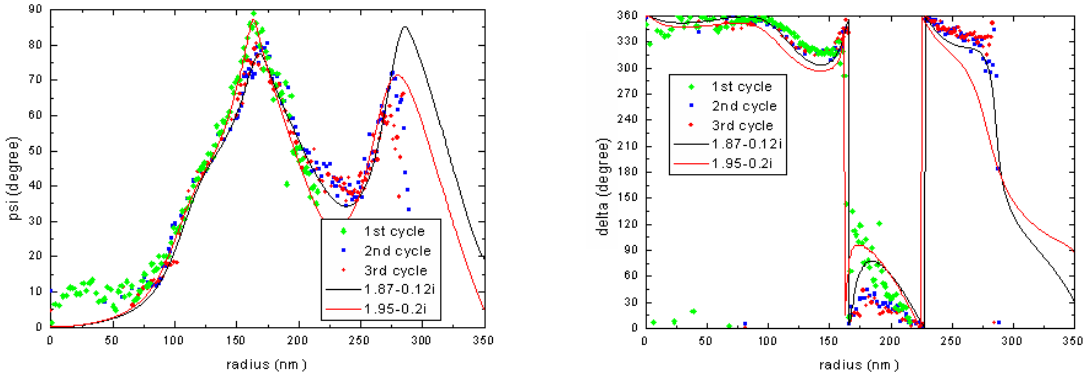

(a) Fit of Ψ (example)

(b) Fit of Δ (example)

Figure V.16: Fitting example of the ellipsometric angles.

nm) with a high refractive index (n = 1.90 to 2), especially in the first cycle, and a softer shell (n = 1.75) that can be compared to a polymer-like carbon film [109].

Data acquired during these series of experiments are currently fitted in Bochum. First results are very promising. They let forebode possible applications to the synthesis of size-controlled multifunctional dust grains.

V.3 Conclusion

In this chapter, we presented results on dust particle formation in methane-based and acetylene-based dusty plasmas. Those experimental results have been obtained on two laboratory experiments: PAMPRE in the "Service d'Aéronomie" in France and an ellipsometry set-up in the "Institut für Experimentalphysik II" in Germany. In both cases, the experiments are dedicated to the study and production of dust particles related to astrophysical concerns: Titan's tholins and InterStellar Dust (ISD) grains.

In the first part, the efficiency of a cc-rf discharge to synthesize analogues of Titan's tholins is demonstrated. It allows to produce dust particles in the plasma volume without any interactions with the walls. The self-bias voltage is shown to be a good tool to monitor dust particle formation in N_2/CH_4 plasmas. It showed that, as in silane-based plasmas, the formation of the first dust particle generation is quite different from the following ones. Moreover, successive generations don't appear to be a systematic feature in N_2/CH_4 plasmas, and seem to be very dependent on the previous surface state of the plasma box. In all cases, the discharge tends to a stationary state after a while (at least on the electrical point of view). The parametric study underlines that the amount of methane (2%) in Titan's atmosphere (mostly composed of nitrogen) is very favorable to aerosol synthesis.. The

most favorable pressure (around 1 mbar) and injected rf power (around 30 W) have also been deduced from this study in our set-up. OES measurements have also been performed. Unfortunatly, they can't be directly correlated to V_{dc} measurements. Maybe the pooling reaction, involved in the line emission, can't be neglected in our case. More investigations are underway in the "Service d'Aéronomie". Electron and ion density evaluations have been realized in pure nitrogen plasmas using the microwave resonant cavity method and a Langmuir probe in the ionic saturation regime. Those results showed a good adequation thus validating the method. Electron density was measured for several dilutions and pressures. The ion density measurements were very fussy to performed and very few data are available in N_2/CH_4 mixtures. However, we can note that the addition of methane in the discharge lowers the electron density and that a minimum value is reached in all dilutions for the most favorable pressure for dust formation. This last result is not explained yet. Finally, we showed that the electron attachment on tholins couldn't be easily deduced from our electron and ion density measurements.

In the second part, we performed a parametric study of dust particle formation in N_2/C_2H_2 plasmas, using a rotating analyzer ellipsometer. This technique allows to obtain the time evolution of the two ellipsometric angles Ψ and Δ. Then, using a pre-defined model of dust particle growth $r_d = f(t)$, Ψ and Δ can be expressed as a function of the dust particle radius. Then, by fitting Ψ and Δ, we can get information concerning the internal structure of the synthesized dust particles. The first information we obtained from the ellipsometric spectra is that, as in silane-based and methane-based plasmas, the formation of the first dust particle generation is quite different from the following ones. In the case of acetylene-based plasmas, successive generations of dust particles are a systematic phenomenon as long as acetylene is provided (as in silane plasmas). This last point can be explained by the fact that C_2H_2 radicals are much easy to obtain from acetylene than from methane. Thanks to the fit of the ellipsometric spectra, we could deduce that the synthesized dust grains have a radius dependent onion-like structure: core + shell(s), as expected from [108, 41]. A study as a function of the amount of acetylene in the discharge and the rf injected power showed that the dust structure is very dependent on both of these parameters. Thus, even without fitting all the data (this work is underway in Bochum in Germany), we can surmise that the optical index of the different parts of the grains also depends on both of these parameters.

Finally, thanks to these two studies, we pointed out that the growth of the first dust particle generation is always different from the following ones in various chemistries: silane-based, methane-based and acetylene-based plasmas. We also showed that the successive generations of dust grains is not a systematic feature in dusty plasmas produced using reactive gases. Some of them, producing more efficiently the first radicals (as silane and acetylene) are more favorable to dust successive generations, while some others (as methane) are less favorable due to the difficulty to obtain radicals. Moreover, the self-bias voltage

based diagnostic has been shown to be an efficient tool to monitor dust particle formation and growth in various dusty plasma chemistries as silane-based and methane-based ones.

V.4 French summary / Résumé en français

Les poussières jouent un rôle important à la fois dans le milieu interstellaire et dans les atmosphères de planètes telles que Titan. Ainsi, les poussières interstellaires (InterStellar Dust grain, ISD grains) sont connues pour influencer les spectres des galaxies [92], tandis que l'atmosphère de Titan est réputée contenir de grandes quantités d'aérosols [2]. Très peu de données sont disponibles concernant ces poussières (taille, composition, propriétés optiques...). Ainsi, la composition des tholins de Titan ou celle des poussières interstellaires n'est toujours pas déterminée précisément. C'est pourquoi différentes expériences de laboratoire ont été développées pour produire des poussières analogues aux tholins de Titan et/ou aux poussières interstellaires.

Les résultats présentés dans ce chapitre ont été obtenus sur deux de ces expériences de laboratoire. Tout d'abord, les expériences concernant les tholins ont été menées sur le dispositif PAMPRE, au Service d'Aéronomie en France, dans le cadre d'une collaboration avec Pr. Cernogora et Dr. Szopa. Les résultats présentés dans la seconde partie, portant sur les poussières interstellaires, ont été obtenus sur un dispositif expérimental de l'"Institut für Experimentalphysik II" en Allemagne lors d'un séjour de recherche, avec l'aide de Pr. Winter et Dr. Hong.

Production d'analogues de tholins de Titan : caractérisation plasma sur PAMPRE

Les premiers documents citant Saturne sont attribués aux Assyriens vers 700 avant JC. Ils y décrivent la planète comme un scintillement dans le ciel et l'appellent l'étoile de Ninib. En 1610, Galilée observe un étrange phénomène grâce à son télescope : la planète semble avoir une forme étirée. En 1659, Christian Huygens élucide cette énigme : cet étirement est est en fait un ensemble d'anneaux gravitant autour de Saturne. Il découvre aussi la présence d'un satellite naturel, Titan. Quelques années plus tard, Jean-Dominique Cassini observe quatre lunes supplémentaires, plus petites que Titan : Japet, Rhéa, Téthys et Dioné.

Titan est la plus grande lune de Saturne, avec un rayon de 2575 km et une masse de $1.34\ 10^{23}$ kg. Sa température en surface est estimée à 93.65 ± 0.25 K et sa pression à 1.467 ± 1 hPa [93]. Titan est situé à 1.4 milliards de kilomètres du Soleil, et reçoit un flux solaire correspondant à 1.1 % de celui de la Terre.

Pourquoi un tel intérêt pour Titan? En fait, la composition actuelle de l'atmosphère de Titan semble être relativement semblable à celle de la Terre primitive, c'est à dire celle de la Terre avant que les premiers êtres vivants ne commencent à produire de l'oxygène. La présence de molécules organiques complexes, identiques à celles qui pourraient être à

l'origine de la vie sur Terre, font de Titan un excellent objet d'étude pour les exobiologistes. A l'heure actuelle, Titan est la seule planète que l'on connaisse qui ait des caractéristiques similaires à celles de la Terre en termes d'atmosphère dense et de surface solide avec de grandes étendues liquides.

Lancée le 15 octobre 1995, la mission Cassini-Huygens est la première mission spatiale consacrée à l'exploration de Saturne. Elle est conduite par la NASA, qui a réalisé le module orbital Cassini, et l'ESA, qui a fourni la sonde Huygens. L'engin spatial s'est inséré dans l'orbite de Saturne le 1er juillet 2004. Cassini collectera des données sur la structure et l'environnement de Saturne et de ses satellites pendant quatre ans. La sonde Huygens a été libérée le 25 décembre 2004 et a atteint Titan le 14 janvier 2005 après une descente de plus de deux heures dans son atmosphère [94]. La figure V.1 donne le synopsis de la mission Cassini-Huygens.

L'analyse de l'atmosphère de Titan a révélé la présence d'azote à 98 % et de méthane à 1.8 %. Le seul gaz rare détecté est l'argon. De l'hydrogène et des hydrocarbures ont aussi été détectés, ce qui n'est pas le cas pour l'eau ou l'oxygène [95]. Lorsque l'on observe Titan, la planète semble brun-orangé et le sol n'est pas visible. Ce phénomène est dû à la présence d'aérosols dans son atmosphère. Ces aérosols, produits par la conversion du méthane dans la stratosphère de Titan, tombent lentement à sa surface. Les images acquises pendant la descente de la sonde Huygens ont révélé la morphologie de la lune comme le montre la figure V.2(a). Les images de Titan après l'atterrissage montrent comme du "sable" et des "pierres" (voir figure V.2(b)).

PAMPRE : Production d'Aérosols en Microgravité par Plasma REactif

L'expérience PAMPRE est consacrée à l'étude des tholins produits dans un mélange N_2/CH_4. Le dispositif expérimental (figure V.3) est basé sur une décharge cc-rf, utilisée à l'origine pour le dépôt de couches minces. Ce dispositif est très similaire à celui décrit dans le chapitre II (expérience Silane). Afin de suivre la formation et la croissance de poudres dans les plasmas de N_2/CH_4, des mesures de V_{dc} ont été réalisées sur deux échelles de temps différentes.

La première série de mesures a été faite dans des conditions typiques de formation de poudres, pour différentes puissances injectées. Ces mesures nous ont permis de mettre en évidence des oscillations dans le signal avec une période d'environ 150 s (figure V.4). Ces oscillations semblent très similaires à celles observées en Ar/SiH_4 lors des générations successives de poudres. Cependant, ces oscillations tendent à s'amortir pour aboutir à un régime stationnaire en N_2/CH_4 alors que ce n'est pas le cas en Ar/SiH_4. Par la suite, les mesures de densités électronique et ionique présentées ont été réalisées dans ce régime stationnaire.

Des mesures simultanées de V_{dc} et de l'intensité de la raie à 337.1 nm de l'azote ont été faites à l'allumage de la décharge, pendant quelques centaines de secondes. L'intensité de

cette raie de l'azote dépend à la fois de la densité et de la température électronique dans le plasma. V_{dc} et I_{3371} répondent tous les deux à la formation de poudres dans la décharge comme on peut le voir sur la figure V.5, mais de façon différente. Cela peut s'expliquer de deux façons. Tout d'abord, V_{dc} reflète l'évolution de la température et de la densité électronique dans tout le volume du plasma tandis que I_{3371} est basée sur une mesure résolue spatialement, au centre du plasma. De plus, les temps de réponse associés aux deux diagnostics diffèrent: V_{dc} est affectée par les électrons alors que I_{3371} est affectée à la fois par les électrons et les molécules de N_2.

Nous avons ensuite mené une étude paramétrique sur l'efficacité de la production de poudres dans les plasmas N_2/CH_4. La puissance injectée, la pression et la dilution du mélange ont été testées. Cette étude a permis de montrer que la formation de poudres semblait être favorisée par des pressions supérieures au mbar en terme de cinétique, et par des pressions autour du mbar en terme de quantité d'aérosols formés. Un optimum dans la cinétique de formation a été mis en évidence autour de 28 W de puissance injectée. De plus, nous avons constaté que les conditions de dilution correspondant à celles de l'atmosphère de Titan (N_2/CH_4 = 98:2) étaient les plus favorables à la formation d'aérosols dans notre cas.

Des mesures de densités électronique (par cavité résonante micro-onde) et ionique (par sonde de Langmuir) ont été réalisées sur PAMPRE. Pour pouvoir interpréter ces mesures, plusieurs hypothèses ont été faites. Tout d'abord, les densités électronique et d'ions positifs sont supposées égales. Ensuite, la température électronique est estimée à 2 eV (une valeur typique dans ce type de plasma). De plus, tous les résultats suivants concernent le régime stationnaire de la décharge. La figure V.9 présente un aperçu des résultats obtenus. Les mesures faites dans les plasmas d'azote pur ont permis de valider la méthode. En effet, les valeurs de densités électronique et ionique dans ce cas sont très proches, et les écarts s'expliquent du fait de l'incertitude sur la température électronique, impliquée dans le calcul de la densité ionique. Concernant les basses pressions, nous ne présentons aucun résultat pour des pressions inférieures à 0.4 mbar, du fait de trop nombreuses incertitudes (température électronique, épaisseur de gaine, précision de la mesure pour de faibles courants) rendant les résultats inexploitables. Les mêmes mesures ont ensuite été faites pour différentes quantités de méthane dans le plasma (figure V.9). Les variations de la densité électronique en fonction de la pression sont assez semblables à celles observées en azote pur. Cependant, l'ajout de méthane dans le décharge diminue considérablement la densité électronique (d'un facteur 2 environ). Pour toutes les dilutions, un maximum est observé autour de 0.4 mbar et un minimum autour de 0.8 mbar. Ce minimum n'est pas expliqué pour l'instant, même si il semble correspondre à un pic d'efficacité dans la production de tholins. Peu de mesures de densité ionique ont été réalisées. En effet, le dépôt organique dans les plasmas N_2/CH_4 tend à rendre la sonde isolante, et génère ainsi de grandes erreurs de mesure. Le peu de résultats obtenus est consistant avec les valeurs de densité électronique. Cependant,

il est impossible de déduire l'attachement électronique sur les tholins à partir de ces mesures.

Ellipsométrie de Mie-Rayleigh dans des plasmas N_2/C_2H_2

L'ellipsométrie est une méthode optique de caractérisation, non-destructrice, très sensible pour analyser les interfaces entre deux milieux. Cette méthode est basée sur la mesure de l'état de polarisation d'un rayon lumineux, qui a été modifié par une réflexion sur la surface d'un échantillon. Le changement de polarisation entre l'onde incidente et l'onde réfléchie permet d'accéder à différentes informations concernant la nature physique de l'échantillon : épaisseur et indice optique. Les données obtenues par la mesure sont appelées les angles ellipsométriques, notés Ψ et Δ. La figure V.10 donne un aperçu de la géométrie d'une mesure ellipsométrique. La quantité mesurée est une intensité lumineuse qui donne ρ correspondant au rapport entre le coefficient de réflexion parallèle et le coefficient de réflexion perpendiculaire. L'équation V.1 donne la relation fondamentale de l'ellipsométrie. TanΨ correspond à la variation d'amplitude après la réflexion sur l'échantillon, tandis que Δ est la différence de phase due à cette même réflexion. Schématiquement, un ellipsomètre est constitué d'une source de lumière, d'un détecteur et d'un certain nombre de composants optiques entre les deux (généralement au moins deux polariseurs, voire trois).

L'ellipsomètre à élément rotatif (le polariseur, l'analyseur ou la compensatrice) est basé sur la mesure de l'intensité réfléchie pour différents angles de l'élément rotatif. Le dispositif le plus utilisé (figure V.11) est celui avec un analyseur rotatif. Ce type d'ellipsomètre est relativement facile à mettre en oeuvre. Cependant, l'alignement des composants optiques et de la source lumineuse est critique afin d'obtenir une précision suffisante sur la mesure. De plus, une incertitude persiste toujours pour les valeurs de l'angle Δ autour de 0 et 180° car la lumière est quasiment polarisée linéairement pour ces angles. Comme la mesure de Δ se fait entre 0 et 180°, il est impossible de déterminer le sens de polarisation de la lumière. C'est pourquoi on insère parfois une compensatrice (qui devient l'élément rotatif) entre l'échantillon et l'analyseur. La vitesse de rotation de l'élément rotatif peut aussi être un facteur limitant pour la résolution temporelle des données acquises. La section V.2.a.i donne un aperçu de l'analyse d'un ellipsomètre à élément rotatif par l'optique matricielle. Dans un souci de simplicité, nous considérons un ellipsomètre à analyseur rotatif, qui s'avère le plus simple à décrire.

Les mesures ellipsométriques peuvent être réalisées sur des poudres en lévitation dans un plasma au lieu d'un substrat. De la même façon que précédemment, l'état de polarisation de la lumière réfléchie par les poussières peut être décrit par les deux angles ellipsométriques Ψ et Δ. Afin de réaliser les mesures d'ellipsométrie de Mie-Rayleigh, nous avons utilisé un ellipsomètre à compensatrice rotative. L'analyse matricielle de cet ellipsomètre est développée dans la section V.2.a.iii. L'ajustement des données est basé sur une méthode suggérée par Hong et al [104]. Pour déterminer l'indice optique des nanoparticules, un profil de

rayon dépendant du temps est utilisé. Ce profil est basé sur l'idée que la croissance des poudres, mesurée par MEB ex-situ, montre un comportement fortement non-linéaire pendant les phases de nucléation et de coagulation, puis devient quasi-linéaire par la suite [34, 106, 103]. Hong et al ont ainsi construit un profil de rayon dépendant du temps à l'aide de la combinaison d'une fonction puissance et d'une fonction linéaire (équation V.29).

Mesures ellipsométriques

Le réacteur utilisé pour réaliser les expériences est une cellule GEC standard. Elle est constituée de deux électrodes parallèles de diamètre 10.2 cm, séparées par 3.1 cm. Un générateur rf (13.56 MHz) est couplé capacitivement à une des électrodes au travers d'une boîte d'accord. La seconde électrode est à la masse [41, 106, 99]. La synthèse de poussières est réalisée dans un mélange N_2/C_2H_2 (8:1 et 8:2 sccm) à une pression d'environ 10^{-1} mbar. La puissance injectée varie entre 10 et 60 W. Le dispositif expérimental utilisé pour les mesures est présenté figure V.12 et détaillé section V.2.b.

La figure V.13 donne un exemple typique de l'acquisition de données lors d'une mesure d'ellipsométrie de Mie-Rayleigh. Sur cette figure, la croissance des poussières apparaît clairement comme un phénomène périodique, et trois cycles sont mis en évidence avec une période de l'ordre de 3 à 4 minutes. Ce premier résultat est parfaitement cohérent avec l'observation des générations successives de poudres que nous avons faite dans les plasmas Ar/SiH_4 (chapitre IV) et celle faite par Hong et Winter [41]. De plus, l'évolution temporelle de ψ et Δ présente différentes variations au cours d'un cycle de croissance. En corrélant ces évolutions au profil de rayon dépendant du temps défini précédemment, il est possible d'obtenir la variation des angles ellipsométriques en fonction du rayon des poussières. Ainsi, la structure interne des poussières peut être déduite grâce à l'ajustement de ces données. Le schéma V.14 montre un diagramme du processus de déduction.

Une étude paramétrique a été menée en faisant varier la dilution du mélange N_2/C_2H_2 (8:1 et 8:2 sccm) et la puissance injectée (de 10 à 60 W). Les résultats montrent qu'à basse puissance injectée, l'augmentation de la quantité d'acétylène dans le mélange tend à rendre la croissance des poussières plus homogène. De la même façon, l'augmentation de la puissance injectée à dilution constante, tend aussi à rendre la croissance plus homogène. Un exemple d'ajustement des données (aimablement mis à disposition par S.H. Hong) est présenté figure V.16. Cette figure met en évidence le fait que la formation de la première génération de poussières diffère toujours des suivantes, qui sont elles relativement similaires. Ainsi la courbe de la première génération peut être ajustée grâce à la courbe rouge (correspondant à un indice optique m = 1.95 - 0.2i), tandis que deux indices optiques (m = 1.95 - 0.2i en rouge et m = 1.87 - 0.12i en noir) sont nécessaires pour ajuster les cycles de croissance suivants. Il est important de noter que les ajustements de Ψ et Δ doivent être faits simultanément, et que l'indice optique retenu est celui qui permet d'ajuster au mieux

les deux angles. La première conclusion qui peut être tirée de cet ajustement est que plus les poussières sont petites, plus leur indice optique est élevé. Ainsi, les poussières présentent un noyau dur ($r < 50$ nm) avec un indice de réfraction élevé ($n = 1.90$ à 2) et une enveloppe plus tendre ($n = 1.75$) qui peut être comparée à une couche PLC (Polymer-Like Carbon) [109]. Les poussières présentent ainsi une structure concentrique relativement similaire à celle observée dans [108, 41].

Les données acquises lors de ces campagnes de mesures sont actuellement en cours de traitement à l'Université de Bochum. Les résultats sont cependant très prometteurs et laissent présager de possibles applications dans le domaine de la production de poudres multifonctionnelles de taille contrôlée.

Chapter VI

Tailoring of silicon nanocrystals at low gas temperatures

Nanocrystals of semiconductor materials (silicon, germanium ...), also named quantum dots, have potential applications in a variety of photonic devices. The size-tunable optical and electrical properties of silicon nanoparticles make silicon nanocrystals interesting candidates for a wide spectrum of applications [3]. As an example, photo- or electroluminescence of Si nanocrystals is tunable through the controlled variation of the nanocluster size [110].

Presently, an easy-to-implement way of controlling silicon nanocrystal size is needed. A way to modify their size can be by modifying the gas temperature in the dust forming plasma. Indeed, high gas temperatures have been shown to have a significant effect on the dust formation kinetics, inducing a delay in their growth [35, 13]. Moreover, increasing the gas temperature tends to lower the nanocrystal size.

We thus investigated the effects of low gas temperatures, expecting to increase the nanocrystal size, and to accelerate the formation kinetics. In the following, we show that gas temperature have a significant effect on Si nanocrystal size in a cc-rf Ar/SiH_4 discharge. Finally, the obtained results are discussed both from a chemical and a thermodynamical point of view.

VI.1 State of the art

The study of the effects of low gas temperature on dust particle formation has been motivated by the already-known effects of high gas temperature on this process. Indeed, these effects, summarized in the following sections, let us think that decreasing the gas temperature in the discharge could allow to tailor bigger silicon nanocrystals, using a well-controlled process in Silane-based plasmas.

VI.1.a High gas temperature effect on kinetics

The effect of high gas temperature on dust particle formation kinetics has been studied for more than ten years now. In 1994, Boufendi and Bouchoule evidenced that an increase of the gas temperature made the kinetics longer. They performed Laser Induced Particle Explosive Evaporation (LIPEE) measurements for gas temperatures ranging from 20℃ to 150 ℃ and obtained the results presented in figure VI.1 [35].

In her PhD thesis, M.C. Jouanny demonstrated that the different steps of dust particle formation are all delayed by increasing the gas temperature [13]. An overview of this study, performed using the V_{dc}/3H diagnostics, is presented in figure VI.2. These results confirmed the ones obtained in [35].

A more detailed analysis of the gas temperature effect on the onset of the aggregation phase has been performed in chapter III. As an example, figure III.12 clearly shows the delay induced by the gas temperature increase on the appearance of the instability, and thus on the aggregation onset.

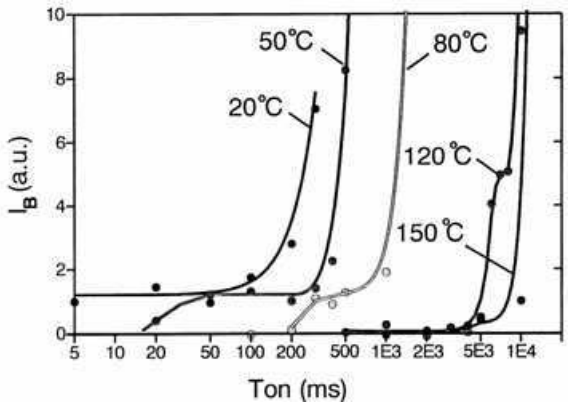

Figure VI.1: LIPEE signal showing a delay of nucleation with increasing gas temperature [35].

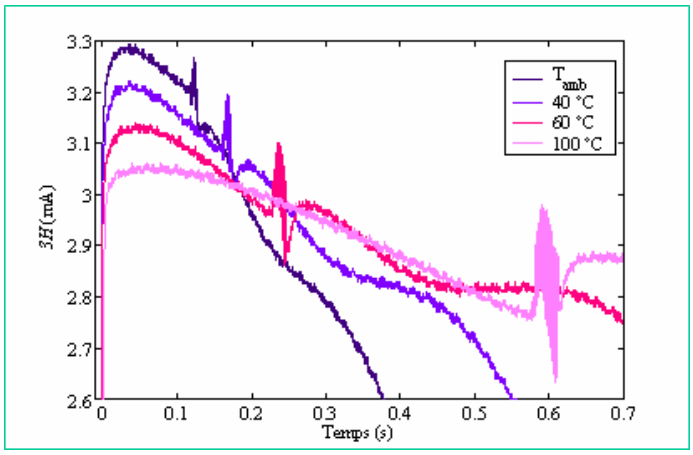

Figure VI.2: Time evolution of 3H as a function of high gas temperatures [13]. Temps (s) is time in seconds, T_{amb} is for room temperature.

VI.1.b Gas temperature effect on dust particle size and structure.

Modifications of the gas temperature also have an effect on the properties of dust particles synthesized in the plasma. The most outstanding effect is the size variation of the nanocrystals. Hadjadj et al showed in [111] that the rugosity of thin films deposited at the end of the nanocrystal accumulation phase tended to decrease when the gas temperature was increased. This result lets surmise that the nanocrystal size decreases when the gas temperature increases.

Characterization of depositions performed at different gas temperatures confirmed these results. Indeed, thanks to TEM analysis, nanocrystals deposited at 100℃ were evidenced to be around 0.9 nm in radius [112]. Using Raman spectroscopy, nanocrystals deposited at respectively 0℃ and 50℃, were shown to be respectively around 2.8 nm and 1.4 nm in radius [112]. These radii have to be compared to the radius value at room temperature, which is around 1.5 nm.

Concerning the nanocrystal structure, two important points are underlined by Viera et al in [39]. First, Si nanocrystals have been shown to be in the fcc phase whatever the gas temperature used to synthesized them. Second, it has been evidenced that the Si nanocrystals maintain the same atomic arrangement once incorporated in a film. This result thus confirms the validity of ex-situ analyses to determine dust particle structure in the gas phase.

VI.2 Experimental conditions

In this section, a brief overview of the method used to cool down the experimental set-up is given, and a succinct description of the method used to characterize synthesized dust particles (the Debye-Scherrer method for x-ray diffraction) is presented.

VI.2.a Experimental set-up

In order to decrease the gas temperature in the whole discharge volume, a liquid nitrogen circulation has been implemented on the set-up described in chapter II (see figure VI.3). The flow rate of liquid nitrogen is controlled thanks to a servovalve. This valve provides a closed valve opening loop response to a gas temperature measurement provided by a J-type thermocouple located in the gas flow, below the plasma box. Temperatures down to -40°C can be reached depending on external conditions such as the room temperature. The gas temperature is maintained in a range of a few degrees around the set point.

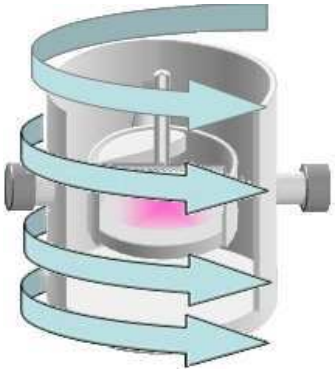

Figure VI.3: Sketch of the liquid nitrogen circulation on the Silane experiment.

VI.2.b Experimental constraints

Cooling down the whole plasma chamber is a limiting factor to get very low gas temperatures in the plasma box. The cooling down process is very time-consuming. As an example, figure VI.4 shows the gas temperature evolution in the chamber as a function of time once the circulation of liquid nitrogen has begun. As one can observe, more than one hour (70 min indeed) are needed to get 0°C in the chamber. This time reaches respectively around 100 min and 150 min to get -10°C and -20°C. Moreover, the equipment we had did not allow a sufficient liquid nitrogen flow rate to get temperatures lower than around -25°C. To reach a gas temperature of -40°C, we used another equipment, allowing to get a more important liquid nitrogen flow rate, kindly made available by another team for a few days.

Due to experimental constraints, depositions had to be performed in the discharge box.

Indeed, several tests were performed in post-discharge, and it appeared that dust particles tended to deposit on the sides of the plasma box instead of landing on its bottom. This effect is certainly due to thermophoresis: as we cool down thanks to a lateral circulation of liquid nitrogen, the sides of the plasma box are expected to be colder than its bottom, thus attracting dust particles. Thus, depositions must be performed in the discharge box to be sure to obtain a sufficient density to allow analyses. This aspect is an important limiting factor: it means that for each sample the plasma chamber has to be opened. For each deposition, the reactor is opened to set the substrate in the plasma box, then the chamber is pumped down and cooled down, the deposition (of a few minutes) is performed, then we have to wait until the chamber warms up to room temperature to open it and get the sample back. This whole process lasts several hours (depending on the gas temperature reached) to obtain a single sample. On average, we needed a whole day to obtain a single sample.

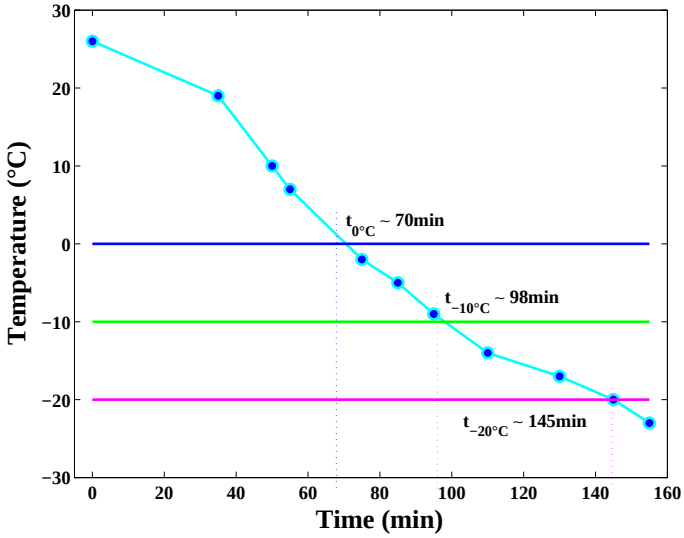

Figure VI.4: Gas temperature decrease as a function of time, once the liquid nitrogen circulation has begun.

VI.2.c Characterizations

To quantify low gas temperature effect on the dust particle formation kinetics, the V_{dc}/3H diagnostics has been used. Synthesized dust particles have been characterized using both scanning electron microscopy (SEM) and x-ray diffraction. The principle of SEM imaging has already been detailed in chapter II. In the following, we will give a summary concerning the Debye-Scherrer method for x-ray diffraction. The so-called Debye-Scherrer method is the most commonly used method to characterize powders. It consists in irradiating a sample with a thin monochromatic x-ray beam. Generally, a x-ray diffraction set-up is

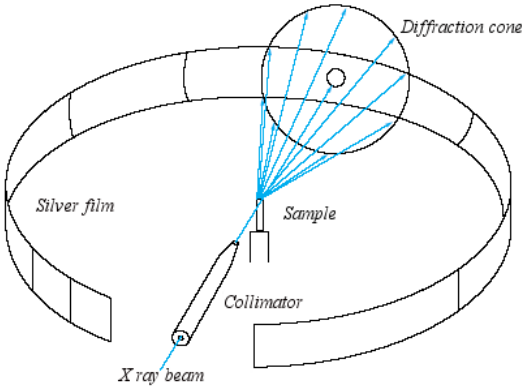

Figure VI.5: Sketch of a Debye-Scherrer chamber for x-ray diffraction (adapted from [114].)

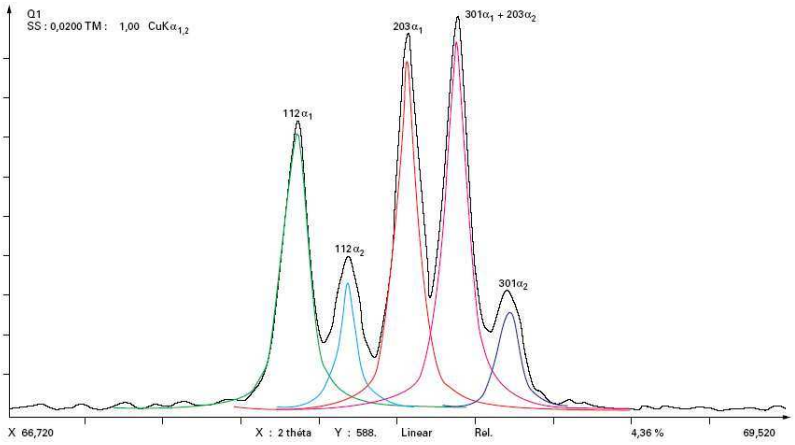

Figure VI.6: Example of a x-ray diffraction spectrum [114].

mainly composed of a x-ray source, the sample to characterize and a detector [113, 114]. Figure VI.5 shows the sketch of a Debye-Scherrer chamber.

A well-defined Debye-Scherrer spectrum corresponds to each crystalline phase. Figure VI.6 gives an example of a diffraction spectrum for Quartz. The black curve is the recorded spectrum, while the colored curves are the fits of each peak. To identify the crystalline phases of the obtained spectrum, the spectrum has to be compared with the ones referenced by the American Society for Testing Material (ASTM). From this spectrum, the crystallite size in the sample can also be determined. For this purpose, Scherrer proposed a simple equation:

$$L_c = \frac{K\lambda}{\beta_p cos\theta_d} \tag{VI.1}$$

with L_c the crystallite size, K a shape factor, λ the wavelength of the diffracted beam, β_p the peak width on the spectrum and θ_d the diffraction angle [114].

VI.3 Preliminary results

In this section, we present the preliminary results on the effect of low gas temperatures on the dust particle formation kinetics, size and structure.

VI.3.a Kinetics

The evolution of the dust particle formation kinetics has been studied for gas temperatures from 301 K down to 248 K using the V_{dc}/3H diagnostics. Figure VI.7 shows the time evolution of 3H for different gas temperatures on a time-scale of about 4 s. Curves are shifted in the vertical axis in order to get a better overview of their evolution. The uppermost curve corresponds to 301 K, while the lowest one corresponds to 248 K. This figure is quite comparable to figure III.14 in chapter III besides the different time-scales. Data of figure VI.7 have been obtained using a slightly different equipment to cool down the gas. It allowed us to reach very low gas temperatures faster, and thus to obtain a wider spectrum of comparable data. In this figure, we can see clearly that all the steps of dust particle formation become shorter when the gas temperature is decreased. This result is in great agreement with the one obtained from figure III.14, which showed that the two first steps of dust particle growth occurred faster at low gas temperatures.

As we deduced the kinetics evolution for high gas temperatures in figure III.13(a) from figure III.12, we can deduce this same kinetics evolution for low gas temperatures from the data of figure VI.7. For this purpose, we noted down the time corresponding to the onset of the aggregation phase, i.e. to the beginning of the aggregation instability as demonstrated in chapter III. The obtained curve (not displayed here) is really comparable to the one presented in figure III.15(a) in chapter III. By gathering all these data, we obtained figure VI.8 that displays the kinetics evolution as a function of the gas temperature in a temperature range comprised between 248 K and 398 K. Red dots are experimental data. The blue curve is a fit of these data. As can be seen in this figure, the lower the gas temperature, the faster the formation kinetics. Thanks to the fit, we can evidence that the kinetics evolves exponentially with the gas temperature, following a law given by $t_{aggregation}(s) = Ae^{B(T(K)-C)}$, where A, B and C are constants used to adjust the fit.

VI.3.b Nanocrystal size

Gas temperature was suspected to have an influence on the size of nanocrystals synthesized in the plasma. In order to confirm this hypothesis, several depositions have been performed for different gas temperatures from 100°C (373 K) down to -40°C (233 K). The nanocrystal mean size has then been evaluated using different methods, depending on the sample. Nanocrystals deposited at 100°C were evidenced to be around 0.9 nm in radius using TEM [112], nanocrystals deposited at respectively 0°C and 50°C were shown to be respectively around 2.8 nm and 1.4 nm in radius using Raman spectroscopy [112], and nanocrystals

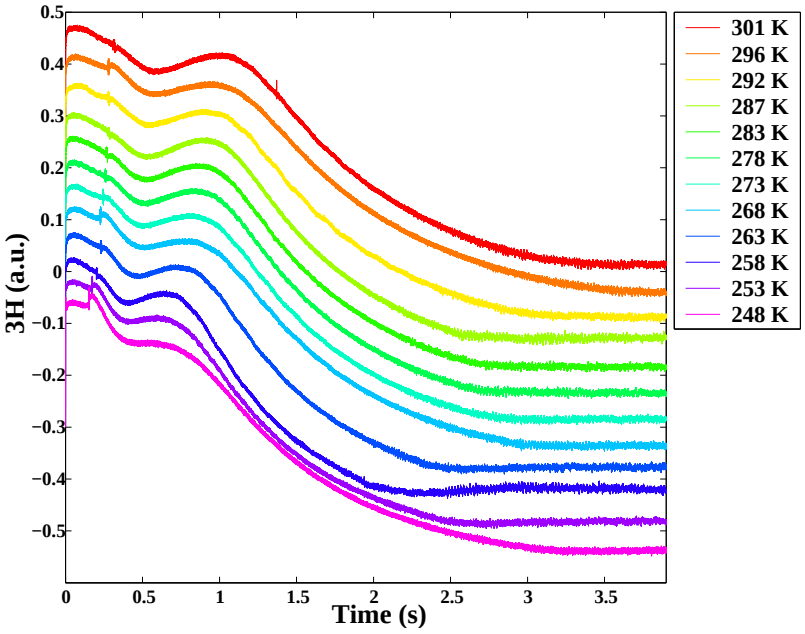

Figure VI.7: Time-evolution of 3H for low gas temperatures.

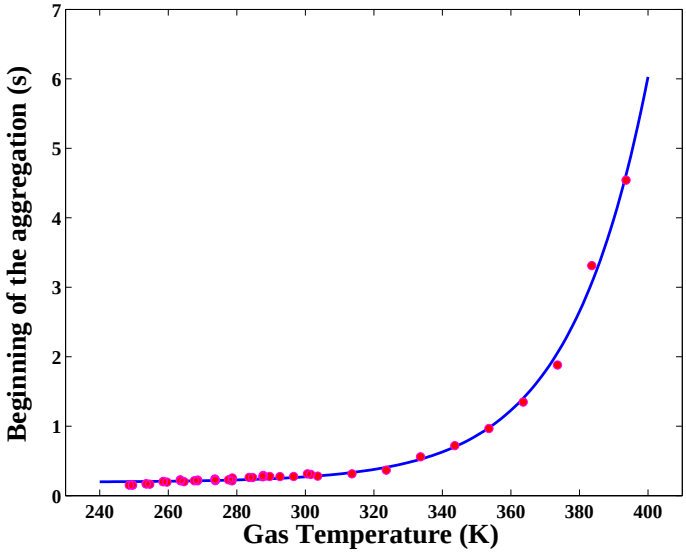

Figure VI.8: Evolution of the dust particle formation kinetics as a function of low gas temperatures.

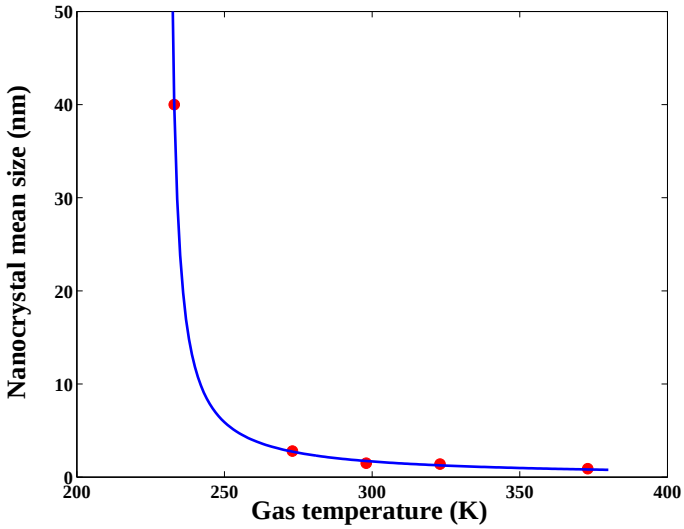

Figure VI.9: Nanocrystal radius as a function of the gas temperature.

deposited at respectively 25℃ and -40℃ were shown to be respectively around 1.5 nm and 40 nm using SEM. Figure VI.9 shows the nanocrystal mean size evolution as a function of the gas temperature in the discharge. Red dots are experimental data. The blue curve is a fit of these data. It clearly appears that decreasing the gas temperature allows to obtain bigger nanocrystals. The most outstanding example is the result obtained for a gas temperature of -40℃. In this case, the nanocrystal size reaches 40 nm in radius as can be seen in the SEM image presented in figure VI.10. Thanks to the fit, we can evidence that the nanocrystal radius increases as $1/(T_g - T_{limit})$. In order to obtain more data, and thus a better statistics, four more samples have been deposited to be analyzed using x-ray diffraction. The analysis is currently underway. The value of T_{limit} giving the best fit is 230 K. Due to experimental constraints, we could not reach this gas temperature on our set-up. So presently, we can not conclude on dust particle formation for gas temperatures around the value of T_{limit}. However, as crystals can not physically grow up endlessly when T_{limit} is attained, two hypothesis can be made. First, the nanocrystal size tends to a "limit" size, which will remains the same whatever the gas temperature below T_{limit}. Second, for gas temperatures below T_{limit}, no more dust particles are synthesized in the plasma, and no dust forming conditions are reached for so low gas temperatures.

VI.3.c Nanocrystal structure

In [39], Viera et al demonstrated that nanocrystals synthesized with a gas temperature ranging from 25℃ to 150℃ are mainly in the fcc phase. However, the electron diffraction pattern also shows that fcc and diamond structures coexist in the sample (with a more important fcc structure contribution). The authors thus assumed that the smallest nanoparticles were

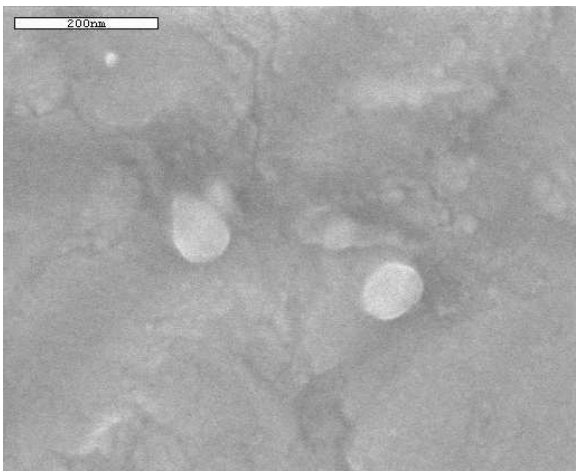

Figure VI.10: SEM image of nanoparticles synthesized for a gas temperature of -40°C.

in the fcc phase and the larger ones were more likely to have a diamond-like structure. In order to predict the structure of the nanocrystals, several parameters have to be taken into account. As an example, Viera et al [39] underlined the role of the Argon dilution on the particle structure by comparing dust particles synthesized in Ar/SiH_4 and pure SiH_4 plasmas. Nanoparticles synthesized in pure Silane plasmas appears to be amorphous, while the ones synthesized in Ar dilution are in the fcc phase. This structure could be the results of collisions of high energetic plasma species with the dust particles. This point suggests that dust particles synthesized in Ar/SiH_4 plasmas present a structure mainly due to the nature of the buffer gas. This result seems to be independent of the gas temperature and could let us think that nanocrystals synthesized at low gas temperature should have the same fcc structure.

Nevertheless, the fcc structure is a metastable phase of Silicon. The existence of this structure for 2 nm nanocrystals may be due to size effects: for such small sizes, the surface effect is suspected to have a predominant role [115]. Indeed, the bonding configuration of atoms on the surface of nanocrystals could be distinct enough from the one of the bulk to reduce the Gibbs free energy [39]. Thus, as nanocrystals seem to be bigger at low gas temperatures, their structure may change. In fact, in small clusters, unusual geometries can sometimes be thermodynamically stable, while in larger nanocrystals, the size effect is not sufficient to stabilize these particular bonding geometries [115]. Several possibilities have to be considered for larger nanoparticle structure. First, larger nanoparticles are not likely to be amorphous: for nanoparticle size lower than 50 nm, a-Si is not predicted to be thermodynamically stable [115]. Second, larger nanocrystals could adopt the structure of the bulk, i.e. diamond-like structure (that is already observed for a few nanocrystals in the nm size range [39]). A last structure could appear: a fcc core embedded in a diamond-like shell. Indeed, in dynamic processes such as crystal growth, it is possible to trap a metastable

structure in larger crystallites [115].

Moreover, ns-films containing silicon nanocrystals are known to be highly hydrogenated [116]. This fact has to be taken into account because the saturation of the nanocrystal surface could also influence the most stable structure [39]. Indeed, Vach et al [117] demonstrated, using numerical modeling, that the only way to obtain crystalline clusters in pure SiH_4 plasmas is be in presence of active atomic hydrogen.

Finally, it appears that the structure of nanoparticles synthesized at low gas temperature is very fussy to predict. However, they are very likely to be crystalline but only an appropriate analysis could determine their exact structure. This work is currently underway.

VI.4 Discussion

The gas temperature has been shown to have a significant effect on dust particle formation kinetics. Various explanations for this effect have been proposed by Fridman et al [38], Perrin et al [80] and Bhandarkar et al [78].

Fridman et al [38], proposed that the nucleation may be delayed by increasing the gas temperature due to the temperature dependence of the de-excitation of vibrationally excited SiH_4. They assumed that the clustering pathway in silane-based plasmas involves chain reactions between anions and excited neutral SiH_4 as explained in chapter I. From Fridman et al [38], an increase in the gas temperature reduces the density of excited species through vibrational-rotranslational transitions described by a Landau-Teller expression. Thus the decrease in the density of vibrationally excited species slows down the clustering chain.

Perrin et al [80] proposed that the electron attachment rate depends on the temperature. Electron attachment to silicon hydrides leads to the formation of anionic species. In some cases a third body is needed to stabilize the created anionic complex. Since the reaction rate for stabilization reactions depends on the number density of the surrounding gas, it is inversely proportional to gas temperature [80]. Thus the higher the gas temperature, the lower is the expected attachment rate, leading to slower anion formation, and thus to a slower nucleation process [80]. However, this hypothesis has been undermined in M.C. Jouanny's PhD thesis [13]. Indeed she demonstrated that the gas temperature has no effect on the formation of negative ions: neither on their quantity nor on their delay of formation [13, 75].

Bhandarkar et al [78] suggest that the temperature dependence of the Brownian diffusion coefficient could delay the nucleation. Dust particles of less than 1 nm in size can only hold one or two negative charges and can be easily neutralized or even positively charged. The neutral and positive particles can escape from the plasma by diffusion or drift in the ambipolar field, respectively [78]. Moreover, the Brownian diffusion coefficient depends on temperature ($\propto T_g^{3/2}$) at constant pressure. Thus, an increase in the gas temperature increases the losses and decreases the growth rate of dust particles [78].

The effects of gas temperature we observed on dust particle formation let think that this process can be compared to the homogeneous nucleation and growth of crystals in supersaturated media [118, 119, 120, 121, 122, 123]. In this case, the probability P_{crit} per particle that a spontaneous fluctuation will result into the formation of a critical nucleus depends on the free energy (Gibbs energy) required to form such a nucleus [121]:

$$P_{crit} = e^{-\Delta G_{crit}/k_B T} \tag{VI.2}$$

The crystal nucleation rate per unit volume J is the product of P_{crit} by the kinetic factor J_0 [119, 120, 121, 122]:

$$J = J_0\, e^{-\Delta G_{crit}/k_B T} \tag{VI.3}$$

Specific features of the kinetics of the process are incorporated via the pre-exponential factor J_0 [123]. For one-component system (as ours), J_0 is notably proportional to the number of possible nucleation centers (SiH_3^- ions in our case) [123]. As we demonstrated that the number of nucleation seeds does not depend on the gas temperature in our experiment (J_0 constant), equation VI.3 clearly shows the gas temperature dependence of the nucleation rate and thus the kinetics. According to equation VI.3, an increase in the gas temperature should make the kinetics longer. Results presented in figure VI.8 are in perfect agreement with this theory.

Assuming an incompressible cluster, with some given concentration c_α and approximately of spherical shape with a radius r, the change of the thermodynamic potential G, due to the formation of an aggregate may be expressed approximately as [123]:

$$\Delta G = -n_\alpha \Delta\mu + \sigma A_c \tag{VI.4}$$

where A_c is the surface area of the cluster, σ the surface or interfacial tension of the cluster, n_α the number of particles in the cluster and $\Delta\mu$ the difference of chemical potential per mole or particle.

In order to express ΔG as a function of the temperature, $\Delta\mu$ can be written as follow:

$$\Delta\mu = k_B T\, lnS \tag{VI.5}$$

where S is the "monomer supersaturation ratio" [119]. In most cases, S is considered as independent of the temperature [119, 122]. Finally, from equations VI.4 and VI.5, ΔG can be written as:

$$\Delta G = -n_\alpha k_B T lnS + \sigma A_c \tag{VI.6}$$

The dependence $\Delta G = \Delta G(r)$ is illustrated in figure VI.11. For clusters with a radius $r < r_c$, the thermodynamic evolution criteria predicts that the cluster will dissolve. Clusters with a radius $r > r_c$ will grow spontaneously up to macroscopic dimensions [123]. The critical size r_c corresponds to a maximum of ΔG. This corresponding radius can be determined approximately via the relation [119, 123]:

$$r_c = \frac{2\sigma}{c_\alpha \Delta\mu} = \frac{2\sigma}{c_\alpha k_B T lnS} \tag{VI.7}$$

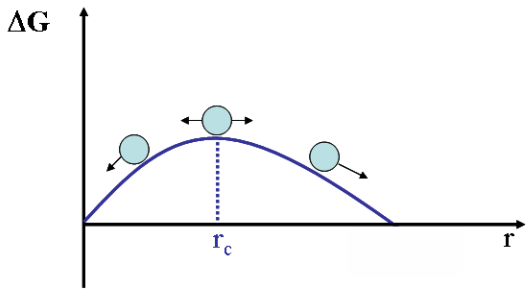

Figure VI.11: Evolution of ΔG as a function of the cluster radius r

From equation VI.7, the critical radius clearly appears to depend on the temperature as $1/T$. Results presented in figure VI.9 perfectly meet the theory, as the evolution of the nanocrystal radius as a function of gas temperature is well-fitted by a $1/T$ law.

VI.5 French summary / Résumé en français

Les nanocristaux semiconducteurs (silicium, germanium), aussi appelés îlots quantiques (*quantum dots*), présentent des applications potentielles dans divers dispositifs photoniques. Les propriétés électriques et optiques des cristaux de silicium sont variables en fonction de leur taille et en font des candidats potentiels pour de nombreuses applications [3]. A titre d'exemple, la photo- ou électroluminescence des nanocristaux de Si est accordable via leur taille [110]. A l'heure actuelle, il est nécessaire de mettre au point un système de contrôle de la taille facile à mettre en oeuvre. Une façon possible de modifier la taille des nanocristaux peut être de modifier la température du gaz dans la décharge.

Etat de l'art

Cette étude sur les effets des basses températures de gaz sur les poudres a été motivée par les connaissances déjà acquises sur les effets des hautes températures de gaz. En effet, les effets connus de la température de gaz laisse penser qu'une diminution de cette dernière pourrait permettre de façonner des nanocristaux de taille plus importante à partir du procédé que nous utilisons en argon-silane.

En 1994, Boufendi et Bouchoule [35] ont montré, grâce à une étude par LIPEE, que l'augmentation de la température de gaz allongeait globalement la cinétique de formation des poussières. Dans sa thèse, M.C. Jouanny [13] a mis en évidence l'allongement de chacune des phases de formation de poussières lorsque la température est augmentée. De plus, l'étude menée sur le démarrage de la phase d'agrégation dans le chapitre III est venue confirmer ces résultats.

Il a aussi été démontré que l'augmentation de la température de gaz diminue la taille

des nanocristaux synthétisés. Des nanocristaux déposés à 100°C présentent un rayon de l'ordre de 0.9 nm (analyse TEM) [112], d'autres nanocristaux déposés respectivement à 0°C et 50°C présentent des rayons respectivement autour de 2.8 nm et 1.4 nm [112].

Concernant la structure des nanocristaux, Viera et al soulignent deux points importants dans [39]. Tout d'abord, les nanocristaux présentent uns structure cubique face centrée (cfc) quelle que soit la température de gaz à laquelle ils ont été synthétisés (entre 25 et 150°C). De plus, le fait de déposer les nanocristaux sur un substrat ne perturbe pas leur structure cristalline, ce qui permet de confirmer la validité des analyses ex-situ.

Conditions expérimentales

Afin d'abaisser la température des gaz dans le réacteur, une circulation d'azote liquide a été mise en place. Le flux d'azote liquide est contrôlé grâce à une vanne pilotée en température. La température est mesurée à l'aide d'un thermocouple de type J, placé dans le flux de gaz sous la boîte à décharge. Grâce à ce dispositif, des températures de l'ordre de -40°C peuvent être atteintes et maintenues à quelques degrés près.

Cependant, refroidir la totalité du réacteur s'avère être un facteur limitant important. Le temps nécessaire au refroidissement est très long : typiquement il faut plus d'une heure pour atteindre 0°C, et aux alentours de 100 min et 150 min pour atteindre -10°C et -20°C. De plus, du fait de contraintes expérimentales principalement dues à la force de thermophorèse induite, les dépôts doivent être réalisés à l'intérieur de la boîte à décharge. C'est le second facteur limitant dans ce cas. Pour chaque dépôt, il est nécessaire d'ouvrir le réacteur pour placer le substrat, puis de pomper et de refroidir, ensuite le dépôt de quelques minutes est réalisé. Il faut ensuite attendre que le réacteur soit revenu à la température ambiante pour pouvoir l'ouvrir et récupérer l'échantillon déposé. Au final, il faut en moyenne une journée pour obtenir un seul et unique échantillon.

Résultats préliminaires

L'évolution de la cinétique de formation des poussières a été étudiée pour différentes températures de gaz entre 248 et 301 K, à l'aide du diagnostic électrique V_{dc}/3H. La figure VI.7 donne un aperçu des résultats sur une échelle de temps d'environ 4 s. Sur cette figure, on voit clairement que toutes les étapes de formation des poussières deviennent plus courtes lorsque la température des gaz est abaissée. Ce résultat vient corroborer les résultats précédemment obtenus sur la phase d'accumulation et d'agrégation à basse température, au chapitre III.

Afin de définir l'évolution de la cinétique pour les basses températures de gaz, nous avons procédé de la même façon que pour définir l'évolution de la cinétique en fonction des hautes températures de gaz au chapitre III. Nous avons donc relevé l'instant correspondant

au démarrage de l'instabilité (donc de l'agrégation) sur chaque courbe. Lorsque que l'on recoupe ces données avec celles obtenues précédemment pour les hautes températures de gaz, on obtient l'évolution de la cinétique de formation entre 248 et 398 K présentée figure VI.8. Comme on peut le constater sur cette figure, plus la température de gaz diminue, plus la cinétique de formation accélère selon une loi du type $t_{aggregation}(s) = Ae^{B(T(K)-C)}$ (où A, B, et C sont des variables d'ajustement).

La température de gaz apparaît comme un bon moyen de contrôle de la taille des nanocristaux de silicium. Afin de compléter les résultats obtenus par Boufendi [112], nous avons réaliser de nouveaux dépôts de nanocristaux, en abaissant significativement la température des gaz dans le réacteur. Ces nouveaux résultats nous ont permis d'obtenir la courbe présentée figure VI.9. On y observe que le rayon des nanocristaux de silicium est très sensible à la température du gaz lors de la synthèse : plus le gaz est froid, plus les cristaux obtenus sont gros. On atteint notamment un rayon de 40 nm environ pour une température de gaz de -40°C. Grâce à l'ajustement des données, on peut mettre en évidence que la taille des cristaux évolue selon une loi du type $1/(T_{gas} - T_{limit})$. La valeur de T_{limit} est de l'ordre de 203 K d'après notre meilleur ajustement. L'existence de cette température limite soulève la question du comportement des cristaux au-delà de cette température. Physiquement, ils ne peuvent pas croître indéfiniment. Nous pouvons donc formuler deux hypothèses : soit ils atteignent une taille limite qu'ils ne dépasseront plus même si l'on continue à diminuer la température de gaz, soit les conditions de formation de poudres ne sont plus réunies pour des températures inférieures à 203 K. Des études complémentaires sont envisagées pour déterminer la valeur de ces hypothèses.

Concernant la structure des nanocristaux, il a été démontré notamment par Viera et al [39], que pour des températures de gaz comprises entre 25 et 150°C, les cristaux conservaient la même structure cfc. Il est cependant difficile de prévoir la structure des nanocristaux obtenus à basse température. En effet, du fait de leur taille plus importante, ils sont susceptibles de présenter une phase cristalline différente. Différentes hypothèses peuvent être proposées. Tout d'abord, les nanoparticules ont peu de chance d'être amorphes : pour des nanoparticules de moins de 50 nm cette phase n'est pas stable thermodynamiquement [115]. Les nanocristaux pourront donc soit adopter la structure du silicium en volume (*bulk*, structure diamant), soit adopter une structure du type cfc entourée d'une enveloppe présentant une structure diamant [115]. Un dernier aspect doit être pris en compte : la forte teneur en hydrogène des nanocristaux peut aussi influer sur leur structure cristalline. Au final, la structure des nanocristaux synthétisés à basse température s'avère extrêmement délicate à prédire, les analyses sont actuellement en cours.

Discussion

Différentes explications ont été proposées afin d'expliquer l'évolution de la cinétique en fonction de la température de gaz. Fridman et al [38] expliquent cette évolution par la dépendance en température de la dé-excitation des molécules de SiH_4 vibrationnellement excitées. Perrin et al [80] l'expliquent par la diminution de la densité d'ions négatifs lorsque la température augmente. M.C. Jouanny a cependant montré dans sa thèse [13] que cette hypothèse n'était pas valable dans notre cas. Bhandarkar et al [78] proposent quant à eux que la dépendance en température du coefficient de diffusion brownienne pourrait expliquer cet effet.

Les effets observés lors de la modification de la température dans notre système laissent penser que la croissance des poussières pourrait être comparée à la nucléation homogène dans les milieux supersaturés [118, 119, 120, 121, 122, 123]. Dans ce contexte, le taux de nucléation dépend explicitement de la température du gaz, et une augmentation de cette température provoque une diminution du taux de nucléation. Nos résultats expérimentaux sont parfaitement en accord avec cette variation. De plus, cette même théorie prévoit une augmentation de la taille des cristaux formés lorsque la température de gaz est abaissée, avec un rayon critique proportionnel à l'inverse de la température. Nos premiers résultats expérimentaux sont en accord parfait avec cette loi, puisque nous avons montré que l'évolution du rayon en fonction de la température pouvait être ajusté par une loi en $1/T$.

Conclusion

Faut pas se laisser gagner par l'euphorie
de croire que l'on est un homme important.
Louise Attaque

Les travaux présentés dans cette thèse s'inscrivent dans le cadre de l'étude des plasmas poussiéreux menée depuis une quinzaine d'années au GREMI au sein de l'équipe "Plasmas poudreux". Motivées à l'origine par les contraintes de propreté de l'industrie de la microélectronique, les études se tournent à l'heure actuelle vers une autre direction : la synthèse de nanoparticules aux propriétés maîtrisées.

Afin d'atteindre cet objectif, il a été nécessaire d'acquérir une bonne connaissance des mécanismes de croissance de poussières, ainsi que de développer les outils de diagnostic indispensables à leur détection. Ce travail de longue haleine a débuté lors des thèses précédemment réalisées dans l'équipe, et s'est poursuivi au cours de cette thèse.

L'objectif de cette thèse était de réussir à synthétiser des poussières de taille et/ou de composition maîtrisée, en nous basant sur les connaissances précédemment acquises dans l'équipe. Pour cela, le travail a été envisagé autour de trois principaux axes :

- La localisation et l'étude du démarrage de la phase d'agrégation des nanocristaux (caractérisée par une instabilité), ainsi que l'étude de l'influence de la croissance de poussières sur la forme et le comportement du nuage de poudres (*void* et instabilités),
- La synthèse d'aérosols analogues aux tholins de Titan et aux grains interstellaires en chimie carbonée,
- Le contrôle de la taille des nanocristaux de silicium via la modification de la température du gaz dans la décharge.

Un certain nombre de résultats s'est dégagé de ces différentes études. Jusqu'à présent, les différentes phases de formation des poussières en plasma d'argon/silane étaient relativement bien identifiées à l'aide des mesures électriques. Cependant, le démarrage exact de la phase d'agrégation des nanocristaux n'était pas encore clairement localisé. Or, il s'agit

d'un point capital pour la synthèse de nanoparticules monocristallines non-agglomérées, puisqu'il est nécessaire de les déposer avant le début de leur agrégation dans le plasma. Nous avons montré, grâce aux mesures électriques et à l'analyse au MEB et à l'AFM de différents dépôts, que le début de l'agrégation provoquait une instabilité du plasma. Cette instabilité, clairement identifiable sur les caractéristiques électriques de la décharge, s'avère un excellent repère du démarrage de la phase d'agrégation. Grâce aux dépôts réalisés avant, pendant et après l'instabilité, nous avons démontré que le démarrage de l'instabilité correspondait exactement à l'agrégation des premiers nanocristaux. Cette instabilité s'est avérée très comparable à celle observée par Descoeudres et al [74] dans les gaz électronégatifs, et expliquée par Nighan et Wiegand [73].

Cette étude nous a de plus permis d'affiner la calibration du diagnostic électrique V_{dc}/3H réalisée au cours de la thèse de M.C. Jouanny. A l'heure actuelle nous savons qu'avant l'instabilité, les poudres sont monocristallines (cubique face centrée) de 2-3 nm de diamètre à température ambiante [39]. Leur forme semble sphérique et leur densité augmente pendant la phase d'accumulation jusqu'à atteindre la valeur critique ($10^{11} - 10^{12}$ cm^{-3}) permettant le début de l'agrégation [9]. Après l'instabilité, il ne reste plus de monocristaux dans le plasma. Les poudres sont constituées de monocristaux agglomérés. Leur taille augmente de 5 nm au début de l'agrégation jusqu'à environ 45 nm à la fin de cette phase [81]. Les poudres sont alors polycristallines, en forme de chou-fleur et présentent une grande surface spécifique.

La croissance de poussières dans la décharge est un phénomène continu et cyclique. En effet, tant que l'on fournit du silane dans la décharge, le plasma est le siège de réactions physico-chimiques menant à la formation de poussières, et provoquant ainsi l'apparition de générations successives de poussières en continu. De ce fait, le plasma n'atteint jamais un état stable et permanent, mais oscille en permanence entre un état où les conditions de formation sont favorisées et un état où le plasma contient un nuage dense de poussières. Le phénomène de générations successives de poussières est bien connu, en gaz réactifs et en pulvérisation, et dans différentes chimies. Il est le plus souvent lié à la présence d'une région vide de poudres au sein du nuage (le *void*), dans laquelle croît la nouvelle génération de poussières. Cependant, la présence d'un *void* n'avait jamais été mise en évidence dans le cas d'un plasma poussiéreux confiné spatialement.

Grâce à la corrélation de trois diagnostics (électrique V_{dc}/3H, diffusion de la lumière laser et spectroscopie optique d'émission), et en faisant l'hypothèse d'un void dans notre plasma, nous avons pu fournir une explication détaillée des phénomènes complexes de croissance de générations successives de poussières en argon/silane. Nous avons notamment montré que la croissance de ces nouvelles générations se base en permanence sur l'équilibre entre les poussières nouvellement formées et les anciennes expulsées du plasma, qui influe directement sur la densité d'électrons libres dans la décharge.

Nous avons par la suite validé expérimentalement l'hypothèse de la présence d'un *void* dans le nuage de poussières. L'imagerie vidéo a mis en évidence une zone d'ionisation plus intense (caractéristique d'un *void*). Parallèlement, des dépôts résolus spatialement ont mis en évidence la forte inhomogénéité du nuage de poudres, avec notamment la présence de très petites poudres au centre et celle de grosses poudres au bord du plasma.

La région de *void* mise en évidence semble instable au cours de la croissance des générations successives. Pendant la partie du cycle dominée par l'expulsion des grosses poudres, le *void* paraît osciller de façon peut ordonnée, tandis que lors de la phase dominée par la croissance de la nouvelle génération, le *void* semble osciller de façon très ordonnée. L'analyse spectrale des signaux électrique et optique met en évidence un schéma de développement extrêmement complexe, impliquant plusieurs branches de fréquences évoluant différemment. Cette instabilité semble intrinsèquement liée aux générations successives de poudres.

D'autres phénomènes d'instabilité liés à la croissance de poussières ont été étudiés en parallèle sur le dispositif PKE. Nous avons notamment mis en évidence que la croissance de la première génération de poussières, créées par pulvérisation, engendrait une instabilité du plasma. Cette instabilité, au spectre très complexe, se déroule en sept étapes clairement identifiées sur les signaux électrique et optiques. Les différences de comportement entre le signal électrique (intégré) et les signaux optiques (résolus spatialement) soulignent l'implication de phénomènes locaux. Afin d'éclaircir ce dernier point, une étude par caméra rapide a été réalisée et les données sont actuellement en cours de traitement.

Un dernier phénomène d'instabilité du *void* a été étudié sur le dispositif PKE : l'instabilité couramment appelée *heartbeat*, qui consiste en une série de contractions et d'expansions du *void*. La corrélation entre les signaux électrique et optiques tend à prouver que cette instabilité est due à la propagation d'une onde d'ionisation au sein du plasma. Nous avons de plus mis en évidence la période d'amortissement (sous forme de pics avortés dans les signaux) qui précède l'arrêt total du *heartbeat*. Les transitions de n à $(n+1)$ pics avortés ont lieu sans aucun signe précurseur. Chaque pic avorté correspond à une contraction incomplète du *void*, qui semble due à une perte d'énergie progressive de l'instabilité.

Les différentes instabilités que nous avons étudiées présentent des schémas de développement complexes liés à la fois à la formation des poussières, au comportement du nuage et/ou à la région de *void*. Une étude bibliographique complète, couplée à nos résultats expérimentaux, montre que les phénomènes d'instabilités et de *void* se retrouvent dans de très nombreux plasmas poussiéreux, quels que soient la chimie, la géométrie, l'origine des poussières, le flux de gaz, l'excitation rf et les conditions de gravité. La comparaison de toutes ces données met en lumière le caractère intrinsèque des instabilités et du *void* aux plasmas poussiéreux. Cependant, cette étude nécessiterait d'être étendue à d'autres décharges afin de vérifier l'influence notamment du type d'excitation sur ces phénomènes.

La maîtrise des procédés de synthèse de poussières par plasma froid permet d'envisager de synthétiser des poussières comparables à celles issues de l'espace, et difficiles à ramener sur Terre pour les étudier. Le dispositif expérimental PAMPRE, au Service d'Aéronomie, a été spécialement conçu en vue de synthétiser des poussières analogues aux tholins de Titan en chimie azote-méthane. Ce dispositif est très similaire à celui utilisé au GREMI en chimie argon-silane. Une étude complète, visant à caractériser le plasma, a été menée sur PAMPRE à l'aide du diagnostic électrique V_{dc}/3H. Cette étude paramétrique, en puissance, pression et dilution, a permis de mettre en évidence un optimum dans la cinétique de formation des poussières. Il est particulièrement intéressant de constater que les conditions optimales de dilution (2% de méthane dans 98% d'azote) correspondent aux conditions atmosphériques de Titan.

Des mesures de densités électronique et ionique ont été réalisées sur PAMPRE. Nous avons ainsi montré que la présence de méthane dans la décharge diminuait la densité électronique par un facteur 2 environ, par rapport à une décharge dans l'azote pur. L'évolution de la densité électronique en fonction de la pression pour différentes dilutions a montré un maximum autour de 0.4 mbar et un minimum autour de 0.8 mbar dans tous les cas. Ce minimum semble correspondre à un pic d'efficacité dans la production de tholins. Les mesures de densité ionique par sonde de Langmuir ne se sont pas avérées concluantes du fait de la pollution de la surface collectrice par un dépôt organique isolant.

Des poussières analogues aux grains interstellaires peuvent être synthétisées en chimie azote-acétylène dans des conditions de décharge très similaires à celles que nous utilisons en argon-silane. Afin d'étudier la structure des poussières ainsi synthétisées en temps réel, l'ellipsométrie in-situ de Mie-Rayleigh constitue un excellent diagnostic. La mise en place de ce diagnostic à l'Institut für Experimentalphysik II s'est avérée très délicate, notamment du fait de l'alignement des nombreuses optiques requises dans un ellipsomètre à élément rotatif. Les premiers résultats obtenus ont cependant été très encourageants. Ils nous ont permis d'obtenir une première idée de l'évolution de la cinétique de formation des poussières en fonction de la dilution et de la puissance injectée. Concernant la structure des poussières synthétisées, les premiers résultats montrent que plus elles sont petites, plus leur indice optique est élevé. Elles semblent de plus présenter un noyau dur entouré d'une enveloppe plus tendre. Le travail à ce sujet se poursuit actuellement à l'Université de Bochum où il fait l'objet d'une thèse en cours.

Les nombreuses applications envisageables pour les nanocristaux de silicium nécessitent de pouvoir contrôler efficacement leur taille lors de la synthèse. Des résultats obtenus dans le cadre de la thèse de S. Huet tendaient à montrer que les hautes températures de gaz avait une influence importante sur la taille des cristaux. Nous avons donc complété ce travail en menant une étude sur les effets des basses températures de gaz sur les nanocristaux. Pour cela, il a été nécessaire de mettre au point un dispositif permettant d'abaisser significa-

tivement la température du gaz dans le réacteur. Grâce à une circulation d'azote liquide, nous avons pu atteindre des températures de l'ordre de -40°C.

Cette étude nous a permis de mettre en avant l'allongement exponentiel du délai de formation des poussières en fonction de la température du gaz. Ce résultat est en bonne adéquation avec la théorie de la nucléation homogène dans les milieux supersaturés, et semble aussi s'expliquer d'un point de vue chimique. De plus, la théorie de la nucléation homogène prédit une augmentation de la taille des nanocristaux (en 1/T) lorsque la température de gaz est abaissée. Les tous premiers résultats expérimentaux obtenus confirment cette tendance. Des études complémentaires sont actuellement en cours.

Les résultats de ces différentes études offrent diverses perspectives de recherche pour l'avenir. En effet, concernant les instabilités, certains phénomènes locaux au coeur du plasma semblent entrer en ligne de compte. Des expériences d'imagerie rapide pourraient permettre d'élucider ces comportement et de mieux appréhender le comportement à la fois du plasma et du nuage de poudres. De plus, l'utilisation d'autres types de décharges (notamment en terme d'excitation électrique) pourrait permettre de conclure quand à la possible universalité de la région de *void* et des instabilités liées à la présence de poudres, dans les plasmas poussiéreux.

Les premiers résultats obtenus sur la taille des nanocristaux en abaissant la température de gaz sont extrêmement encourageants. Ce paramètre semble particulièrement adapté pour contrôler efficacement la taille des nanocristaux lors de leur synthèse en phase plasma. Une étude plus approfondie permettrait de confirmer ces premiers résultats et d'explorer des gammes de températures plus étendues.

Bibliography

[1] G. S. Selwyn, J. Singh, and R. S. Bennett. In situ laser diagnostic studies of plasma-generated particulate contamination. *J. Vac. Sci. Technol. A*, **7**:2758, 1989.

[2] Cyril Szopa, Guy Cernogora, Laifa Boufendi, Jean J. Correia, and Patrice Coll. Pampre: A dusty plasma experiment for titan's tholins production and study. *Planet. Space Sci.*, **54**:394, 2006.

[3] A. Bapat, C. Anderson, C.R. Perrey, C. Barry Carter, S.A. Campbell, and U. Kortshagen. Plasma synthesis of single-crystal silicon nanoparticles for novel electronic device applications. *Plasma Phys. Control. Fusion*, **46**:B97, 2004.

[4] A. Surawijaya, H. Mizuta, and S. Oda. Observation and Analysis of Tunneling Properties of Single Spherical Nanocrystalline Silicon Quantum Dot. *Jpn. J. of Appl. Phys.*, **45**:3638, April 2006.

[5] S. Tiwari, F. Rana, H. Hanafi, A. Hartstein, and E. F. Crabbé. A silicon nanocrystals based memory. *Appl. Phys. Lett.*, **68**:1377, 1996.

[6] Y. Tsuchiya, K. Takai, N. Momo, T. Nagami, H. Mizuta, S. Oda, S. Yamaguchi, and T. Shimada. Nanoelectromechanical nonvolatile memory device incorporating nanocrystalline Si dots. *J. Appl. Phys.*, **100**:4306, 2006.

[7] P. Roca i Cabarrocas, S. Kasouit, B. Kalache, R. Vanderhaghen, Y. Bonnassieux, M. Elyaakoubi, and I. French. Microcrystalline silicon : An emerging material for stable thin-film transistors. *Journal of the SID*, **12**, 2004.

[8] P. Roca i Cabarrocas, N. Chaabane, A.V. Kharchenko, and S. Tchakarov. Polymorphous silicon thin films produced in dusty plasmas : application to solar cells. *Plasma Phys. Control. Fusion*, **46**:B235, 2004.

[9] L. Boufendi, J. Gaudin, S. Huet, G. Viera, and M. Dudemaine. Detection of particles of less than 5nm in diameter formed in an argon-silane capacitively coupled radio-frequency discharge. *Appl. Phys. Lett.*, **79**:4301, 2001.

[10] J.Ph. Blondeau. *Formation de particules dans les mélanges Argon-Silane en décharge RF basse pression : -diagnostics in-situ par méthodes laser -caractérisation et modélisation des plasmas poudreux.* PhD thesis, Université d'Orléans, 1992.

[11] L. Boufendi. *Origine et comportement d'un nuage dense de particules submicroniques dans une décharge radiofréquence en milieu argon-silane basse pression.* PhD thesis, Université d'Orléans, 1994.

[12] S. Huet. *Etude de la phase initiale de croissance d'agrégats de silicium dans un plasma argon-silane : Application à la croissance de couches minces de silicium nanostructurées.* PhD thesis, Université d'Orléans, 2001.

[13] M.C. Jouanny. *Etude et contrôle de la phase initiale de formation de poudres nanométriques dans les plasmas froids, basse pression en dilutions argon-silane et hydrogène-silane.* PhD thesis, Université d'Orléans, 2005.

[14] I. Langmuir. Oscillations in ionized gases. *Proceedings of the National Academy of Sciences*, **14**:627, 1928.

[15] CEA (Commisariat à l'Energie Atomique). Qu'est-ce qu'un plasma? 2001.

[16] M. A. Lieberman and A. J. Lichtenberg. *Principles of plasma discharges and materials processing.* John Wiley & sons, Inc., New York, 1994.

[17] R.J. Goldston and P.H. Rutherford. *Introduction to plasma physics.* IOP publishinhg, 1995.

[18] P. K. Shukla and A. A. Mamun. *Introduction to dusty plasmas.* IOP Publishing, 2002.

[19] J.M. Rax. *Physique des plasmas.* Dunod, 2005.

[20] A. M. Pointu, J. Perrin, and J. Jolly. Plasmas froids de décharge : Applications et diagnostic. *Techniques de l'ingénieur*, **D2835**, 1997.

[21] Yu. P. Raizer. *Gas Disharge Physics.* Springer, Berlin, 1991.

[22] A. Bogaerts, E. Neyts, R. Gijbels, and J. van der Mullen. Gas discharge plasmas and their applications. *Spectrochim. Acta Part B*, **57**:609, 2002.

[23] M. Mohamed Salem and J.F. Loiseau. Experiments to sort out theoretical models concerning the area ratio law for plasma reactors. *J. Phys. D: Appl. Phys.*, **29**:1181, 1996.

[24] H.R. Koenig and L.I. Maissel. Application of rf discharges to sputtering. *IBM J. Res. Dev.*, **14**:168, 1970.

[25] S. Maniv. Modelling for rf discharge characteristics. *J. Appl. Phys.*, **63**:1022, 1988.

[26] A.M. Pointu. Modélisation des propriétés électriques de décharges rf diode. *Revue Phys. Appl.*, **24**:257, 1989.

[27] G. Turban. *Interactions Plasmas froids - Matériaux.* Oléron : Ed. de Physique, 1988.

[28] R.M. Roth, K.G. Spears, G.D. Stein, and G. Wong. Spatial dependence of particle ligth scattering in an rf silane discharge. *Appl. Phys. Lett.*, **46**:253, 1985.

[29] Y. Watanabe, M. Shiratani, Y. Kubo, I. Ogawa, and S. Ogi. Effect of low-frequency modulation on rf discharge chemical vapor deposition. *Appl. Phys. Lett.*, **14**:1263, 1988.

[30] A. Bouchoule, A. Plain, L. Boufendi, J. Ph. Blondeau, and C. Laure. Particle generation and behavior in a silane-argon low-pressure discharge under continuous or pulsed radio-frequency excitation. *J. Appl. Phys.*, **70**:1991, 1991.

[31] C. Böhm and J. Perrin. Spatially resolved optical emission and electrical properties of SiH_4 rf discharges at 13.56 MHz in a symmetric parallel-plate configuration. *J. Phys. D: Appl. Phys.*, **24**:865, 1991.

[32] A.A. Howling, Ch. Hollenstein, and P.-J. Paris. Direct visual observation of powder dynamics in rf plasma-assisted deposition. *Appl. Phys. Lett.*, **59**:1409, 1991.

[33] E. Stoffels, W.W. Stoffels, G.M.W. Kroesen, and F.J. de Hoog. Dust formation and charging in an ar/sih4 radio-frequency discharge. *J. Vac. Sci. Technol. A*, **14**:556, 1996.

[34] A. Bouchoule. *Dusty Plasmas: Physics, Chemistry and Technological impacts in Plasma Processing.* Wiley, New York, 1999.

[35] L. Boufendi and A. Bouchoule. Particle nucleation and growth in a low-pressure argon-silane discharge. *Plasma Sources Sci. Technol.*, **3**:262, 1994.

[36] K. Koga, Y. Matsuoka, K. Tanaka, M. Shiratani, and Y. Watanabe. In situ observation of nucleation and subsequent growth of clusters in silane radio frequency discharges. *Appl. Phys. Lett.*, **77**:196, 2000.

[37] Ch. Hollenstein, W. Schwarzenbach, A.A. Howling, C. Courteil, J.L. Dorier, and L. Sansonnens. Anionic clusters in dusty hydrocarbon and silane plasmas. *J. Vac. Sci. Technol. A*, **14**:535, 1996.

[38] A. A. Fridman, L. Boufendi, T. Hbid, B. V. Potapkin, and A. Bouchoule. Dusty plasma formation: Physics and critical phenomena. Theoretical approach. *J. Appl. Phys.*, **79**:1303, 1996.

[39] G. Viera, M. Mikikian, E. Bertran, P. Roca i Cabarrocas, and L. Boufendi. Atomic structure of the nanocrystalline Si particles appearing in nanostructured Si thin films produced in low-temperature radiofrequency plasmas. *J. Appl. Phys.*, **92**:4684, 2002.

[40] A. Bouchoule, L. Boufendi, J. Hermann, A. Plain, T. Hbid, G. Kroesen, and E. and W.W. Stoffels. Formation of dense submicronic clouds in low pressure Ar-SiH_4 reactor: Diagnostics and growth processes from monomers to large size particulates. *Pure and Appl. Chem.*, **68**:1121, 1996.

[41] S.-H. Hong and J. Winter. Size dependence of optical properties and internal structure of plasma grown carbonaceous nanoparticles studied by in situ Rayleigh-Mie scattering ellipsometry. *J. Appl. Phys.*, **100**:4303, September 2006.

[42] L. Boufendi, A. Bouchoule, and T. Hbid. Electrical characterization and modelling of a dust forming plasma in a radio frequency discharge. *J. Vac. Sci. Technol. A*, **14**:572, 1996.

[43] T. Matsoukas and M. Russell. Particle charging in low-pressure plasmas. *J. Appl. Phys.*, 77:4285, 1995.

[44] J. E. Daugherty, R. K. Porteous, and D. B. Graves. Electrostatic forces on small particles in low-pressure discharges. *J. Appl. Phys.*, **73**:1617, 1993.

[45] S. Hamaguchi and R. T. Farouki. Polarization force on a charged particulate in a nonuniform plasma. *Phys. Rev. E*, **49**:4430, 1994.

[46] L. Talbot, R. K. Cheng, R. W. Schefer, and D. R. Willis. Thermophoresis of particles in a heated boundary layer. *J. Fluid Mech.*, **101**:737, 1980.

[47] H. Rothermel, T. Hagl, G. E. Morfill, M. H. Thoma, and H.M. Thomas. Gravity compensation in complex plasmas by application of a temperature gradient. *Phys. Rev. Lett.*, **89**:175001, 2002.

[48] M. S. Barnes, J. H. Keller, J. C. Forster, J. A. O'neill, and D. K. Coultas. Transport of dust particles in glow-discharge plasmas. *Physi. Rev. Lett.*, **68**:313, 1992.

[49] S.A. Khrapak, A. V. Ivlev, G. E. Morfill, and H. M. Thomas. Ion drag force in a complex plasma. *Phys. Rev. E*, **66**:046414, 2002.

[50] M. Mikikian, L. Boufendi, A. Bouchoule, H. M. Thomas, G. E. Morfill, A. P. Nefedov, V. E. Fortov, and the PKE-Nefedov team. Formation and behaviour of dust particle clouds in a radio-frequency discharge: results in the laboratory and under microgravity conditions. *New J. Phys.*, **5**:19, 2003.

[51] J. Goree, G. E. Morfill, V. N. Tsytovich, , and S. V. Vladimirov. Theory of dust voids in plasmas. *Phys. Rev. E*, **59**(6):7055, 1999.

[52] V. N. Tsytovich. Evolution of voids in dusty plasmas. *Phys. Scripta*, **T89**:89, 2001.

[53] V. N. Tsytovich, S. V. Vladimirov, and G. E. Morfill. Theory of dust and dust-void structures in the presence of the ion diffusion. *Phys. Rev. E*, **70**:066408, 2004.

[54] A.A. Mamun, P.K. Shukla, and R. Bingham. Plasma voids (holes) in a dusty plasma. *Phys. Lett. A*, **298**:179, 2002.

[55] G. Praburam and J. Goree. Experimental observation of very low-frequency macroscopic modes in a dusty plasma. *Phys. Plasmas*, **3**:1212, 1996.

[56] D. Samsonov and J. Goree. Instabilities in a dusty plasma with ion drag and ionization. *Phys. Rev. E*, **59**:1047, 1999.

[57] M. Mikikian and L. Boufendi. Experimental investigations of void dynamics in a dusty discharge. *Phys. Plasmas*, **11**(8):3733, 2004.

[58] L. Boufendi, A. Bouchoule, R.K. Porteous, J.Ph. Blondeau, A. Plain, and C. Laure. Particle-particle interactions in dusty plasmas. *J. Appl. Phys.*, **73**:2160, 1993.

[59] Air Liquide. Fiche de données de sécurité du silane. 2002.

[60] G.E. Morfill, H.M. Thomas, U. Konopka, H. Rothermel, M. Zuzic, A. Ivlev, and J. Goree. Condensed plasmas under microgravity. *Phys. Rev. Lett.*, **83**:1598, 1999.

[61] M. Klick. Non linearity in the radio-frequency sheath. *J. Appl. Phys.*, **79**:3445, 1996.

[62] P. F. Combe and D. R. Crampagne. Circuits passifs hyperfréquences : Filtres et cavités. *Techniques de l'ingénieur*, **EAB1402**, 2002.

[63] P. F. Combe and D. R. Crampagne. Circuits passifs hyperfréquences : Guides d'ondes métalliques. *Techniques de l'ingénieur*, **EAB1401**, 2002.

[64] R. Papoular and J. Balazard. *Applications des ondes hyperfréquences et infrarouges à l'étude des plasmas.* Dunod, (1965).

[65] M. Haverlag, G.M.W. Kroesen, T.H.J. Bisschops, and F.J. de Hoog. Measurement of electron densities by a microwave cavity method in 13.56 MHz RF plasmas of Ar, CF_4, C_2F_6 and CHF_3. *Plasma Chem. and Plasma Process.*, **11**:357, 1991.

[66] G. Videen and W.S. Bickel. Light-scattering resonances in small spheres. *Phys. Rev. A*, **45**:6008, 1992.

[67] A. Renoux and D. Boulaud. Physique des aérosols - partie 2. *Techniques de l'ingénieur*, **AF3613**, 2003.

[68] J. P. Eberhart. *Analyse structurale et chimique des matériaux*. Dunod, 1997.

[69] C. Le Gressus. Microscopie électronique à balayage. *Techniques de l'ingénieur*, **PE865**, 1995.

[70] G. Coulon. Imagerie de surface de polymères : microscopie à force atomique. *Techniques de l'ingénieur*, **AM3280**, 2000.

[71] F. Salvan and F. Thibaudau. Microscopie à sonde locale. *Techniques de l'ingénieur*, **P895**, 1999.

[72] M. Mikikian, M. Cavarroc, N. Chaumeix, and L. Boufendi. Instabilities in a dense cloud of grown dust particles. *31th EPS conference on controlled fusion and plasma physics*, ECA Vol.**28B**:O–2.13, 2004.

[73] W.L. Nighan and W.J. Wiegand. Influence of negative-ion processes on steady-state properties and striations in molecular gas discharges. *Phys. Rev. A*, **10**:922, 1974.

[74] A. Descoeudres, L. Sansonnens, and Ch. Hollenstein. Attachment-induced ionization instability in electronegative capacitive RF discharges. *Plasma Sources Sci. Technol.*, **12**:152, 2003.

[75] M. Cavarroc, M. C. Jouanny, K. Radouane, M. Mikikian, and L. Boufendi. Self-excited instability occurring during the nanoparticle formation in an ar-sih4 low pressure radio frequency plasma. *J. Appl. Phys.*, **99**:064301, 2006.

[76] M. Cavarroc, M. Mikikian, G. Perrier, and L. Boufendi. Single-crystal silicon nanoparticles: An instability to check their synthesis. *Appl. Phys. Lett.*, **89**:013107, 2006.

[77] A Bouchoule and L Boufendi. High concentration effects in dusty plasmas. *Plasma Sources Sci. Technol.*, **3**:292, 1994.

[78] U. Bhandarkar, U. Kortshagen, and S. L. Girshik. Numerical study of the effect of gas temperature on the time for the onset of particle nucleation in argon-silane low-pressure plasmas. *J. Phys. D : Appl. Phys.*, **36**:1399, 2003.

[79] J. Perrin, O. Leroy, and M.C. Bordage. Cross-sections, rate constants and transport coefficients in silane plasma chemistry. *Contrib. plasma phys.*, **36**:3, 1996.

[80] J. Perrin, C. Böhm, R. Etemadi, and A. Lloret. Possible routes for cluster growth and particle formation in RF silane discharges. *Plasma Sources Sci. Technol.*, **3**:252, 1994.

[81] L. Boufendi and A. Bouchoule. Industrial developpements of scientific insights in dusty plasmas. *Plasma Sources Sci. Technol.*, **11**:A211, 2002.

[82] F. Vivet, A. Bouchoule, and L. Boufendi. Synthesis and characterization of SiC:H ultrafine powder generated in an argon/silane/methane low-pressure radio-frequency discharge. *J. Appl. Phys.*, **83**:7474, 1998.

[83] M. Mikikian, M. Cavarroc, L. Couëdel, and L. Boufendi. Low frequency instabilities during dust particle growth in a dusty plasma. *Phys. Plasmas*, **13**:092103, 2006.

[84] M. Mikikian, L. Couëdel, M. Cavaaroc, Y. Tessier, and L. Boufendi. Self-excited void instability in dusty plasmas: Plasma and dust cloud dynamics during the heartbeat instability. *New J. Phys.*, 9:268, 2007.

[85] M. Cavarroc, M. Mikikian, Y. Tessier, and L. Boufendi. Dust successive generations in complex plasmas: A cyclic phenomenon in the void region. *Phys. Rev. Lett.*, Submitted, 2007.

[86] A. Melzer, A. Homann, A. Piel, V. A. Schweigert, and I. V. Schweigert. Very Low Frequency Void Instability in Silane Discharge. *AIP Conference Proceedings*, 446:168, 1998.

[87] J.L. Dorier, Ch. Hollenstein, and A.A. Howling. Spartiotemporal powder formation and trapping in radio frequency silane plasmas using two-dimensional polarization-sensitive laser scattering. *J. Vac. Sci. Technol. A*, **13**:918, 1995.

[88] J.C. Schauer, S. Hong, and J. Winter. Electrical measurements in dusty plasmas as a detection method for the early phase of particle formation. *Plasma Sources Sci. Technol.*, **13**:636, 2004.

[89] J. Goree, R.A. Quinn, G. Morfill, H. Thomas, T. Hagl, U. Kopoka, and H. Rothermel ad M. Zuzic. Plasma dust crystallization. In *Proceedings of the 4th Microgravity Fluid Physics and Transport Phenomena Conference*, Cleveland, 1999.

[90] M. Mikikian, M. Cavarroc, N. Chaumeix, and L. Boufendi. Instabilities of the void region in a dense cloud of grown dust particles. *AIP Conference Proceedings*, **799**:323, 2005.

[91] G. Cernogora and C. Szopa. Private communication. 2006.

[92] B. T. Draine. Interstellar Dust Grains. *Annual Review of Astronomy & Astrophysics*, **41**:241, 2003.

[93] M. Fulchignoni, F. Ferri, F. Angrilli, A.J. Ball, A. Bar-Nun, M.A Barucci, C. Bettanini, G. Bianchini, W. Borucki, G. Colombatti, M. Coradini, A. Coustenis, S. Debei, P. Falkner, G. Fanti, E. Flamini, V. Gaborit, R. Grard, M. Hamelin, A.M. Harri, B. Hathi, I. Jernej, M.R. Leese, A. Lehto, P.F. Lion Stoppato, J.J. Lopez-Moreno, T. Mäkinen, J.A.M. McDonnell, C.P. McKay, G. Molina-Cuberos, F.M. Neubauer, V. Pirronello, R. Rodrigo, B. Saggin, K. Schwingenschuh, A. Seiff, F. Simoes, H. Svedhem, T. Tokano, M.C. Towner, R. Trautner, P. Withers, and J.C. Zarnecki. *In situ* measurements of the physical characteristics of Titan's environment. *Nature*, **438**:785, 2005.

[94] J.P. Lebreton, O. Witasse, C. Sollazzo, T. Blancquaert, P. Couzin, A.M. Schipper, J.B. Jones, D.L. Matson, L.I. Gurvits, D.H. Atkinson, B. Kazeminejad, and M. Pérez-Ayùcar. An overview of the descent and landing of the Huygens probe on Titan. *Nature*, **438**:758, 2005.

[95] H.B. Niemann, S.K. Atreya, S.J. Bauer, G.R. Carignan, J.E. Demick, R.L. Frost, D. Gautier, J.A. Haberman, D.N. Harpold, D.M. Hunten, G. Israel, J.I. Lunine, W.T. Kasprzak, T.C. Owen, M. Paulkovich, F. Raulin, E. Raaen, and S.H. Way. The abundances of constituents of Titan's atmosphere from the GCMS instrument on the Huygens probe. *Nature*, **438**:779, 2005.

[96] M. G. Tomasko, B. Archinal, T. Becker, B. Bézard, M. Bushroe, M. Combes, D. Cook, A. Coustenis, C. de Bergh, L. E. Dafoe, L. Doose, S. Douté, A. Eibl, S. Engel, F. Gliem, B. Grieger, K. Holso, E. Howington-Kraus, E. Karkoschka, H. U. Keller, R. Kirk, R. Kramm, M. Küppers, P. Lanagan, E. Lellouch, M. Lemmon, J. Lunine, E. McFarlane, J. Moores, G. M. Prout, B. Rizk, M. Rosiek, P. Rueffer, S. E. Schröder, B. Schmitt, C. See, P. Smith, L. Soderblom, N. Thomas, and R. West. Rain, winds and haze during the Huygens probe's descent to Titan's surface. *Nature*, **438**:765, 2005.

[97] C. Sagan and W. R. Thompson. Production and condensation of organic gases in the atmosphere of Titan. *Icarus*, **59**:133, August 1984.

[98] E. L. O. Bakes, C. P. McKay, and C. W. Bauschlicher. Photoelectric Charging of Submicron Aerosols and Macromolecules in the Titan Haze. *Icarus*, **157**:464, June 2002.

[99] S. Hong, J. Berndt, and J. Winter. Growth precursors and dynamics of dust particle formation in the Ar/CH_4 and Ar/C_2H_2 plasmas. *Plasma Sources Sci. Technol.*, **12**:46, 2003.

[100] A. Mezeghrane. Private communication. 2007.

[101] G. H. P. M. Swinkels. *Optical studies of micron-sized particles immersed in a plasma.* PhD thesis, Technische Universiteit Eindhoven, 1999.

[102] G. Gebauer. *In-situ-Nano-Partikel-Diagnostik im Plasma durch Mie-Ellipsometrie.* PhD thesis, Ruhr Universität Bochum, 2002.

[103] S.Hong. *From thin films to nanoparticles: Investigation of polymerization processes in capacitively coupled hydrocarbon plasmas.* PhD thesis, Ruhr-Universität Bochum, 2004.

[104] S.Hong and J.Winter. Size dependence of optical properties and internal structure of plasma grown carbonaceous nanoparticles studied by in situ Rayleigh-Mie scattering ellipsometry. *J. Appl. Phys.*, **100**:064303, 2006.

[105] W. J. Wiscombe. Improved Mie scattering algorithms. *Applied Optics*, **19**:1505, 1980.

[106] S. Hong, J. Berndt, and J. Winter. In-situ study of dust particle formation in Ar/CH_4 and Ar/C_2H_2 mixtures. *Surface and Coatings Technology*, **174-175**:754, 2003.

[107] G. Gebauer and J. Winter. In situ nanoparticle diagnostics by multi-wavelength Rayleigh-Mie scattering ellipsometry. *New J. Phys.*, **5**:38, April 2003.

[108] S.-H. Hong and J. Winter. Micro-Raman spectroscopy on a-C:H nanoparticles. *J. Appl. Phys.*, **98**:4304, December 2005.

[109] S.H.Hong. Private communication. 2006.

[110] W.D. King, D.L. Boxall, and C.M. Lukehart. Nanoclusters of silicon and germanium. *Journal of Cluster Science*, **8**:267, 1997.

[111] A. Hadjadj, A. Beorchia, P. Roca i Cabarrocas, L. Boufendi, S. Huet, and J.L. Bubendorff. Effects of the substrate temperature on the growth and properties of hydrogenated nanostructured silicon thin films. *J. Phys. D: Appl. Phys.*, **34**:690, 2001.

[112] L. Boufendi. Private communication.

[113] M. Moncel. Méthodes physiques d'analyse en métallurgie. *Techniques de l'ingénieur*, **MB5**:M260, 1991.

[114] N. Broll. Caractérisation de solides cristallisés par diffraction X. *Techniques de l'ingénieur*, **TA1**:P1080, 1996.

[115] S.H. Tolbert, A.B. Herhold, L.E. Brus, and A.P. Alivisatos. Pressure-induced structural transformations in Si nanocrystals: Surface and shape effects. *Phys. Rev. Lett.*, **76**:4384, 1996.

[116] P. Roca i Cabarrocas, S. Hamma, S.N. Sharma, G. Viera, E. Bertran, and J. Costa. Nanoparticle formation in low-pressure silane plasmas: bridging the gap between a-Si:H and μ-Si films. *J. Non-Cryst. Solids*, **227-230**:871, 1998.

[117] H. Vach and Q. Brulin. Controlled growth of silicon nanocrystals in a plasma reactor. *Phys. Rev. Lett.*, **95**:165502, 2005.

[118] B.J. Anderson and J. Hallett. Supersaturation and time dependence of ice nucleation from the vapor on single crystal substrates. *J. Atmos. Sci.*, **33**:823, 1976.

[119] B.T. Draine. Time-dependent nucleation theory and the formation of interstellar grains. *Astrophys. Space Sci.*, **65**:313, 1979.

[120] J.W.P. Schmelzer and J. Schmelzer Jr. Kinetics of nucleation at increasing supersaturation. *J. Colloid Interface Sci.*, **215**:345, 1999.

[121] S. Auer and D. Frenkel. Prediction of absolute crystal-nucleation rate in hard-sphere colloids. *Nature*, **409**:1020, 2001.

[122] P. Peeters, J.J.H. Gielis, and M.E.H. van Dongen. The nucleation behavior of supercooled water vapor in helium. *J. Chem. Phys.*, **117**:5647, 2002.

[123] J.W.P. Schmelzer. Kinetic and thermodynamic theories of nucleation. *Mater. Phys. Mech.*, **6**:21, 2003.

List of symbols, constants and abbreviations

Constants

c	light velocity (299792458 $m.s^{-1}$)	64
h	Planck constant ($6.6260755.10^{-34}$ $J.s^{-1}$ = $4.135669.10^{-15}eV.s^{-1}$)	66
π	3.1415926....	25
ϵ_0	permittivity of vacuum ($8.85419.10^{-12}$ $F.m^{-1}$)	26
e	elementary charge ($1.6.10^{-19}$ C)	26
k_B	Boltzmann constant ($1.380658.10^{-23}$ $J.K^{-1}$)	25

Chemistry notations

Ar	Argon	32
Ar^*	Argon excited state	33
Ar^+	Argon ion	33
CH_4	Methane	142
C_2H_2	Acetylene	144
H_2	Hydrogen	142
H_20	Water	142
He	Helium	52
N_2	Nitrogen	50
N_2^+	Nitrogen ion	144
Ne	Neon	52
O_2	Oxygen	142
Si	Silicon	169
SiH_4	Silane	31
SiH_3^-	Silicon hydrid anion	31
SiO_2	Silicon oxyde	55
a-Si:H	amorphous hydrogenated silicon	34
a-Si	amorphous silicon	178

Symbols

α	normalized Fourier coefficient	152
α_i	ionization degree	25
α_{th}	corrective coefficient for thermophoresis	39
β	normalized Fourier coefficient	152
β_p	peak width on the spectrum	174
Δ	ellipsometric angle	150
$\Delta\mu$	difference of chemical potential per particle	180
ϵ_r	permittivity of the plasma	63
κ_T	gas thermal conductivity	39
λ	wavelength	58
λ_D	Debye length	26
λ_{De}	electron Debye length	26
λ_{Di}	ion Debye length	26
λ_{DL}	linearized Debye length	26
μ	reduced mass	40
μ_r	dielectric permeability	64
ν	emitted photon wavelength	66
ν_e	electron collision frequency	64
ω	pulsation	64
ω_0	pulsation of the microwave caviti (vacuum)	64
ω_p	plasma pulsation	27
ω_{pe}	electron plasma pulsation	27
ω_{pi}	ion plasma pulsation	27
ω_{pd}	dust plasma pulsation	32
Ω	complex pulsation of the microwave cavity	63
ϕ	azimutal angle	65
Ψ	ellipsometric angle	150
ρ	silicon mass density (ρ = 2330 kg.m^{-3})	38
θ	scattering angle	69
θ_d	diffraction angle	174
σ	surface or interfacial tension of the cluster	180
σ_{coll}	collection cross section	40
σ_{coul}	momentum cross section	40
a	constant	152
a_n	Mie scattering coefficient (n = 1,2,3...)	69
A	corrective factor for the electron density in the microwave cavity calculation	64
A_c	cluster surface area	180
A_{driven}	driven electrode surface area	30
A_e	analyzer azimuth with respect to the incidence plane	153
$A_{grounded}$	grounded electrode surface area	30
b	constant	152
b_{coll}	collection parameter	40
$b_{\pi/2}$	collection parameter giving a $\pi/2$ deviation	40

b_n	Mie scattering coefficient (n = 1,2,3...)	69
b_α	cluster concentration	180
C_B	cut-off varying capacitor	53
C_C	off setting varying capacitor	53
C_e	compensator azimuth with respect to the incidence plane	154
C_F	capacitor	53
C_s	sheath capacitance	28
d	intergrain distance	36
$\vec{e}_r$	r direction	68
$\vec{e}_y$	y direction	68
$\vec{e}_z$	z direction	69
$\vec{E}_0$	electric field	38
$\vec{E}$	electric field in the microwave cavity	63
E'	energy level	66
E"	energy level	66
$E_{detector}$	electric field at the detector	153
$E_{dissociation}$	dissociation energy of N_2	143
$E_{incident}$	incident electric field	153
$\vec{E}_{i\perp}$	incident field: component perpendicular to the scattering plane	68
$\vec{E}_{i//}$	incident field: component parallel to the scattering plane	68
$\vec{E}_{s\perp}$	scattered field: component perpendicular to the scattering plane	68
$\vec{E}_{s//}$	scattered field: component parallel to the scattering plane	68
E_x	$\vec{E}$ component on the x-axis	65
E_y	$\vec{E}$ component on the y-axis	65
E_z	$\vec{E}$ component on the z-axis	65
f_j	velocity distribution function for the species j	25
f_0	resonance frequency of the microwave cavity (vacuum)	63
f_{pd}	dust plasma frequency	88
f_{pe}	electron plasma frequency	27
f_{pi}	ion plasma frequency	27
f_r	resonance frequency of the microwave cavity (plasma)	63
F_{coll}	collection force	40
F_{coul}	Coulomb force	40
$\vec{F}_e$	electrostatic force	38
$\vec{F}_g$	gravitational force	38
F_i	ion drag force	41
$\vec{F}_n$	neutral drag force	39
$\vec{F}_{th}$	thermophoretic force	39
$\vec{g}$	gravitational field (g = 9.8 m.s^{-2})	38
G	thermodynamic potential	180
i	current collected by the Langmuir probe	62
i_{is}	ion saturation current of the Langmuir probe	63
I_0	incident intensity	70
I_{3371}	intensity of the N_2 line at 337.1 nm	145

$I_{750.38}$	intensity of the Ar line at 750.38 nm	107
I_d	scattered intensity	70
$I_{detector}$	light intensity at the detector	153
I_e	electron current	36
I_i	ion current	36
I_k	currents on the grain	36
I_p	current on the probe	59
I_{rf}	radio frequency current	28
J	crystal nucleation rate	180
J_0	kinetic factor	180
J_1	first-order Bessel function	65
J(x)	first-order Bessel function	69
k	field wave vector	63
k_a	attachment coefficient	96
k_i	ionization coefficient	96
k_s	wave vector of the scatered field	68
K	shape factor	174
l	sheath length	37
L	coil	53
L_c	crystallite size	174
m	optical index	69
m_d	mass of the dust particle	32
m_e	mass of the electron	27
m_i	mass of the ion	27
m_j	mass of the species j	25
m_n	mass of the neutral	39
m_p	mass of the particle	27
n	refraction index	64
n-	negative ion density	25
n_α	number of particles in the cluster	180
n_e	electron density	21
n_{e0}	electron density in the center of the discharge	65
n_i	ion density	21
n_j	density of the species j	25
n_n	neutral density	25
n_p	particle density	27
N	number of diffusing dust particles	70
N_d	dust particle density	32
p	impact parameter	40
P	pressure	55
P_e	input polarizer azimuth with respect to the incidence plane	152
P_n^1	n^{th} Legendre's polynome	69
P_n	phases of the DPGI, n = 1 to 7	127
P_{rf}	injected rf power	55

q_-	negative ion charge	25
q_e	electron charge (-1.6.10^{-19} C)	25
q_i	positive ion charge	25
q_p	particle charge	27
Q	quality factor of the microwave cavity (plasma)	64
Q_0	quality factor of the microwave cavity (vacuum)	64
Q_d	dust particle charge	32
Q_{Ar}	Argon flow rate	55
Q_{SiH_4}	Silane flow rate	55
r	radius / radial coordinate	26
r_c	critical cluster radius	180
r_d	dust particle radius	32
R_1	lower limit of the nonlinear growth	156
R_2	upper limit of the nonlinear growth	156
R_p	parallel reflection coefficient	150
R_s	perpendicular reflection coefficient	150
S	surface area of the Langmuir probe	68
S	monomer supersaturation ratio	180
S_1	first term of the Stokes'matrix	69
S_2	second term of the Stokes'matrix	69
S_3	third term of the Stokes'matrix	69
S_4	fourth term of the Stokes'matrix	69
$T_{attente}$	time between two cycles	56
T_e	electron temperature	21
T_g	gas temperature	21
T_i	ion temperature	21
$T_{inflamation}$	Silane inflamation temperature	52
T_{limit}	lower temperature of nanocrystal formation	177
T_j	temperature of the species j	25
T_n	neutral temperature	25
T_{off}	time the discharge is off	55
T_{on}	time the discharge is on	55
$\vec{u}_d$	dust particle velocity	39
$\vec{u}_n$	neutral velocity	39
v_i	ion velocity	39
$v_{th,n}$	neutral thermal mean velocity	40
V_{dc}	self-bias voltage	29
V_{driven}	driven electrode potential	29
V_f	plasma floating potential	62
$V_{grounded}$	grounded electrode potential	29
V_i	ion flux measurement	82
V_{out}	probe output voltage	59
V_p	plasma potential	29
V_{polar}	potential applied to the Langmuir probe	62

V_{rf}	radio frequency voltage	27
w_j	velocity of the species j	25
Y(x)	second-order Bessel function	69
z	height / axial coordinate	59
Z_T	probe transfer impedance	59

Abbreviations

1H	first harmonic of the discharge current	82
3H	third harmonic of the discharge current	49
cc	capacitively coupled	29
dc	direct current	143
icp	inductively coupled plasma	143
fps	frame per second	58
rf	radio frequency	27
AFM	Atomic Force Microscopy	55
CCD	Charge Couple Device	58
DPGI	Dust Particle Growth Instabilities	103
ESA	European Space Agency	140
FCC	Face Centered Cubic	87
FFT	Fast Fourier Transform	82
GCMS	Gas Chromatograph Mass Spectrometer	142
GEC	Gaseous Electronic Conference	108
GREMI	Groupe de Recherche sur l'Energetique des Milieux Ionisés	49
ISD	InterStellar Dust	139
ISS	International Space Station	42
IR	Infra Red	50
ITER	International Thermonuclear Experimental Reactor	21
LIPEE	Laser Induced Particle Explosive Evaporation	34
LLS	Laser Light Scattering	70
MF	Melamine Formaldehyde	31
NASA	National Aeronautics and Space Administration	140
OES	Optical Emission Spectroscopy	66
OML	Orbital Motion Limited	36
PAMPRE	Production d'Aérosols en Microgravité par Plasma REactif	49
PKE	Plasma Kristall Experiment	49
RAE	Rotating Analyzer Ellipsometer	152
RCE	Rotating Compensator Ellipsometer	154
RT	Room Temperature	54
SEM	Scanning Electron Microscopy	55
SGI	Successive Generation Instability	103
SR-OER	Spatialy Resolved Optical Emission Recording	121
TEM	Transmission Electron Microscopy	55

TM	Transverse Magnetic	65
UV	UltraViolet	50

Published articles

- M. Cavarroc, M.C. Jouanny, K. Radouane, M. Mikikian and L. Boufendi
  Self-excited instability occuring during the nanparticle formation in an Ar-SiH_4 low-pressure radio-frequency plasma
  J. Appl. Phys. **99**, 064301 (2006)

- M. Cavarroc, M. Mikikian, G. Perrier and L. Boufendi
  Single-crystal silicon particles: An instability to check their synthesis
  Appl. Phys. Lett. **89**, 013107 (2006)

- M. Mikikian, M. Cavarroc, L. Couëdel and L. Boufendi
  Low frequency instabilities during dust particle growth in a radio-frequency plasma
  Phys. Plasmas **13**, 092103 (2006)

- M. Mikikian, L. Couëdel, M. Cavarroc, Y. Tessier and L. Boufendi
  Self-excited void instability in dusty plasmas: plasma and dust cloud dynamics during the heartbeat instability
  New J. Phys. **9**, 267 (2007)

Self-excited instability occurring during the nanoparticle formation in an Ar–SiH_4 low pressure radio frequency plasma

M. Cavarroc,[a] M. C. Jouanny, K. Radouane, M. Mikikian, and L. Boufendi
GREMI-Polytech'Orléans, 14 Rue d'Issoudun, BP 6744, 45067 Orléans cedex 2, France

(Received 12 July 2005; accepted 3 February 2006; published online 17 March 2006)

An experimental investigation of an instability occurring during dust nanoparticle formation is presented in this paper. The present study has been performed in radio frequency low pressure plasma in an argon-silane mixture. The formation and growth of nanoparticles is followed, thanks to the analysis of the amplitude of the third harmonics (40.68 MHz) of the discharge current and the self-bias voltage (V_{dc}). In some cases, at the end of the accumulation phase of the nanocrystallites an instability occurs. It seems to be an attachment induced ionization instability as observed in electronegative plasmas. A detailed study of the influence of different operating conditions (injected power, gas temperature, and silane flow rate) on this instability behavior and frequencies is presented. The paper concludes by examining a very particular case of the instability. © *2006 American Institute of Physics*. [DOI: 10.1063/1.2179973]

I. INTRODUCTION

In the past few years, there has been an increasing interest in dusty plasmas generated in radio frequency (rf) discharges, and now represents one of the most rapidly growing branch of plasma physics. The range of interest spreads over both industrial plasma processing systems[1] and astrophysical plasma environments. Besides, an active research into particle formation and behavior has been induced by contamination phenomena in industrial plasma reactors used for etching, sputtering, and plasma enhanced chemical vapor deposition (PECVD). In the laboratory, two main ways are used to grow particles in rf low pressure discharges: reactive gases such as silane (SiH_4) and target sputtering by ion bombardment. In both cases a dense cloud of submicron particles is formed, tending to fill in the whole interelectrode gap.

Many theoretical[2,3] and experimental[4,5] studies have dealt with the detection and dynamics of particles in silane mixture discharge. In particular, Boufendi *et al.*[6] have clearly brought to the fore the way particles grow in the discharge from initial nanocrystallites (smaller than 5 nm). Presently, many studies are being carried out on nanometer size particles generated in PECVD processes, especially in the field of polymorphous silicon (pm-Si:H) deposition recently used to manufacture solar cells.[7] This material consists of nanometer size silicon crystallites embedded in a hydrogenated amorphous silicon matrix[8–10] and shows improved transport properties and stability with respect to hydrogenated amorphous silicon. Moreover, some instabilities induced by the presence of dust particles in plasma have been reported for ten years now.[11–14] All these instabilities have been observed in particle clouds due to sputtering or particle injection. However, the instability we report in this paper, occurring in the earlier phase of the particle formation, seems to be comparable to those already reported. The phenomenon is followed through its influence on the discharge characteristics. The electrical diagnostic used in this work has been developed in the GREMI laboratory. It allows us to follow the time evolution of the amplitude of the third harmonics (3H) of the discharge current and the amplitude of the self-bias voltage (V_{dc}). This diagnostic has been shown to be able to follow the particle formation and growth in different chemistries such as silane or methane.[15]

The main objective of this paper is to present our observations concerning a self-excited instability during the particle formation and growth in a silane based plasma. The effects of different parameters on this instability are also reported.

II. EXPERIMENTAL SETUP

The experimental setup used to carry out the plasma analysis has already been described in detail in previous papers.[5,16,17] The rf discharge is produced in a grounded cylindrical plasma box (13 cm inner diameter and 3.3 cm for interelectrode distance). The discharge structure is surrounded by a cylindrical oven. The whole system is enclosed in a vacuum chamber. The upper electrode (driven electrode) is a shower-head one in order to ensure a homogenous gas distribution at the entrance of the plasma zone. This electrode is connected to a 13.56 MHz radio frequency generator through a matchbox including a blocking capacitor. The power can be varied from 0 up to 20 W. The gas temperature is controlled from room temperature up to 150 °C and is measured in the gas flow just below the plasma box by a thermocouple. The current and voltage probes are inserted between the matchbox and the powered electrode. The curves are visualized on a LeCroy scope LT364L (500 MHz bandwidth and 1 GS/s) and the results are collected via a computer.

In this work, certain measurement conditions were kept constant in most cases: the argon flow rate remains 30 SCCM (SCCM denotes cubic centimeter per minute at STP) and the total pressure is always around 12 Pa. The reference for injected power was 10 W corresponding to

[a]Electronic mail: marjorie.cavarroc@univ-orleans.fr

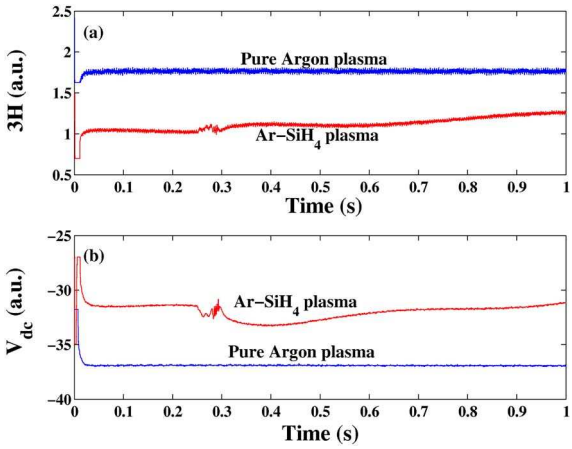

FIG. 1. (Color online) Time evolution of the third harmonics and the self-bias voltage (a) in pure argon and (b) in argon-silane plasmas under standard conditions.

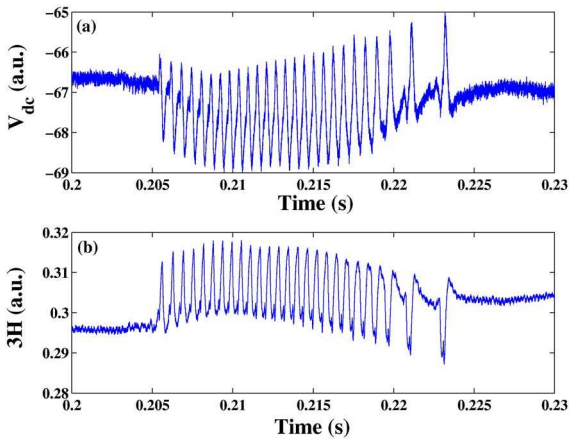

FIG. 2. (Color online) Time evolution of the instability (a) on the self-bias voltage and (b) on the third harmonics of the discharge current.

about 400 V peak to peak. The adjustment is fixed at optimal steady state conditions in argon. The current probe measures the amplitude of the 3H of the total current and the voltage probe gives the self-bias voltage (V_{dc}).

III. RESULTS AND DISCUSSION

In previous experimental and theoretical works,[4,18,19] it has been shown that particle formation in $Ar-SiH_4$ low pressure plasma is a four step process. These steps are now clearly identified: growth of the nanocrystallites (2–3 nm) from molecular species, accumulation phase, fast coagulation, and growth by deposition of the plasma species on the particle surface. The growth of particles in the discharge leads to considerable modifications in the plasma characteristics. Indeed the presence of charged dust grains affects many of the physical properties of the plasma (electron density, temperature, electrical field, impedance, etc.). The modification of the plasma impedance due to particle formation and growth led us to develop a diagnostic based on the measurements of the amplitude of V_{dc} and 3H. Thus, in a pure argon plasma, their amplitude remains constant in time as shown in Fig. 1(a). When silane is added to the the mixture, i.e., in a dust forming plasma, V_{dc} and 3H show a time evolution due to the formation and growth of dusts in the discharge [see Fig. 1(b)]. These electrical measurements are a good diagnostic to control the particle occurrence in the plasma and hence the reactor contamination. All the following observations have been performed using electrical measurements, with different operating conditions.

A. Instability

In most of our experimental conditions, we observed that an instability appears between the end of the accumulation phase and the beginning of the coalescence both on 3H and V_{dc} curves (see Fig. 1). The typical behavior of the self-bias voltage and the third harmonics of the discharge current in this region is shown on Fig. 2 (for $P_{rf}=6$ W and $Q_{SiH_4}=0.8$ SCCM). The frequency of this signal, given by a fast Fourier transform (FFT) analysis, is shown on Fig. 3 and evolves during the instability. We can first observe an increase of the frequency that could correspond to the formation of the instability. Once the instability is established, the frequency decreases until the end of the phase where it becomes difficult to define the frequency. In the following, we will present some results about the frequency at the beginning and at the end of the instability. Those two frequencies are not measured in the same way. The frequency at the beginning is the average value of the frequency taken on the six first periods, whereas the frequency at the end is given by the last value of the FFT, with an uncertainty range due to the software used to compute the data.

It is known that during the coalescence phase, the particle density decreases while the particle radius and mass increase because of the coalescence of the nanocrystallites. Scanning electron microscopy (SEM) analyses of nanoparticles deposited at three different times: just before, at the beginning and in the middle of the instability, have been performed. Just before the instability, only nanocrystallites are observed (around 2 nm). At the beginning and in the middle of the instability, there are both nanocrystallites and small aggregates. These results confirm that the beginning of the instability corresponds to the beginning of the coalescence phase. Therefore, during the instability, there is an increase in the mean mass of dust particles. The increase of the particle mass could explain the decrease of the instability

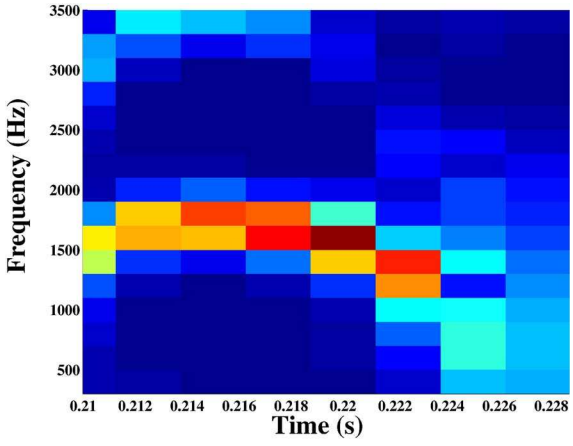

FIG. 3. (Color online) Time evolution of the frequency of the instability.

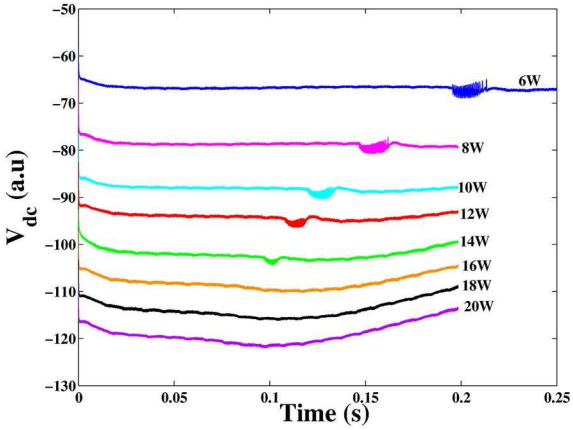

FIG. 4. (Color online) Time evolution of the self-bias voltage vs the injected power.

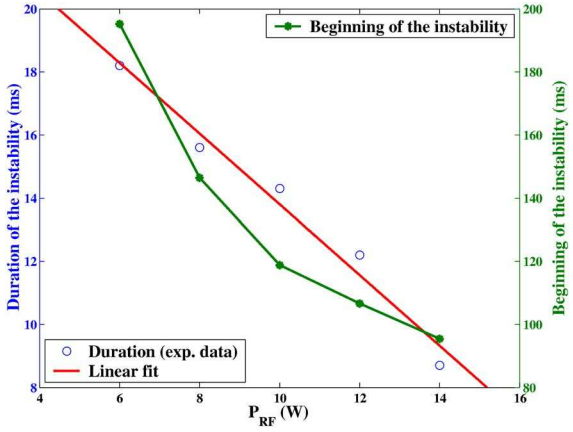

FIG. 5. (Color online) Beginning and duration of the instability as a function of the injected power.

frequency since when a plasma is instantaneously disturbed from its equilibrium, collective motions appear. They are characterized by a frequency of oscillations called the plasma frequency ω_p. This frequency is not the same for electrons, ions, and dust but depends on the mass, charge, and density of the plasma particles.[20] Dust particles oscillate around their equilibrium position with the dust plasma frequency $\omega_{\mathrm{pd}} = \sqrt{Q_p^2 N_p / \epsilon_0 m_p}$ where Q_p and N_p are, respectively, the particle mean charge and the particle density. Assuming N_p to be the critical particle density (10^{12} cm^{-3}),[6] $Q_p \approx 10^{-3} e$, and 1 nm$\leqslant r_p \leqslant$2 nm for silicon particles,[2] we get 1 kHz$\leqslant f_{\mathrm{pd}} \leqslant$3 kHz (assuming $f_{\mathrm{pd}} = \omega_{\mathrm{pd}}/2\pi$). These frequencies correspond to the ones we observed for the instability in different conditions.

The SEM analysis of depositions made at the end of the instability shows that most of the deposited dust particles are small aggregates. At the same time, we observe a drastic decrease in the electron density due to the attachment and to the increase in the ionization rate ($\alpha - \gamma'$ transition).[2]

B. Parameter effect

As for the different phases of particle formation and growth, the region of the instability is affected by different discharge parameters such as injected power, silane flow rate, or gas temperature.

1. Effect of the injected power

The effect of the injected power has been studied for different gas mixture rates of Ar/SiH_4 with silane flow rate varying from 0.4 up to 1.6 SCCM. The following observations correspond to a synthesis of all the results obtained. Figure 4 shows the time evolution of the self-bias voltage for different injected powers. In this particular case the amount of silane in the gas mixture was relatively small ($Q_{\mathrm{SiH_4}}$ =0.8 SCCM), as when the silane flow rate is too high, the instability rapidly disappears when injected power is increased, and no pertinent study can be done. In this case, the instability appears only for low powers between 6 and 14 W. For higher silane flow rate, the instability tends to disappear around 10 W. When the power is increased in the discharge, all the phases of particle formation and growth become shorter and so does the instability (see Fig. 5). This is due to the fact that increasing the injected power increases the ionization process, thus increasing the electron density. Consequently the formation of the particles becomes faster. The instability also starts earlier for high injected power as shown in Fig. 5. The amplitude of the instability also decreases when power increases. For high injected power the kinetics is very fast, leading to the disappearance of the instability. The frequency of the instability has been shown to evolve in time, decreasing between the beginning and the end of the phase. In addition, the frequencies at the beginning and at the end seem to depend linearly on the injected power (see Fig. 6). Indeed, assuming that at the end of the accumulation phase r_p and N_p are constant whatever the injected power is, then ω_{pd} is proportional to the particle charge Q_p. The instability frequency evolves linearly with the rf power. Between 6 and 20 W, the electron temperature remains constant (around 2 eV before the $\alpha - \gamma'$ transition). Hence when the injected power is increased, the particle mean charge also increases.

2. Effect of the silane flow rate

The effects of the silane flow rate have been studied in an argon/silane plasma with an injected power of 10 W. The

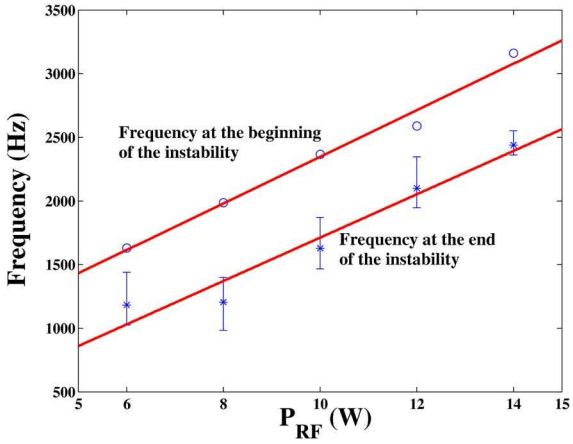

FIG. 6. (Color online) Frequency at the beginning and at the end of the instability as a function of the injected power.

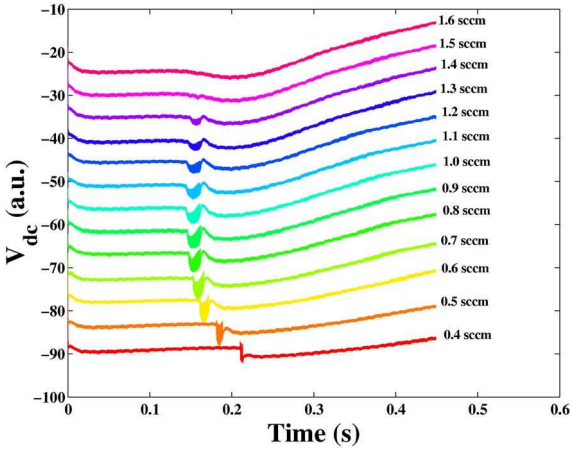

FIG. 7. (Color online) Time evolution of the self-bias voltage vs the silane flow rate. The curves are shifted on the self-bias voltage axis in order to have a better overview.

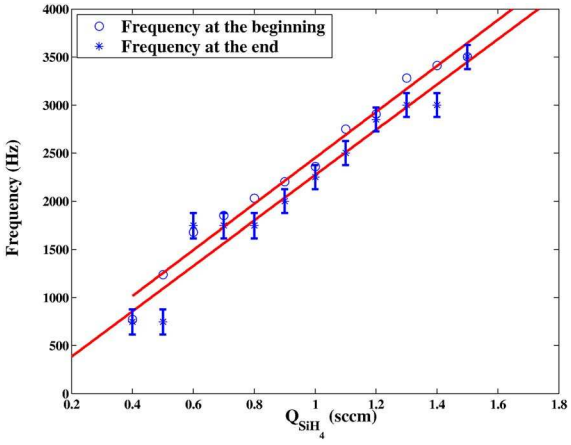

FIG. 9. (Color online) Frequency at the beginning and at the end of the instability as a function of the silane flow rate.

amount of silane in the discharge was varied from 0.4 up to 1.6 SCCM, keeping all the other parameters constant. The induced pressure variation is negligible ($\sim 3-4$ μbars) with respect to the total pressure ($p \approx 120$ μbars). Figure 7 shows the time evolution of the self-bias voltage as a function of the silane flow rate in the discharge. The curves are shifted in the self-bias axis in order to give a better overview. In the case we present here, the injected power is low since, as it has been shown before, when the injected power is too high, no instability can be observed. For 10 W injected power, the instability appears even for very small flow rates and tends to disappear for silane flow rates higher than 1.5 SCCM. The instability duration is maximum for 1 SCCM silane flow rate as shown in Fig. 8. From 0.4 to 1 SCCM the duration of the instability increases when silane flow rate is increased (see Fig. 8). For silane flow rates higher than 1 SCCM, the instability is increasingly short until it disappears. However, overall the amplitude of the instability seems to decrease when increasing the silane flow rate, until it becomes undetectable on the curves. For silane flow rates comprised between 0.4 and 1 SCCM, the instability was observed to begin earlier when increasing the flow rate. From 1 SCCM, this value seems to increase slightly until the disappearance of the phenomenon (see Fig. 8). When the quantity of silane in the discharge is increased, the amount of precursors is increased. Indeed, the dissociation degree of silane is constant and independent of the silane flow rate.[21] The initial, accumulation, and coagulation phases are therefore quicker. The silane flow rate acts on chemical reactions in the discharge. However, it seems that above a given limit (around 1 SCCM in our case) an equilibrium is reached, and the reactions no longer speed up. The frequency of the instability has been shown to have a time evolution. Figure 9 shows the evolution of the frequency at the beginning and at the end of the instability as a function of the silane flow rate. These two frequencies seem to depend linearly on the amount of silane in the discharge.

3. Effect of the temperature

The influence of the gas temperature on particle formation and growth was the subject of many papers.[4,22–25] When the gas temperature is increased, particle formation is delayed. In this work, the influence of the gas temperature has been studied from room temperature (RT) up to 120 °C (measured in the gas flow with a thermocouple just below the plasma box) at constant gas number density. We observed that the instability region is also affected by the temperature. Figure 10 shows the time evolution of the self-bias voltage

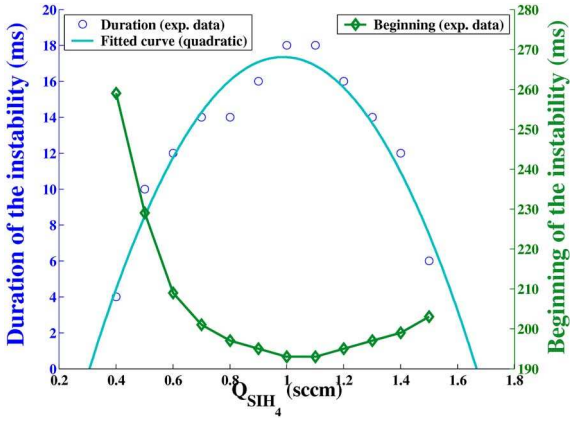

FIG. 8. (Color online) Beginning and duration of the instability as a function of the silane flow rate.

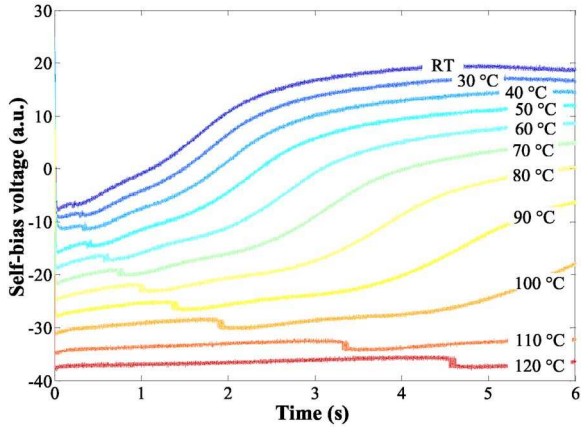

FIG. 10. (Color online) Time evolution of the self-bias voltage vs the temperature. The curves are shifted on the self-bias voltage axis in order to have a better overview.

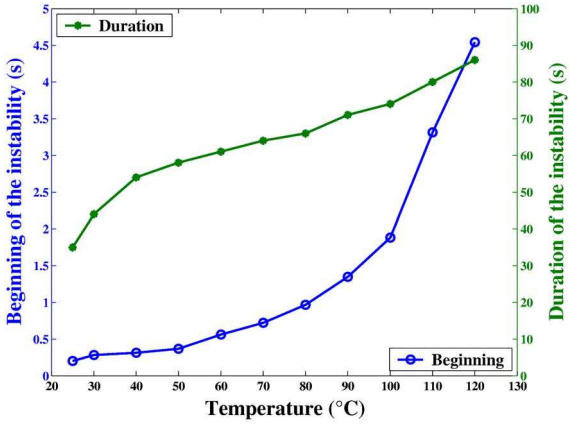

FIG. 11. (Color online) Beginning and duration of the instability as a function of the gas temperature.

versus the gas temperature. The curves are shifted in the self-bias axis in order to have a better overview. When the temperature is increased, the appearance of the instability is delayed (see Fig. 11). The duration of the instability is also affected by the gas temperature: the higher the temperature, the longer the instability (Fig. 11). The instability behaves like the different phases of particle formation and growth: it is delayed and it lasts longer when the temperature is increased. Figure 12 shows the time evolution of the instability frequency as a function of the gas temperature. The time scale has been normalized by the instability duration in order to give a good overview of the evolution. The frequency at the beginning decreases as the temperature increases, while the frequency at the end remains the same at around 0.6 kHz (except on the curve taken at 30 °C). This last point suggests that the frequency at the end of the instability could be linked to the particle density in the plasma. In fact, the end of the instability could correspond to the beginning of the coalescence phase that cannot start unless the critical particle density value (10^{11}–10^{12} cm^{-3}) has been reached.

4. Particular case of the instability

In some very specific conditions a particular case of the instability was observed. Figure 13 shows the shape of the

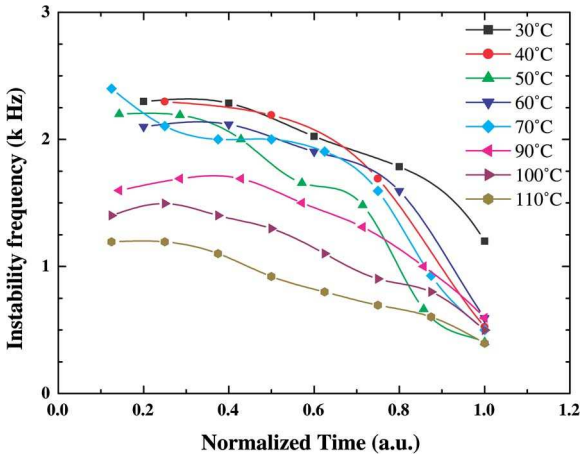

FIG. 12. (Color online) Time evolution of the frequency of instability vs the temperature. The time scale has been normalized by the instability duration to have a significant overview.

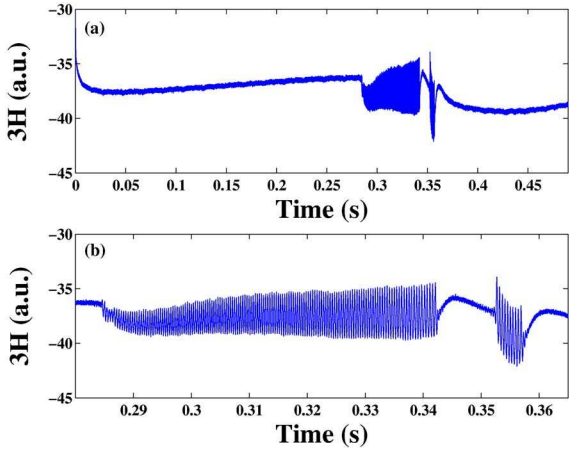

FIG. 13. (Color online) Particular case of the instability on the self-bias voltage (a) on the plasma duration. (b) Zoomed image of the first part of the curve.

instability in this case. In the first part, it behaves in the same way as the "common" instability, then it finishes before briefly restarting. This has been confirmed by a frequency analysis (FFT analysis) (see Fig. 14). We can observe a time evolution of the frequency and a range of frequencies similar to those previously observed (between 2 and 3 kHz). The second part seems to be a sort of replica of the end of the first part, with exactly the same frequencies. This phenomenon is highly sensitive to the operating conditions, appearing only for very low injected power (around 6 W) and in a very tight range of silane flow rates (several appearances between 2 and 3 SCCM). Moreover, a temperature variation of only a few degrees Celsius leads to the disappearance of the phenomenon. This particular case of the instability seems to correspond to dust critical formation conditions, as the slightest modification of one of the parameters leads to the disappearance of the phenomenon. However, we observed this particular instability in at least two different sets of parameters. This observation leads us to surmise that a special pair particle density/particle radius could favor a special behavior of the dense particle cloud trapped in the discharge.

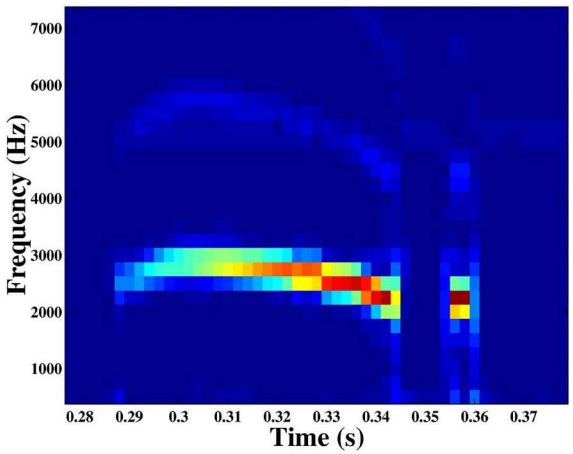

FIG. 14. (Color online) Time evolution of the frequency of the instability in the particular case.

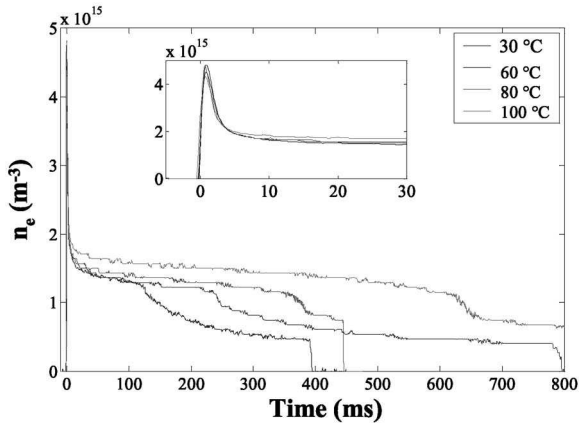

FIG. 15. Time evolution of the electron density for different gas temperatures. The insert is a zoom of the early beginning of the curve.

C. Discussion

A wide range of instabilities is observed in dusty and nondusty plasmas. A possible explanation for the phenomenon observed here is the attachment induced ionization instabilities observed in low pressure rf discharges in electronegative gases.[26,27] The main parameters responsible for these instabilities are the electron temperature T_e and density n_e. In fact, instabilities need two conditions to appear. First, the attachment rate coefficient has to increase more rapidly than the ionization one with the electron temperature. Second, the electron and negative ion densities must be of the same order of magnitude. Thus a small increase in the electron density can be rapidly amplified through a decrease of the electron temperature. Nighan and Wiegand gave a criterion for the appearance of the instability,

$$R = \frac{\partial k_a/\partial T_e}{\partial k_i/\partial T_e} > 1, \tag{1}$$

where k_a and k_i are, respectively, the attachment and ionization coefficients.[26]

As dust particles are charged, they behave like large negative ions. The instabilities we observed may therefore be related to attachment induced ionization instabilities. During the accumulation phase, the nanocrystallites have been shown to grow and accumulate in the gas phase.[22] Their concentration increases until it reaches a critical value from which the coalescence phase starts. This critical value has been measured to be around 10^{11}–10^{12} cm^{-3}.[6] However, less than 0.1% of the dust particles are charged by electron attachment. The concentration of negatively charged nanocrystallites is therefore of the same order of magnitude as the electron density, just before the instability. Furthermore the electron temperature has been shown to be constant and equal to 2 eV during the accumulation phase.[4] Figure 15 shows the time evolution of the electron density n_e measured by the microwave resonant cavity method for different gas temperatures. The first very narrow peak (shown in the insert) corresponds to the SiH_3^- ion formation. Those ions are the first nuclei involved in the particle formation. Then, the electron density remains constant during the accumulation phase. Just at the onset of the coalescence, a slight decrease of the electron density can be observed (see the circle in Fig. 15) while the ion density remains constant. That means that at the beginning of the instability k_a increases while k_i remains constant ($\partial k_i/\partial T_e \to 0$). And so R becomes larger than 1.

IV. CONCLUSION

In this paper we have presented experimental results concerning a self-excited instability in silane based dusty plasma. These results have been obtained during particle nucleation and growth. We show that the instability has a complex form and that its frequency evolves in time. The effects of different parameters on the instability behavior are also reported, and a particular case has been evidenced. A possible explanation is also put forward, thanks to a comparison with the instabilities observed in electronegative discharges. In the future, a comparison between the instabilities observed in Ref. 13 and those we observed will be investigated.

ACKNOWLEDGMENTS

The authors would like to thank Maurice Dudemaine and Sébastien Dozias for their help in electronics and Elizabeth Jolivet for her precious advice.

[1] L. Boufendi and A. Bouchoule, Plasma Sources Sci. Technol. **11**, A211 (2002).
[2] L. Boufendi, A. Bouchoule, and T. Hbid, J. Vac. Sci. Technol. A **14**, 572 (1995).
[3] J. Boeuf, Phys. Rev. A **46**, 7910 (1992).
[4] A. Fridman, L. Boufendi, T. Hbid, B. Potapkin, and A. Bouchoule, J. Appl. Phys. **79**, 1303 (1995).
[5] A. Bouchoule, A. Plain, L. Boufendi, J. Blondeau, and C. Laure, J. Appl. Phys. **70**, 1991 (1991).
[6] L. Boufendi, J. Gaudin, S. Huet, G. Viera, and M. Dudemaine, Appl. Phys. Lett. **79**, 4301 (2001).
[7] P. Roca i Cabarrocas, N. Chaabane, A. Kharchenko, and S. Tchakarov, Plasma Phys. Controlled Fusion **46**, B235 (2004).
[8] P. Roca i Cabarrocas, J. Non-Cryst. Solids **266–269**, 31 (2000).
[9] P. Roca i Cabarrocas, S. Kasouit, B. Kalache, R. Vanderhaghen, Y. Bonnassieux, M. Elyaakoubi, and I. French, J. Soc. Inf. Disp. **12/1**, 1 (2004).
[10] G. Viera, M. Mikikian, E. Bertran, P. Roca i Cabarrocas, and L. Boufendi, J. Appl. Phys. **92**, 4684 (2002).
[11] G. Praburam and J. Goree, Phys. Plasmas **3**, 1212 (1996).
[12] D. Samsonov and J. Goree, Phys. Rev. E **59**, 1047 (1999).
[13] M. Mikikian and L. Boufendi, Phys. Plasmas **11**, 3733 (2004).
[14] M. Mikikian, M. Cavarroc, N. Chaumeix, and L. Boufendi, Proceedings of the 31st EPS Conference on Plasma Physics, London, 2004, edited by P. Norrey and H. Hutchinson (European Physical Society), ECA Vol. 28G, pp. O-2.13.
[15] A. Mezeghrane, M. Jouanny, M. Cavarroc, M. Mikikian, O. Lamrous, and L. Boufendi, Proceedings of the 31st EPS Conference on Plasma Physics, London, 2004 (European Physical Society), ECA Vol. 28G, pp. O-1.09.
[16] L. Boufendi, A. Plain, J. Blondeau, A. Bouchoule, C. Laure, and M. Toogood, Appl. Phys. Lett. **60**, 169 (1992).
[17] L. Boufendi, A. Bouchoule, R. Porteous, J. Blondeau, A. Plain, and C. Laure, J. Appl. Phys. **73**, 2160 (1993).
[18] L. Boufendi, Ph.D. thesis, University of Orléans, 1994.
[19] M. Shiratani, T. Fukuzawa, and Y. Watanabe, Jpn. J. Appl. Phys., Part 1 **38**, 4542 (1999).
[20] P. Shukla and A. Mamun, *Introduction to Dusty Plasma Physics* (IOP, Bristol, 2002).

[21]A. Bouchoule and L. Boufendi, Plasma Sources Sci. Technol. **3**, 292 (1994).
[22]L. Boufendi, J. Hermann, A. Bouchoule, B. Dubreuil, E. Stoffels, W. Stoffels, and M. de Giorgi, J. Appl. Phys. **76**, 148 (1994).
[23]U. Bhandarkar, U. Kortshagen, and S. L. Girshik, J. Phys. D **36**, 1399 (2003).
[24]J. Perrin, O. Leroy, and M. Bordage, Contrib. Plasma Phys. **36**, 1 (1996).
[25]J. Perrin, C. Bohm, R. Etemadi, and A. Lloret, Plasma Sources Sci. Technol. **3**, 252 (1994).
[26]W. Nighan and W. Wiegand, Phys. Rev. A **10**, 922 (1974).
[27]A. Descoeudres, L. Sansonnens, and C. Hollenstein, Plasma Sources Sci. Technol. **12**, 152 (2003).

Single-crystal silicon nanoparticles: An instability to check their synthesis

M. Cavarroc,[a] M. Mikikian, G. Perrier, and L. Boufendi
GREMI-Polytech'Orléans, 14, Rue d'Issoudun, BP 6744, 45067 Orléans Cedex 2, France

(Received 6 March 2006; accepted 2 June 2006; published online 5 July 2006)

An instability occuring in electrical signals of the discharge is used as a mark to detect the end of the single-crystal silicon nanoparticle formation in Ar/SiH_4 rf plasmas. Scanning electron microscopy and atomic force microscopy studies of depositions show that the exact beginning of the coalescence phase corresponds to the onset of the instability. At the end of the instability, no single-crystal nanoparticles are remaining in the gas phase. These results based on a nonperturbative method allow to control depositions of single-crystal silicon nanoparticles of a well-defined size distribution with the highest density available during dust particle growth. © *2006 American Institute of Physics*. [DOI: 10.1063/1.2219395]

Dusty plasmas generated in radio frequency (rf) discharges have been widely studied in the past few years. The range of interest spreads over industrial[1] as well as astrophysical concerns.[2] An active research has been induced by contamination phenomena in industrial plasma reactors. However, new applications of dust production have emerged. It can be used to produce analog aerosols of planet atmospheres like Titan.[2] The single-crystal nanoparticles obtained by this way can be incorporated in thin film layers in order to improve their mechanical and/or optoelectronical properties,[3] or used for single electron device fabrication.[4] Many theoretical[5,6] and experimental[7,8] studies have dealt with the detection and dynamics of particles in silane based plasmas. Presently, many studies are being carried out on the production of silicon nanoparticles generated in plasma processes.[9]

In previous experimental and theoretical works,[7,10,11] the way particles grow has been brougth to the fore. The dust particle formation in $Ar-SiH_4$ low pressure rf plasmas has been shown to be a four step process occuring in the gas phase: nanocrystal growth (2–3 nm in diameter) from molecular species, accumulation phase, coalescence, and growth by deposition of the plasma species on the particle surface. Particle growth in the discharge leads to strong modifications of the plasma characteristics. Indeed dust grains affect many of the physical properties of the plasma (electron density, temperature, electric field, impedance, etc.). The modification of the plasma impedance due to the particle formation and growth led us to use a diagnostic based on the time evolution of the amplitude of the third harmonic (3H) of the discharge current and the amplitude of the self-bias voltage (V_{dc}).[11] This electrical diagnostic has been developed in the GREMI laboratory. The current and voltage probes are inserted between the matchbox and the powered electrode. The curves are visualized on a LeCroy scope LT364L (500 MHz bandwidth and 1 GS/s) and the results are recorded via a computer. This diagnostic has been shown to be able to follow the particle formation and growth in different chemistries such as silane and methane based ones.[12] Thus, in a pure argon plasma, the amplitude of 3H and V_{dc} remains constant in time. When silane is added to the the mixture, i.e., in a dust forming plasma, V_{dc} and 3H show a time evolution due to the formation and growth of dusts in the discharge. The main formation steps (accumulation phase, coalescence, and growth by surface deposition) can be clearly identify thanks to this electrical diagnostic (Fig. 1). Even though, some uncertainties remain concerning the exact transition from one step to another. As can be seen in the Fig. 1 insert, an instability occurs in between accumulation and coalescence phase.[13]

Until now it was still quite difficult to exactly define when the coalescence starts. The end of the accumulation phase is the most interesting point for nanocrystal deposition. In a previous study performed in our group in the same experimental conditions, nanocrystals have been shown to be single-crystal silicon nanoparticles of 2–3 nm in the fcc phase[14] and the critical density (i.e., the greater density of nanocrystals in the discharge) is reached just at the end of this phase. A precise control of the nanocrystal phase is very important for all industrial applications in nanotechnologies in which a well known nanocrystal size and density are required.[15] The aim of the present work is to determine the point on electrical signals corresponding to the exact end of the accumulation phase (i.e., to the exact beginning of the coalescence phase).

The experimental setup has already been described in detail in a previous paper.[8] The rf discharge is produced in a grounded cylindrical plasma box (13 cm inner diameter and 3.3 cm for interelectrode distance). The whole system is enclosed in a vacuum chamber. The upper electrode (driven electrode) is a shower-head one in order to ensure a homogeneous gas distribution at the entrance of the plasma zone. This electrode is connected to a 13.56 MHz rf generator through a matchbox including a blocking capacitor. The

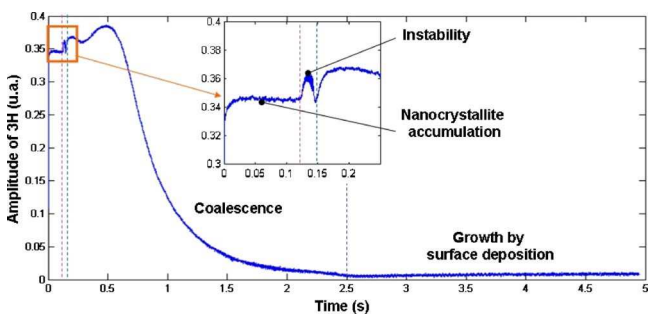

FIG. 1. (Color online) Time evolution of the amplitude of the discharge current third harmonic in a dust forming plasma.

[a]Electronic mail: marjorie.cavarroc@univ-orleans.fr

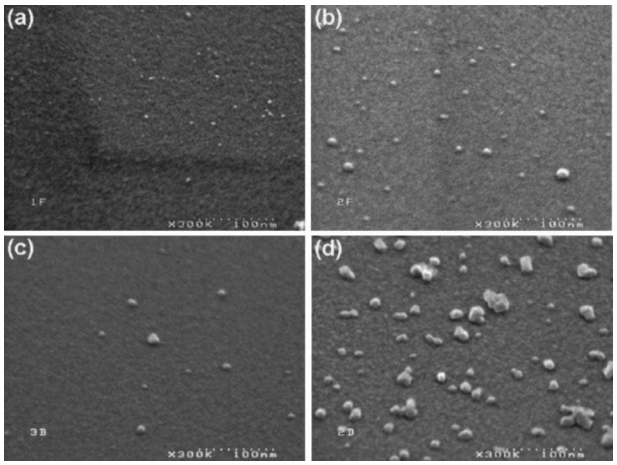

FIG. 2. SEM images of the samples deposited (a) just before, (b) at the beginning of, (c) during, and (d) after the instability.

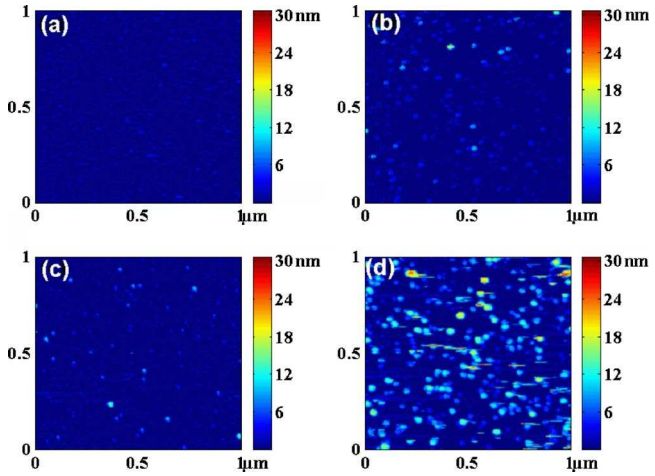

FIG. 3. (Color online) AFM images of the samples deposited (a) just before, (b) at the beginning of, (c) during, and (d) after the instability.

power can be varied from 0 up to 20 W. The experimental conditions are the following: 12 Pa total pressure, 20 SCCM (SCCM denotes cubic centimeter per minute at STP) of argon flow rate, 1.2 SCCM of silane flow rate, and 10 W of injected power, at room temperature.

In this work, depositions of dust particles at different instances have been performed. We used the instability occuring in the electrical signals as a mark. This instability has been studied in detail in a previous work.[13] We realized three different types of samples: a first one just before, a second one during, and a last one after the instability. Structural morphology of the formed dust particles is qualitatively analyzed from topographical observations of the samples by means of atomic force microscopy (AFM) operating in the tapping mode and scanning electron microscopy (SEM). The SEM images obtained are shown in Fig. 2.

Just before the instability [Fig. 2(a)], there are only single nanocrystals (around 2–3 nm) on the substrate. At the beginning and in the middle of the instability [Figs. 2(b) and 2(c)], two populations can be distinguished: there are both nanocrystals and small polycrystalline aggregates. At the end of the instability [Fig. 2(d)] deposited dust particles are mainly small polycrystalline aggregates. These results seem to place the beginning of the coalescence phase at the beginning of the instability. The AFM images obtained from the same samples are shown in Fig. 3. They are all normalized to the same height size scale in order to make the comparison easier. In the nanocrystal case, the AFM tip size is of the same order as the nanocrystal size. We are confronted to convolution troubles in the x and y directions. The only dimension we can use is the height because this dimension is less concerned by convolution troubles. The results are quite similar to the ones obtained by SEM. Before the instability [Fig. 3(a)], there are only small nanocrystals around 2–3 nm in height. At the beginning and in the middle of the instability [Figs. 3(b) and 3(c)], two populations of dust particles are present, one around 2–3 nm and another one around 4–5 nm. After the instability [Fig. 3(d)], a single population is visible, around 10 nm. Those results confirm the ones obtained by SEM.

The radius distribution of dust particles corresponding to the first sample [Fig. 4(a)] shows a single peak centered at 1.5 nm (corresponding to 3 nm in height). The same analysis performed on a sample deposited during the instability [Fig. 4(b)] shows two peaks located at different heights. The higher peak around 1.5 nm corresponds to the nanocrystals and the smaller one around 4 nm corresponds to the first coalesced polycrystalline nanoparticles. On the last sample [Fig. 4(c)], a single peak appears around 5 nm, corresponding to bigger coalesced polycrystalline nanoparticles. Those dust particle radius distributions confirm our qualitative topographical observation.

The third harmonic/self-bias based diagnostic does not need any optical access to the plasma. Once it is calibrated, this diagnostic can provide precise information concerning the dust particle nature in the discharge. We performed the calibration for the first phases of formation (formation and accumulation of nanocrystals and beginning of the coalescence) in a typical dust forming Ar/SiH_4 plasma generated in a rf discharge. Presently, we can conclude that before the instability, the dust particles are single-crystal silicon nanoparticles of 2–3 nm in diameter in the fcc phase.[14] Their shape appears to be spherical and their density increases during the accumulation phase until reaching the critical value estimated to 10^{11}–10^{12} cm^{-3} at room temperature.[11] Thereby, just before the instability the single-crystal silicon nanopar-

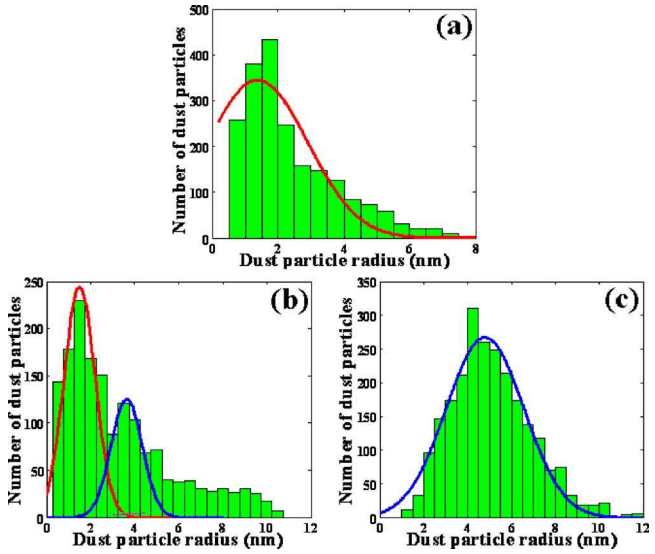

FIG. 4. (Color online) Radius distribution diagrams corresponding to a sample deposited (a) before, (b), during, and (c) after the instability.

ticle density in the plasma is the highest that can be reached. During the instability, nanocrystals agglomerate together to form the first polycrystalline dust nanoparticles of 4–5 nm. All the nanocrystals begin to agglomerate at least two by two. This is the early beginning of the coalescence phase and two populations can be distinguished. The first one corresponds to nanocrystals while the second one corresponds to first coalesced polycrystalline particles. At the end of the instability, no more single nanocrystals remain in the gas phase. Thus, the onset of the instability exactly corresponds to the beginning of the coalescence phase. This instability is certainly due to a charge effect of the nanoparticles becoming bigger and starting to attach more electrons. It can be related to attachment induced ionization instabilities observed in electronegative gases.[13,16,17] After the instability the dust nanoparticles are made of agglomerated nanocrystals. Their size increases from 5 nm at the beginning of the coalescence to about 45 nm at the end of the phase.[1] The dust particles are now polycrystalline and present a high specific surface [up to 115 $m^2 g^{-1}$ (Ref. 18)] that can be of interest for applications in catalysis.

The authors would like to thank M. Dudemaine, S. Dozias, M. Vayer, T. Baron, and K. Aissou for technical support.

[1] L. Boufendi and A. Bouchoule, Plasma Sources Sci. Technol. **11**, A211 (2002).
[2] G. Cernogora, C. Szopa, L. Boufendi, P. Coll, J. M. Bernard, and C. Pintassilgo, AIP Conf. Proc. **799**, 69 (2005).
[3] P. Roca i Cabarrocas, N. Chaabane, A. V. Kharchenko, and S. Tchakarov, Plasma Phys. Controlled Fusion **46**, B235 (2004).
[4] S. Tiwari, F. Rana, H. Hanafi, A. Hartstein, and E. F. Crabb, Appl. Phys. Lett. **68**, 1377 (1996).
[5] L. Boufendi, A. Bouchoule, and T. Hbid, J. Vac. Sci. Technol. A **14**, 572 (1996).
[6] J. P. Boeuf, Phys. Rev. A **46**, 7910 (1992).
[7] A. A. Fridman, L. Boufendi, T. Hbid, B. V. Potapkin, and A. Bouchoule, J. Appl. Phys. **79**, 1303 (1995).
[8] A. Bouchoule, A. Plain, L. Boufendi, J. Ph Blondeau, and C. Laure, J. Appl. Phys. **70**, 1991 (1991).
[9] A. Bapat, C. Anderson, C. R. Perrey, C. B. Carter, S. A. Campbell, and U. Khortshagen, Plasma Phys. Controlled Fusion **46**, B97 (2004).
[10] M. Shiratani, T. Fukuzawa, and Y. Watanabe, Jpn. J. Appl. Phys., Part 1 **38**, 4542 (1999).
[11] L. Boufendi, J. Gaudin, S. Huet, G. Viera, and M. Dudemaine, Appl. Phys. Lett. **79**, 4301 (2001).
[12] A. Mezeghrane, M. Jouanny, M. Cavarroc, M. Mikikian, O. Lamrous, and L. Boufendi, *Proceedings of the 31th EPS Conference on Plasma Physics, London*, edited by P. Norrey and H. Hutchinson (European Physical Society, London, 2004), Vol. 286.
[13] M. Cavarroc, M. C. Jouanny, K. Radouane, M. Mikikian, and L. Boufendi, J. Appl. Phys. **99**, 064301 (2006).
[14] G. Viera, M. Mikikian, E. Bertran, P. Roca i Cabarrocas, and L. Boufendi, J. Appl. Phys. **92**, 4684 (2002).
[15] K. Nishiguchi, X. Zhao, and S. Oda, J. Appl. Phys. **92**, 2748 (2002).
[16] W. L. Nighan and W. J. Wiegand, Phys. Rev. A **10**, 922 (1974).
[17] A. Descoeudres, L. Sansonnens, and Ch. Hollenstein, Plasma Sources Sci. Technol. **12**, 152 (2003).
[18] F. Vivet, A. Bouchoule, and L. Boufendi, J. Appl. Phys. **83**, 7474 (1998).

Low frequency instabilities during dust particle growth in a radio-frequency plasma

Maxime Mikikian,[a] Marjorie Cavarroc, Lénaïc Couëdel, and Laïfa Boufendi
GREMI, Groupe de Recherches sur l'Energétique des Milieux Ionisés UMR6606, CNRS/Université d'Orléans, 14 rue d'Issoudun, BP6744, 45067 Orléans Cedex 2, France

(Received 1 June 2006; accepted 26 July 2006; published online 6 September 2006)

In this paper, instabilities appearing in a dusty plasma are experimentally investigated. These low frequency self-excited instabilities appear during dust particle growth and are characterized by a frequency spectrum evolving during this process. The onset, the time evolution and the main characteristics of these instabilities are investigated thanks to electrical and optical measurements. Both signals show a clear evolution scheme with a well-defined succession of phases. From the beginning to the end of this scheme, regular oscillations and/or chaotic regimes are observed. Finally, instabilities stop when the dust particle size reaches a few hundreds of nanometers and a stable three-dimensional dust cloud is obtained. A dust-free region called void is then usually observed in the plasma center. © *2006 American Institute of Physics*. [DOI: 10.1063/1.2337793]

I. INTRODUCTION

In a plasma, dust particles can be grown using reactive gases like silane[1–3] or by ion bombardment on materials.[4–9] This formation is actively studied due to strong consequences that can arise from the presence of dust in plasma processing reactors[10,11] for microelectronics where cleanliness is a major requirement.[12] Furthermore, the interest is actually increasing due to the fact that nanometer dust particles can be useful for industrial applications like solar cells[13] or memories.[14] Laboratory dusty plasmas are also a very efficient way to produce and study astrophysical dusty media like planet atmospheres.[15] In capacitively coupled radio-frequency discharges, a dense cloud of submicrometer dust particles filling the whole space between the electrodes can be obtained. During their growth, dust particles acquire a negative charge by attaching more and more electrons.[16–18] Consequently, the growth can be studied through its influence on the plasma characteristics and in particular on the discharge current harmonics. Indeed, the current third harmonic is a robust tool to accurately follow and identify growth steps.[19] Dust particle growth strongly affects plasma properties and can induce plasma instabilities. Self-excited instabilities have been observed in silane plasmas[20] (frequencies of few kHz for dust particles of few nanometers) and also in dusty plasmas produced by sputtering a carbon target[7,8] (frequencies around 100 Hz for dust particles around hundred nanometers). In this last experiment, the authors describe two different instability modes called the filamentary mode and the great void mode. The first one appears approximately 1 min after the plasma ignition and is characterized by a broadband spectrum centered around 100 Hz. It corresponds to a beamlike striation of dust density and plasma glow. As dust particles are still growing, this stage is then followed by the great void mode, which corresponds to the formation of a dust-free region called void[7,9,21–23] and its rotation in a horizontal plane in between the electrodes. The void region is due to the equilibrium between various forces acting on the negatively charged dust particles. These forces are principally due to ion drag, electric fields, thermal gradients, gas flow, and gravity, and they define the cloud shape. The ion drag force is presently actively studied because it is suspected to be the main responsible of the void formation,[8,24–33] pushing the dust particles away from the discharge center. In this paper, observations and analyses of instabilities appearing during dust particle growth are performed. These instabilities look like the filamentary and great void modes in some stage of their evolution. Nevertheless, their time evolution is much more complicated and seven different regimes can be identified. Indeed, well-defined frequencies are observed and the associated spectrum strongly evolves during the growth process. The instability complex shape underlines the coexistence of different phenomena that could interact and give regular or chaotic oscillations. The instability time evolution reveals drastic and sudden changes in shape and frequency that could not be easily correlated to dust particle size and density. A detailed analysis of the instability main characteristics is performed in order to underline and bring to the fore the complex phenomena that could arise in a plasma containing changing dust particles.

II. EXPERIMENTAL BASIS

A. Experimental setup

The work presented here is performed in the PKE-Nefedov (Plasma Kristall Experiment) chamber designed for microgravity experiments.[34] The experimental setup consists of a parallel plate rf discharge where an argon plasma (0.2–2 mbar) is created in a push-pull excitation mode (0–4 W). The electrodes are separated by 3 cm and their diameter is 4 cm. The dust cloud is illuminated by a thin laser sheet perpendicular to the electrodes and the scattered light is recorded at 90° with two standard charge-coupled device (CCD) cameras at 25 images per second. In the first

[a]Electronic mail: maxime.mikikian@univ-orleans.fr

stages of growth, dust particles are very small and the scattered light is maximum in the laser direction. Consequently, a third camera is watching the cloud with an angle lying approximately between 20° and 30° with respect to the incident laser direction. Instabilities are characterized by two different diagnostics. First, the time evolution of the amplitude of the discharge current fundamental harmonic is recorded. This electrical measurement is representative of global changes in plasma properties, especially concerning the electron density. The second diagnostic is based on spatially resolved optical measurements. Five optical fibers are horizontally aligned (5 mm in between each fiber) and record the total plasma light with a spatial resolution of about 3 mm. This diagnostic gives local measurements that are of interest to detect any plasma motion or localized changes in order to better understand the integrated electrical measurements.

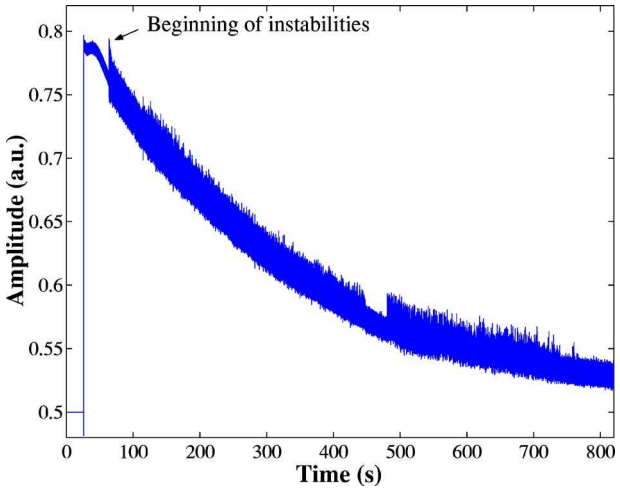

FIG. 1. (Color online) Time evolution of the amplitude of the discharge current fundamental harmonic during dust particle growth. Instabilities appear around 40 s after plasma ignition.

B. Dust particle growth

Dust particles are grown by sputtering a polymer layer deposited on the electrodes and coming from previously injected dust particles (3.4 μm, melamine formaldehyde). A typical working pressure is around 1.6 mbar and rf power is about 2.8 W. With these parameters dust particles start to be detected by the cameras approximately 1 min after the plasma ignition. A more complete description of the experimental setup and some results concerning dust particle growth are given in Ref. 9. The growth process leads to various shapes of the dust cloud (few layers, domelike shape, three-dimensional dense cloud) due to the fact that we do not control precisely the size and density of grown dust particles. Indeed, the growth process seems to be highly sensitive to gas purity. This effect is amplified by the fact that experiments are performed at static pressure (no gas flow). At least 1 h of pumping between each experiment is needed to eliminate species formed during the previous run and/or coming from the outgassing of the walls and/or from the sputtered matter. This behavior is well observed on successive runs by using emission spectroscopy. Impurities like N_2 and OH are observed and their effect on dust particle formation is under investigation. Until now it is not clear if their presence prevents the sputtering or if the sputtering occurs but the growth cannot takes place. This effect of the gas purity has been previously reported in similar experiments.[8] Possible precursors like carbon molecules C_2, CN, and CH appear and the C_2 molecule seems to be a good indicator of dust formation.[35]

A very high dust density is obtained when base pressure before an experiment is sufficiently low (few 10^{-6} mbar). A base pressure of few 10^{-5} mbar drastically reduces the amount of grown dust particles. This base pressure dependence is even more drastic on the instability appearance. Indeed, in our experimental conditions, they are observed only if the base pressure is lower than 4×10^{-6} mbar. Consequently, unstable conditions depend on gas purity and/or on dust particle density.

III. DUST PARTICLE GROWTH INSTABILITIES

Dust particle growth instabilities (DPGI) typically appear a few tens of seconds after plasma ignition. Their appearance is well observed on both electrical and optical measurements.[36,37] Due to their low frequency and strong amplitude, the beginning of DPGI is also well detected by the naked eye looking at the plasma glow.

When dust particles are growing in a plasma, the amplitude of the discharge current fundamental harmonic is decreasing due to the electron attachment on the dust particle surface. This decrease is well observed in Fig. 1 from around 20 s (plasma ignition) to 800 s. The appearance of DPGI is also clearly evidenced by an increase of the fluctuation amplitude becoming a real oscillation. DPGI can last several minutes (more than 12 min in Fig. 1) and different regimes are evidenced. Their starting time is slightly changing from one experiment to another due to differences in dust particle density, which is strongly dependent on gas purity. Nevertheless, statistics performed on several experiments allow to deduce some general behavior. For example, the pressure dependence is shown in Fig. 2. A decreasing exponential variation of DPGI appearance time as a function of pressure is observed: the higher the pressure, the shorter the appearance time. This variation underlines the relation between the instability appearance and dust particle density. Indeed, DPGI are observed only when a huge dust particle density is obtained. From our previous experiments,[35] we define the threshold pressure permitting dust particle growth at around 1.2 mbar. At higher pressures, a shorter delay before formation of a dense cloud is measured. This delay is well evidenced in Fig. 2. At 1.4 mbar, nearly 2 min are necessary to initiate DPGI while only 40 s are required at 1.8 mbar. Two possibilities can explain this delay at low pressures: either a longer time is required to attain the critical dust density necessary to initiate DPGI or the dust density is lower and for DPGI to begin it needs bigger dust particles (i.e., longer

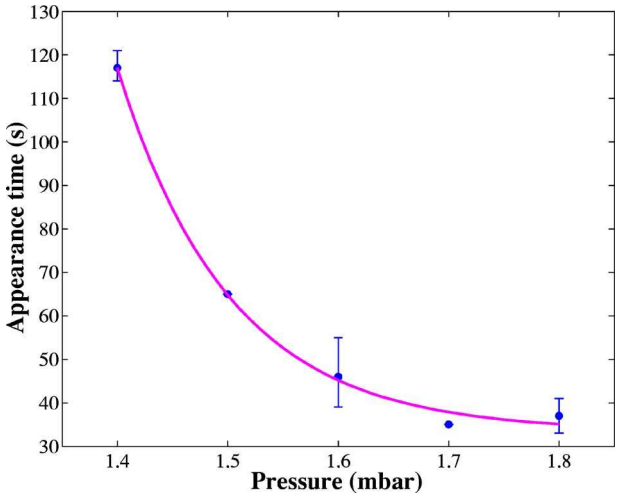

FIG. 2. (Color online) Instability appearance time as a function of argon pressure.

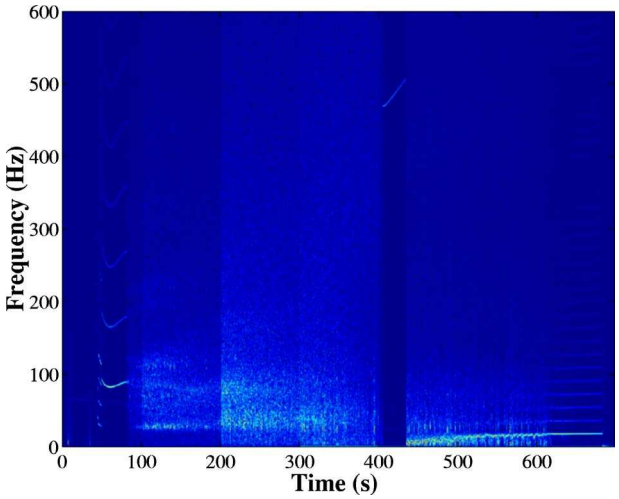

FIG. 4. (Color online) Spectrogram of electrical measurements corresponding to Fig. 3 and describing the frequency evolution of DPGI as a function of time.

time). These explanations are consistent with another observation: the lower the rf power, the longer the appearance time.

IV. PHASE IDENTIFICATION: ELECTRICAL AND OPTICAL MEASUREMENTS

As can be seen in Fig. 1, different regimes characterize DPGI. These different phases are easily brought to light by performing the same electrical measurements but in ac mode in order to improve oscilloscope vertical resolution. The resulting curve is presented in Fig. 3. The beginning of DPGI is detected around 40 s and clear phases, numbered from 1 to 7, are observed. These different phases are better evidenced by performing Fourier analysis of the electrical signals. A typical spectrogram is given in Fig. 4. In order to emphasize small ordered domains, the spectrogram intensity has been normalized inside each 100 s range (from 0 to 100 s intensity has been normalized to its maximum value inside this time domain and so on). The same Fourier analysis performed on spatially resolved optical measurements shows roughly the same spectrogram features and phases. From Figs. 3 and 4 we can identify seven different regimes (a precise analysis of these different phases will be presented in the following sections):

- Three ordered phases P1, P2, P3 (from ≃40 s to ≃80 s).
- Chaotic phase P4 (from ≃80 s to ≃405 s).
- High frequency phase P5 (from ≃405 s to ≃435 s).
- Chaotic phase becoming more and more regular P6 (from ≃435 s to ≃600 s).
- Regular oscillation phase P7 (from ≃600 s to ≃680 s).

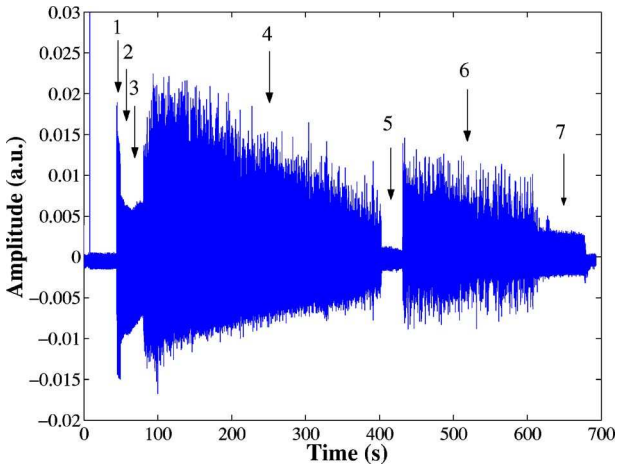

FIG. 3. (Color online) Time evolution of the amplitude of the discharge current fundamental harmonic during dust particle growth (ac component). Instabilities appear around 40 s after plasma ignition. Successive phases are numbered from 1 to 7.

All these phases are observed on both electrical and optical measurements, confirming their real correlation to an unstable state of the plasma-dust particle system. The global scheme of these instabilities is different from the one describe in Refs. 7 and 8, where a filamentary mode (that could be related to our chaotic regime) is followed by a regular phase (great void mode). In our experiment, instabilities begin with regular oscillations (P1, P2, P3) followed by a long chaotic regime (P4). This chaotic phase (P4) suddenly ends with a high-frequency phase (P5) and starts again (P6), becoming more and more ordered. Finally, the system reaches a regular phase (P7) that can be sustained for a long time (in the example given here the plasma has been switched off at 680 s).

A. First three ordered phases

DPGI begin with a succession of three ordered phases separated by clear transitions (Fig. 5). The P1 and P2 phases are short and are not detected in all experiments while the P3 phase lasts longer and is regularly observed. The three phases are well separated and evolve as a function of time. To explain the observed transitions between phases, it is necessary to also analyze the corresponding time series. As an example, Fig. 6 represents an electrical measurement obtained with a very short P2 phase in order to illustrate on the

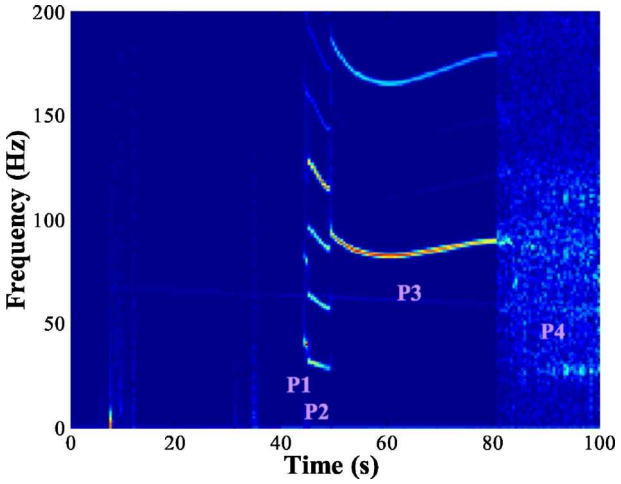

FIG. 5. (Color online) First three ordered phases of DPGI and transition to a chaotic regime.

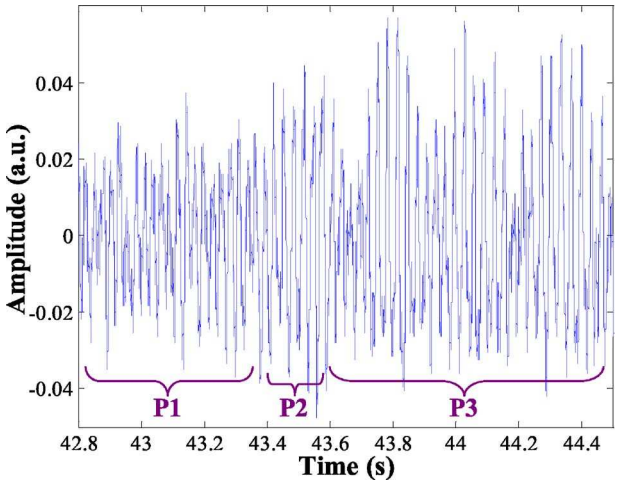

FIG. 7. (Color online) Transitions between the first three ordered phases observed on optical measurements performed near the plasma edge.

same figure the P1–P2 and P2–P3 transitions. In Fig. 6, the P1 phase is characterized by wide separated peaks with a mean frequency of about 40 Hz. The transition from P1 to P2 corresponds to the growth of two small peaks between these higher amplitude patterns. The Fourier analysis traduces this change by a frequency decrease from about 40 Hz in P1 to about 30 Hz in P2. The small peaks continue to grow (P2 phase) and the higher amplitude ones decrease. Finally, all peaks reach the same amplitude characterizing the P3 phase. The frequency of the P3 phase is then approximately three times the P2 frequency (around 94 Hz). The P3 phase is robust (nearly always observed in our experiments) and lasts a sufficiently long time to evolve with dust particle growth (Fig. 5). Its frequency time evolution is always the same, it decreases, reaches a minimum value, and then slightly increases until DPGI enter in the chaotic regime. Furthermore, the frequency range of the P3 phase seems to be linearly dependent on the phase duration: the higher the frequency, the shorter the time duration. The time evolution

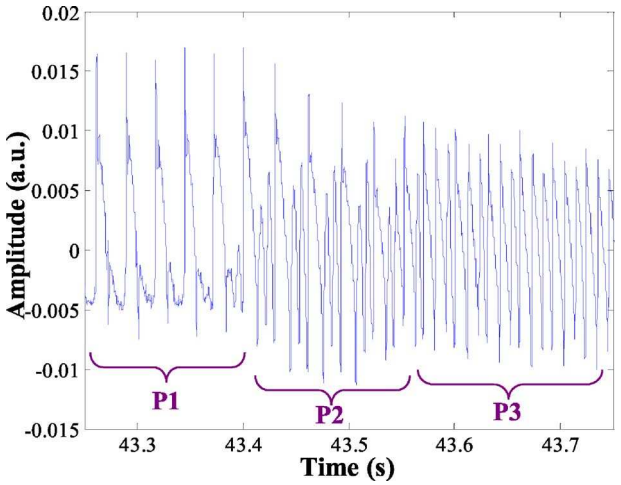

FIG. 6. (Color online) Transitions between the first three ordered phases observed on electrical measurements.

of these three ordered phases is better observed on the frequency harmonics appearing due to the nearly sawtooth shape of the electrical signals (Fig. 6).

Optical measurements recording the plasma light (integrated on all wavelengths) at different positions also show three ordered phases (Fig. 7). Nevertheless, these P1, P2, and P3 phases have different characteristics than the ones observed on electrical measurements. Concerning the oscillation shape, the transition between the P1 and P2 phases is here revealed by an increase of oscillation amplitude (Fig. 7). The P3 phase is strongly marked by a clear amplitude modulation, which is better evidenced near the plasma edge than in the plasma center. Concerning the oscillation frequency, some small discrepancies with electrical measurements are also observed, especially on the P3 phase (Figs. 5 and 8). Indeed, the P1 and P2 phases are similar but when DPGI enter in the P3 phase, the typical frequency is not tripled, like in electrical measurements, but remains around the same value than during the P2 phase. Furthermore, optical measurements of this P3 phase are slightly different depending on the observed plasma region. The signal recorded by the optical fiber watching the plasma center [Figs. 8(a) and 8(c)] is not exactly the same as the one recorded near the plasma edge [Figs. 8(b) and 8(d)]. Indeed, the central fiber gives a main frequency around 26 Hz and a small amplitude component around 31 Hz [Fig. 8(c)]. The near plasma edge fiber gives the same frequencies but also additional ones: one in between 26 and 31 Hz and another one around 3 Hz [Fig. 8(d)] that corresponds to the strong modulation observed in Fig. 7. These observations underline that some spatial considerations must be made to interpret this P3 phase. The first local indication concerns the frequency that is three times lower than for electrical measurements. This point seems to signify that a phenomenon oscillating at around 94 Hz affects the plasma, and consequently the electrical measurement, but is detected only one time out of three by the optical fibers. One possible explanation is that a plasma modification either appears successively in different places, or moves and comes back in front of an optical fiber with a frequency of about 30 Hz. This plasma modification appears successively

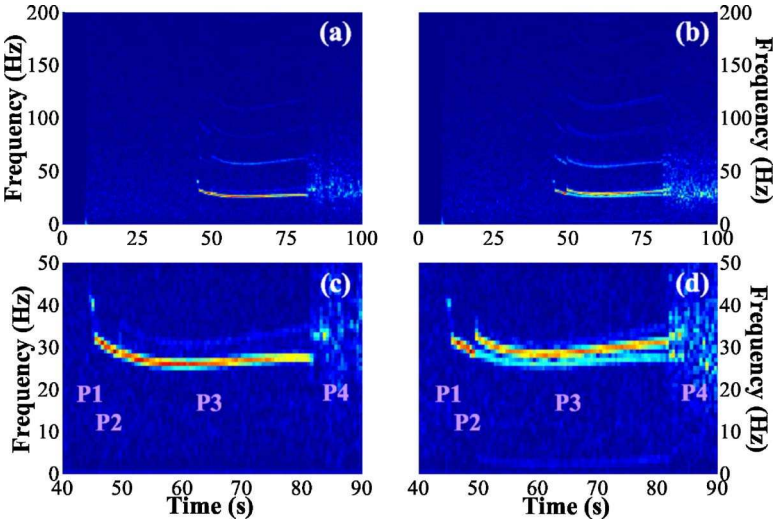

FIG. 8. (Color online) Spectrogram of optical measurements recorded (a) in the plasma center, (b) near the plasma edge. (c) Zoom of (a), (d) zoom of (b).

in distinct locations of the plasma because it is not detected at 94 Hz by any optical fiber looking at the plasma center or edge. Investigations concerning this hypothesis are currently underway using a high speed camera. The second local indication giving credit to this hypothesis is the difference between observations given by each optical fiber. Indeed, even if their Fourier spectrum is nearly similar and shows only small discrepancies, the recorded time series bring more information. Optical measurements performed by the near plasma edge fiber is in phase opposition with the ones in the center. This behavior, coupled with the fact that a stronger modulation is observed near the plasma edge, could confirm a possible motion, or appearance in different places, of a modified plasma region.

B. Chaotic regime

After three different ordered phases, DPGI enter in a chaotic regime P4 (Fig. 5 after 80 s) with a strong increase in DPGI amplitude (Fig. 3). Then, the amplitude slowly decreases during the whole phase. P4 is also characterized by structured oscillations appearing in a transient manner. These structured regions are identified by some bright spots on electrical and optical spectrograms. On time series they appear as bursts of order. In Fig. 9(a), electrical signals reveal a clear transition between the P3 phase and the chaotic regime. This regime change is indicated by an arrow and a burst of order is encircled. A zoom of this burst of order is shown in Fig. 9(b). During the chaotic regime, structured oscillations in electrical signals always appear following a three peak structure [see, for example, between 94 s and 94.04 s in Fig. 9(b)] that could be related to the three peaks observed in the P2 or P3 phases. Indeed, it could be a reemergence of these phases during the chaotic regime. To compare our observations with the filamentary mode,[7,8] a Fourier spectrum of the whole chaotic regime (from 80 to 405 s) has been performed in Fig. 10. For electrical signals [Fig. 10(a)], a noisy main frequency around 28 Hz is observed and is equal to the frequency at the end of the P2 phase, confirming the possible reemergence of this phase. This frequency corresponds to the occurrence frequency of the three peak structure regularly appearing during the chaotic regime [Fig. 9(b)]. Due to these structures, multiple frequencies (54 Hz, 83 Hz, and 107 Hz corresponding to the frequency between two successive peaks of one single three peak structure) are also detected in Fig. 10(a). For optical measurements [Fig. 10(b)], differences with electrical ones are the same than in the P3 phase: one optical oscillation corresponds to a three peak structure and consequently only the 28 Hz frequency appears [Fig. 10(b)]. These spectra are very similar to the one obtained for the filamentary mode[8] even if in our experiments the presence of more ordered domains is observed. Thus, we can surmise that the chaotic regime we observe could be similar to this filamentary mode.

C. High-frequency phase

In some experiments, the chaotic regime is suddenly interrupted by a strong frequency change (at 405 s in Figs. 3 and 4). Indeed, this phase P5 is not always observed but when it is present, its general characteristics are nearly always the same. This new phase appears after a continuous

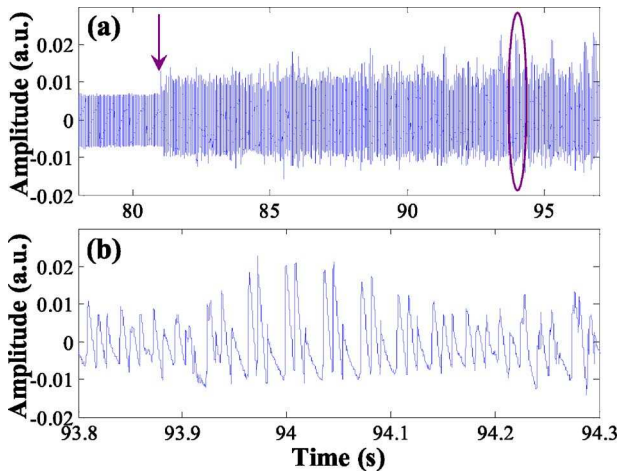

FIG. 9. (Color online) Electrical measurements: (a) transition between P3 and P4 phases and encircled burst of order, (b) zoom of the encircled part of (a).

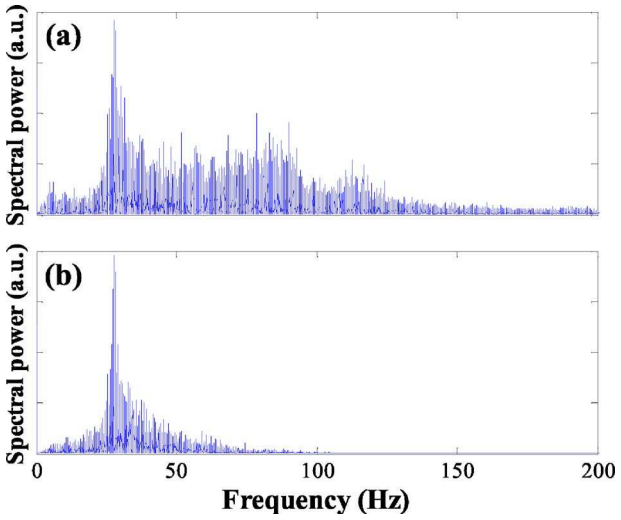

FIG. 10. (Color online). Fourier spectrum of the first chaotic regime on (a) electrical measurements, (b) central optical fiber measurements

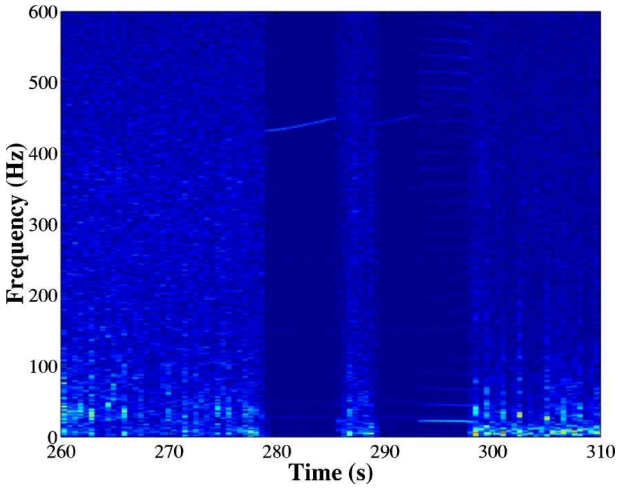

FIG. 12. (Color online) Spectrogram of a particular case of the high-frequency phase. This phase is interrupted by a chaotic regime and is transformed in regular oscillations just before turning again in a chaotic regime.

decrease of the P4 phase amplitude and is defined by a radical change in DPGI amplitude and frequency. Indeed, DPGI turn into a low-amplitude and high-frequency (around 500 Hz) oscillations as shown in Fig. 11. This change happens suddenly when no fast modifications in dust particle size and density are expected. Furthermore, the phase frequency increases with time. In Fig. 4, this increase is nearly linear but nonlinear behaviors have also been observed in certain cases. As previously mentioned, this phase is not always observed, which means relatively precise conditions must be fulfilled for its existence. This effect is well confirmed in the experiment described in Fig. 12, where this phase is interrupted before starting again. Small modifications in plasma or dust particle properties can easily turn the system from the high-frequency phase to the chaotic one. Furthermore, this P5 phase can also be transformed in regular oscillations as shown in Fig. 12 at $t=294$ s. From these experimental results it can be assumed that this high-frequency phase is a particular case of DPGI, obtained in a tight set of parameters and that can be easily turned in ordered or chaotic regimes.

D. Second chaotic regime

After the high-frequency phase, a second chaotic regime is usually observed. Two different types of this P6 phase are observed. The most usual is presented in Fig. 4 between 435 and 600 s. It corresponds to a phase similar to P4 but with more and more ordered regions. Figure 4 clearly shows that DPGI tend to stabilize to regular oscillations ($\simeq$600 s). This transition appears as a small and continuous increase in DPGI frequency. Nevertheless, some experiments show a slightly different behavior as in Fig. 13. Instead of slowly increasing, the frequency decreases and enters (still decreasing) in a regular oscillation phase. This behavior corresponds to void rotation in a horizontal plane, which is clearly evi-

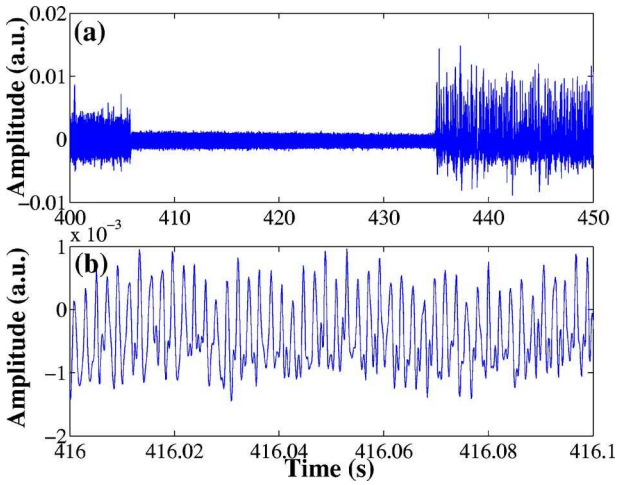

FIG. 11. (Color online) (a) Appearance of the high-frequency phase in between two chaotic regimes. (b) Zoom of (a).

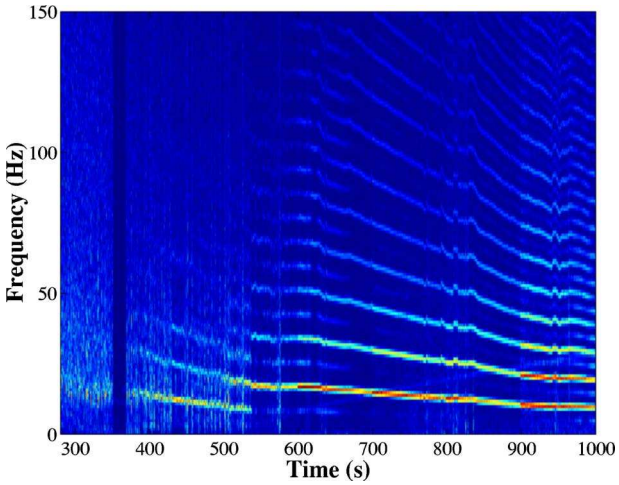

FIG. 13. (Color online) Spectrogram of a particular case of the second chaotic regime corresponding to void rotation in a horizontal plane.

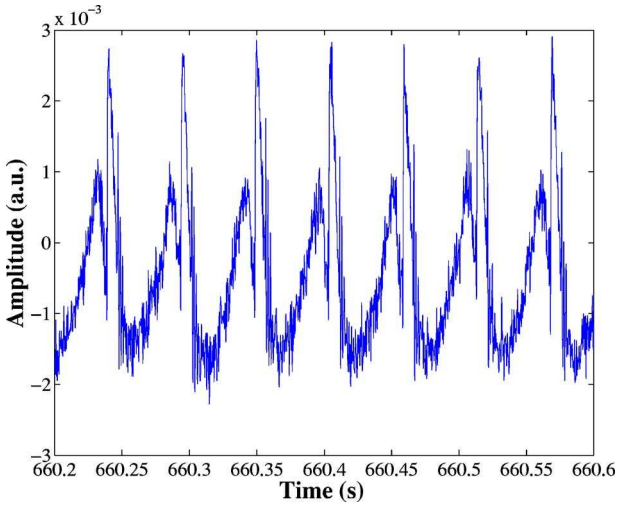

FIG. 14. (Color online) Electrical measurements corresponding to the final regular oscillation phase.

denced thanks to CCD camera images. The corresponding spectrogram is nearly similar to the one obtained in Ref. 8 and related to the great void mode.

E. Final regular oscillation phase

The final step of DPGI often corresponds to a regular oscillation phase characterized by a spectrogram with a typical frequency around 18 Hz (Fig. 4) and its harmonics. The corresponding electrical signal is shown in Fig. 14. The signal shape is in particular marked by a sharp peak appearing at each period. This shape is similar to what is obtained during the "heartbeat" instability,[23,38] which corresponds to regular contractions and expansions of the void size. At this stage of DPGI, this regular oscillation phase can last for minutes and is robust, meaning that once it is set up it does not turn in another regime. Optical measurements performed in the plasma center show an evolution similar to the electrical one except near the sharp peak region as observed in Ref. 36. Furthermore, the near edge optical fiber signal is in phase opposition with the central one (as in Ref. 36), emphasizing the similarity with the heartbeat instability.

V. DISCUSSION AND CONCLUSIONS

In this paper, self-excited instabilities induced by the formation of submicrometer dust particles are investigated. These instabilities appear when a sufficiently high dust particle density is reached. Instability frequency and shape change during the growth process and direct correlation with dust particle size and density cannot be easily deduced. Indeed, effects of both parameters on discharge behavior are difficult to separate: a high density of small particles can have roughly the same effect than a lower density of bigger particles, assuming that the total collection surface is identical and consequently the same amount of electrons can be captured. The only way to conclude on this point is to measure dust particle size and density but most commonly used *in situ* diagnostics cannot be implemented on our experimental setup. Furthermore, an easy systematic collection of dust particles coming from one and only one experiment is not possible in our reactor. DPGI reproducibility can be obtained only with very low base pressures not reached in the case of regular reactor opening. By comparing Fig. 1 with electrical characteristics obtained in silane based discharges,[39] we can speculate that DPGI occur during the "coalescence phase" and last during the so-called "surface deposition phase." These phases[40] are characterized by a significant amount of negatively charged dust particles strongly impacting on plasma stability. This comparison with dust particle growth process in silane based chemistry must be taken carefully because the analogy has not been strictly proven yet. From visual observations we know that when DPGI occur, dust particles are not detected yet by our video system and are certainly smaller than 100 nm. When instabilities stop, the dust particle size could be of a few hundreds of nanometers. The instability development follows a well-defined succession of phases that can be ordered or chaotic. At least seven different regimes have been evidenced and their occurrence is strongly dependent on plasma and dust particle properties. Complex transitions between different ordered phases or between ordered and chaotic ones have been evidenced and underline the nonlinear behavior of these instabilities. Two observed phases seem to correspond to the ones reported in previous papers.[7,8] These phases, called the filamentary mode and the great void mode, can be a part of a more general behavior described in this paper. The new phases described here underline the complexity of the phenomena behind observations and their high sensitivity to plasma and dust particle properties. Indeed, the complete scheme with seven phases can be observed in very specific experimental conditions usually encountered in this work. Striations (in our case, enhanced ionization regions appearing as bright spots or filaments) seem to be responsible for the different observed phases. The various regimes could be related to the way striations appear. Indeed, we can surmise that the ordered regimes could be striations appearing periodically and nearly at the same places. Following this hypothesis, the often observed three peak structure can correspond to three different striations. By analogy, chaotic regimes can be due to randomly appearing (in time and in space) striations. Optical measurements performed in different plasma positions bring to the fore that these instabilities need to be analyzed with spatial considerations. Differences with works reported in Refs. 7 and 8 can be the consequence of different plasma and/or dust particle properties, geometrical considerations, or gas flow. Furthermore, our observations show that void formation is not a consequence of these instabilities as proposed in Ref. 24. The void can be formed with or without instabilities preceding its appearance. In some conditions, the void is formed before instability begins. In this case, the instability evolution scheme does not describe all the phases presented here. Similarities between the final regular oscillation phase and the heartbeat instability concerning the void region have been observed. It could indicate that dust particle growth instabilities and the heartbeat instability could be different aspects of the same physical phenomena.

ACKNOWLEDGMENTS

The PKE-Nefedov chamber has been made available by the Max-Planck-Institute for Extraterrestrial Physics, Germany, under the funding of DLR/BMBF under Grant No. 50WM9852. The authors would like to thank S. Dozias for electronic support, J. Mathias for optical support, and Y. Tessier for experimental support.

This work was supported by CNES under contract No. 793/2000/CNES/8344.

[1] A. Bouchoule, A. Plain, L. Boufendi, J.-P. Blondeau, and C. Laure, J. Appl. Phys. **70**, 1991 (1991).
[2] Y. Watanabe, M. Shiratani, Y. Kubo, I. Ogawa, and S. Ogi, Appl. Phys. Lett. **53**, 1263 (1988).
[3] A. Howling, C. Hollenstein, and P. Paris, Appl. Phys. Lett. **59**, 1409 (1991).
[4] G. Jellum and D. Graves, J. Appl. Phys. **67**, 6490 (1990).
[5] W. Yoo and C. Steinbrüchel, J. Vac. Sci. Technol. A **11**, 1258 (1993).
[6] B. Ganguly, A. Garscadden, J. Williams, and P. Haaland, J. Vac. Sci. Technol. A **11**, 1119 (1993).
[7] G. Praburam and J. Goree, Phys. Plasmas **3**, 1212 (1996).
[8] D. Samsonov and J. Goree, Phys. Rev. E **59**, 1047 (1999).
[9] M. Mikikian, L. Boufendi, A. Bouchoule, H. Thomas, G. Morfill, A. Nefedov, V. Fortov, and the PKE-Nefedov Team, New J. Phys. **5**, 19.1 (2003).
[10] R. Roth, K. Spears, G. Stein, and G. Wong, Appl. Phys. Lett. **46**, 253 (1985).
[11] G. Selwyn, J. Singh, and R. Bennett, J. Vac. Sci. Technol. A **7**, 2758 (1989).
[12] L. Boufendi and A. Bouchoule, Plasma Sources Sci. Technol. **11**, A211 (2002).
[13] P. Roca i Cabarrocas, P. Gay, and A. Hadjadj, J. Vac. Sci. Technol. A **14**, 655 (1996).
[14] S. Tiwari, F. Rana, H. Hanafi, A. Hartstein, and E. Crabbé, Appl. Phys. Lett. **68**, 1377 (1996).
[15] C. Szopa, G. Cernogora, L. Boufendi, J. Correia, and P. Coll, Planet. Space Sci. **54**, 394 (2006).
[16] B. Walch, M. Horanyi, and S. Robertson, IEEE Trans. Plasma Sci. **22**, 97 (1994).
[17] A. Melzer, T. Trottenberg, and A. Piel, Phys. Lett. A **191**, 301 (1994).
[18] C. Arnas, M. Mikikian, and F. Doveil, Phys. Rev. E **60**, 7420 (1999).
[19] L. Boufendi, J. Gaudin, S. Huet, G. Viera, and M. Dudemaine, Appl. Phys. Lett. **79**, 4301 (2001).
[20] M. Cavarroc, M. Jouanny, K. Radouane, M. Mikikian, and L. Boufendi, J. Appl. Phys. **99**, 064301 (2006).
[21] J. Dorier, C. Hollenstein, and A. Howling, J. Vac. Sci. Technol. A **13**, 918 (1995).
[22] G. Morfill, H. Thomas, U. Konopka, H. Rothermel, M. Zuzic, A. Ivlev, and J. Goree, Phys. Rev. Lett. **83**, 1598 (1999).
[23] M. Mikikian and L. Boufendi, Phys. Plasmas **11**, 3733 (2004).
[24] J. Goree, G. Morfill, V. Tsytovich, and S. Vladimirov, Phys. Rev. E **59**, 7055 (1999).
[25] M. Akdim and W. Goedheer, Phys. Rev. E **65**, 015401 (2001).
[26] V. Tsytovich, V. Vladimirov, G. Morfill, and J. Goree, Phys. Rev. E **63**, 056609 (2001).
[27] G. Gozadinos, A. Ivlev, and J.-P. Boeuf, New J. Phys. **5**, 32.1 (2003).
[28] K. Avinash, A. Bhattacharjee, and S. Hu, Phys. Rev. Lett. **90**, 075001 (2003).
[29] C. Zafiu, A. Melzer, and A. Piel, Phys. Plasmas **10**, 1278 (2003).
[30] A. Ivlev, S. Zhdanov, S. Khrapak, and G. Morfill, Phys. Rev. E **71**, 016405 (2005).
[31] M. Kretschmer, S. Khrapak, S. Zhdanov, H. Thomas, G. E. Morfill, V. Fortov, A. Lipaev, V. Molotkov, A. Ivanov, and M. Turin, Phys. Rev. E **71**, 056401 (2005).
[32] S. Vladimirov, V. Tsytovich, and G. Morfill, Phys. Plasmas **12**, 052117 (2005).
[33] V. Land and W. Goedheer, New J. Phys. **8**, 8 (2006).
[34] A. Nefedov, G. Morfill, V. Fortov, H. Thomas, H. Rothermel, T. Hagl, A. Ivlev, M. Zuzic, B. Klumov, A. Lipaev, *et al.*, New J. Phys. **5**, 33.1 (2003).
[35] M. Mikikian, L. Boufendi, and A. Bouchoule, in *Proceedings of the 30th EPS Conference on Controlled Fusion and Plasma Physics*, St. Petersburg, edited by R. Koch and S. Lebedev (2003), Vol. 27A of ECA, pp. O–3.1B, http://epsppd.epfl.ch/StPetersburg/PDF/O3-001B.PDF.
[36] M. Mikikian, M. Cavarroc, N. Chaumeix, and L. Boufendi, in *Proceedings of the 31st EPS Conference on Plasma Physics*, London, edited by P. Norreys and H. Hutchinson (European Physical Society, Petit-Lancy, 2004), Vol. 28G of ECA, pp. O–2.13, http://epsppd.epfl.ch/London/pdf/02_13.pdf.
[37] M. Mikikian, M. Cavarroc, and L. Boufendi, in *New Vistas in Dusty Plasmas*, edited by L. Boufendi, M. Mikikian, and P. Shukla, AIP Conf. Proc. No. 799 (AIP, Melville, NY, 2005), p. 319.
[38] M. Mikikian, M. Cavarroc, and L. Boufendi, in *New Vistas in Dusty Plasmas*, edited by L. Boufendi, M. Mikikian, and P. Shukla, AIP Conf. Proc. No. 799 (AIP, Melville, NY, 2005), p. 323.
[39] M. Cavarroc, M. Mikikian, G. Perrier, and L. Boufendi, Appl. Phys. Lett. **89**, 013107 (2006).
[40] A. Bouchoule, L. Boufendi, J. Hermann, A. Plain, T. Hbid, G. Kroesen, and W. W. Stoffels, Pure Appl. Chem. **68**, 1121 (1996).

New Journal of Physics
The open-access journal for physics

Self-excited void instability in dusty plasmas: plasma and dust cloud dynamics during the heartbeat instability

M Mikikian, L Couëdel, M Cavarroc, Y Tessier and L Boufendi
GREMI, Groupe de Recherches sur l'Energétique des Milieux Ionisés, UMR6606, CNRS/Université d'Orléans, 14 rue d'Issoudun, BP6744, 45067 Orléans Cedex 2, France
E-mail: maxime.mikikian@univ-orleans.fr

New Journal of Physics **9** (2007) 268
Received 30 March 2007
Published 15 August 2007
Online at http://www.njp.org/
doi:10.1088/1367-2630/9/8/268

Abstract. When a three-dimensional dust cloud is present in a plasma, a dust-free region, called a void, is usually obtained in the plasma centre. Under certain conditions, this region exhibits a self-excited unstable behaviour consisting of successive contractions and expansions of its size. In this paper, this low frequency instability (few Hz), called a 'heartbeat', is characterised by various diagnostics. Electrical and optical measurements both correlated with high speed imaging brought to the fore the main features of this instability. Forces involved in the void existence are an inward electrostatic force and an outward ion drag one. The force balance ensures an open void but this equilibrium can be disturbed, leading to the observed instabilities. As these forces are strongly dependent on local ionisation conditions, correlations between physical processes in the plasma volume and the dust cloud motion are investigated through experimental results.

PII: S1367-2630(07)47353-0

Contents

1. Introduction

Dusty plasmas are relatively complex systems where new phenomena arise from the presence of solid dust particles trapped inside the plasma. Usually, this trapping is a consequence of the negative charge acquired by the dust particles [1]–[6] immersed in a medium partly composed of free electrons. The full dust particle dynamics is then described by charge dependent forces (mainly electric and ion drag forces) and other ones like gravity, neutral drag and thermophoresis. Relative amplitudes of these forces are strongly dependent on the dust particle size. In the micrometre range, dust particles are usually directly injected in the plasma volume. Their weight is non-negligible and some phenomena are only observed under microgravity conditions [7, 8]. Nevertheless, their big size allows an easy and precise visualisation in laboratory experiments. In the submicrometre range, dust particles are usually grown in the plasma using methods based on reactive gases or material sputtering.

Reactive gases are used due to their ability to form dust particles by following a rather complicated succession of growth phases. One of the most studied and well-known reactive gas is silane (SiH_4) [9]–[15]. The interest for silane based chemistry is mainly due to its implication in microelectronics and/or nanotechnology. Indeed, in the late 1980s, dust particle formation in the gas phase has been evidenced in reactors used for silicon based device fabrication [9, 16]. In some processes, cleanliness is a major requirement and a lot of studies began for understanding dust particle formation and growth in order to avoid their deposition. More recently, silicon nanocrystal formation [17] became of high interest for their incorporation in thin films in order to improve their properties. Indeed, their use in solar cell technology enhances optoelectronic properties of deposited films [18]. Single electron devices (SED) like transistors [19] or memories [20] can also be built, thanks to these silicon nanocrystals. Dust particle formation in hydrocarbon based gases like methane (CH_4) [21]–[23] or acetylene (C_2H_2) [21, 22, 24, 25] has also been studied. Indeed, CH_4 and C_2H_2 are used for deposition

of diamond-like carbon (DLC) films [26] or nanocrystalline diamond [27] used in industry for their unique properties like extreme hardness. Hydrocarbon gases are also of great interest for the astrophysical community dealing with planet atmospheres like Titan, where dust particles are created from a mixture of methane and nitrogen [28].

Another process for dust particle production is material sputtering [29]–[32]. This phenomenon can appear in industrial reactors and also in fusion devices [33] like Tore Supra [34] where graphite walls can be severely eroded by ion bombardment. Produced dust particles can strongly limit performances of the fusion plasma. This aspect is of great importance for the future ITER reactor.

Dust particles levitating in the full plasma volume can be obtained under microgravity (for micrometre dust particles) or in the laboratory (for submicrometre dust particles). Usually, the three-dimensional dust cloud exhibits a specific feature consisting of a centred egg-shaped region free of dust particles. This region, called a 'void' [7, 31, 32], [35]–[47], seems to be controlled by an equilibrium between the charge dependent forces (inward electrostatic and outward ion drag forces). This stable state is sometimes disturbed and void size oscillation can occur. This self-excited instability is named the 'heartbeat' instability [36, 46, 48, 49]. It has been previously observed during microgravity experiments with injected micrometre dust particles and has since also been studied in the laboratory with grown submicrometre dust particles [49]–[52]. In these last experiments, investigations of the heartbeat instability have been performed using both electrical and spatially resolved optical diagnostics. These measurements allowed to identify complex behaviours in recorded signals roughly related to dust particle motion. Furthermore, the threshold behaviour of this self-excited instability has been brought to the fore [51, 52]. Nevertheless, the presence of a sharp peak in electrical measurements and its absence in optical ones was still unclear. Further investigations have been conducted using high speed imaging to record dust particle cloud motion. These preliminary results gave first insights concerning dust cloud motion and void size evolution correlated with electrical signals [51, 52]. In the present paper, new results on the heartbeat instability are obtained thanks to a second high speed imaging experiment. Behaviour of both dust cloud and plasma glow is investigated and correlations between both types of data are deduced. These results are compared to electrical measurements and previous spatially resolved optical ones. The void dynamics during the instability is now better characterised and, for example, the sharp peak presence can be correlated with plasma glow changes.

2. Experimental set-up

2.1. Reactor

Experiments are performed in the Plasma Kristall Experiment (PKE)-Nefedov chamber [8, 32]. The plasma is produced by a capacitively coupled radio frequency (rf) discharge operating in push–pull mode at 13.56 MHz. The planar parallel electrodes are 4 cm in diameter and are separated by 3 cm. In this chamber, argon is introduced to a typical pressure of 1.6 mbar and the plasma is ignited with a rf power of typically 2.8 W. Dust particles are grown by sputtering a polymer layer deposited on the electrodes and constituted of previously injected melamine formaldehyde dust particles.

2.2. Diagnostics

Grown dust particles are observed by laser light scattering using a thin laser sheet produced by a laser diode at 685 nm and three standard charge coupled device (CCD) cameras (25 frames per second) equipped with narrow-bandwidth interference filters. Two of these cameras record the scattered light at 90° with different magnifications. The third one looks at the cloud with an angle lying approximately between 20° and 30° with respect to the incident laser direction. This camera allows the observation of grown dust particles when their size is too small to observe them at 90°.

Plasma and dust particle cloud behaviours are strongly linked and a modification in one of these media is usually reflected in the other. Therefore, diagnostics able to analyse both systems are used in order to better characterise the heartbeat instability.

The first one consists of the measurement of the time evolution of the amplitude of the discharge current fundamental harmonic. Indeed, this diagnostics is representative of global changes in plasma properties and can be related to electron density variations. It allows to monitor the total current during the various phases of the instability very easily. Thus, it is used as our reference diagnostics. It shows that the heartbeat instability has different signatures depending on the pressure, power and dust particle density [49].

The second diagnostics is based on spatially resolved optical measurements performed in two different ways. The time evolution of either the intensity of an argon line or the total plasma light is recorded in different plasma regions. For the total plasma light recording, five optical fibres are horizontally aligned (separated by 5 mm) with a spatial resolution of about 3 mm. This diagnostic is complementary to the electrical one because it can detect any plasma motion or local behaviours that cannot be evidenced by a global measurement.

The third diagnostics consists of high speed imaging. The observed instability oscillates at relatively low frequencies (10–200 Hz) but too high to be finely characterised by standard CCD cameras at 25 frames per second. Indeed, as previously observed [49], some features of the instability, like the sharp peak, take place during a typical time scale of about 1 ms. A high speed video camera system with 1789 frames per second (Mikrotron MC 1310) is used to observe either the plasma glow or the dust cloud. Thus, two successive frames are separated by around 560 μs. For the last observation, the high speed camera takes the place of the third standard CCD camera in order to record more light scattered by the dust cloud.

As already mentioned, the heartbeat instability has different signatures and measurements show a wide variety of frequencies and shapes. In the following sections, both dust cloud and plasma glow will be analysed in two different cases considered as sufficiently different to cover a wide range of experimental observations: a low repetition rate one (contraction–expansion sequences are well separated and original conditions, i.e. stable void, are nearly restored between each sequence) and a high repetition rate one (continuous motion of the void). The high repetition rate occurs when the instability is well established (higher values of injected rf power) whereas low repetition rate occurs at lower powers when the instability tends to slow down before stopping. Plasma glow will be mainly discussed through its intensity (thus ‘glow intensity’ is referred as ‘glow’ in the following), except when spatial concerns are well specified. Following results will mainly concern the fully developed instability. Another interesting phenomenon, consisting of failed contractions [51, 52] appearing near the instability existence threshold, will be analysed in a further article.

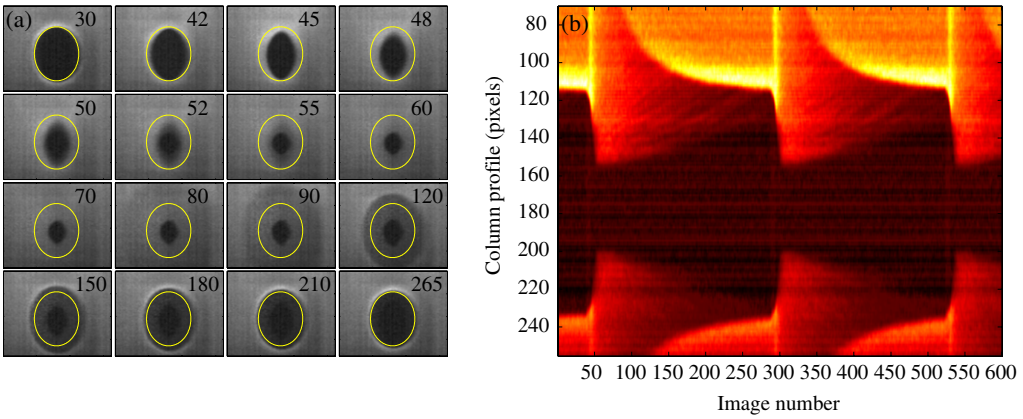

Figure 1. Heartbeat instability for a low repetition rate observed on the dust cloud. (a) Some images of the void region during one contraction–expansion sequence. The yellow ellipse delineates position of the stable open void. (b) Time evolution of central column profile (vertical line passing through the void centre) constructed from the entire video in false colours (from dark red to bright yellow) (see also movie 1, 3.9 MB MPEG).

3. Dust cloud and plasma glow behaviours near the void region

In order to characterise the heartbeat instability, a first approach consists of a direct visualisation of the void with its surrounding dust cloud. Typical unstable voids have a size of about a few millimetres. Beyond a certain size, voids are usually stable and no instability has been observed in the explored parameter range. Indeed, in this case, their stability is not disturbed even by decreasing the pressure or increasing the power (these changes are known to be able to initiate the heartbeat instability [49]).

3.1. Sequences with a low repetition rate

A video corresponding to a low repetition rate and showing three successive contraction–expansion sequences is available in figure 1. Some extracted images from the first sequence are shown in figure 1(a). Image aspect ratio is distorted due to the view angle compressing the horizontal direction. Image numbers appear on the top right part of each image. The drawn ellipse represents the position of the stable open void determined from image 30. Small but detectable motion starts at image 40 (not shown) and clearly appears at image 42 where dust cloud boundaries are clearly inside the drawn ellipse. Contraction lasts up to image 55 where the void reaches its minimum size. From this instant, the empty inner part slowly increases in size while a light grey corona region (i.e. lower dust density region) starts to be detected in image 80 and slowly reduces in size. These two regions meet and the stable open void state is nearly reached anew in image 265.

In order to better depict this contraction–expansion sequence, the time evolution of a column profile is shown in figure 1(b). To construct this false colour image, the vertical line passing through the void centre is extracted from each video image. Time is represented by image number in the x-axis and column profile is given in the y-axis. Using the video as a reference, this representation is of interest in that it gives in one single image a clear

characterisation of the instability in both time and space. Low dust density regions appear dark while high dust density ones appear bright. Three contractions and two expansions are clearly evidenced and give a frequency of about 7 Hz. For the first sequence, images 1–40 show the higher dust density region usually observed in the void boundaries. Then, the contraction takes place and the void reaches its minimum size approximately 2.5 times smaller than the stable void size. At this moment, the two previously described phenomena (size increase of the dark inner part and size decrease of an intermediate grey corona region) are well resolved in time. The regular size increase of the inner part can be directly correlated to the void size increase assuming that the term 'void' stands for the null dust density region. From figure 1, the behaviour of the corona region seems to correspond to the motion of dust particles attracted to the plasma centre during the contraction and going back to their original stable position. This motion is characterised by a moving boundary between a region of high dust density and another one of low dust density. It appears that the speed of this moving boundary decreases as it approaches the original void position. The dust particles which are the closest to the centre, react last with the smallest speed. Furthermore, the corona region in its maximum extension is larger than the size of the stable void indicating that the instability affects the dust cloud over a long distance and not only in the close vicinity of the void. Collective motions can take place on long distances due to the strong interaction between dust particles and their strong coupling with plasma changes. Finally, figure 1(b) shows that inner and corona regions meet (around image 280) and the high dust density boundaries are restored just before another contraction occurs.

To complete these observations, the interference filter is removed from the high speed camera in order to record plasma glow evolution without changing the camera position. The obtained image series is acquired approximately 2 s after the one presented in figure 1, checking that the instability does not change neither in frequency nor in shape. In order to synchronise dust cloud images with plasma glow ones, small residual plasma glow signal passing through interference filter is used (slightly visible in figure 1(b) in the black inner part of the void but not allowing analysis). Electrical measurements are used to check that instability characteristics remain unchanged. Typical images are presented in figure 2(a). In order to bring out changes, a reference image is subtracted and false colours are used. Plasma glow images shown in figure 2(a) correspond to the dust cloud ones shown in figure 1(a). For comparison, the same ellipse as in figure 1(a) is superimposed on the glow images. By correlating both dust cloud and glow images, it clearly appears that the void contraction seems to correspond to a glow enhancement in the plasma centre. Intermediate images of the glow variation are shown in figure 2(b). It appears that the concerned plasma region is bigger than the original void region even if maximum glow values are inside the void. This aspect can explain why the light grey corona region observed in figure 1 has a maximum extension bigger than the stable void. In fact, the first image showing the glow increase is image 10 in figure 2(b), where the bright region is already bigger than the drawn ellipse. Due to camera speed limitation, some data are missing between images 9 and 10. Consequently it cannot be concluded if, at the early beginning, the enhancement is bounded by the void and then propagates, or if it concerns directly a bigger size region. After reaching its maximum value (around image 13), plasma glow decreases and reaches a minimum below the mean glow value (darker image 19 in figure 2(a)). Certainly due to dust particle inertia, the void continues to shrink (figure 1(a)) but when the central glow (i.e. ionisation and consequently ion drag force) starts to increase slowly (from image 26 in figure 2(a) corresponding to image 55 in figure 1(a)), the contraction stops and expansion occurs.

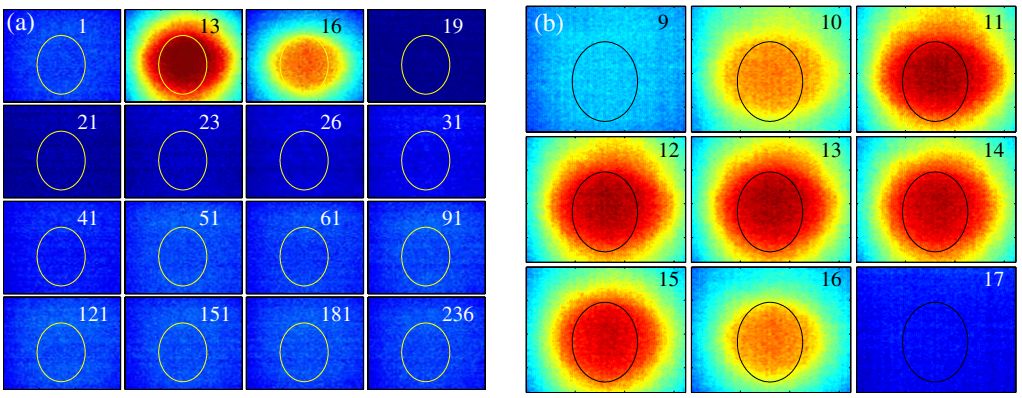

Figure 2. Heartbeat instability for a low repetition rate observed on the plasma glow. (a) Some images of the void region (in false colours from dark blue to red) during one contraction–expansion sequence (image 1 corresponds to image 30 of figure 1 and so on). The yellow ellipse delineates position of the stable open void. (b) Intermediate images of (a) during fast plasma glow modifications.

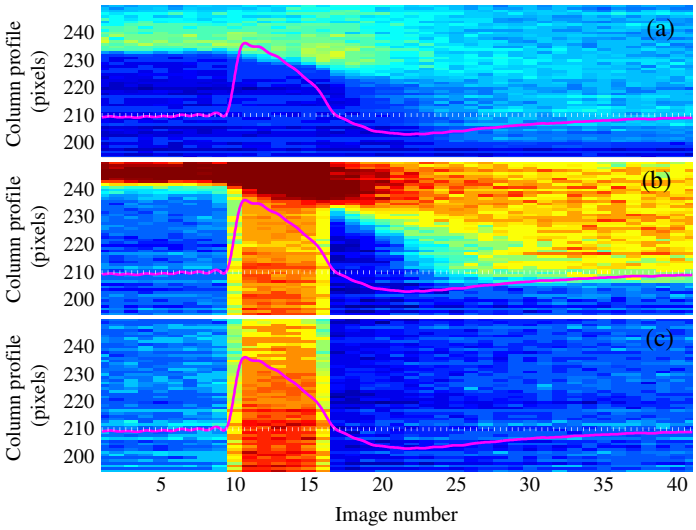

Figure 3. Heartbeat instability for a low repetition rate: electrical measurements superimposed on column profiles from (a) only dust cloud; (b) dust cloud and plasma glow, (c) only plasma glow. Parts (a), (b) and (c) in false colours (from dark blue to red).

Column profiles of these different series can be compared. Figure 3 shows synchronised profiles obtained from videos showing (a) the dust cloud (laser and camera with interference filter), (b) dust cloud and glow (laser and camera without interference filter) and (c) plasma glow (neither laser nor interference filter). Electrical measurements are superimposed with their mean value (dotted line) corresponding to the stable open void. In figure 3(c) it appears that there is a good correlation between plasma glow and electrical measurements as the main variations are related. The fast signal increase corresponds to glow enhancement. It is followed by a decrease in both sets of data. A small shoulder appearing in electrical measurements (slope change) is

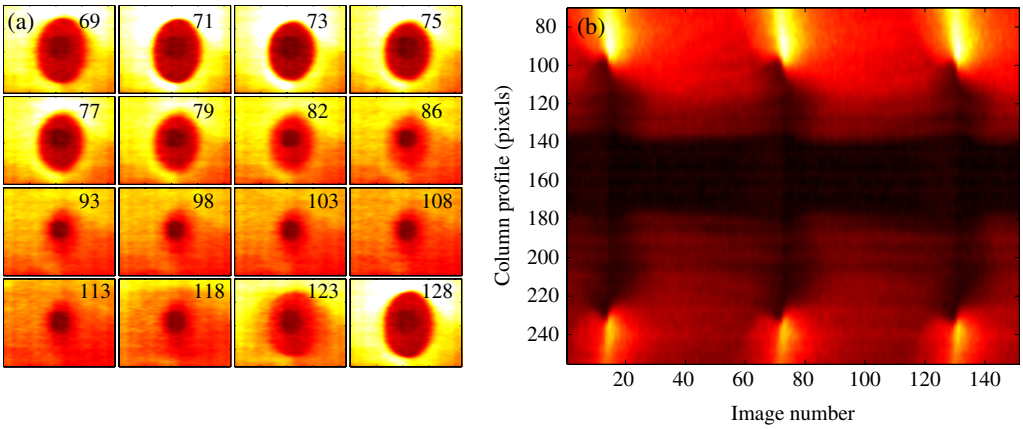

Figure 4. Heartbeat instability for a high repetition rate observed on the dust cloud: (a) some images of the void region (in false colours from dark red to bright yellow) during one contraction–expansion sequence; (b) time evolution of central column profile constructed from the entire video (see also movie 2, 2.3 MB).

related to a more drastic decrease of the central plasma glow. Then, the following minimum values of both data are close in time. After this point, the next plasma glow increase towards the mean state is well observed in electrical measurements slowly tending towards the mean value. As mentioned, global variations are similar but some discrepancies exist due to the fact that electrical measurements are integrated on all the plasma volume, and contain information on plasma variation occurring outside the plasma centre. This aspect will be explored in section 4, where a precise analysis of the entire plasma glow is performed. Concerning the dust cloud, the void contraction is related to glow and electrical signal increase (figures 3(a) and (b)), meaning that it corresponds to ionisation increase in the plasma centre. Nevertheless, it can be observed that contraction continues even when the electrical signal starts decreasing and is still not stopped when electrical measurements and plasma glow are below their original value. It confirms the direct comparison between dust cloud and plasma glow performed through figures 1 and 2.

3.2. Sequences with a high repetition rate

Analysis of a high repetition rate sequence is more fussy due to the fast and constant motion of the dust cloud without any clear stable position giving a fixed reference. A movie is available in figure 4 and in the same way as in the low repetition rate case, extracted images and column profile are given respectively in figure 4(a) and (b). In order to increase contrast, false colours are also used for extracted images. The constant motion clearly appears: no horizontal bright regions, corresponding to high dust density void boundaries, are observed in figure 4(b). This figure gives a frequency instability of about 31 Hz. Furthermore, the inner part of the void region, which is never filled with dust particles, exhibits only small variations. Indeed, all the motion takes place in the low dust density region between the dense dust cloud and the void inner part. From the nearly isolated case (figure 1), this region has been identified to consist of dust particles going back to their original position. In the high repetition rate case, the new

contraction occurs while dust particles from the previous contraction are still inside the void and try to reach their original position. Indeed, a new contraction starts around image 69 of figure 4(a) (complex motions do not allow precise determination) while dust particles are still inside the void region. At this time the plasma glow is close to its maximum value in the centre (determined from a plasma glow video correlated to the present one). This complex behaviour leads to the relatively constant regions (black inner part and grey intermediate part) observed in figure 4(b). The dust cloud is always moving even so spatial dust density appears more or less constant.

3.3. Asymmetry in void contraction

Another interesting phenomenon concerning dust cloud motion during the heartbeat instability, is the observable delay appearing in the response of horizontal and vertical directions. Indeed, in some conditions (currently not clearly defined) the dust cloud shrinks horizontally before shrinking vertically [51, 52]. As an example, a record containing both dust cloud and plasma glow information has been performed for a sequence where a stable open void suddenly starts a size oscillation. First and second contraction–expansion sequences are shown in figure 5 where a movie can also be found. Image 135 clearly shows the stable open void with the corresponding drawn ellipse. In image 142 plasma glow starts increasing and reaches its maximum value at 144. In this last image, it appears that the plasma glow enhancement affects a region bigger than the void size and correlation with the corona region well observed in figure 1 can be suggested again. This hypothesis is correct assuming that the intensity increase in the surrounding dust cloud is entirely due to plasma glow changes and not due to any dust density modification. Thanks to the drawn ellipse, it clearly appears that the void shrinks first in the horizontal direction (starting from image 143) and then in the vertical one (starting around image 147). As images are already compressed in the horizontal direction, a detectable motion in this direction clearly indicates a real dust cloud response and cannot be an optical illusion. The plasma glow reaches its minimum value in image 148 and, as already observed, the void continues to shrink to its minimum size in image 155. From this point, the void inner part slowly increases in size and the grey intermediate region, constituted of dust particles going back to their original position, becomes gradually visible. The next contraction occurs before the original state has been completely reached again (image 241).

These various steps are well observed on the column profile shown in figure 6(a). For better understanding, temporal evolution of plasma glow in the central pixel of the void is superimposed at the bottom of the image. The stable open void is accurately defined with its constant size and its high dust density boundaries (between images 100 and 142). When plasma glow increases, the void shrinks. Its minimum size is reached while plasma glow in the centre has already reached its minimum value and has started to slowly increase again. Then, the glow stays relatively constant in the void centre while dust particles are expelled to their original position. It clearly appears that the void did not reach its original size when the new glow increase occurs. This effect is traduced, firstly by the dark inner part which does not rejoin the position of the stable void and secondly by the intermediate corona region which is bigger than the original void size. This last point means that the ‘wave front’ formed by returning dust particles is still moving towards the original void boundaries. The speed of this wave front appears to slow down when approaching the original conditions. Furthermore, it is clearly visible that the instability is in a setting up phase. Indeed, starting from a stable open void,

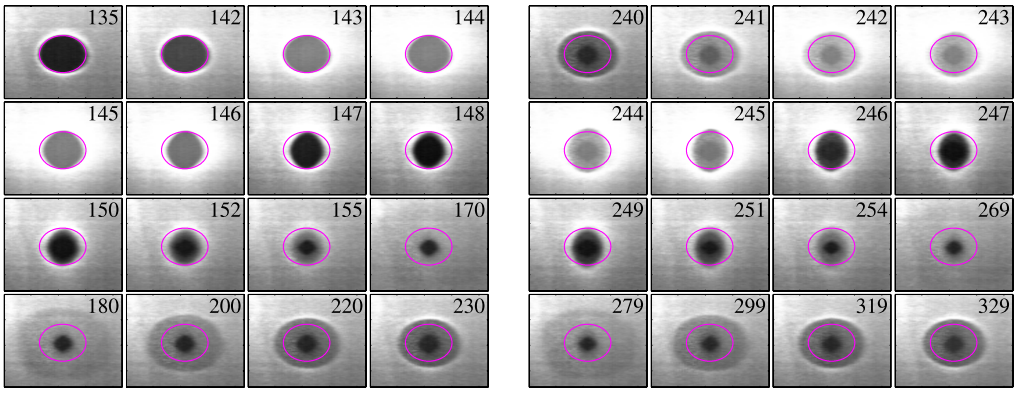

Figure 5. Simultaneous record of dust cloud and plasma glow in the void region during the setting up of the heartbeat instability. From image 135: stable open void (delineated by a pink ellipse) followed by a first contraction, and new contraction at image 241 while original conditions are not restored (see also movie 3, 2.6 MB).

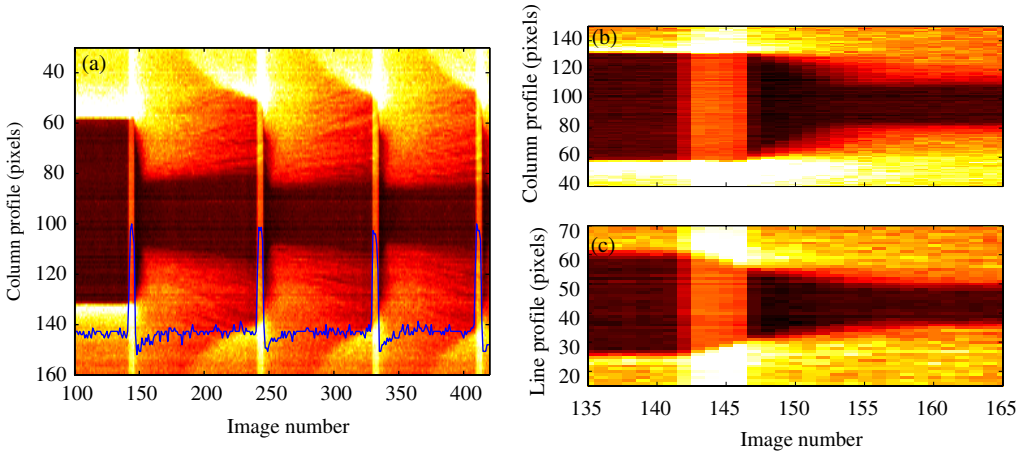

Figure 6. (a) Column profile (in false colours from dark red to bright yellow) calculated from image series presented in figure 5 with central plasma glow evolution superimposed (blue curve corresponding to line 95 of figure 6(a)), (b) zoom of (a), (c) corresponding line profile.

the characteristics of first and second contraction–expansion sequences are slightly different in terms of minimum void size and re-opening time duration. Concerning the time delay appearing in the vertical direction (as observed in figure 5) it can also be evidenced by comparing column and line profiles extracted from the video. These two profiles are shown respectively in figures 6(b) and (c). Previous results also showed that some correlation can be found between the different times of collapse and different slopes in electrical measurements [52]. Reasons why this effect appears in some cases are unclear due to a lack of statistics and spatiotemporal limitations of video acquisition. Nevertheless, one possible explanation is related to reactor geometry where confining conditions are different in the two directions. The electrode diameter is around 4 cm and glass boundaries are at approximately 3 cm of the electrode edges.

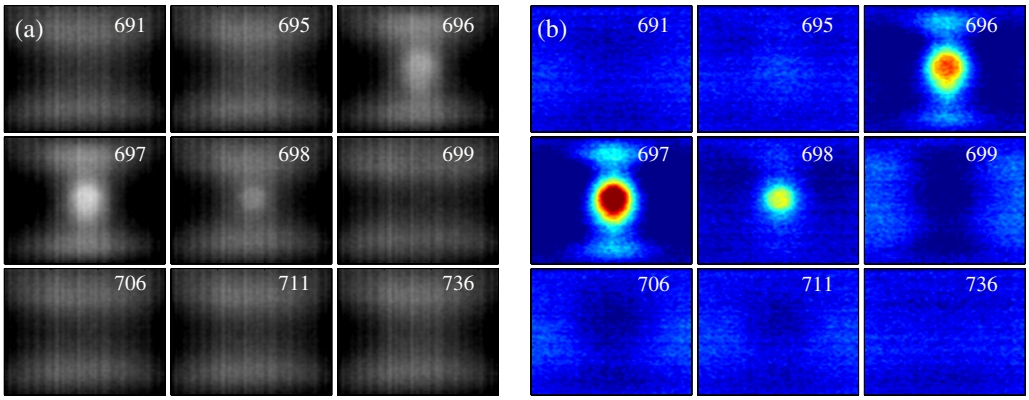

Figure 7. Heartbeat instability for a low repetition rate observed on the total plasma glow: (a) some images in true colours during one contraction–expansion sequence, (b) same images as in (a) with post-processing and false colours (from dark blue to red).

Consequently, the plasma usually extends beyond the electrodes towards the lateral sides. The plasma width is then nearly twice as large as the height and it is nearly the same for the trapped dust cloud and the void. No strong electrostatic barrier exists due to the distance to the glass boundaries, thus, plasma and void modifications in these directions are relatively free. On the contrary, the electrodes imposed a strong electrostatic barrier and vertical modifications and motions are then drastically controlled by the sheaths.

4. Plasma glow behaviour in the whole discharge

Plasma glow in the whole interelectrode volume is recorded during the instability in the two different cases (low and high repetition rate). This analysis is performed in order to understand global evolution of the plasma and not only central part behaviour as in the previous section. It can identify some side effects already suggested (relation between a sharp peak in electrical measurements and brighter glow regions near plasma horizontal boundaries [49, 51]) and that are inaccessible through the analysis presented in section 3.

4.1. Sequences with a low repetition rate

The total plasma glow recorded by fast imaging during a contraction–expansion sequence is shown in figure 7(a). Both bright presheath regions are clearly evidenced on the upper and lower parts of the images (electrodes are not visible). Before the contraction–expansion sequence (stable situation with an open void), the central plasma region is relatively uniform and not very bright (image 691). Then, the glow increases fast and concentrates in the discharge centre before disappearing and leaving a darker region in the centre as observed in the previous section. This scheme is better evidenced by representing the same images in false colours and by subtracting a reference image (stable situation) as shown in figure 7(b). The relatively homogeneous glow (image 691) changes into a bright (i.e. higher ionisation) central region and dark (i.e. lower ionisation) edges during the contraction (image 697). A reverse situation (dark centre and bright

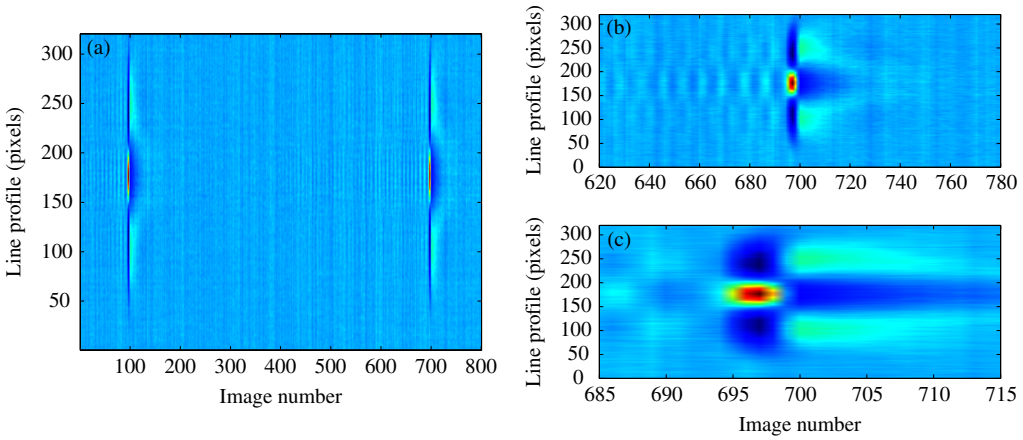

Figure 8. (a) Line profile (in false colours from dark blue to red) calculated from the image series presented in figure 7; (b) and (c) are different magnifications of (a).

edges) starts just before the re-opening (image 699). Then, the glow becomes slowly uniform again (image 736).

Time evolution of a line profile is presented in figure 8(a) and magnified in figures 8(b) and (c). To construct this false colour image, the horizontal line passing through the middle of the discharge is extracted from each video image. This line has been chosen because it passes through the region of biggest changes. In order to extract changes occurring during the instability, a temporal average value is subtracted. A smoothing filter is also applied for noise reduction and better delimitation of changing regions. Column profiling has also been performed for the plasma glow analysis but no original information has been extracted partly due to the limiting conditions imposed by electrodes.

Nearly isolated contraction–expansion sequences often have a short time duration. Figure 8 shows an instability frequency of about 3 Hz. In between each sequence, original conditions have time to be restored. From figures 8(b) and (c), plasma glow behaviour is well observed and its complete evolution analysis is more easily performed than from direct images like in figure 7. First, some small oscillations are observed before the real sequence. This phenomenon has already been observed [51, 52] and corresponds to failed contractions appearing sometimes near the instability existence threshold. This behaviour does not change the following analysis and will be described in a future article. Figure 8 confirms that when the void contracts, the plasma glow suddenly concentrates in the centre leaving dark border regions. The void re-opening occurs during the reverse situation with two symmetrical bright regions surrounding the plasma centre. Then, these regions seem to diffuse slowly to the centre until a homogeneous glow is obtained once again.

In the previous section, only the central part of the plasma was observed when the interference filter was removed. Indeed, the observed region was too small and due to the viewing angle, out of focal plane information was lost. The whole plasma recording allows to identify the dark (during contraction) and bright (during expansion) plasma edge regions. These observations show that the increase of plasma glow in the centre is really a concentration of the plasma towards the centre at the expense of the plasma edges. After that, the reverse situation occurs with plasma edges brighter than in the stable void situation.

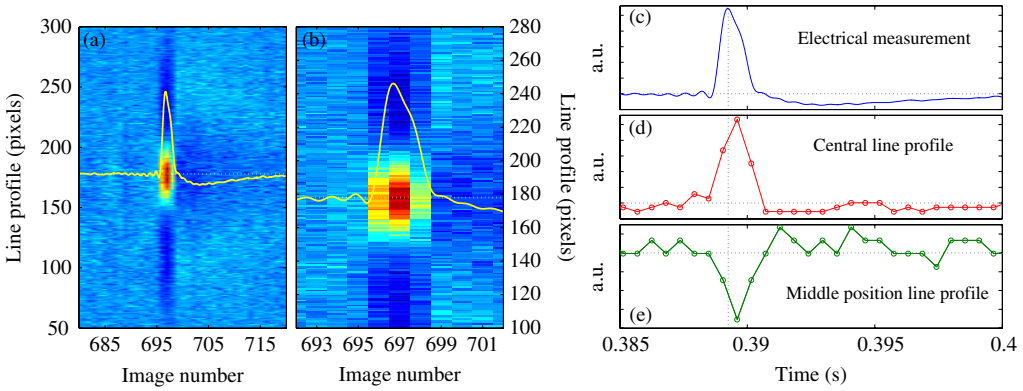

Figure 9. (a) Line profile (in false colours from dark blue to red) calculated from the image series presented in figure 7 with electrical measurements superimposed; (b) zoom of (a); (c) electrical measurements; (d) central line (line 178) profile of (a); (e) middle position line (line 105) profile of (a).

Correlation with electrical results is presented in figures 9(a) and (b) with non smoothed images in order to get pixel precision. The dotted curve is the current continuous component. From this superimposition it can be deduced that the contraction corresponds to an increase in the global ionisation (i.e. electron density). Indeed, increase of central plasma glow corresponds to an increase of electrical signal amplitude meaning that this central increase is not compensated by the decrease in the near plasma edge. Then, when the reverse situation occurs, ionisation appears to be below the stable situation value (as indicated by electrical measurements). Indeed, the dark central region is not balanced by the larger but slightly brighter near edge regions. Finally, these regions tend to rejoin in the centre following the slow increase observed in electrical measurements. These behaviours are also visible by comparing electrical measurements with line profiles (figures 9(c)–(e)) extracted from figure 9(a) (not to be confused with temporal evolution of line profile extracted from video images) and physically corresponding to the time evolution of individual pixels taken in (d) plasma centre and in (e) the near edge.

4.2. Sequences with a high repetition rate

When the heartbeat instability frequency increases, contraction–expansion sequences are closer in time, and no exact return to original stable conditions is achieved. Indeed, the next sequence happens while the void size has not reached its stable state. The case presented here is quite similar to the one shown in figures 5 and 6. The corresponding video is presented in figure 10 showing three successive contraction–expansion sequences. Images extracted from one sequence appear in figure 10(a). Figure 10(b) is obtained from figure 10(a) in the same way as figure 7(b). As the sequence lasts longer, better time resolution is obtained and variation of plasma glow is well evidenced. In comparison with the low repetition rate case, the change from bright centre and dark edges to the reverse is here more strongly marked. The different phases of the contraction–expansion sequence that have been already described, are highly visible here.

The deduced line profile is very significant and summarises nearly all results concerning plasma glow evolution during the heartbeat instability (figure 11). Indeed, starting from a void

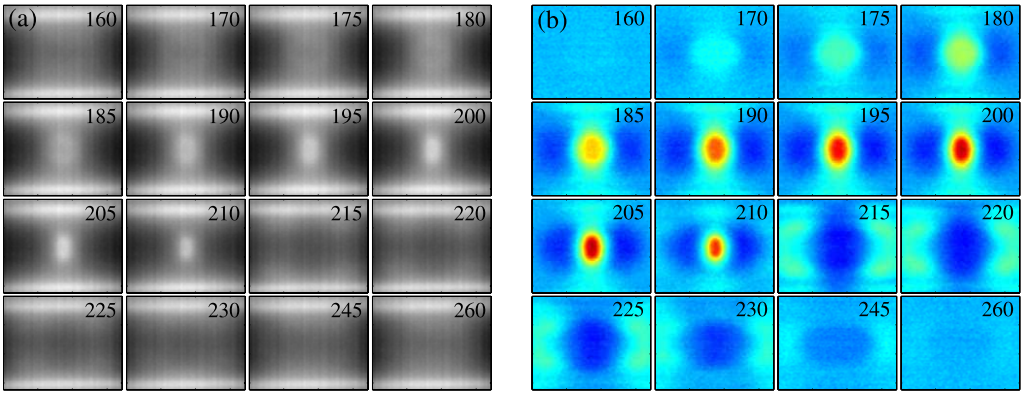

Figure 10. Heartbeat instability for a high repetition rate observed on the total plasma glow: (a) some images in true colours during one contraction–expansion sequence; (b) same images as in (a) with post-processing and false colours (from dark blue to red) (see also movie 4, 2.7 MB).

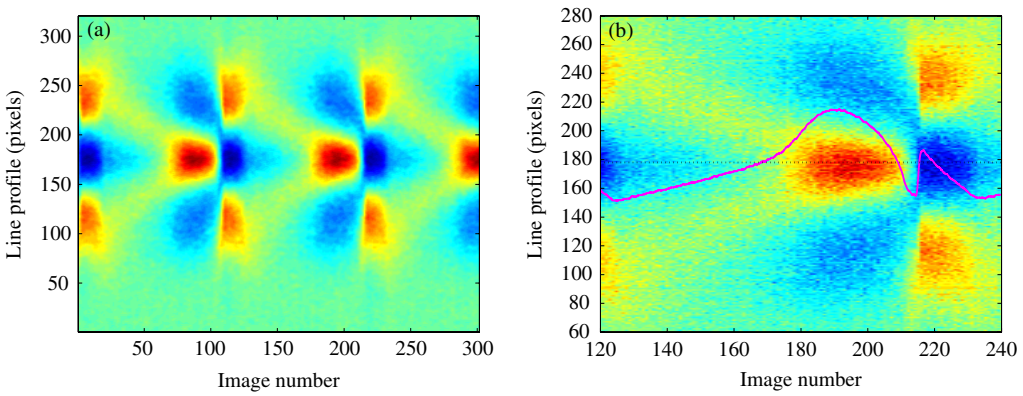

Figure 11. (a) Line profile (in false colours from dark blue to red) calculated from image series presented in figure 10; (b) zoom of (a) with electrical measurements superimposed.

expansion (dark inner part and bright plasma edges), slow concentration of the glow from the plasma edge towards the centre takes place. This motion can be correlated to the grey corona region observed in the dust cloud and presented in section 3. Furthermore, it clearly appears that the two brighter edge regions do not meet completely and no homogeneous plasma is restored as in figure 8. Indeed, the central glow increases at the expense of plasma edges before the brighter glow regions fully converge towards the plasma centre. This central enhancement is then followed by a strong and fast reversal. Electrical measurements are superimposed on the line profile in figure 11(b). The bright region moving from the plasma edge towards the plasma centre corresponds to a continuous increase of the current. Then, it appears that the strong brightness reversal is related to the presence of a sharp peak in the current. Measurements without peak certainly correspond to cases where the brightness reversal between plasma centre and edges exists, but is not strongly marked (figure 9). This sharp peak is an interesting feature already observed but not fully explained. Indeed, in [49], preliminary results suggested that this peak could be correlated to a strong glow decrease in the centre and increase in the

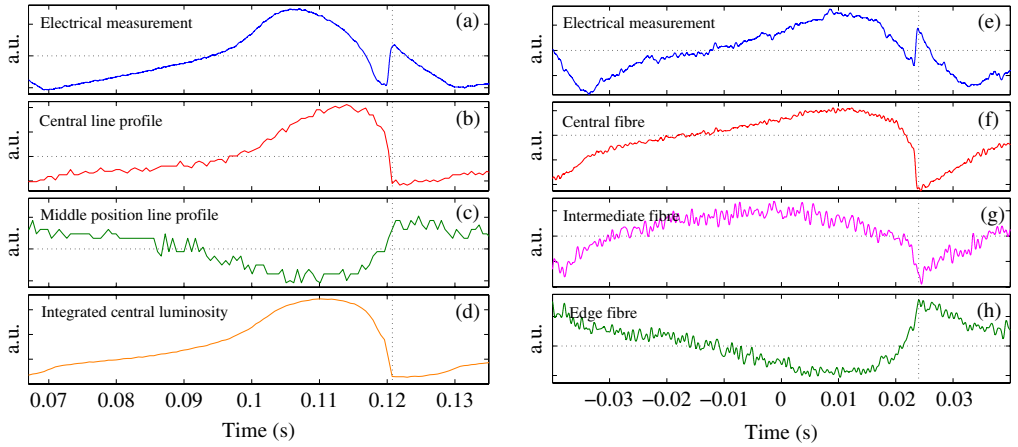

Figure 12. Extracted data from figure 11: (a) electrical measurements; (b) central line profile; (c) line profile in the glow reversal region. (d) Plasma glow integrated on a small central volume from complete image series of figure 10. Previous measurements in similar conditions for (e) electrical measurements; (f) light recorded by a centred optical fibre; (g) intermediate fibre; (h) edge fibre (same observed region as (c)).

plasma edge. These measurements were performed thanks to a spatially resolved (four different positions) analysis of an argon line emission at 750.4 nm. Further results with five optical fibres (also used for characterisation of dust particle growth instabilities [53]) and integrating all plasma wavelengths gave similar results [51] but no complete description was available. Present results greatly enhance spatiotemporal resolution of this phenomenon and clearly correlate the sharp peak with an enhancement of the plasma glow outside the central region. Variations of electrical measurements are representative of global changes of the plasma (spatially integrated measurement). From the present analysis it appears that electrical measurements are not only dominated by the plasma core.

These effects are also evidenced in figure 12 by direct comparison of (a) electrical measurements, with data extracted from figure 11: (b) central line profile (i.e. physically corresponding to central pixel variation), (c) middle position line profile (i.e. variation of a pixel in the glow reversal zone) and from the video in figure 10: (d) integrated central luminosity (i.e. variation integrated in a small centred volume assumed to represent plasma core). Comparison of figure 12(a), (b) and (d) shows that the main central plasma changes are observed in electrical measurements. Nevertheless, it appears that the maximum value of central glow occurs while electrical measurements have already decreased. In fact, at this time, electrical measurements are affected by the edge plasma glow decrease as observed in figure 12(c). Finally, the sharp peak region is well understood thanks to figure 11(b) and figure 12(a)–(d). Opposite behaviour of electrical measurements and central glow is directly related to the strong and fast enhancement of plasma edges while the centre becomes the less luminous part.

In order to show consistency of the new results, previous measurements performed in similar instability conditions (i.e. similar electrical measurements) with the optical fibre diagnostics, are presented in figure 12(e)–(h). Here, the edge fibre (figure 12(h)) observes the region corresponding to the middle line profile of figure 12(c). The intermediate fibre observes

a region in between the centre and the edge. Its maximum value appearing before the one of figure 12(f) traduces the plasma concentration towards centre. Main features concerning the sharp peak region are observed: the peak corresponds to a glow reversal between the centre and the edge. This comparison is of major interest because it confirms that no artefacts, neither in the way measurements are performed nor in data retrieval from images, are implied for explanation of the sharp peak region.

5. Discussion and conclusion

From the different analyses, several features of the heartbeat instability can be brought to the fore: the void contraction corresponds to an increase of the central plasma glow. These observations tend to show that a sudden higher ionisation in the plasma centre enhances the ratio between the inward electrostatic force and the outward ion drag force. Then, the void centre becomes darker but dust particles continue to move towards the centre due to their inertia. Their motion seems more or less continuous (at relatively constant speed) and is stopped suddenly (see for example figure 1). The void is not entirely filled by dust particles meaning that a force prevents further motion towards its centre. This force also exceeds gravity that should induce void collapse by acting on, among others, dust particles constituting the upper part of the void. At this time the central glow is not very bright. Furthermore, it appears more or less homogeneous, a property usually associated with a weak electric field. The force stopping dust particles is then supposed to be the ion drag.

Dust particles located near the plasma centre are then nearly immobile while a dust particle 'wave front' coming from the plasma edge starts to be detected. At this time, a corona region of higher ionisation is observed in plasma glow images. This region surrounds the plasma centre and moves slowly towards it. Correlating dust cloud images with plasma glow ones, this moving region seems to correspond to the dust particle wave front. Darker centre and brighter edge can create an outward electrostatic force near the corona region. This hypothesis is assumed by analogy with the contraction phase when an enhanced glow region attracts dust particles. Thus, central dust particles are immobile (far from this interface) and the wave front corresponds to dust particles close to the corona region and moving towards it. As dust particles move, local conditions change and the corona region moves towards the centre attracting inner dust particles one after the other. As the plasma becomes more and more homogeneous, the wave front speed decreases and the last dust particles to move are finally the closest to the plasma centre.

In the case of low repetition rate sequences, the original stable position of the void is restored between each sequence that can be considered as isolated and independent. On the contrary, high repetition rate conditions lead to a continuous motion of the dust particles. Indeed, while central dust particles return to their original position, a new contraction occurs.

An asymmetry in void contraction has been evidenced in some cases. This behaviour can find its origin in the discharge geometry, confined by electrodes in the vertical direction and more free to diffuse in the horizontal one. It is confirmed by the observed corona region in plasma glow images. Indeed, it is better observed near the horizontal edges than near the vertical ones where it is merged with the bright presheath regions.

The sharp peak in electrical measurements can be associated with the glow reversal from bright centre and dark edges to bright edges and dark centre. It appears when this phenomenon is strongly marked. It is replaced by a change in signal slope in other cases. This reversal is very fast and our camera system does not allow to resolve this phenomenon in time. The optical

fibre diagnostics have a high time resolution but noise is relatively important and the data do not show if there is a wave propagation between centre to edge during the reversal. The reversal seems to be instantaneous and its physical origin is under investigation.

Acknowledgments

The PKE-Nefedov chamber has been made available by the Max-Planck-Institute for Extraterrestrial Physics, Germany, under the funding of DLR/BMBF under grants No. 50WM9852. We would like to thank S Dozias for electronic support and J Mathias for optical support. ESA and Kayser-Threde GmbH are acknowledged for providing the high speed camera system in the framework of the IMPACT programme. This work was supported by CNES under contract 02/CNES/4800000059.

References

[1] Walch B, Horanyi M and Robertson S 1994 *IEEE Trans. Plasma Sci.* **22** 97
[2] Melzer A, Trottenberg T and Piel A 1994 *Phys. Lett.* A **191** 301
[3] Arnas C, Mikikian M and Doveil F 1999 *Phys. Rev.* E **60** 7420
[4] Samarian A A and Vladimirov S V 2003 *Phys. Rev.* E **67** 066404
[5] Ratynskaia S *et al* 2004 *Phys. Rev. Lett.* **93** 085001
[6] Couëdel L, Mikikian M, Boufendi L and Samarian A A 2006 *Phys. Rev.* E **74** 026403
[7] Morfill G E, Thomas H M, Konopka U, Rothermel H, Zuzic M, Ivlev A and Goree J 1999 *Phys. Rev. Lett.* **83** 1598
[8] Nefedov A P *et al* 2003 *New J. Phys.* **5** 33
[9] Roth R M, Spears K G, Stein G D and Wong G 1985 *Appl. Phys. Lett.* **46** 253
[10] Watanabe Y, Shiratani M, Kubo Y, Ogawa I and Ogi S 1988 *Appl. Phys. Lett.* **53** 1263
[11] Bouchoule A, Plain A, Boufendi L, Blondeau J P and Laure C 1991 *J. Appl. Phys.* **70** 1991
[12] Howling A, Hollenstein C and Paris P J 1991 *Appl. Phys. Lett.* **59** 1409
[13] Bouchoule A, Boufendi L, Hermann J, Plain A, Hbid T, Kroesen G, Stoffels E and Stoffels W W 1996 *Pure Appl. Chem.* **68** 1121
[14] Boufendi L, Gaudin J, Huet S, Viera G and Dudemaine M 2001 *Appl. Phys. Lett.* **79** 4301
[15] Cavarroc M, Jouanny M C, Radouane K, Mikikian M and Boufendi L 2006 *J. Appl. Phys.* **99** 064301
[16] Selwyn G S, Singh J and Bennett R S 1989 *J. Vac. Sci. Technol.* A **7** 2758
[17] Cavarroc M, Mikikian M, Perrier G and Boufendi L 2006 *Appl. Phys. Lett.* **89** 013107
[18] Roca i Cabarrocas P, Gay P and Hadjadj A 1996 *J. Vac. Sci. Technol.* A **14** 655
[19] Dutta A, Lee S P, Hayafune Y, Hatatani S and Oda S 2000 *Japan. J. Appl. Phys.* **39** 264
[20] Dutta A, Hayafune Y and Oda S 2000 *Japan. J. Appl. Phys.* **39** L855
[21] Deschenaux C, Affolter A, Magni D, Hollenstein C and Fayet P 1999 *J. Phys. D: Appl. Phys.* **32** 1876
[22] Hong S, Berndt J and Winter J 2003 *Plasma Sources Sci. Technol.* **12** 46
[23] Pereira J, Géraud-Grenier I, Massereau-Guilbaud V and Plain A 2005 *Thin Solid Films* **482** 226
[24] Stefanović I, Kovačevic E, Berndt J and Winter J 2003 *New J. Phys.* **5** 39
[25] De Bleecker K, Bogaerts A and Goedheer W 2006 *Phys. Rev.* E **73** 026405
[26] Robertson J 2002 *Mater. Sci. Eng.* R **37** 129
[27] Zhou D, McCauley T G, Qin L C, Krauss A R and Gruen D M 1998 *J. Appl. Phys.* **83** 540
[28] Szopa C, Cernogora G, Boufendi L, Correia J J and Coll P 2006 *Planet. Space Sci.* **54** 394
[29] Selwyn G S, McKillop J S, Haller K L and Wu J J 1990 *J. Vac. Sci. Technol.* A **8** 1726
[30] Ganguly B, Garscadden A, Williams J and Haaland P 1993 *J. Vac. Sci. Technol.* A **11** 1119
[31] Praburam G and Goree J 1996 *Phys. Plasmas* **3** 1212

[32] Mikikian M, Boufendi L, Bouchoule A, Thomas H M, Morfill G E, Nefedov A P, Fortov V E and PKE-Nefedov Team 2003 *New J. Phys.* **5** 19
[33] Winter J 1998 *Plasma Phys. Control. Fusion* **40** 1201
[34] Arnas C, Dominique C, Roubin P, Martin C, Brosset C and Pégourié B 2006 *J. Nucl. Mater.* **353** 80
[35] Dorier J L, Hollenstein C and Howling A 1995 *J. Vac. Sci. Technol.* A **13** 918
[36] Goree J, Morfill G E, Tsytovich V N and Vladimirov S V 1999 *Phys. Rev.* E **59** 7055
[37] Samsonov D and Goree J 1999 *Phys. Rev.* E **59** 1047
[38] Akdim M R and Goedheer W J 2001 *Phys. Rev.* E **65** 015401
[39] Jovanović D and Shukla P K 2003 *Phys. Lett.* A **308** 369
[40] Gozadinos G, Ivlev A V and Boeuf J P 2003 *New J. Phys.* **5** 32
[41] Avinash K, Bhattacharjee A and Hu S 2003 *Phys. Rev. Lett.* **90** 075001
[42] Tsytovich V N, Morfill G, Konopka U and Thomas H 2003 *New J. Phys.* **5** 66
[43] Zafiu C, Melzer A and Piel A 2003 *Phys. Plasmas* **10** 1278
[44] Schauer J C, Hong S and Winter J 2004 *Plasma Sources Sci. Technol.* **13** 636
[45] Kretschmer M, Khrapak S A, Zhdanov S K, Thomas H M, Morfill G E, Fortov V E, Lipaev A M, Molotkov V I, Ivanov A I and Turin M V 2005 *Phys. Rev.* E **71** 056401
[46] Vladimirov S V, Tsytovich V N and Morfill G E 2005 *Phys. Plasmas* **12** 052117
[47] Land V and Goedheer W J 2006 *New J. Phys.* **8** 8
[48] Goree J, Quinn R A, Morfill G E, Thomas H M, Hagl T, Konopka U, Rothermel H and Zuzic M 1998 *Proc. 4th Microgravity Fluid Physics and Transport Phenomena Conf.* (*Cleveland*)
[49] Mikikian M and Boufendi L 2004 *Phys. Plasmas* **11** 3733
[50] Mikikian M, Boufendi L and Bouchoule A 2003 *Proc. 30th EPS Conf. on Contr. Fusion and Plasma Phys.* (*St Petersburg*) (ECA vol 27A) ed R Koch and S Lebedev pp O–3.1B online at http://epsppd.epfl.ch/StPetersburg/pdf/O3_001b.pdf
[51] Mikikian M, Cavarroc M, Chaumeix N and Boufendi L 2004 *Proc. 31st EPS Conf. on Plasma Phys.* (*London*) (ECA vol 28G) ed P Norreys and H Hutchinson (Petit-Lancy: European Physical Society) pp O–2.13. Online at http://epsppd.epfl.ch/London/pdf/O2_13.pdf
[52] Mikikian M, Cavarroc M and Boufendi L 2005 *New Vistas in Dusty Plasmas* ed L Boufendi, M Mikikian and P K Shukla *AIP Conf. Proc.* vol 799 p 323
[53] Mikikian M, Cavarroc M, Couëdel L and Boufendi L 2006 *Phys. Plasmas* **13** 092103

Nucléation, croissance et comportement de poussières dans les plasmas réactifs radiofréquence basse pression : Des nanocristaux aux grains submicroniques polycristallins

Les gaz ionisés contenant des particules solides, appelés plasmas poussiéreux, sont principalement utilisés pour le dépôt de couches minces et la synthèse de nanoparticules aux propriétés maîtrisées.

L'objectif de cette thèse était de synthétiser des poussières de taille et/ou composition chimique connues en vue d'applications en microélectronique, photovoltaïque (nanocristaux de silicium) et astrophysique (tholins, ISD grains).

La localisation et l'étude du démarrage de la phase d'agrégation des nanocristaux, par l'étude paramétrique d'une instabilité, ont été réalisées dans des plasmas d'Argon/Silane. Puis, une étude de la forme et du comportement du nuage de poussières a été menée dans deux décharges différentes. Elles ont mis en évidence la forte influence de la croissance des poussières sur le plasma et sur le nuage, et d'optimiser nos paramètres de dépôt pour les nanocristaux de silicium non-agglomérés. Une étude paramétrique des caractéristiques électriques du plasma (courant, tension et densités électronique et ionique) en Azote/Méthane a permis de cibler les meilleurs paramètres pour synthétiser des tholins (aérosols analogues de Titan). Par ailleurs, l'ellipsométrie *in-situ* de Mie-Rayleigh en chimie Azote/Acétylène nous a donné certaines informations sur les analogues de poussières interstellaires synthétisés (structure, indice optique). Finalement, l'effet des basses températures de gaz a été exploré afin d'augmenter la taille des nanocristaux de silicium. Différentes hypothèses (chimiques et thermodynamiques) sont discutées dans le but d'expliquer les effets observés : accélération de la cinétique de croissance et augmentation de la taille des nanocristaux.

Mots-Clés : nanocristaux, silicium, PECVD, plasmas poussiéreux, nanoparticules, gaz réactifs, void, instabilités, décharge rf, couches minces nanostructurées, poussières

Nucleation, growth and behavior of dust particles in reactive low pressure radiofrequency plasmas: From nanocrystals to submicron polycrystalline grains.

Ionized gases containing fine solid particles, called dusty plasmas, are used mainly to deposit nanostructured thin film layers and to synthesize nanoparticles with controlled properties.

The main objective of this PhD thesis was to succeed in synthesizing dust particles of desired size and/or chemical composition, for applications in microelectronics, photovoltaic conversion (silicon nanocrystals) and astrophysics (tholins, ISD grains).

The localization and the study of the beginning of the aggregation phase have been performed through a parametric study of an instability in Argon/Silane plasmas. Then, a study of the dust cloud shape and behavior has been performed in two different discharges. Those studies brought to the fore the strong influence of dust particle growth on both the plasma characteristics and the dust cloud. They allowed us to optimize our deposition parameters to synthesize single-crystal silicon nanoparticles. A parametric study of the electrical characteristics of the plasma (current, voltage, electron and ion densities) in Nitrogen/Methane allowed us to target the best parameters to synthesize tholins (Titan's aerosol analogues). Moreover, *in-situ* Mie-Rayleigh ellipsometry in Nitrogen/Acetylene plasmas gave us information concerning the synthesized ISD grains structure, optical index). Finally, low gas temperature effects have been investigated in order to increase the size of the single-crystal silicon nanoparticles. Different hypothesis (chemical and thermodynamical) are discussed in order to explain the obtained results: dust formation kinetics accelerated and increase in the nanocrystal size.

Key-words : single crystal silicon nanoparticles, silicon, PECVD, dusty plasmas, nanoparticles, reactive gases, void, instabilities, rf discharge, nanostructured thin layers, dust grains

Discipline : Physique des plasmas

GREMI (Groupe de Recherches sur l'Energétique des Milieux Ionisés)

UMR 6606 CNRS/Université d'Orléans

14 rue d'Issoudun, BP 6744, 45067 Orléans Cedex 2, France